AN INVESTIGATION OF MULTI-LAYER INTEGRATED PASSIVE STRUCTURES FOR APPLICATION AS THREE-PHASE EMI FILTERS

by

KYLIE DE JAGER

Dissertation submitted in partial fulfilment of the requirements for the degree of

MASTER IN ENGINEERING

in

ELECTRICAL AND ELECTRONIC ENGINEERING

in the

FACULTY OF ENGINEERING

at the

UNIVERSITY OF JOHANNESBURG

Supervisor: Dr. I. W. Hofsajer

June, 2006

Summary

The advent of the integration of discrete passive components is a direct result of the drive towards the minimisation of power electronic converters and filters. To this end Integrated Power Passive Modules (IPPMs) have been utilised in the past. The IPPMs discussed in this dissertation refer to structures consisting of dielectric layers sandwiched between layers of conductive material. The use of these types of structures in various applications has been well documented. However, the applications have been single-phase in nature and the exact configuration of the IPPMs has been largely dependent on the designers' past experience with the modules.

The development of a synthesis procedure to identify the required configuration for any particular application would be of great benefit to designers. The foundation of such a synthesis procedure was laid through an exhaustive search of all possible configurations that can be realised with a three conductive layer IPPM. From this exhaustive search a number of general trends, between the configurations and their associated frequency response, were observed. Furthermore, a number of principles underlying the functionality of the configurations were highlighted during the course of the exhaustive search.

The validity of some of these results was experimentally investigated through the design and implementation of an integrated EMI filter. The EMI filter considered in this study differed from integrated EMI filters, previously reported on, through the fact that the filter considered herein was to be implemented in a three-phase application.

To this end a set of configurations that realise low pass filters were identified from the results of the exhaustive search. The application of these configurations was expanded from single-phase to three-phase by mapping the configurations onto a building block component used to realise the three-phase application. Simulations of these three-phase filters were used to analyse the filter performance. From this analysis a subset of configurations were identified as displaying the best performance characteristics. The configurations within this subset were further analysed using the results of the exhaustive search. In so doing two configurations were isolated for use in a practical realisation of the three-phase filters.

The physical design and construction of the integrated three-phase filters, as well as the test bench, was considered. The performance of the filters was investigated through comparative measurements of common mode and differential mode currents, in the test bench, in the presence and absence of the filters. From this investigation significant reduction in the conducted EMI noise was seen through the introduction of the filters into the system.

Opsomming

Die koms van integrasie vir diskrete, passiewe komponente is direk as gevolg van die aanvraag vir kleiner drywingsomsetters en filters. Hiervoor was "Integrated Power Passive Modules" (IPPM's) in die verlede gebruik. Die IPPM's wat bespreek word in hierdie Magisterondersoek verwys na strukture wat bestaan uit dielektriese lae geset tussen lae geleidende materiaal. Die gebruik van hierdie tipe strukture vir allerlei toepassings is reeds goed gedokumenteer. Hierdie toepassings is alhoewel van 'n enkelfase geaardheid en die presiese konfigurasies van die IPPM's hang grootendeels van die ontwerper se ondervinding af.

Die ontwikkeling van 'n simulasie prosedure om verlangde konfigurasies vir spesifieke doeleindes te identifiseer sal baat vind by ontwerpers. Die basis vir so 'n prosedure was gelê deur 'n soektog na alle konfigurasies wat moontlik realiseerbaar is deur 'n drie geleier laag IPPM. Vanuit hierdie soektog kan 'n hoeveelheid tendense tussen konfigurasies en hulle ooreenkomstige frekwensie respons waargeneem word. Verder is 'n hoeveelheid riglyne uitgelig aangaande die funksionaliteit van die konfigurasies gedurende die ondersoek.

Die geldigheid van sekere resultate was eksperimenteel ondersoek deur die ontwerp en implimentering van 'n geïntegreerde Elektromagnetiese Steuring (EMS) filter. Die EMS filter wat oorweeg was in hierdie ondersoek verskil van intergreerde EMS filters wat voorheen beskou was, op grond van die feit dat die filters wat hier ondersoek was vir 'n driefase toepassing gebruik was.

'n Stel konfigurasies wat 'n laaglaatfilter realiseer was uitgelig uit die resultate van die soektog. Die toepassing van hierdie konfigurasies was uitgebrei van enkelfase na driefase deur die konfigurasies te projekteer na 'n boublok komponent gebruik om driefase toepassings te realisieer. Simulasies van hierdie driefase filters was gebruik om die filtergedrag te analiseer. Vanuit hierdie analise was 'n groepering konfigurasies geidentifiseer volgens beste verrigting. Die konfigurasies in hierdie groepering was nog verder ondersoek deur gebruik te maak van die resultate van die soektog. Sodoende was twee konfigurasies geisoleer vir die praktiese realisering van 'n driefase filter.

Die fisiese ontwerp en vervaardiging van die geïntegreerde driefase filters, sowel as die toetsapparaat was oorweeg. Die verrigting van die filters was ondersoek deur vergelykende metings van gemene modus en differensiële modus strome in die toetsopstelling te neem, tydens aan- en afwesigheid van die filters. Vanuit hierdie ondersoek was noemenswaardige vermindering van versende EMS ruis opgelet deur die byvoeging van hierdie filters in die sisteem.

The author would like to thank:

- The Creator for the privilege
- Dr. I. W. Hofsajer for his guidance and for allowing me to approach my studies as I saw fit
- My family, Marco and my friends for their support and patience
- My fellow Master students in and out of the NIET group
- The manufacturers and distributors of *Coca-Cola*^{TM}

"Attempt the end, and never stand to doubt;
Nothing's so hard, but search will find it out."

- Robert Herrick

Content

List of tables

List of figures

List of symbols

Latin letters

Symbol	Unit	Description
a		Three-phase CM current fraction in line 1
A	m^2	Plate area of a parallel plate capacitor
b		Three-phase CM current fraction in line 2
Ba		Barium
BaTiO$_3$		Barium Titanate
$C_{1,2}$	F	Quasi-distributed model shunt capacitance
C	F	Capacitance
$C_{bootstrap}$	F	Bootstrap capacitance
C_{fu}		Coupling coefficient between filter-units
C_o		Coupling coefficient
Cu		Copper
d	m	Distance between plates of a parallel plate capacitor
f_1	Hz	Fundamental inverter frequency
f	Hz	Frequency of operation
f_s	Hz	Switching frequency of inverter
f_{start}	Hz	Minimum frequency of IPPM simulation
f_{stop}	Hz	Maximum frequency of IPPM simulation
H$_{1,2,3}$		High side MOSFET gate signal
H		Traditional transfer function
H_{ideal}		Traditional transfer function with ideal coupling
H_{RC}		RC filter transfer function
H_{sys}		System transfer function
$H_{sys-ideal}$		System transfer function with ideal coupling
i_{cm}	A	Total three-phase CM current
$i_{dm1,2,3}$	A	Three-phase DM current inherent to lines 1, 2 and 3
$i_{L1,2,3}$	A	Current flowing through inductors L_1, L_2 and L_3
$I_{1,2,3}$	A	Total three-phase line currents
I_{1-meas}	A	Three-phase line current measurement
$I_{Cbs(leak)}$	A	Bootstrap capacitor leakage current
$I_{cm1,2}$	A	Single-phase CM current in lines 1 and 2

$I_{cm\text{-}meas}$	A	Measured three-phase CM current
$I_{CM1,2,3}$	A	Three-phase CM current components
I_{dm1}	A	Single-phase DM current in lines 1 and 2
$I_{dm\text{-}meas1,2,3}$	A	Measured three-phase DM current on lines 1, 2 and 3
I_D	A	MOSFET drain current
$I_{DM1,2,3}$	A	Three-phase DM current components
I_F	A	Diode forward current
$I_{qbs(max)}$	A	Quiescent current for high side driver circuitry
I/O$_i$		Element of a set of I/O connections
$L_{1,2,3}$	H	Quasi-distributed model series inductance
L$_{1,2,3}$		Low side MOSFET gate signal
L	H	Self inductance
M	H	Mutual inductance
m_a		Amplitude modulation ratio
n		Number of conductive layers in an IPPM
N_{config}		Number of configurations
N_{connec}		Number of connection matrices associated with an IPPM
$N_{I/O}$		Number of I/O matrices associated with an IPPM
p		Number of I/O connections in a configuration
PB_r		Pass-band ratio
Q$_{1,2,3,4,5,6}$		MOSFET switches of PWM inverter
Q_{bs}	C	Minimum charge to be supplied by bootstrap capacitor
Q_g	C	Gate charge of high side MOSFET
Q_{ls}	C	Level shift charge per cycle
r_{on}	Ω	MOSFET on resistance
R	Ω	Resistance
R$_c$	Ω	Interconnection resistance of IPPM simulation
$R_{f1,2,3,4,5,6}$	Ω	Terminal impedance of IPPM simulation
$R_{g1,2,3}$	Ω	Quasi-distributed model shunt conductance
R_l	Ω	Load resistance of single-phase IPPM simulation
R_{ly}	Ω	Star connected load of three-phase IPPM simulation
R_{ld}	Ω	Delta connected load of three-phase IPPM simulation
$R_{s1,2,3}$	Ω	Quasi-distributed model series resistance
R$_s$	Ω	Source resistance of IPPM simulation
$sig_{1,2,3}$		Control signals of the PWM inverter

Ti		Titanium
t_{rr}	s	Diode reverse recovery time
$v_{1,2,3}$	V	Potential difference across inductors L_1, L_2 and L_3
$v_{a,b,c}$	V	Potential difference across coupled inductors
$v_{control}$	V	PWM control signal
v_{saw}	V	PWM saw tooth waveform
$V_{A,B,C,D,E,F,x,y}$	V	Absolute potential at terminal of inductor string
V_{bsuv}	V	Undervoltage lockout
V_{bus}	V	Bus voltage
V_{cc}	V	Low side fixed supply voltage
$\hat{V}_{control}$	V	Peak value of PWM control signal
V_{ds}	V	Drain-source voltage
V_f	V	Forward voltage drop across diode
V_{GH}	V	Voltage drop across a CM impedance
V_{in}	V	Voltage at input terminal of IPPM
V_{in-dB}	dB	Voltage in dB at input terminal of IPPM
V_{IJ}	V	Voltage drop across a DM impedance
V_{LLrms}	V	Inverter line-to-line output voltage
V_{LS}	V	Voltage drop across the low side MOSFET
V_{min}	V	Minimum voltage across bootstrap capacitor
V_{out}	V	Voltage at output terminal of IPPM
V_{out-dB}	dB	Voltage in dB at output terminal of IPPM
V_{RRM}	V	Diode peak repetitive reverse voltage
$V_{s1,2,3}$	V	Voltage sources of three-phase DM IPPM simulation
V_s	V	Voltage source of IPPM simulation
$\hat{V}_{saw}$	V	Peak value of PWM saw tooth waveform
Z	Ω	Impedance magnitude
Z_{cm}	Ω	CM impedance
Z_{dm}	Ω	DM impedance
Z_{in}	Ω	Input impedance seen by voltage source
Z_{LCI}	Ω	Single-port network impedance
Z_{LCII}	Ω	Two-port network impedance

Greek letters

Symbol	Unit	Description
α		Fraction of three-phase DM current on return lines
β		Fraction of three-phase DM current on return lines
γ		Fraction of three-phase DM current on return lines
ε_o	F/m	Permittivity of free space
ε_r		Relative permittivity
θ	rad	Impedance angle
ω	rad/s	Frequency
ω_c	rad/s	Cut-off frequency

Acronyms

BPF	Band Pass Filter
BSEI	Back Scattered Electron Image
BSF	Band Stop Filter
CM	Common Mode
DM	Differential Mode
DUT	Device Under Test
EMI	Electromagnetic Interference
ESR	Equivalent Series Resistance
HF	High Frequency
HPF	High Pass Filter
I/O	Input/Output
IPPM	Integrated Power Passive Module
KCL	Kirchoff's Current Law
KVL	Kirchoff's Voltage Law
LF	Low Frequency
LPF	Low Pass Filter
MEMS	Microelectromechanical Systems
PWB	Printed Wiring Board
PWM	Pulse-Width-Modulated
RF	Radio Frequency
VSI	Voltage Source Inverter

CHAPTER 1

Introduction and problem statement

In the power electronics field there has been a drive towards the minimisation of components in an attempt to increase the power density of converters and filters. As a result, much research has been done on the integration of discrete passive components, into what has become known as Integrated Power Passive Modules (IPPMs) [1]. These IPPMs have been implemented in a number of different applications [2, 3, 4]. However, the manner in which the IPPM is implemented for each application has always been based on the designers' past experience with the modules as not much generic design information is available for the IPPMs.

Not only this, the applications for which the IPPMs have been considered and investigated have generally been single-phase in nature. After extensive searching it would appear that the use of IPPMs as filters in a three-phase system has not been considered to date.

As a means of determining the feasibility of the three-phase application of IPPMs, an investigation into the integration of a three-phase electromagnetic interference (EMI) filter was performed. The approach taken towards the study was not to realise a high performance integrated filter, but rather to investigate a more generalised IPPM design procedure. This was achieved by performing an exhaustive search of all possible manners in which a particular subgroup of passive IPPMs could be implemented. The novelty of such an exhaustive search lay in the fact that this type of approach has not been used before in the design and implementation of the integrated modules. The results of this analysis were used to design and manufacture the integrated three-phase EMI filter, the performance of which was tested in a practical setup. In so doing the design procedure and some of the principles investigated were validated.

A pulse-width-modulated (PWM) inverter variable speed induction motor drive was used as the test bench for the filters. This application was selected as it is one of the most typical three-phase filter applications in industry.

Before the integrated filters could be realised it was first necessary to gain a better understanding of the selected test bench setup and the EMI issues to be addressed in such a system. It was also necessary to review aspects of the IPPMs that have been previously investigated and to clarify certain terminology used throughout this dissertation. In this chapter these issues are addressed. Many of the aspects brought to light herein serve as a reference for the direction taken during the course of the investigation.

1.1   EMI in induction motor drives

The induction motor and its speed drive were the constituent parts of the test bench that would eventually be used to evaluate the performance of the integrated filter. The variable speed drive was realised with a voltage source (VSI) switch mode three-phase inverter. Various topologies [5] and control schemes [6] of such inverters exist. In this study however, the most commonly used six-pulse three-phase in-

verter topology [5] and a carrier-based PWM switching scheme [6] were used for simplicity. This was due to the fact that the main focus of the study was the feasibility of the three-phase implementation of the IPPMs, and not the design of the motor drive.

The large di/dt and dv/dt associated with the switch mode operation of these inverters produces unwanted electrical signals, known as EMI [7]. EMI signals tend to occur at high frequencies and do not carry large amounts of energy. These signals can be divided into two categories: radiated EMI and conducted EMI [5]. Radiated EMI is characterised as electronic noise that radiates into free space. However, this form of EMI is not applicable to this study and no further consideration was given to it. Conducted EMI manifests itself in the form of common mode (CM) and differential mode (DM) noise [8]. In an inverter motor drive the exact frequency spectrum of conducted EMI is dependent on the choice of topology and switching scheme used in the inverter, as well as the response of the system to these excitation sources [9]. However, regardless of these choices conducted EMI in the induction motor drive application gives rise to bearing currents and shaft voltages in the induction motor. These phenomena are detrimental to the motor and normally responsible for shortening the lifetime of the motor [7, 10].

1.2   EMI filters for motor drives

In practice filters are commonly used to combat conducted EMI related effects such as bearing currents and shaft voltages. The EMI filters considered here are introduced on the lines connecting the inverter to the motor. By eliminating the EMI signals the filter allows the inverter to more closely approximate an ideal variable frequency three-phase power supply, as seen from the motor terminals [11]. Fig. 1.1 shows a schematic representation of the placement of the inverter, filter and motor, relative to one another.
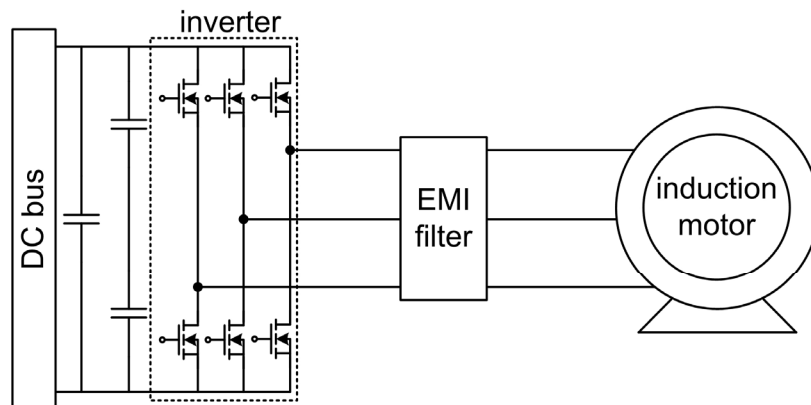
Fig. 1.1: Schematic representation of the practical setup

In practice both active and passive EMI filters are employed in various applications. However, the IPPMs considered in this study were passive in nature. Consequently only passive filters are discussed. Much research has been done into various topologies used to realise these filters. The constituent components of the passive filters are generally inductors, capacitors, resistors and diodes [11].

A large number of passive filter topologies exist for the purposes of eliminating conducted EMI. Each of these filter topologies are merely a different arrangement of capacitors and inductors [12]. In [11] a simple three-phase EMI filter using discrete components was discussed.

The filter was seen to comprise two main parts, namely a CM filter and a DM filter. Fig. 1.2 shows the general topology of each of these constituent filters. The topologies shown are not the exact topology discussed in [11] but are more beneficial towards developing an understanding of the mechanisms required of the filters for the suppression of either CM or DM noise. In order to develop such an understanding a very general definition of three-phase CM and DM noise should be kept in mind. The definition is given in [13] as "ground-loop noise" for CM noise and "line-to-line" noise for DM noise.
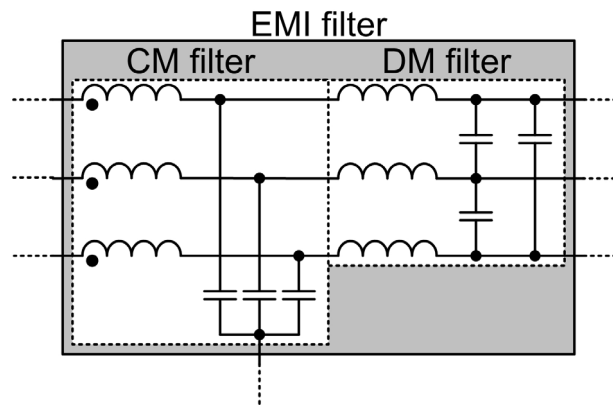
Fig. 1.2: Basic topology of CM and DM filters

The CM filter is seen to consist of a CM inductor, realised by coupling the inductors of the three lines together. The capacitors are connected in star formation due to the fact that the CM current uses the ground path as a return path.

The DM filter is similar to the CM filter, except for the fact that the inductors are not coupled together, thereby realising so-called DM inductors. The realisation of either a star or delta formation with the capacitors can be used in this filter.

When comparing these discrete filters to the IPPM technology discussed in the next section, it was seen that the construction of these filters would lend itself well towards integration. Albeit a direct mapping of the discrete filters to the integrated filters was not the aim of this study.

1.3 Passive IPPMs

In order to be able to develop a filter with the passive IPPMs considered in this study it was necessary to explore the research background of these modules. Previously the IPPMs have been referred to as spiral integrated power passive modules [1]. The structure of such IPPMs consists of a number of conductive layers separated by dielectric layers. Fig. 1.3(a) shows a pictorial representation of such a structure with two conductive layers, henceforth referred to as a two-layer IPPM. In practice, this structure is wound around a core, as shown in Fig. 1.3(b) for a single-turn three-layer IPPM. Through the use of these IPPMs it was possible to realise both an inductance and a capacitance in the same space. These structures were to serve as the fundamental building blocks of the integrated EMI filters. Fig. 1.3(c)

shows a schematic representation of the "unwound" two-layer IPPM. This schematic representation is advantageous as it shows the functionality of the materials, but without the complicated three-dimensional detail. Furthermore, the four terminals of the IPPM, A through D, are explicitly shown.
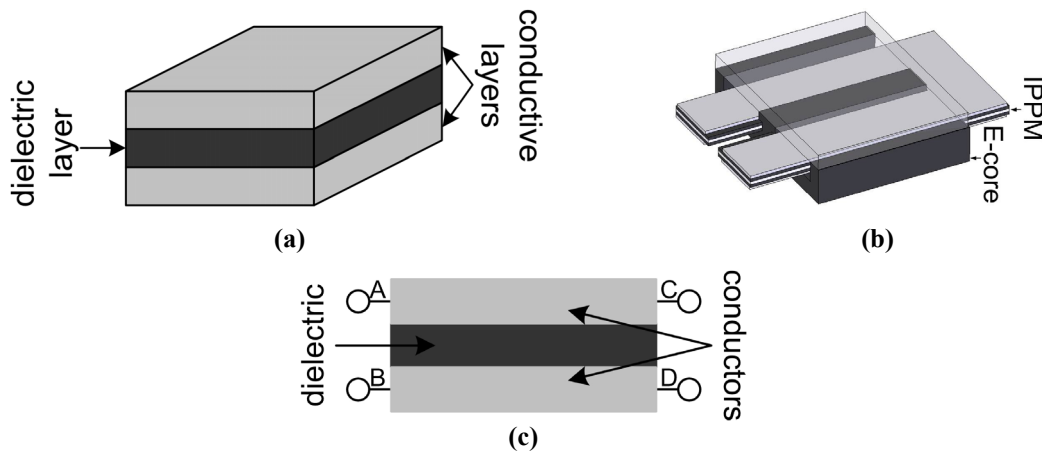
Fig. 1.3: (a) A two-layer IPPM (b) A three-layer IPPM wound around an E-core (c) Schematic representation of a two-layer IPPM

Common convention defines a configuration of an electrical system as the geometrical placement of the system elements relative to one another. A topology is defined as the functional relationship of the system elements [14]. In this dissertation the use of these two terms does not always abide by these standard conventions as both terms were used to refer to functional relationships. Instead these two terms were defined as follows:

Configuration
The configuration of an IPPM referred to the absence or presence of interconnections between the terminals of the IPPM and the assignment of input, output and/or ground terminals to the IPPM.

Topology
The topology referred to the manner in which two or more IPPMs were interconnected or coupled with one another.

For the sake of clarity it was necessary to use these definitions for the two terms as the IPPMs used to realise a single topology could themselves realise a large number of different configurations. This concept had relevance when the single-phase application of the IPPMs, discussed in the following section as well as in Chapters 2 and 3, were expanded to a three-phase application in Chapter 4.

1.3.1 Two-layer IPPMs

Previous investigation [1] into two-layer IPPMs has shown that it is possible to realise various filter responses with the IPPMs merely by altering their configuration. In this section these previous results are summarised. This formed a starting point for the exhaustive search, discussed in Chapter 2, through the introduction of the configuration concept and by giving examples of the various filter responses that it was possible to realise with the IPPMs.

Different configurations changed the "arrangement" of the inductive and capacitive components of the structure relative to one another. The most common configura-

tions realised with these two-layer IPPMs were defined as parallel resonant, series resonant and low pass filter (LPF) configurations [1].

Parallel resonant configuration

A parallel combination of an inductance and capacitance can be realised with the two-layer IPPM as shown in Fig. 1.4(a). It was possible to consider this configuration in terms of a mapping onto an equivalent circuit, as shown in Fig. 1.4(b). A band pass filter (BPF) response using the two-layer IPPM thus configured was obtained.

(a)   **(b)**

Fig. 1.4: (a) Parallel resonant configuration as realised with a two-layer IPPM (b) Equivalent circuit

Series resonant configuration

(a)   **(b)**

Fig. 1.5: (a) Series resonant configuration as realised with a two-layer IPPM (b) Equivalent circuit

It was possible to effectively realise a series combination of a capacitance and inductance using the two-layer IPPM, configured as shown in Fig. 1.5(a). The equivalent circuit representation can be found in Fig. 1.5(b). It was possible to realise a number of filter responses using this configuration depending on whether terminals B, C or D were used as the output terminal.

LPF configuration

A standard LPF configuration could be realised with the two-layer IPPMs as shown in Fig. 1.6(a) and (b). This configuration differed from the previous configurations through the introduction of a ground connection to one of the terminals.

(a)   **(b)**
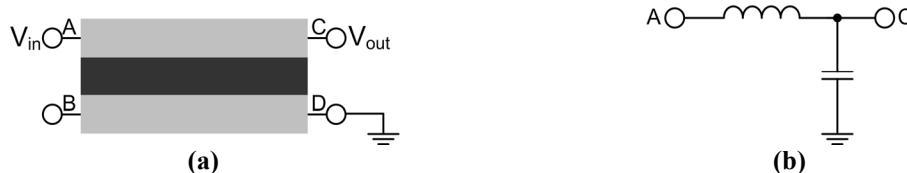
Fig. 1.6: (a) LPF configuration as realised with a two-layer IPPM (b) Equivalent circuit

1.3.2 Three-layer IPPMs

For the purpose of realising an integrated three-phase EMI filter it was decided to use three-layer IPPMs. Three-layer IPPMs are the next level of complexity in the field of integrated passives, as the two-layer IPPMs have been previously investigated [1]. Consequently, a three-layer IPPM investigation would contribute new findings to the field. The rest of this dissertation focuses on the three-layer IPPMs as a result.

Further substantiation for the use of three-layer IPPMs can be considered from a practical point of view. If it is required to realise more capacitance with the IPPM structures a dielectric with a high relative permittivity, ε_r, such as Barium-Titanate (BaTiO$_3$), could be used. However, such BaTiO$_3$ is normally in its ceramic form, which is by nature exceptionally brittle. To bypass this problem, other dielectrics with lower ε_r can be used which implies more dielectric layers would be necessary. Consequently, when considering the energy storage component capacity of the two IPPMs it can be seen that the three-layer IPPMs can realise greater values of inductance and capacitance than their two-layer counterparts.

During the investigation it was seen that the type of behaviour realised with any given configuration was not dependent on the number of layers present in the IPPM. Consequently, it is speculated that the results of the investigation of three-layer IPPMs could be used for IPPMs with more than three conductive layers as well. However the extent to which this statement is valid is left for future work and is outside the scope of this study.

In the exhaustive search two separate cases of configuration types were considered. The first case was referred to as single-port network configurations. These configurations were characterised by the presence of an input voltage terminal, V_{in}, and an output voltage terminal, V_{out}. Fig. 1.7(a) shows a schematic representation of such a single-port network as applied to a three-layer IPPM.

The second case was referred to as two-port network configurations. In this case a third terminal that was common to the input and output voltage terminals was introduced as shown in Fig. 1.7(b). This third terminal was referred to as a ground terminal, G_{rnd}.
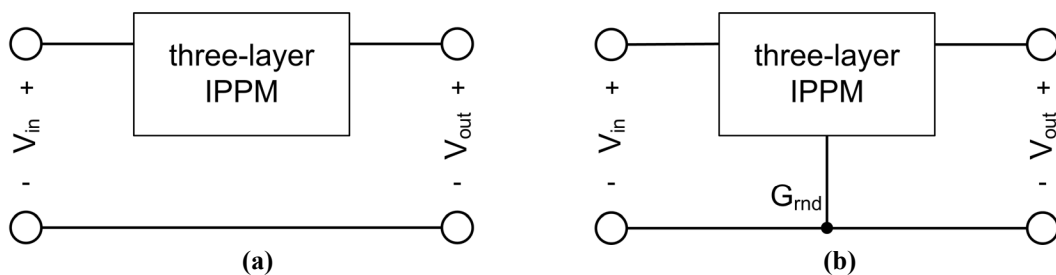
Fig. 1.7: Schematic representation of (a) a single-port network and (b) a two-port network

It should be noted that according to standard convention the two cases should be referred to as two-terminal and three-terminal two-port networks respectively [15, 16]. However, to keep ideas distinct from one another, the term *terminal* was solely used to describe the terminals of the IPPMs, while the term *port* was used in reference to the two cases considered here. These two cases were considered for this investigation as the most common types of applications require these two types of networks.

The results of the exhaustive search for both cases were divided into categories according to the type of filter behaviour observed from a configuration. These categories were defined as the standard filter types:

- LPFs

- High Pass Filters (HPFs)

- BPFs

- Band Stop Filters (BSFs)

In the case of LPFs and HPFs the response obtained from the configurations corresponded well with that of conventional filter responses. However, in the case of the BPFs and BSFs the responses were not those of conventional filters, although similar trends were observed. The so-called BPFs suppressed signals at both the low and high frequencies. In the case of the BSFs a notch at the intermediate frequencies was seen that suppressed the signal.

1.4   Problem statement and objectives

As mentioned earlier, the design and implementation of IPPMs in various systems is heavily dependent on the designers' past experience with the modules. A generalised theory for the design and development of the passive IPPMs does not exist.

Another consideration is the fact that the IPPMs have been extensively used in single-phase application while three-phase applications have not been thoroughly investigated. Bearing these points in mind, the objectives of this dissertation were defined as follows:

- To investigate the relationship between IPPM configurations and the behaviour obtained from the IPPM. From this the possibility of a set of guidelines as well as deeper insight into the functionality of the passive IPPMs could be explored. Such an approach towards the design of IPPM configurations has not been used before.

- To determine the feasibility of realising an integrated three-phase EMI filter with three-layer IPPMs, for application in an induction motor drive. The final filter design was based on the previous IPPM configuration investigation, thereby validating the results of the investigation.

It should be noted that the EMI filter discussed in this study was only a prototype. As a result the final filter performance was not evaluated in terms of efficiency or requirements stipulated by EMI standards. Rather, the performance was evaluated in terms of whether or not it was seen to be possible to suppress CM and DM noise with the integrated filters.

1.5   Dissertation outline

In *Chapter 2* the relationship between the configuration of the IPPMs and the resultant filter-type behaviour obtained was investigated. This was achieved by performing an exhaustive search of all possible configurations that could be realised with a three-layer IPPM. The various configurations were identified using a matrix repre-

sentation of the configurations. The configurations were then simulated using a quasi-distributed model of the three-layer IPPM. The results obtained from these simulations were used to classify the various configurations into the standard filter types, namely LPFs, HPFs, BPFs and BSFs. A fifth group of miscellaneous filters was also defined where the IPPM behaviour could not be classified into one of the aforementioned filter types.

From the exhaustive search performed in Chapter 2 a number of features of the IPPM configurations, that caused certain behaviour, were brought to light. These features are discussed in *Chapter 3*. It was seen that certain interconnections, as well as various ways in which the IPPMs could be manipulated had a predictable influence on the IPPM behaviour.

Chapter 4 isolated the configurations that were found to behave as LPFs in single-phase applications. These configurations were investigated in a three-phase application through the introduction of filter-units and topologies. The three-phase filters were simulated and the results analysed. From these results, and through application of the features discussed in Chapter 3, it was possible to reduce the number of three-phase EMI filters, to be considered for practical implementation, to only two.

Once the design of the three-phase integrated EMI filter had been completed it was necessary to physically construct the filter, as discussed in *Chapter 5*. Firstly, the material used to realise the IPPMs was investigated. From this investigation the specifications of the PWM inverter induction motor drive were found. A test bench meeting these specifications was built. The design and construction of the filters is also discussed.

In order to confidently evaluate the performance of the filters, both the experimental setup and measurement procedures used during the experimental verification of the filters were considered. *Chapter 6* documents the exact nature of the experimental setup. The measurement procedures for both CM and DM currents are described and justified through characterisation of the test bench. The performance of the filters was investigated through experimental measurements and compared to the predicted simulation results given in Chapter 4.

Finally, *Chapter 7* revisits the main conclusions of the study. Some aspects of the passive IPPMs that would lend themselves well to future investigation are also pointed out.

CHAPTER 2

Investigation into relationships between IPPM configurations and behaviour

As already mentioned in Chapter 1, no general guidelines for the design of IPPM configurations exist. The choice of the configuration to use in an application has been largely based on past experience with the modules. With the advent of new technology such as RF Microelectromechanical systems (MEMS) reconfigurable integrated circuits are being realised, which makes the need for configuration design guidelines ever more prevalent [17].

In this study, in order to implement a three-phase EMI filter, it was necessary to determine which configurations would enable the IPPM to behave as a LPF. It would also prove to be beneficial to identify the configurations that would serve as the best possible realisation of a LPF.

Consequently, it was decided to perform an exhaustive search of the configurations that can be realised with an IPPM. In so doing, it was possible to ascertain the filter types obtainable with these structures. However, as there are almost limitless possibilities in the nature and shape of the IPPMs the investigation presented here was limited to a three-layer IPPM.

Through this approach, three outcomes were realised:

- A number of general trends in various configurations that produced the same behaviour were identified. This will hopefully serve as a foundation for the development of a generalised design theory for passive IPPMs.

- A number of configuration traits that predictably manipulated the behaviour of the IPPMs were identified, as discussed in Chapter 3. Knowledge of these traits lends itself to a better understanding of the IPPMs.

- All three-layer IPPM configurations that would serve as a LPF filter were identified and investigated further for application in a three-phase EMI filter, as discussed in Chapter 4.

The method employed to perform the exhaustive search is outlined by the flow chart given in Fig. 2.1.

A new matrix representation of the configurations, realisable with the three-layer IPPMs, was developed. Using these matrices it was possible to generate the set of all possible matrices, thereby identifying the set of all possible configurations. This step was executed through the use of MATLAB for both single-port and two-port networks. As already mentioned a single-port network was defined as a configuration that had an input and an output terminal; while a two-port network had a ground terminal in addition to the input and output terminals.

A large number of the identified configurations did not have practical use. These configurations were isolated and eliminated from the configuration set for both single-port and two-port networks.
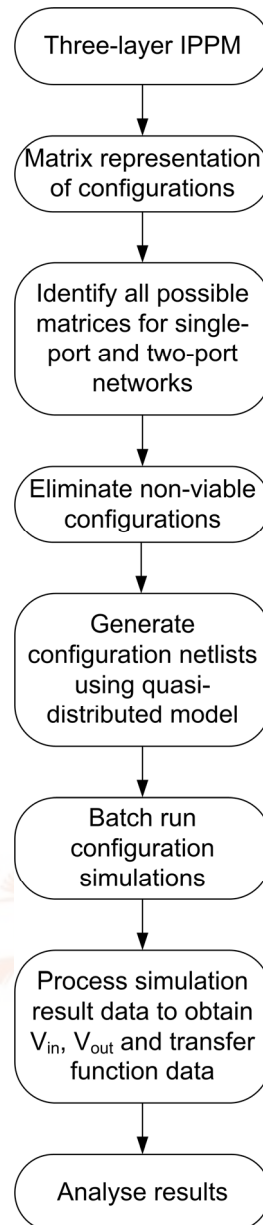
Fig. 2.1: Flow chart of the procedure followed to perform the exhaustive search

SPICE type circuit simulation was then used to determine the behaviour of the various configurations. This was accomplished by using the final set of configurations, in conjunction with a quasi-distributed model of the IPPM structure, to produce a netlist for each configuration. The netlists were generated using MATLAB and batch run in a SPICE program.

The data output from these simulations was processed using MATLAB to determine the input voltage, V_{in}, and output voltage, V_{out}, frequency responses, as well as the transfer function of each configuration. The behaviour of the configurations was categorised through analysis of these three frequency responses. From this analysis it was seen that all filter types: LPF, HPF, BPF and BSF, as well as a fifth group of miscellaneous filters, were realisable with the IPPMs.

Each of these steps used to perform the exhaustive search will now be discussed in greater detail.

2.1   Matrix representation of configurations

The three-layer IPPM considered for the exhaustive search can be schematically represented as shown in Fig. 2.2. The six terminals, A through F, of the IPPM are explicitly shown.
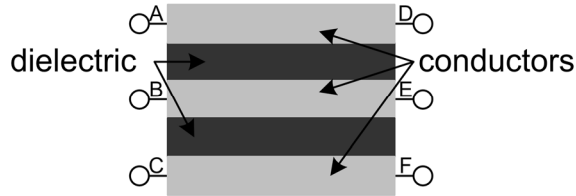
Fig. 2.2: Schematic representation of a three-layer IPPM

As discussed in Chapter 1, a configuration is defined as a specific set of interconnections and the assignment of input, output and/or ground terminals, henceforth referred to as I/O connections. A matrix representation of the configurations was developed to hold this data for each configuration. The two matrices used for this purpose are shown in Fig. 2.3(a) and (b).

(a)   (b)

Fig. 2.3: The two matrices used to represent a configuration, namely (a) the connection matrix and (b) the I/O matrix

2.1.1 Connection matrix

The connection matrix was defined as a $2n \times 2n$ matrix where n represents the number of conductive layers present in the IPPM. Hence $2n$ corresponds with the number of terminals associated with the IPPM. For the three-layer IPPM the connection matrix was seen to be a 6×6 matrix. This matrix was used to indicate the absence or presence of interconnections between the terminals.

Further consideration of the connection matrix revealed that an interconnection from terminal A to terminal B (AB) was the same as interconnection BA. Applying this fact to all possible interconnections represented in Fig. 2.3(a) it was found that the connection matrix was in actual fact a symmetric matrix as shown in Fig. 2.4 (a).

The connection matrix associated with the configuration of the IPPM shown in Fig. 2.2 is given in Fig. 2.4(b). A 1 signifies the presence of an interconnection between two terminals while a 0 implies no interconnection is present.

	A	B	C	D	E	F
A	AA	AB	AC	AD	AE	AF
B	AB	BB	BC	BD	BE	BF
C	AC	BC	CC	CD	CE	CF
D	AD	BD	CD	DD	DE	DF
E	AE	BE	CE	DE	EE	EF
F	AF	BF	CF	DF	EF	FF

(a)

	A	B	C	D	E	F
A	1	0	0	0	0	0
B	0	1	0	0	0	0
C	0	0	1	0	0	0
D	0	0	0	1	0	0
E	0	0	0	0	1	0
F	0	0	0	0	0	1

(b)

Fig. 2.4: The symmetric connection matrix in (a) symbolic form and (b) as applied to the configuration of Fig. 2.2

2.1.2 I/O matrix

The I/O matrix was defined as a column matrix, the length of which corresponded with the number of terminals, $2n$. It detailed which terminals were connected to a set of I/O connections, $\{I/O_i\}$. This is shown for a set of three such connections in Fig. 2.3(b). Only one entry for each I/O connection was present in the matrix, indicating that each I/O connection was connected to only a single terminal. The connection of any one of the I/O connections to more than one terminal was reflected in the connection matrix by means of an interconnection, instead of in the I/O matrix.

For the single-port network, two I/O connections were found in the I/O matrix, while three I/O connections were present in the matrix for the two-port network configurations.

Both the connection and I/O matrices were used to identify the unique configurations realisable with a three-layer IPPM.

2.2   Search for unique configurations

As a result of the symmetry of the connection matrix only one half of this matrix was considered when identifying all possible configurations of an IPPM. Using this fact and the fact that the elements of the connection matrix were either a 1 or a 0, the number of connection matrices, N_{connec}, for an n-layer structure could be found as in equation (2.1).

$$N_{connec} = 2^{n(2n-1)} \tag{2.1}$$

Associated with each of these connection matrices would be the set of all possible I/O matrices. The size of this set, $N_{I/O}$, can be calculated by means of a permutation as in equation (2.2). The variable p represents the number of I/O connections.

$$N_{I/O} = \frac{2n!}{(2n-p)!} \tag{2.2}$$

It should be noted that the restriction $p \le 2n$ is inherently implied due to the physical limitation of the IPPMs.

12

The total number of possible configurations that can be represented with the matrices is then found as in equation (2.3).

$$N_{config} = N_{connec} \cdot N_{I/O}$$

(2.3)

Due to the nature of the three-layer IPPM and its application there are a large number of these configurations that are not feasible to investigate, either due to the fact that the configurations are in essence identical or a practical realisation of the configuration is not worth considering. Consequently these configurations were identified, according to five conditions, and eliminated from the set of configurations to be investigated.

2.2.1 Implicit interconnections

All the connection matrices were examined for the presence of implicit interconnections. An implicit interconnection was defined as an interconnection that was implied due to the presence of other interconnections but not indicated in the connection matrix. For instance, if interconnections AB and BC were indicated in a connection matrix an implicit interconnection AC exists. By forcing the set of connection matrices to reflect all implicit interconnections the number of possible connection matrices, N_{connec}, was drastically reduced.

2.2.2 Rotation of IPPMs

The three-layer IPPMs have an inherent symmetry which results in the ability to rotate both the interconnections and I/O connections of a configuration about the x-axis, y-axis or both (a diagonal rotation). This is accomplished without actually changing the configuration, as depicted for an arbitrary configuration in Fig. 2.5.
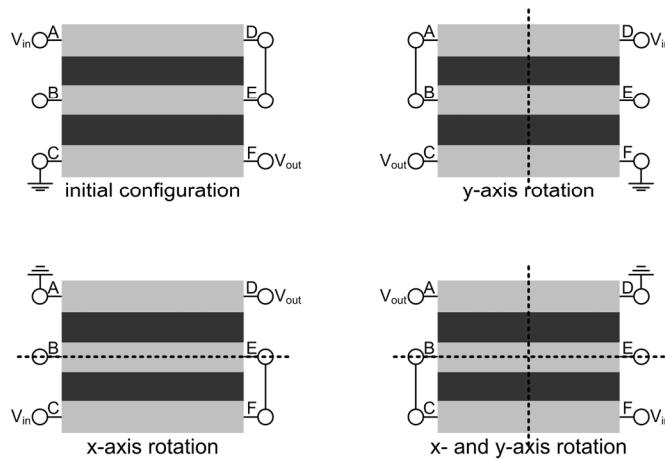
Fig. 2.5: An arbitrary configuration rotated about the x-axis only, the y-axis only and about both the x- and y-axes

	A	B	C	D	E	F
initial	A	B	C	D	E	F
x-rotation	C	B	A	F	E	D
y-rotation	D	E	F	A	B	C
xy-rotation	F	E	D	C	B	A

Fig. 2.6: The permutation matrix

	A	B	C	D	E	F
A	CC	CB	CA	CF	CE	CD
B	CB	BB	BA	BF	BE	BD
C	CA	BA	AA	AF	AE	AD
D	CF	BF	AF	FF	FE	FD
E	CE	BE	AE	FE	EE	ED
F	CD	BD	AD	FD	ED	DD

(a)

	A	B	C	D	E	F
A	DD	DE	DF	DA	DB	DC
B	DE	EE	EF	EA	EB	EC
C	DF	EF	FF	FA	FB	FC
D	DA	EA	FA	AA	AB	AC
E	DB	EB	FB	AB	BB	BC
F	DC	EC	FC	AC	BC	CC

(b)

	A	B	C	D	E	F
A	FF	FE	FD	FC	FB	FA
B	FE	EE	ED	EC	EB	EA
C	FD	ED	DD	DC	DB	DA
D	FC	EC	DC	CC	CB	CA
E	FB	EB	DB	CB	BB	BA
F	FA	EA	DA	CA	BA	AA

(c)

Fig. 2.7: The modified connection matrices reflecting a rotation about (a) the x-axis, (b) the y-axis and (c) both the x- and y-axes

A permutation matrix, Fig. 2.6, was found that indicated the mapping of the terminals A through F onto one another, that would realise each of the three rotations considered. These terminal mappings were applied to the connection matrix of Fig. 2.4(a) to obtain modified connection matrices that represented the various rotated configurations, Fig. 2.7(a) through (c). These matrices were used to rotate a specific configuration. The rotated versions of this configuration, that were already present in the set of configurations, could thereby be identified and eliminated.

2.2.3 Symmetric configurations and reflections of I/O connections about their axes of symmetry
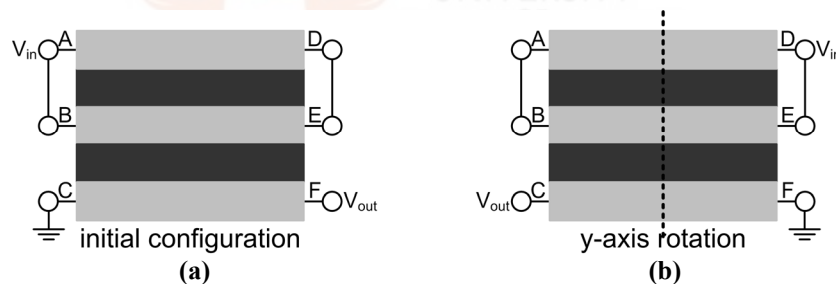
Fig. 2.8: (a) A symmetric configuration (b) The mapping of the I/O connections that yields a redundant configuration

The configurations considered in this section are a special case of the rotated configurations discussed previously. Certain configurations were found to be symmetric about the x-axis, y-axis or the diagonal when considering only the interconnections represented by the connection matrix. Fig. 2.8(a) shows an example of such a configuration that was found to be symmetric about the y-axis. Due to this symmetry a mapping, or reflection, of only the I/O connections about the axis of symmetry (as shown in Fig. 2.8(b)) yielded a configuration identical to the initial configuration.

Fig. 2.9 shows the modified I/O matrices used to map the I/O connections for the three different axes of symmetry. These matrices were used to identify a symmetric configuration so that it could be eliminated from the set of configurations.

The only reason that the symmetric configurations were considered separately from the rotated configurations of section 2.2 is due to the fact that the numerical method implemented in MATLAB, to identify the rotated configurations, did not identify

the symmetric configurations as well. Consequently these configurations had to be separately identified and eliminated.

A	C	A	D	A	F
B	B	B	E	B	E
C	A	C	F	C	D
D	F	D	A	D	C
E	E	E	B	E	B
F	D	F	C	F	A

(a)   (b)   (c)
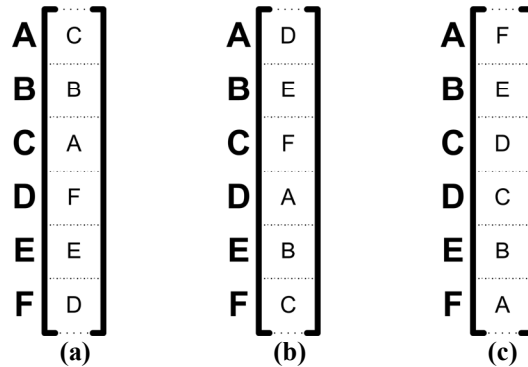
Fig. 2.9: The I/O connection mappings for a connection matrix found to be symmetric about the (a) x-axis, (b) y-axis and (c) both the x- and y-axes

2.2.4 Forbidden configurations

A forbidden configuration was defined as a configuration that had an interconnection between two or more terminals that were in turn connected to two or more I/O connections. An example of such a configuration for three I/O connections is shown in Fig. 2.10. As before, these configurations were identified and eliminated.
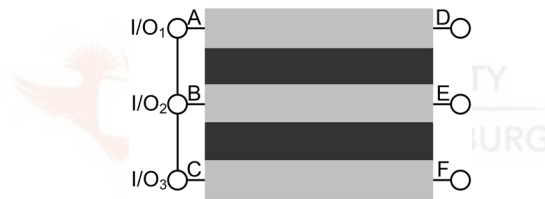
Fig. 2.10: A configuration displaying the presence of a forbidden connection

2.2.5 Redundant configurations

Some of the configurations were deemed redundant due to the presence of a similar configuration as shown in Fig. 2.11. Redundant configurations occurred when two or more of the terminals were connected together to form a node. An I/O connection was placed at each of the node terminals in consecutive configurations. A practical implementation of two such configurations would be deemed identical. Consequently only one configuration from such a set was retained in the set of configurations.

(a)   (b)
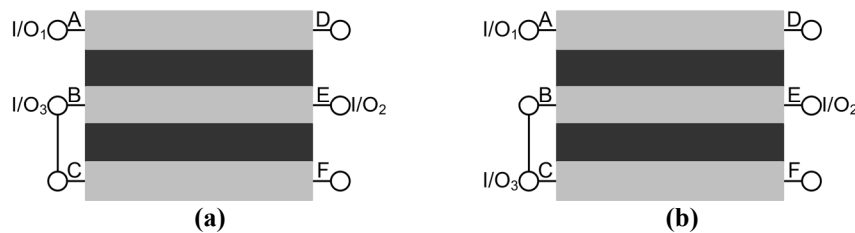
Fig. 2.11: (a) An arbitrary configuration and (b) a redundant configuration for a set of three I/O connections

2.3   Single-port and two-port network configuration sets

The matrices and unique configuration principles discussed were numerically implemented in order to identify the configuration sets for both single-port and two-port networks. The number of terminals and I/O connections were used to find initial values for N_{connec}, $N_{I/O}$ and N_{config} for each network. The five conditions used to identify unique configurations were then applied to the set of configurations for both networks. The number of configurations remaining in the set, for each case, after each condition was applied, is tabulated in Table 2-I.

Table 2-I: Number of unique configurations found for the two cases considered

Criteria	Single-port network	Two-port network
$2n$	6	6
p	2	3
initial N_{connec} (eq.(2.1))	2^{15}	2^{15}
$N_{I/O}$ (eq.(2.2))	30	120
N_{config} (eq.(2.3) & initial N_{connec})	983 040	3 932 160
Implicit connections: implicit N_{connec} (numerically determined) N_{config} (eq.(2.3) & implicit N_{connec})	203 6 090	203 24 360
Rotation of structures: N_{config} (numerically determined)	2 220	8 880
Symmetric configurations: N_{config} (numerically determined)	1 538	6 090
Forbidden configurations: N_{config} (numerically determined)	1 142	2 310
Redundant configurations: N_{config} (numerically determined)	499	882
Total number of configurations that were further investigated:	499	882

It is possible that a few configurations that were supposed to be eliminated slipped through. In the event that this happened the only result would be that more configurations would be analysed than was necessary. No change in the results of the exhaustive search would be seen.

2.4   Simulation of configurations

Once all of the unique configurations for the two networks had been identified, each of the configurations was simulated. The simulations employed a quasi-distributed model of the IPPMs, albeit with a number of arbitrarily chosen values and assumptions. The model was used in a SPICE type circuit simulation environment. The assumptions used for the model were justified through comparison between experimental and simulated results. A MATLAB program was written that generated the netlists for each configuration, using the quasi-distributed model. These netlists were then batch run from MATLAB in a SPICE program.

2.4.1 Quasi-distributed IPPM model

A number of models have been developed for the passive IPPM structures. An over-view of which is given in [18]. Three main groups of models are seen to exist, namely, lumped parameter models, quasi-distributed models and distributed models. One of the main downfalls of the first two models is the fact that the representation of the IPPM structures is accurate only in a limited frequency range. The distributed models become necessary to obtain accurate predictions of the structure behaviour at the higher frequencies, particularly when transmission line effects need to be considered. [18] developed a distributed model using a generalised transmission line structure of infinitesimal length. This structure was then used to find differential equations that describe the behaviour of the IPPM. However, the model proposed in [18] was specifically developed for two-layer IPPM structures. This model was expanded for application to multi-layer IPPM structures in [19].

A slightly altered version of the multi-layer transmission line structure presented in [19] was used to form a cell. The cell used in this study differed from that of [19] through the omission of a capacitance and conductance between a cell node and the ground plane. These parameters were used to model the flow of common mode currents from the IPPM into the ground plane. However, the presence of such currents was outside the scope of this dissertation.

A quasi-distributed model was constructed by connecting a finite number of these cells in cascade. The greater the number of cells connected in cascade the closer the quasi-distributed model accuracy would be to that of the distributed model at the higher frequencies. Bearing in mind that the application of the IPPMs considered here was only within the frequency range of conducted EMI, a quasi-distributed model consisting of ten cells was found to be sufficiently accurate. This was seen to be the case in section 2.4.3 where excellent correlation between measured and simulated results was found. The quasi-distributed model did not however account for any losses and was only an approximation of the real world structures. The model was also considered to be linear as no frequency dependencies were incorporated into it.

A single cell used to construct the quasi-distributed model is shown in Fig. 2.12. The cell was seen to consist of resistances, R_{s1} through R_{s3}, and coupled inductances, L_1 through L_3 (the coupling coefficient of which was given by C_o). These components were connected in series and corresponded with each conductive layer of the IPPM. A shunt capacitance, C_1 and C_2, and a shunt conductance, modelled by the resistors R_{g1} through R_{g3}, represent the various layers of dielectric.
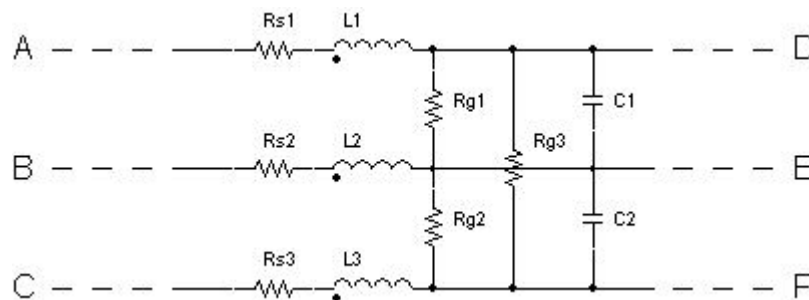
Fig. 2.12: A single cell used in the quasi-distributed model of the three-layer IPPMs

Table 2-II: Cell parameter values used in the quasi-distributed model

Cell parameters	Value
R_{s1} - R_{s3}	1mΩ
L_1 - L_3	10µH
R_{g1} - R_{g3}	100MΩ
C_1, C_2	1nF
C_o	1

The values assigned to each of the parameters in a cell are listed in Table 2-II. The series resistance and shunt conductance were chosen so that their influence on the behaviour of the structure was kept minimal. The values of the overall inductance per conductive layer and capacitance per dielectric layer were chosen so as to correspond with values that are practically realisable. These values were then divided by the number of cells used in the model to obtain the values of the components in each cell. Variation in these values was seen to influence the cut-off frequency of the voltage response of the structures and not the type of behaviour predicted by the model.

The coupling between all three inductors of a cell was modelled for the ideal case of a coupling coefficient of 1. The model was setup in this manner so that the "best case scenario", in terms of the behaviour of the IPPMs, was obtained for further investigation.

2.4.2 Simulation environment

The quasi-distributed model was used in a SPICE type circuit simulation as shown in Fig. 2.13. All of the terminals of the model can be seen to be connected to ground by means of a series of large resistances, R_{f1} through R_{f6}. These resistances were necessary for convergence of the simulation by ensuring that the simulation software did not interpret the terminals as floating nodes.
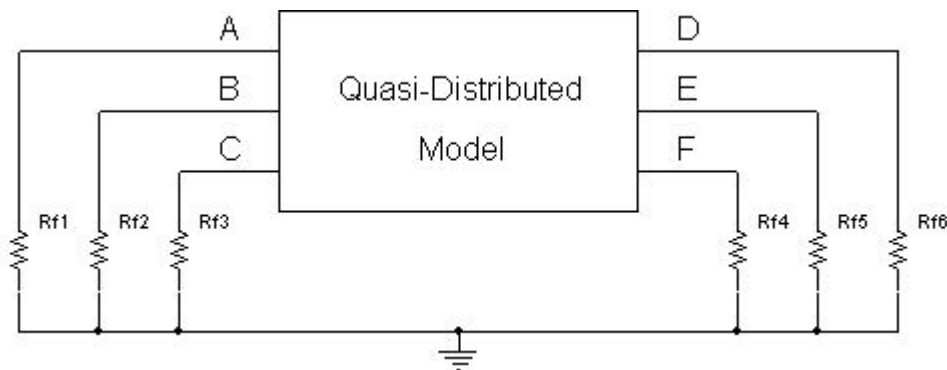
Fig. 2.13: The IPPM setup used in the simulations to prevent floating terminals on the quasi-distributed model

Each of the single-port and two-port network configurations previously identified were realised as shown for an arbitrary two-port network configuration in Fig. 2.14. The resistances R_{f1} through R_{f6} have been omitted from the figure for the sake of clarity.

18
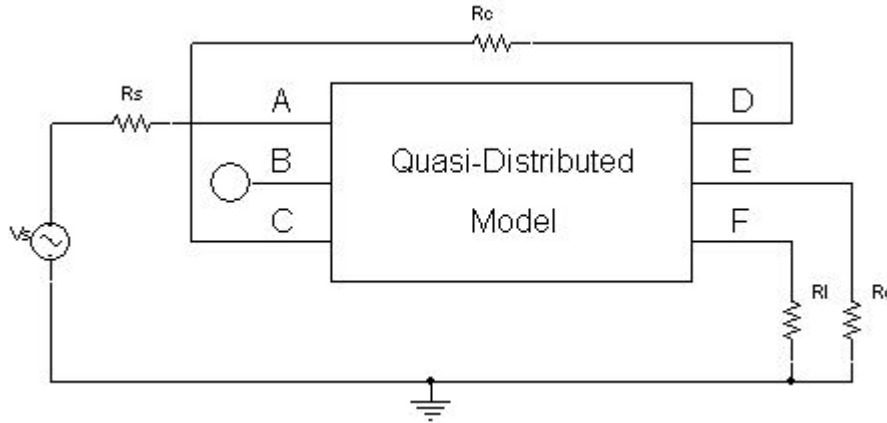
Fig. 2.14: The simulation setup used for an arbitrary configuration where the resistances R_{f1} through R_{f6} are not shown so as not to crowd the image

The voltage source, V_s, used in the simulations, as the input to the structure, was modelled as an ideal source. By introducing resistance R_s, the voltage source could be modelled as a non-ideal source instead. In so doing the input voltage, V_{in}, measured at the input terminal of the IPPM, varied depending on the current being drawn from the source.

The output voltage, V_{out}, of the structure was measured as the voltage drop over a load resistance R_l. The size of the load resistance was determined as in equation (2.4). The values of the inductance, L_1, and the capacitance, C_1, were the values of the corresponding parameters found in the IPPM model. By so doing the frequency responses of the configurations were found to be in the region of critical damping. By changing the load resistance value from that found in equation (2.4) the behaviour of the configurations became noticeably either over- or under-damped.

$$R_l = \sqrt{\frac{L_1}{C_1}} \qquad (2.4)$$

For the case of the two-port networks the ground terminal was realised by connecting the relevant terminal to circuit ground by means of a small series resistance, R_c. Interconnections between terminals were similarly realised.

A frequency sweep analysis was performed on the configurations, the range of which, $f_{start} - f_{stop}$, was made excessively large in order to ensure that the entire response of the configurations was captured.

The values of the various components were kept the same for all the configurations investigated. A list of the components and the values used can be found in Table 2-III.

Table 2-III: Additional parameter values used in the simulation of IPPM configurations

Parameter	Value
R_{f1} - R_{f6}	100MΩ
V_s	1V
R_s	50Ω
R_l	100Ω
R_c	1mΩ
f_{start}	10Hz
f_{stop}	10GHz

19

2.4.3 Quasi-distributed model justification

The use of the quasi-distributed model discussed here was experimentally justified. This was achieved through the physical construction of a number of arbitrarily chosen configurations. The details as to the practical construction of the IPPMs used to realise these configurations can be found in Chapter 5. The various transfer functions of the configurations were measured, at low excitation levels into a 50Ω load with the aid of an HP4195A network analyser, and numerically found through simulations incorporating the quasi-distributed model.

In section 2.5 it is shown that the transfer function of a configuration may be misleading when interpreting the behaviour of the configuration. However, in the justification of the use of the quasi-distributed model, the transfer function was used due to the fact that the network analyser was only able to measure the transfer function and not the input and output voltage frequency responses. This was considered to be acceptable as a correlation between measured and simulated results for a transfer function can reasonably be assumed to indicate a similar correlation between measured and simulated voltage responses.

The correlation between the measured and simulated results was found to be similar for all the configurations investigated. Consequently only the results of one such configuration are shown in Fig. 2.15.
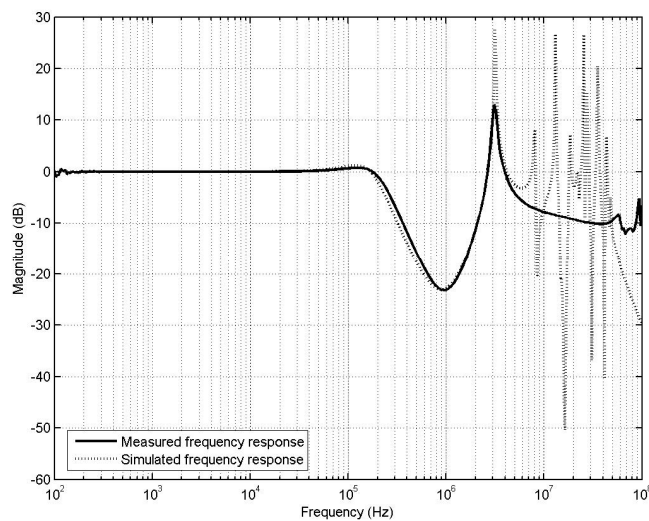
Fig. 2.15: Measured and simulated transfer functions for an arbitrary configuration

In the practical realisation of the configurations the coupling between the conductive layers of the IPPM are no longer ideal. Consequently, in order to obtain good correlation between the simulated and measured results, the coupling coefficient in the simulation was changed to be slightly less than ideal, normally in the region of 0.99. The value of the load resistor was also altered to obtain a similarly damped response as experimentally measured. The other parameter values used in the simulation remained unchanged from the values used in the exhaustive search.

From Fig. 2.15 it can be seen that the simulated and measured results show excellent correlation at the lower frequencies but start to deviate significantly at frequencies greater than approximately 5MHz. This can be attributed to the fact that the performance of the E-core material used in the measurements degrades at high frequencies due to hysterisis losses. The E-core has a damping effect on the waveforms

under these circumstances, which the quasi-distributed model does not take into account. This is in actual fact one of the shortcomings of the model used, namely the fact that frequency dependent losses are not included in the model. These losses manifest in the form of hysterisis losses in the E-core as well as losses attributed to skin and proximity effects within the IPPM structure.

At frequencies greater than 50MHz, noise can be seen to be introduced onto the measured frequency response as well. This can be explained by the fact that at higher frequencies transmission line effects come into play in the practical setup, due to the presence of cables and connectors.

In spite of the fact that the model did not include these loses the simulated response was seen to correlate well with the measured results over almost the entire frequency range of interest. It was thus concluded that the model discussed was sufficiently accurate for the purposes of the exhaustive search.

2.4.4 Aspects of the quasi-distributed model

A few aspects pertaining to the model should be mentioned.

Firstly, no coupling, capacitive or inductive, was considered to exist between different cells. In so doing the quasi-distributed model presented here was referred to as a so-called unwound structure model. Such a structure can be thought of as a single-turn implementation of the IPPM in a practical realisation. This model, in its current form, would not be sufficient to model multiple turns of the three-layer IPPM [18].

Secondly, the model does not take end effects into account. However, due to the excellent correlation between the simulated and measured results the end effects were considered to have negligible influence on the functioning of the IPPM.

2.5   Interpretation of simulated results

The simulation data for each configuration was processed and the input and output voltage frequency responses obtained. The transfer function of each configuration was also found by calculating the ratio of output voltage to input voltage over the entire frequency range investigated. Fig. 2.16 shows an arbitrary configuration. The frequency response results for this configuration are shown in Fig. 2.17. These results are typical of those found for all the configurations.

From Fig. 2.17 it can be seen that the transfer function indicates that the configuration has a steep drop-off and reaches a steady state value at the higher frequencies. However, examination of the input and output voltage responses shows no such steady state response.
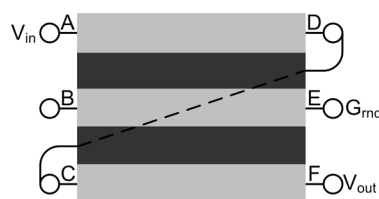
Fig. 2.16: Schematic representation of an arbitrary three-layer IPPM configuration
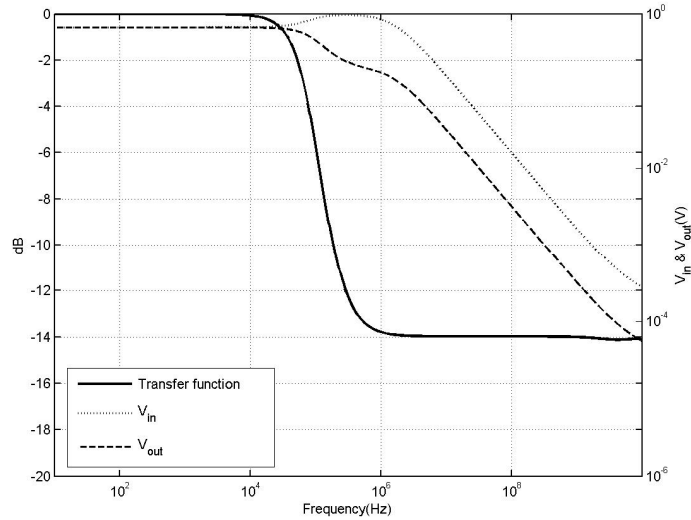
Fig. 2.17: The transfer function, input voltage and output voltage plotted as a function of frequency for an arbitrary configuration

The fact that the behaviour of the configuration as indicated by the two frequency responses disagree with one another can be attributed to a common misinterpretation of the transfer function concept. By definition the transfer function "describes the way the behaviour of the circuit depends on the frequency of the input [20]". However, the normal interpretation of transfer functions is incorrectly assumed to indicate the output voltage magnitude in the presence of a constant input voltage magnitude as opposed to the voltage gain concept actually given by the transfer function amplitude [21]. Although such an interpretation of the transfer function is correct if the input voltage magnitude is indeed constant, it can lead to the incorrect interpretation in the event that the input voltage magnitude varies. From Fig. 2.17, this can be seen to be the case for the configuration considered here.

This misleading interpretation of the transfer function can be illustrated by applying conventional circuit analysis to the configurations. From such an analysis it can also be seen whether or not the interpretation of the traditional transfer function is in fact misleading. However it was found to be difficult to apply this method to all the configurations, as some configurations lend themselves better to standard circuit analysis than others. In Appendix A such an approach was applied to the arbitrary configuration shown in Fig. 2.16.

A more general approach towards the validity of the interpretation of the transfer function, through consideration of impedances, can be applied to all the configurations. However, this approach needs to be handled slightly differently for the single-port and two-port networks considered.

2.5.1 Single-port network

The single-port network configurations can be seen to realise an impedance, Z_{LCI}, as shown schematically in Fig. 2.18. This impedance can be found through application of the voltage divider rule as in equation (2.5).

$$Z_{LCI} = \frac{V_{in}R_l}{V_{out}} - R_l \tag{2.5}$$

22
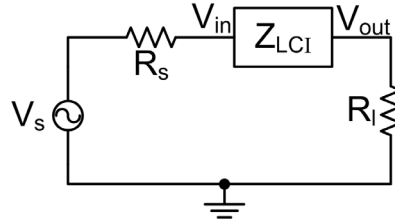
Fig. 2.18: Simplification of the simulation setup used to determine the impedance seen by the voltage source for single-port network configurations

A relation between V_{in}, V_{out} and V_s is also found as follows:

$$V_{in} = \frac{Z_{LCI} + R_l}{R_s + Z_{LCI} + R_l} V_s \qquad (2.6)$$

$$V_{out} = \frac{R_l}{R_s + Z_{LCI} + R_l} V_s \qquad (2.7)$$

The value of Z_{LCI} is frequency dependent due to the inductive and capacitive nature of the IPPMs. Consequently, it is possible for the magnitude of the impedance to approach zero at some frequency. When this happens the values of V_{in} and V_{out} become approximately equal and are related to V_s as shown in equation (2.8).

$$V_{in} \approx V_{out} \approx \frac{R_l}{R_s + R_l} V_s \qquad (2.8)$$

In this circumstance the input voltage will attenuate. If V_{in} is pulled to a value that is significantly smaller than V_s the interpretation of the transfer function becomes misleading. This occurs if $R_s \gg R_l$. However, this was not the case in the single-port network application. In this particular case the minimum possible magnitude of V_{in} and V_{out} was found through substitution of the R_s and R_l component values into equation (2.8). The result is shown in equation (2.9).

$$V_{in} \approx V_{out} \approx \frac{2}{3} V_s \qquad (2.9)$$

As the value of V_{in} would not be significantly smaller than V_s at any frequency it was seen that the transfer function could be used to investigate the structure behaviour in this particular application.

2.5.2 Two-port network

The two-port network configurations differed from the single-port networks due to the presence of the ground terminal. As a direct result of the presence of this connection, the impedance of the structure itself, Z_{LCII}, was no longer readily defined. Consequently the input impedance, Z_{in}, seen by the voltage source, was used instead. A schematic representation of the two-port network configurations can be seen in Fig. 2.19 where the impedances discussed are indicated.

The input impedance is seen to be a combination of the structures impedance and the load resistance. The value of Z_{in} could be calculated from the voltage data obtained from the simulations as in equation (2.10).

$$Z_{in} = \frac{V_{in}}{I_{in}} = \frac{V_{in} R_s}{V_s - V_{in}} \qquad (2.10)$$

23
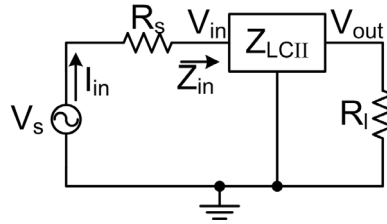
Fig. 2.19: Simplification of the simulation setup used to determine the impedance seen by the voltage source for the two-port network configurations
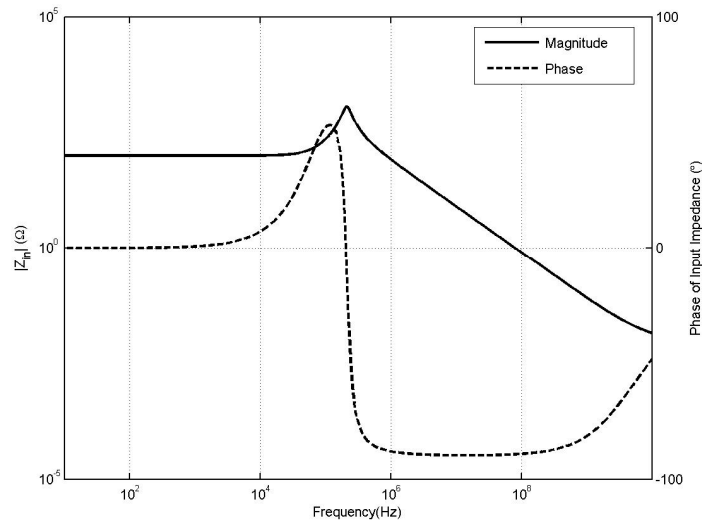
Fig. 2.20: The magnitude and phase for the impedance Z_{in} of an arbitrary configuration

The input impedance of the arbitrary configuration shown in Fig. 2.16 was calculated using equation (2.10). The impedance magnitude and phase plots are shown in Fig. 2.20.

It can clearly be seen that the magnitude of this impedance is much less than 1Ω at the higher frequencies and can be considered to approach zero. This would imply that the value of V_{in} would be pulled low as in fact is seen to be the case in Fig. 2.17.

The majority of the two-port network configurations showed this trend where the magnitude of Z_{in} approached zero at some point in the frequency range. Due to this inconsistency in the value of the input voltage seen at the input terminal of the structure the transfer function can be misleading. Consequently the behaviour of the two-port network configurations was investigated by considering the frequency response of the input and output voltages.

The phase of Z_{in} shown in Fig. 2.20 was included merely to indicate that there was nothing out of the ordinary in the phase response of the IPPM.

2.6 Configuration terminology

From the simulations it was seen that the configurations could be subdivided into groups according to the behaviour of the respective configurations. Within these groups commonalities were found between the configurations in terms of the pres-

24

ence or absence of certain types of interconnections or signal paths. It is therefore necessary to introduce certain terminology used to describe these attributes.

2.6.1 Connection terminology

Certain connections were found to influence the behaviour of the configurations. In order to describe these connections the following terminology was defined with reference to the three-layer IPPM shown in Fig. 2.2.

Adjacent terminals
Terminals found on opposite sides of a conductive layer, e.g. terminals A and D.

Same-side terminals
The set of terminals found on the same-side of the structure, e.g. terminals A, B and C.

Opposite-side terminals
Terminals found on opposite sides of the structure, e.g. terminal A is an opposite-side terminal to all three terminals D, E and F. Adjacent terminals inherently realise opposite-side terminals as well.

Cross-connection
An interconnection between terminals in one set of same-side terminals to the terminals in another set of same-side terminals. An example of such a connection can be found in Fig. 2.16, where a cross-connection exists between terminals C and D.

2.6.2 Signal paths

Due to the capacitive and inductive nature of the structures a low frequency (LF) and a high frequency (HF) signal path is found to inherently exist in the structures.

Low frequency signal path
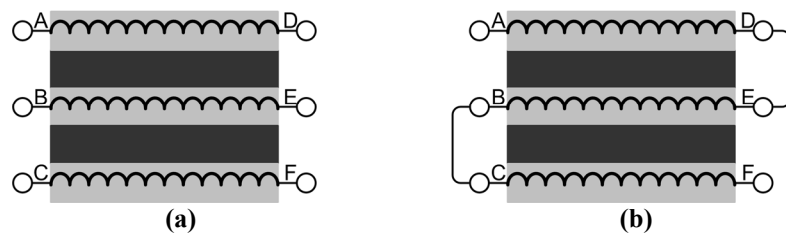
Fig. 2.21: LF path between (a) adjacent terminals and (b) terminals A through F (The inductive coupling between the terminals that is responsible for the LF paths is explicitly shown)

A LF signal path is realised when the path between the terminals is inductive in nature. Fig. 2.21(a) illustrates how adjacent terminals will always have LF paths between them. A LF path can be created between any two non-adjacent terminals, as in Fig. 2.21(b), through the use of interconnections.

High frequency signal path

A HF signal path is defined as a signal path between terminals that are capacitively coupled with one another. A HF path will inherently exist between same-side terminals, as is shown in Fig. 2.22(a). The presence of a cross-connection will however introduce a high frequency path between opposite-side terminals; refer to Fig. 2.22(b).

(a)   **(b)**
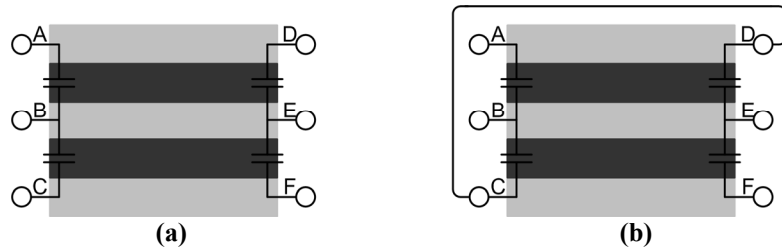
Fig. 2.22: HF path between (a) same-side terminals and (b) all six terminals (The capacitive coupling between the terminals that is responsible for the HF paths is explicitly shown)

It should be noted that an interconnection between any two terminals was in actual fact merely a short-circuit and consequently served as both a LF and a HF path.

2.7   Results of exhaustive search

As discussed the single-port and two-port networks were analysed using either the transfer function or the output voltage response obtained from the simulations. Through this analysis it was possible to group the configurations according to the type of behaviour observed from a configuration. The configurations were then examined to determine the type of interconnections and I/O connections that caused the IPPMs to behave in a particular manner.

2.7.1 Single-port network results

The transfer function of each of the configurations was found and used to classify the configurations into groups according to the type of filter realised. The four classical filter types, as discussed in Chapter 1, were found to be present; namely the LPF, HPF, BPF and BSF. A fifth group of miscellaneous filters was also created in which configurations, whose transfer functions could not be classified as any one of the aforementioned filter types, were placed.

The transfer functions within each group were further divided into subgroups according to whether or not these transfer functions were considered to be identical to one another. This was executed by means of a MATLAB program.

The configurations associated with each of these transfer functions were also compared with one another. Through this procedure it was possible to identify certain interconnections and the placement of I/O connections, in the configurations, that resulted in the structures behaving in a particular manner.
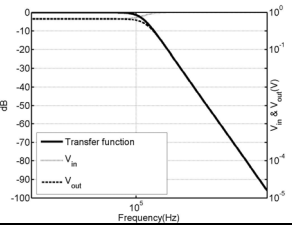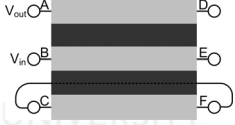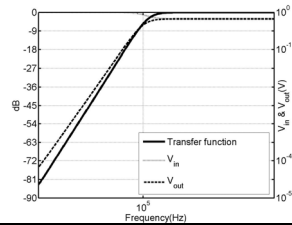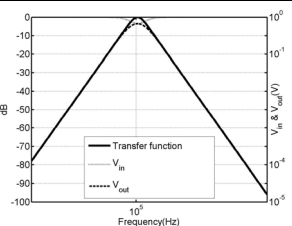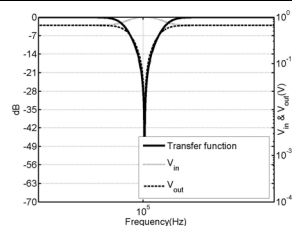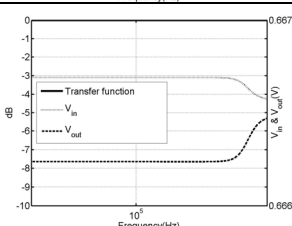
A few of the configurations' characteristics within each subgroup were investigated and the results tabulated. The characteristics examined were:

- The drop-off of the transfer function in dB/dec.

- The value of the pass-band of the transfer function in dB.

- The cut-off frequency, ω_c, of the transfer function. The cut-off frequency was defined as the frequency where the transfer function had a value of 3dB less than that found in the pass-band.

- Whether or not any of the configurations in the subgroup had a cross-connection present.

- The placement of V_{in} and V_{out} relative to one another in terms of the type of terminals to which they were connected.

- Whether or not a LF or HF path was present between V_{in} and V_{out}.

Table 2-IV contains examples of the typical configurations found in each filter group. The associated transfer function and input and output voltage frequency responses are also shown.

Table 2-IV: Typical configurations from each filter group and their respective transfer functions

At the end of the section the results are summarised in Table 2-IX. This summary shows the general trends found in the configurations to realise the four classical filter categories without the subgroup detail.

Low pass filter

All the configurations that resulted in a LPF were found to have near identical transfer functions. Consequently only one subgroup was found. The configurations in this group were all found to have the characteristics as listed in Table 2-V.

Table 2-V: Characteristics found for the subgroups of the LPF category

Criteria	Subgroup	1
1	Drop-off (dB/dec)	-20
2	Pass-band (dB)	0
3	ω_c (Hz)	155k
4	Cross-connections	None
5	V_{in} & V_{out} terminals	Always opposite-side, sometimes adjacent
6	V_{in} & V_{out} signal paths	LF

Only a LF path was found to exist between the terminals connected to V_{in} and V_{out}. This LF path was also seen to consist of effectively only one conductive layer. As a result, the inductance realised by all the configurations was effectively the same. Furthermore, it was seen that all of the transfer functions in the category had a drop-off of -20dB/dec. This implied that only the inductive component of the structure was utilised as in the case of a first-order filter. Further substantiation for this claim was found by considering the well-known cut-off frequency for a standard RL circuit, as given in equation (2.11).

$$\omega_c = \frac{R}{L} \tag{2.11}$$

Substituting the values of R_l and ten times L_1 (thereby using the overall inductance per conductive layer of the IPPM model) into equation (2.11) yielded a cut-off frequency of 159kHz. This value was close enough to the simulated cut-off frequency of 155kHz to imply that the dielectric was not utilised in any of these configurations.

High pass filter

The configurations that realised HPFs could be divided into eight subgroups. The characteristics of each of these subgroups are given in Table 2-VI.

A HF path was present between V_{in} and V_{out} in all eight subgroups. The HF path was realised through the fact that V_{in} and V_{out} were connected to same-side terminals and/or the fact that a cross-connection was present in the configurations.

The drop-off of the transfer function for all of the configurations in this category was 20dB/dec which once again corresponds with that of a first-order filter. This implied that only the capacitive component of the structure was utilised. However, the manner in which the dielectric was utilised differed from subgroup to subgroup as is implied by the variation in cut-off frequencies. The dielectric utilisation in the configurations of each subgroup is further investigated in Chapter 3 using the dominant configuration concept.

Band pass filter

The configurations whose transfer functions yielded BPFs were subdivided into four subgroups, the characteristics of which are given in Table 2-VII.

All 4 subgroups showed no direct LF or HF path between V_{in} and V_{out}. Further, the drop-off was found to be 20dB/dec for both the rising and falling slopes of the transfer functions which implies that the filters realised were only first-order filters.

Table 2-VI: Characteristics found for the subgroups of the HPF category

Criteria	Subgroup	1	2	3	4
1	Drop-off (dB/dec)	20	20	20	20
2	Pass-band (dB)	0	0	0	0
3	ω_c (Hz)	162k	331k	162k	81k
4	Cross-connections	Sometimes			
5	V_{in} & V_{out} terminals	Sometimes opposite-side, sometimes same-side, never adjacent			
6	V_{in} & V_{out} signal paths	HF			
Criteria	Subgroup	5	6	7	8
1	Drop-off (dB/dec)	20	20	20	20
2	Pass-band (dB)	0	0	0	0
3	ω_c (Hz)	89k	59k	72k	48k
4	Cross-connections	All			
5	V_{in} & V_{out} terminals	Sometimes opposite-side, sometimes same-side, never adjacent	All opposite-side, never same-side, or adjacent	Sometimes opposite-side, all same-side, never adjacent	All opposite-side, never same-side, or adjacent
6	V_{in} & V_{out} signal paths	HF			

Table 2-VII: Characteristics found for the subgroups of the BPF category

Criteria	Subgroup	1	2	3	4
1	Drop-off (dB/dec)	20	20	20	20
		-20	-20	-20	-20
2	Pass-band (dB)	-0.1	0	0	-0.1
3	ω_c (Hz)	98k	162k	100k	58k
		263k	316k	257k	219k
4	Cross-connections	Never			
5	V_{in} & V_{out} terminals	All opposite-side, Never same-side or adjacent			
6	V_{in} & V_{out} signal paths	None			

Band stop filter

The configurations that realised BSFs were divided into ten subgroups. The characteristics of each of these subgroups are given in Table 2-VIII. It should be noted that the BSFs realised did not have large stop bands. The transition from pass-band to stop-band was also found to be exceptionally steep. Consequently the drop-off values were excluded from further analysis as these values were difficult to obtain accurately.

All the configurations in all ten subgroups had a cross-connection present. Both a LF and a HF path were also found to be present between V_{in} and V_{out}.

Table 2-VIII: Characteristics found for the subgroups of the BSF category

Criteria	Subgroup	1	2	3	4	5
2	Pass-band (dB)	0	0	0	0	0
		0	0	0	0	0
3	ω_c (Hz)	98k	37k	79k	35k	115k
		263k	692k	159k	355k	437k
4	Cross-connections	All				
5	V_{in} & V_{out} terminals	Sometimes opposite-side, same-side or adjacent	Always opposite-side, never same-side or adjacent	Sometimes opposite-side, same-side or adjacent	Always opposite-side, sometimes same-side, never adjacent	Always opposite-side and adjacent, sometimes same-side
6	V_{in} & V_{out} signal paths	LF & HF				
Criteria	Subgroup	6	7	8	9	10
2	Pass-band (dB)	0	0	0	0	0
		0	0	0	0	0
3	ω_c (Hz)	39k	32k	58k	17k	17k
		1.35M	162k	89k	309k	741k
4	Cross-connections	All				
5	V_{in} & V_{out} terminals	Always opposite-side, never same-side or adjacent	Always opposite-side or same-side, never adjacent	Always opposite-side, same-side & adjacent	Always opposite-side, never same-side or adjacent	
6	V_{in} & V_{out} signal paths	LF & HF				

Miscellaneous filters

The transfer functions in this category could not be classified as any of the four traditional filter types. However, all of the transfer functions in this group were found to show that $V_{in} \approx V_{out}$ over the entire frequency range investigated. This was due to one of two possible reasons. Either an interconnection existed in each of the configurations that caused the voltage gradient across the structure to approach zero, i.e. a shorting-connection; or, an interconnection existed that forced the absolute voltage of V_{in} and V_{out} to the same value, a vertical-connection. These types of interconnections are discussed in Chapter 3.

Table 2-IX: Summary of results for single-port networks

Single-port networks			
Filter Category	Signal path between V_{in} & V_{out}	Placement of V_{in} & V_{out}	Cross-connection
LPF	LF	Opposite-side	None
HPF	HF	Never adjacent	Present only if V_{in} & V_{out} on same-side terminals
BPF	Neither LF/HF	Non-adjacent opposite-side	None
BSF	LF & HF	Opposite-side/ same-side	Always

Table 2-X: Typical configurations from each V_{in} group and their respective voltage frequency responses

Typical configuration	Typical transfer function	Typical configuration	Typical transfer function
V_{in} consistently high		V_{in} low at high frequencies	
LPF:		LPF:	
HPF:		BPF:	
BPF:		V_{in} low at mid frequencies only	
		HPF:	
V_{in} low at low frequencies			
HPF:		BSF:	
V_{in} high at mid frequencies only		V_{in} consistently low	
BPF:			

2.7.2 Two-Port Network Results

As the two-port network configurations yield more complex structures than in the case of a single-port network, the approach used to analyse the configurations differed somewhat from the approach used previously. It has already been discussed that the transfer function could yield misleading results for the two-port network case. To circumvent this problem the input voltage waveform over the frequency range under investigation was considered in order to initially classify the configurations. The magnitude of the input voltage frequency response was defined as being "low" when the value of V_{in} was roughly less than half of the original value of the source, V_s. Conversely it was said to be "high" when the magnitude of V_{in} was greater than half the source voltage. Once this initial classification of configurations was completed, the

31

output voltage waveform within each category was evaluated in order to determine the "type" of filter each configuration realised, namely LPFs, HPFs, BPFs, BSFs or miscellaneous filters.

Table 2-X shows examples of the typical configurations and their input and output voltage frequency responses that realised each filter type in all six categories.

Once again a summary of the results can be found in Table 2-XVI at the end of the section. The behaviour of any configuration, which can not be classified according to the criteria in the table, did not have any practical use.

V_{in} consistently high

The magnitude of V_{in} was found to be high over the entire frequency range investigated. All the configurations within this group shared a few characteristics as listed below.

- No LF or HF path was found to be present between V_{in} and G_{rnd}.

- No cross-connections were present in any of the configurations.

- V_{in} and G_{rnd} were always connected to opposite-side terminals but never to adjacent terminals.

- No connections were found to be present in any of the configurations that resulted in a zero voltage gradient across the structure.

By examining the output voltage for the configurations within this group it was found that these configurations could be further subdivided into three types of filters, namely LPFs, HPFs and BPFs. The configurations that realised the respective filter types were further investigated and the results are given in Table 2-XI.

From the data in Table 2-XI the following connections were seen to be necessary in the configurations in order to yield the three different filter types:

- A LF path between V_{in} and V_{out} in combination with a HF path between V_{out} and G_{rnd} resulted in a LPF.

- A HPF was realised if a HF path was present between V_{in} and V_{out} as well as either a LF path between V_{out} and G_{rnd} or the fact that the load resistance behaved as a pull-down resistor for V_{out} at the low frequencies.

- The presence of a HF path between V_{out} and G_{rnd} and the load resistor acting as a pull-down resistor at low frequencies resulted in BPF behaviour.

Table 2-XI: Subdivisions of the "V_{in} consistently high" category

Filter type	LPF	HPF		BPF
LF path	V_{in}-V_{out}	V_{out}-G_{rnd}	-	-
HF path	V_{out}-G_{rnd}	V_{in}-V_{out}	V_{in}-V_{out}	V_{out}-G_{rnd}

V_{in} low at high frequencies

The magnitude of V_{in} was found to be high at low frequencies and to be pulled low at high frequencies. The configurations that fell into this category were found to share a number of traits:

- Only HF paths exist between V_{in} and G_{rnd}, no LF paths present.

- The HF path was realised either by the presence of a cross-connection or through the fact that V_{in} and G_{rnd} were connected to same-side terminals.

The configurations in this category were subdivided into two filter types, namely LPFs and BPFs, the specifics of which are given in Table 2-XII.

Table 2-XII: Subdivisions of the "V_{in} low at high frequencies" category

Filter type	LPF	BPF		
LF path	V_{in}-V_{out}	-	V_{out}-G_{rnd}	-
HF path	V_{in}-V_{out}-G_{rnd}	V_{in}-V_{out}-G_{rnd}	V_{in}-V_{out}-G_{rnd}	V_{in}-G_{rnd}

The following connections were seen to be necessary for the configurations to behave as either a LPF or a BPF:

- The LPFs were realised when a LF path was found to be present between V_{in} and V_{out}.

- Either the presence of a LF path between V_{out} and G_{rnd}, or, the load resistor acting as a pull-down resistor for V_{out} at low frequencies, resulted in a BPF realisation.

The remainder of the configurations within this category were found to yield no usable result as the magnitude of V_{out} was pulled low over the entire frequency range. This was found to occur with two types of configurations. Firstly, a LF path was present between V_{out} and G_{rnd}. Secondly V_{out} was isolated at the lower frequencies and pulled to ground by means of the load resistor. A large number of these configurations were also found to have a shorting-connection present that forced the voltage gradient to zero. As already mentioned, such interconnections are discussed in Chapter 3.

V_{in} low at low frequencies

The configurations in this category had a low input voltage at low frequencies and a high input voltage at high frequencies. The configurations all shared the following traits:

- LF paths between V_{in} and G_{rnd}.

- No cross-connections were found in any of the configurations.

- V_{in} and G_{rnd} were always connected to opposite-side terminals.

Table 2-XIII: Subdivisions of the "V_{in} low at low frequencies" category

Filter type	HPF	
LF path	V_{in}-G_{rnd}	V_{in}-V_{out}-G_{rnd}
HF path	V_{in}-V_{out}	V_{in}-V_{out}

It was found that HPFs could be realised with the configurations in this category, the details of which are given in Table 2-XIII.

A HF path was also found to exist between V_{in} and V_{out} for all the configurations within this group. Consequently the configurations were seen to yield results similar to that of the traditional HPF.

As in the previous case a number of configurations in this category did not yield results that could be used for filters as the output voltage was considered to be low over the entire frequency range. This was due to the combination of the output voltage being pulled low at low frequencies in addition to the output voltage being pulled low at high frequencies due to the presence of a HF path between V_{out} and G_{rnd}.

V_{in} low at mid frequencies only

The input voltage, for certain configurations, was pulled low at mid frequencies but remained high at both the low and high frequencies. These configurations also had certain traits that they all shared:

- No LF or HF paths were found to exist between V_{in} and G_{rnd}.

- No cross-connections were present.

- V_{in} and G_{rnd} were connected to opposite-side terminals but not adjacent terminals.

- No connections were present that forced the voltage gradient to zero.
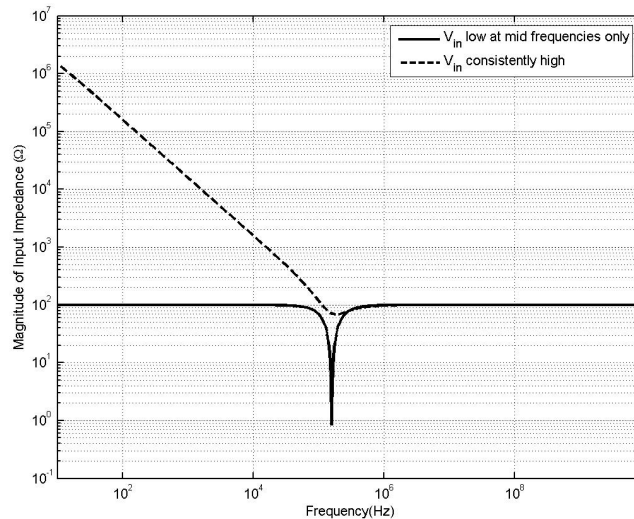
Fig. 2.23: Typical impedance magnitude plots for configurations where the input voltage was either "consistently high" or "low at mid-frequencies only"

Close inspection of these characteristics showed that they are identical to the characteristics of the configurations placed in the "V_{in} consistently high" category. The difference between the two groups was attributed to the input impedance of the structures as shown in Fig. 2.23. Here it can be clearly seen that the magnitude of the input impedance has a higher minimum for the configurations classified as "V_{in} consistently high" as compared to that of the minimum impedance value found for the configurations where "V_{in} was low at mid frequencies only".

The configurations in this category were used to realise HPFs and BSFs. The main characteristics of these configurations that helped to realise these filters are given in Table 2-XIV.

Table 2-XIV: Subdivisions of the "V_{in} low at mid frequencies" category

Filter type	HPF	BSF
LF path	-	V_{in}-V_{out}
HF path	V_{in}-V_{out}	V_{in}-V_{out}

The two filter types were determined by the following connections:

- If only a HF path exists between V_{in} and V_{out} a response similar to a HPF was realised. At low frequencies V_{out} was pulled to ground by the load resistor acting as a pull-down resistor.

- Conversely, if both a LF and a HF path existed between V_{in} and V_{out} a response similar to that of a BSF was realised where the value of V_{out} was pulled high at the two frequency extremes.

As before a number of configurations in this category were of no value for further investigation as V_{out} was consistently low. This was attributed to the fact that V_{out} was pulled to ground at low frequencies either due to the pull-down resistor effect of the load resistance and/or due to the presence of a LF path between V_{out} and G_{rnd}. A HF path between V_{out} and G_{rnd} was inherent in all the remaining configurations.

V_{in} high at mid frequencies only

V_{in} was found to be low at both low and high frequencies, while remaining high at the mid frequencies for configurations that had a LF and a HF path present between V_{in} and G_{rnd}. All of the configurations within this category had a cross-connection present.

It was found that BPFs could be realised with these configurations, as shown in Table 2-XV.

Table 2-XV: Subdivisions of the "V_{in} high at mid frequencies" only category

Filter type	BPF	
LF path	V_{in}-V_{out}-G_{rnd}	V_{in}-G_{rnd}
HF path	V_{in}-V_{out}-G_{rnd}	V_{in}-V_{out}-G_{rnd}

All of the configurations that resulted in BPFs were seen to have a HF path between V_{out} and G_{rnd}.

Once again a number of configurations yielded filter responses that had no practical use due to the fact that V_{out} was low over the entire frequency range. This was due to the fact that either a LF path existed between V_{out} and G_{rnd} or V_{out} was isolated at the lower frequencies thereby forcing the load resistor to act as a pull down resistor. At high frequencies a HF path was found to exist between V_{out} and G_{rnd}.

V_{in} consistently low

There was a large group of configurations that did not yield any filter responses that had practical value due to the fact that the input voltage was pulled to ground over the entire frequency range. The configurations that fell into this category showed the following traits:

- A LF and a HF path existed between V_{in} and G_{rnd}.

35

- One of two other factors was also found to be present in the configurations. Firstly a zero voltage gradient was found to be present due to phenomena such as shorting-connections or loop configurations, as discussed in Chapter 3. Secondly V_{in} and G_{rnd} were forced to equal potentials due to vertical-connections, also to be discussed in Chapter 3.

As no practical use could be obtained from these configurations, they were not investigated any further.

Table 2-XVI: Summary of results for two-port networks

Two-port network				
V_{in} behaviour category	Signal paths		Cross-connection	Placement of V_{in} & V_{out}
	LF	HF		
LPF				
Consistently high	V_{in}-V_{out}	V_{out}-G_{rnd}	None	V_{in}-G_{rnd}: non-adjacent opposite-side
Low @ high frequencies	V_{in}-V_{out}	V_{in}-V_{out}-G_{rnd}	Sometimes	V_{in}-G_{rnd}: same-side if no cross-connection present
HPF				
Consistently high	V_{out}-G_{rnd}/ RI pull down resistor	V_{in}-V_{out}	None	V_{in}-G_{rnd}: non-adjacent opposite-side
Low @ low frequencies	V_{in}-G_{rnd} & RI pull down resistor/ V_{in}-V_{out}-G_{rnd}	V_{in}-V_{out}	None	V_{in}-G_{rnd}: opposite-side
Low @ mid frequencies only	RI pull down resistor	V_{in}-V_{out}	None	V_{in}-G_{rnd}: non-adjacent opposite-side
BPF				
Consistently high	RI pull down resistor	V_{out}-G_{rnd}	None	V_{in}-G_{rnd}: non-adjacent opposite-side
Low @ high frequencies	RI pull down resistor/ V_{out}-G_{rnd}	V_{in}-V_{out}-G_{rnd}/ V_{in}-G_{rnd}	Sometimes	V_{in}-G_{rnd}: same-side if no cross-connection present
High @ mid frequencies only	V_{in}-V_{out}-G_{rnd}/ V_{in}-G_{rnd} & RI pull down resistor	V_{in}-V_{out}-G_{rnd}	Always	No general pattern
BSF				
Low @ mid frequencies only	V_{in}-V_{out}	V_{in}-V_{out}	None	V_{in}-G_{rnd}: non-adjacent opposite-side

2.8 Conclusion

In this chapter a matrix representation of the IPPM configurations was developed. These matrices could be used to represent the configurations of any *n*-layer IPPM structure. In the discussion presented here they were specifically used for a three-layer IPPM. The matrices were seen to perform two main functions. Firstly, they could be used to concisely store the interconnection and I/O connection information of a particular configuration. Secondly, the matrices could be used to numerically identify all the configurations that could possibly be realised with an IPPM. This fact was illustrated through the use of the matrices to identify the configurations for both the single-port and two-port networks. This identification process involved generating a set of all possible configurations. This set was then further processed using permutation matrices to eliminate configurations from the set that were not practical to investigate.

The configuration behaviour was investigated by performing a SPICE type circuit simulation. To this end it was necessary to be able to model the IPPM structure. A quasi-distributed model was discussed that was used for this purpose. The model consisted of a number of cells connected in cascade. The simulation environment in which this model was used was also discussed. From the simulations the transfer function, input voltage frequency response and the output voltage frequency response were obtained. The accuracy of the model was validated by comparing the simulated transfer function of a configuration to that of an experimentally measured transfer function. From this it was seen that the results of the quasi-distributed model correlated well with a practical realisation of the IPPMs.

The configurations were then categorised through analysis of the various frequency responses. The choice as to which frequency response to use had to be considered. For the single-port networks it was shown that the transfer function could be readily used for the analysis. However, in the case of the two-port networks the transfer function sometimes yielded misleading results. Consequently the analysis of the input and output voltage responses proved to be more beneficial.

From this analysis both the single-port and two-port network configurations were divided into the standard filter types, i.e. LPFs, HPFs, BPFs and BSFs. A fifth group was also introduced for configurations that did not fall into one of the four filter categories. All the configurations in this final group were seen to have no practical value as these configurations had little or no influence on the output voltage frequency response.

The type of behaviour realised by any given configuration was seen to be attributed to the presence of LF and HF paths within the structure. These paths were seen to inherently exist in the IPPMs between certain terminals. The placement of the I/O connections on the relevant terminals caused these paths to be either absent or present between the I/O connections. The introduction of interconnections into the configuration enabled the LF and HF signal paths to be manipulated so as to yield a certain type of behaviour from the IPPMs.

The configuration behaviour could thus be seen to be related to the geometric placement of interconnections and I/O connections within a configuration. No dependence on the number of conductive or dielectric layers was seen to exist. Consequently the results discussed here can in all likelihood be used in the design and development of configurations for IPPMs with more than three conductive layers. However, further investigation of this assumption is designated for future work.

CHAPTER 3

IPPM features highlighted by exhaustive search

In the previous chapter an exhaustive search of the possible configurations that can be realised with a three-layer IPPM was performed. From this investigation various filter behaviour was seen to be realised with the configurations. The interconnections of the structure's terminals, as well as the positioning of the I/O connections, within a given configuration, were seen to determine the type of filter that the structure realised.

During the exhaustive search other characteristics inherent to the IPPMs were brought to light. Although not all of these characteristics influence the type of filter realised with the structures, they can prove useful in manipulating the structure so as to alter the utilisation of the dielectric. Some of these characteristics also indicate inefficient ways to configure the structures, which should be avoided during a design procedure. An example of this can be seen in Chapter 4 where these characteristics were used during the configuration selection process for the EMI filter. All of these characteristics lend themselves to a better understanding of the functionality of the structures.

A final concept discussed in this chapter is that of a dominant configuration. This concept was used to better understand the behaviour of some of the single-port network configurations. However, the investigation presented here on the dominant configurations is not very detailed in nature, as it was not the main focus of the study. It was felt to be necessary to still touch upon the concept as it may indicate a research avenue for future work.

3.1 Voltage gradients across IPPMs

(a)   (b)
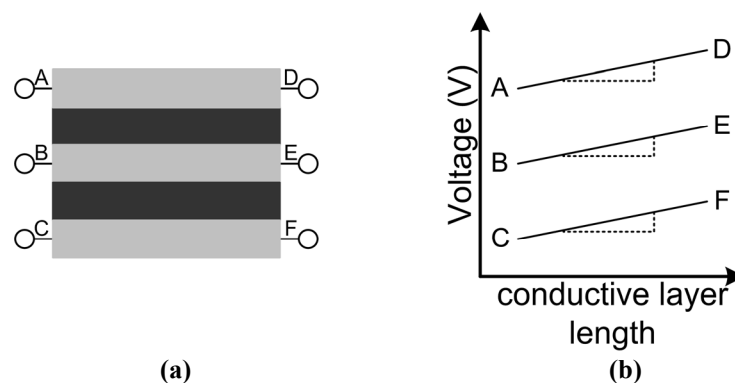
Fig. 3.1: (a) A schematic representation of a three-layer IPPM and (b) a schematic representation of the voltage gradients found across the conductive layers of the structure

In Appendix B a discussion about the voltage drop across coupled conductive layers was presented. Through this discussion it was seen that the voltage drop across each of the conductive layers in an IPPM will be the same if the coupling is ideal. This can be interpreted as an identical voltage gradient found along the length of the conductive layers. In Fig. 3.1(a) the schematic representation of the three-layer

IPPM is shown again for ease of reference. Fig. 3.1(b) gives a schematic representation of the general trend of the voltage gradients that would ideally be found across this structure. The absolute potential found at each of the terminals is arbitrary.

In a practical realisation of the IPPMs the coupling will not be ideal. In Chapter 2 the simulated and measured results were seen to correspond when a coupling of 0.99 was used in the simulation. However provided that the coupling is only slightly less than unity, as is the case for a coupling of 0.99 and provided that the structures are electrically large, i.e. transmission line effects do not come into play, the voltage gradients can be considered to be identical.

A number of interconnections were found that influenced the behaviour of the IPPMs. These interconnections manipulated the absolute potentials of certain terminals and influenced the absolute potentials of other terminals using the fact that the voltage gradients had to remain identical.

It was also seen that the relative placement of the I/O connections could also influence the voltage gradient.

3.1.1 Influence of certain interconnections upon absolute voltages and voltage gradients

Cross-Connections
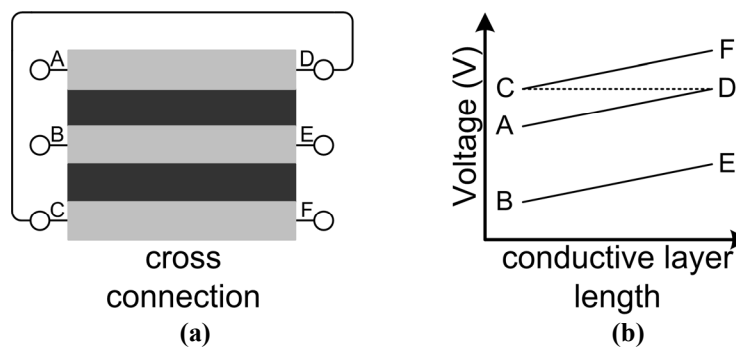
Fig. 3.2: (a) An example of an arbitrary cross-connection and (b) the influence this connection is seen to have on the absolute potential of the terminals

In Chapter 2 the idea of a cross-connection was introduced as a connection between one or more of the terminals on the left hand side of the structure (as seen in the schematic representation) with one or more of the terminals on the right hand side of the structure. The cross-connection was also seen to introduce a HF path between opposite-side terminals. Fig. 3.2 illustrates the influence that a cross-connection has on the absolute potentials of the IPPM terminals. In the figure the cross-connection causes the absolute potential of terminals C and D to be forced to the same value. This aspect of the cross-connections has great influence on the behaviour of the configuration when a particular type of cross-connection, known as a shorting-connection is found to be present in the configuration.

Shorting-connections

A shorting-connection, as shown in Fig. 3.3(a), occurs when adjacent terminals are connected together. In so doing the absolute potential of these two terminals are forced to the same value, which results in a zero voltage gradient across all of the

conductive layers. This is diagrammatically shown in Fig. 3.3(b). Such a connection effectively eliminates the effect of the main magnetic energy storage mechanism, namely the inductance of the structure. All that remains is the magnetic storage due to leakage effects. It can be argued that this type of connection is very wasteful of the magnetic material as the same effect could be accomplished by different means. In particular, the E-core could be removed to no detrimental influence on the behaviour of the IPPM.
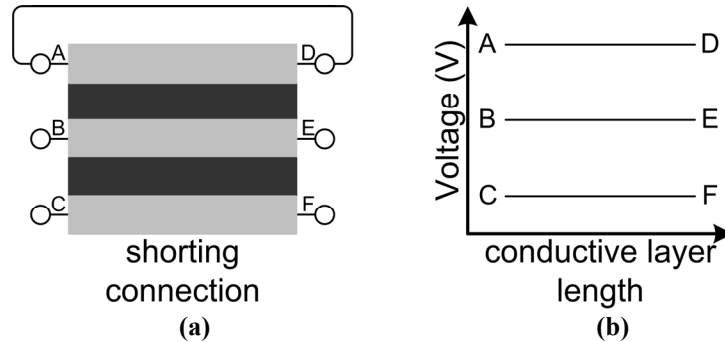
Fig. 3.3: (a) An example of an arbitrary shorting-connection and (b) the influence this connection is seen to have on the absolute potential of the terminals

A zero voltage gradient across the structure can also be realised without the presence of a shorting-connection. This is found for two particular groupings of cross-connections. These groupings have been termed a loop-configuration and a cross-configuration. Schematic representations of these two configurations, and plots of their voltage gradients, are shown in Fig. 3.4.
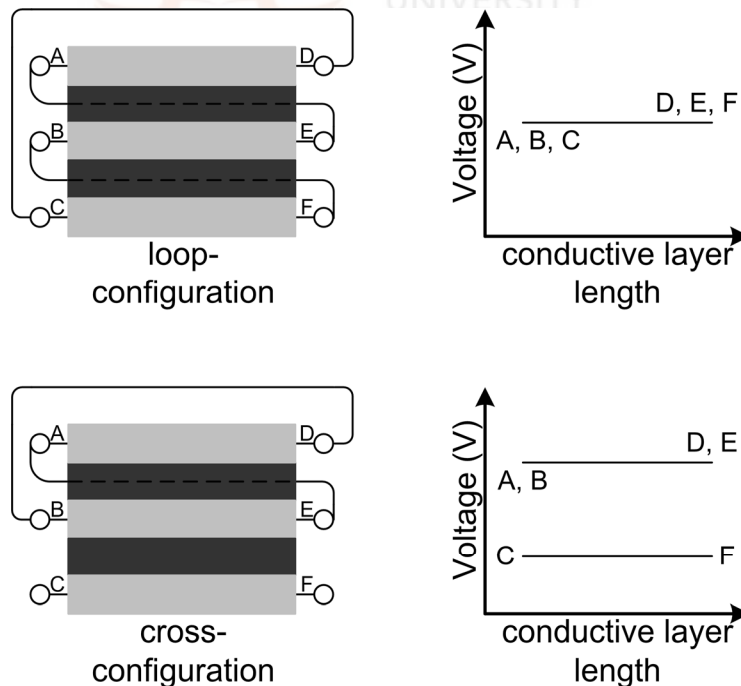
Fig. 3.4: Schematic representations of the loop-configuration and the cross-configuration with their associated voltage gradients

In the case of the loop-configuration the absolute potential of the terminals found within three distinct sets of non-adjacent opposite-side terminals are forced to the same value. In so doing the voltage gradients across the layers are forced to zero.

The cross-configuration forces the absolute potential of opposite-side terminals found on two distinct conductive layers, to the same value. This scenario can only be realised if a zero voltage gradient occurs across these two conductive layers. The third layer, although not necessarily at the same absolute potential as the other two layers will also have a zero voltage gradient across its length.

Vertical-connections
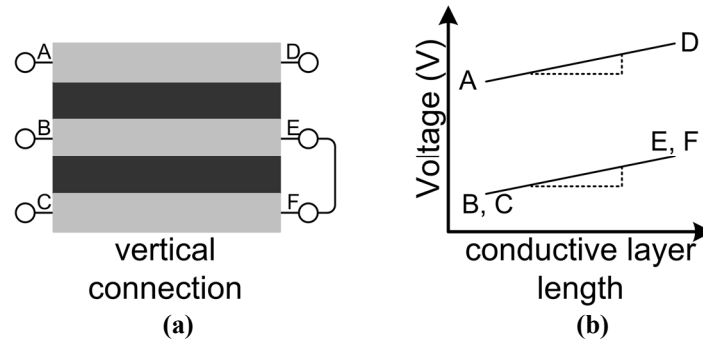
Fig. 3.5: (a) An example of an arbitrary vertical-connection and (b) the influence this connection is seen to have on the absolute potential of the terminals

A vertical-connection is characterised by an interconnection between same-side terminals, as shown in Fig. 3.5(a), which inherently forces these two terminals to the same absolute potential. The terminals adjacent to those forming the vertical-connection are also forced to the same absolute potential with respect to one another, refer to Fig. 3.5(b). This happens due to the fact that the voltage gradients across the conductive layers must remain identical.

Depending on the placement of the vertical-connections the utilisation of the dielectric layers of the IPPM may vary. It was also found that certain placements of the vertical-connections relative to the I/O connections had no discernible influence on the behaviour of the configurations.

Dielectric utilisation

Two definitions are introduced for the purpose of clarity:

Vertically adjacent layers
Conductive layers that are situated directly on top of one another.

Vertically non-adjacent layers
The top and bottom conductive layers of a three-layer IPPM.
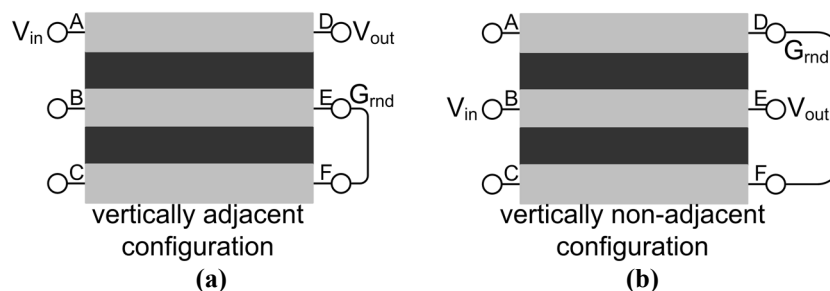
Fig. 3.6: Typical vertical-connections between (a) vertically adjacent layers and (b) vertically non-adjacent layers

If the vertical-connection is placed between vertically adjacent layers the introduction of equipotential layers on either side of a dielectric layer effectively eliminates the dielectric. This can be seen as a poor utilisation of the dielectric layers of the structure. However, if the vertical-connection is between vertically non-adjacent layers, depending on the placement of the I/O connections, the utilisation of the dielectric can be enhanced.

This is shown by considering the two configurations found in Fig. 3.6. The first configuration has a vertical-connection present between vertically adjacent layers, while the vertical-connection of the second configuration is between vertically non-adjacent layers. The difference in dielectric utilisation of the two configurations can be seen through investigation of the configurations' voltage responses, shown in Fig. 3.7. The two configurations are seen to behave similarly except for a shift in cut-off frequency in the output voltage response. It is well known that the cut-off frequency of a second-order filter is given by equation (3.1).
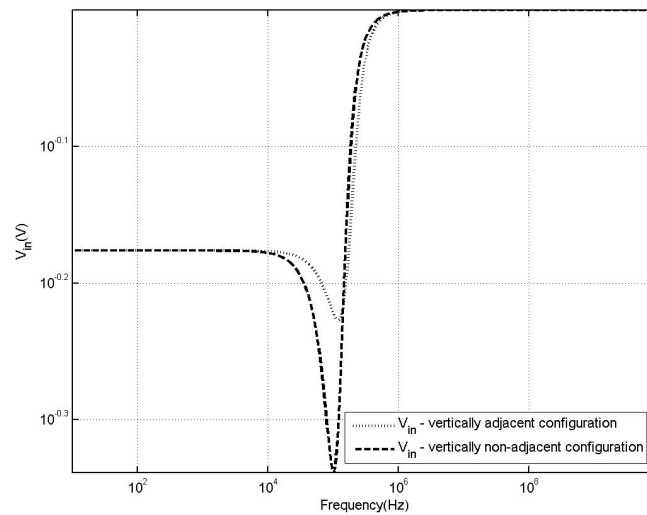
(a)
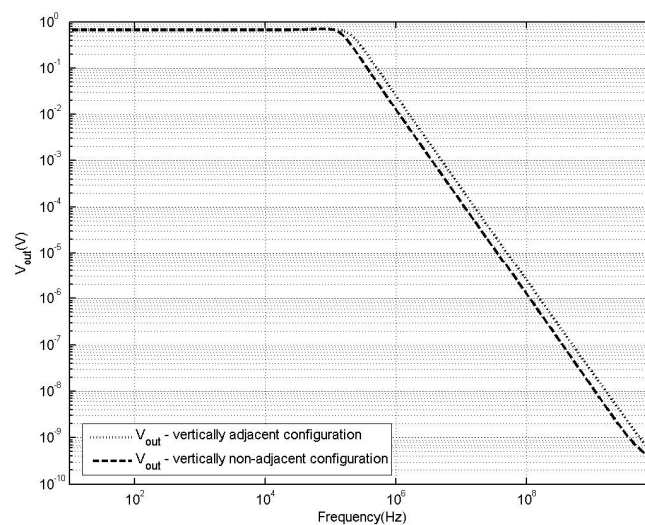
(b)

Fig. 3.7: (a) The input voltage response and (b) the output voltage response of the two configurations shown in Fig. 3.6

$$\omega_c = \frac{1}{\sqrt{LC}} \qquad (3.1)$$

Due to the similar placement of the I/O connections relative to one another in the two configurations, the inductance realised by the two configurations can be considered to be the same. Consequently, the capacitance, or the dielectric utilisation of the two configurations is the only parameter that can cause a shift in the cut-off frequency. From equation (3.1) it can also be seen that the capacitance realised by the vertically adjacent layer configuration must be smaller than the capacitance realised by the vertically non-adjacent layer configuration. This is due to the fact that the cut-off frequency of the former configuration is greater than that of the latter configuration.
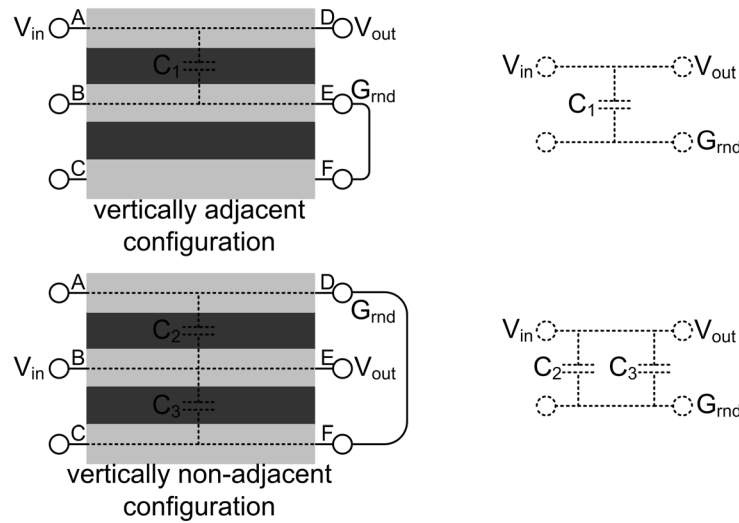
Fig. 3.8: The effective capacitance realised by the configurations with a vertical-connection between vertically adjacent layers and vertically non-adjacent layers

This can be explained with reference to Fig. 3.8. Only a single layer of dielectric is utilised in the first configuration. In the second configuration the dielectric layers are seen to be connected in parallel, thereby increasing the capacitance realised by the configuration, as compared to that of the first configuration.

Placement of vertical-connections and I/O connections
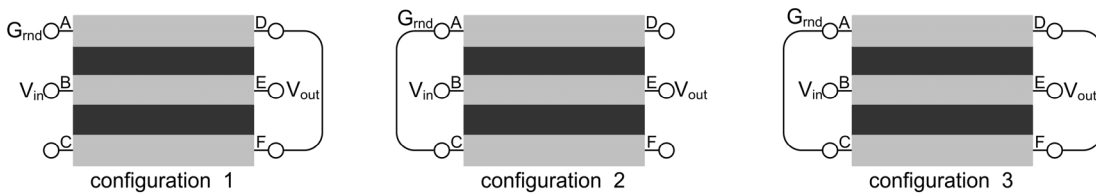
Fig. 3.9: Three configurations that have the same voltage response even though the location of the vertical-connection is different

It was also found that the influence that a vertical-connection has on the response of a configuration is not influenced by which side of the IPPM the connection is located, as shown in configurations 1 and 2 of Fig. 3.9. Further, a second vertical-connection forming a mirror image of the first connection about the y-axis of the structure, as discussed in Chapter 2, can be considered a redundant interconnection. The interconnection is redundant as the behaviour of the configuration remains the same regardless as to whether or not the interconnection is present. Such a vertical-

connection is illustrated in configuration 3 of Fig. 3.9. The input and output voltage responses of the three configurations are shown in Fig. 3.10(a) and (b) respectively, and are seen to overlap as a consequence of the identical voltage gradients. A slight deviation at the higher frequencies is most likely due to convergence issues in the simulations but can be disregarded due to the order of magnitude of the voltage at which they occur.

Another aspect of the placement of the I/O connections relative to the vertical-connections was noticed. Consider the configurations shown in Fig. 3.11.

Configuration 2 is the same configuration 2 as the one shown in Fig. 3.9. Configuration 4 is a similar configuration where the placement of the I/O connections relative to the vertical-connection has merely been interchanged. However, the dielectric utilisation of the IPPM remains the same. This results in identical voltage responses as shown in Fig. 3.12.
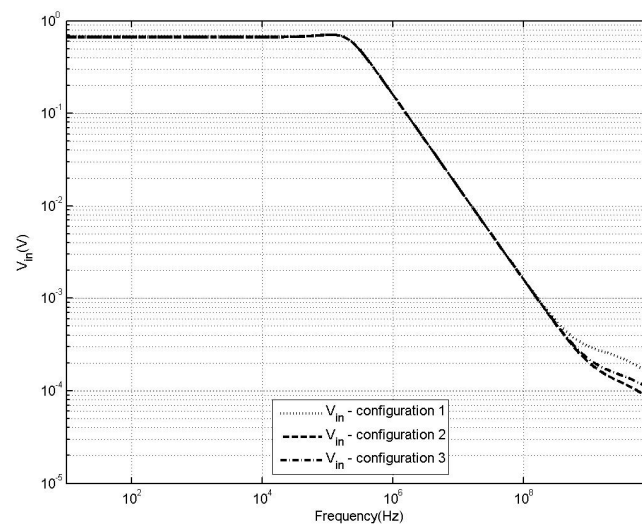
(a)
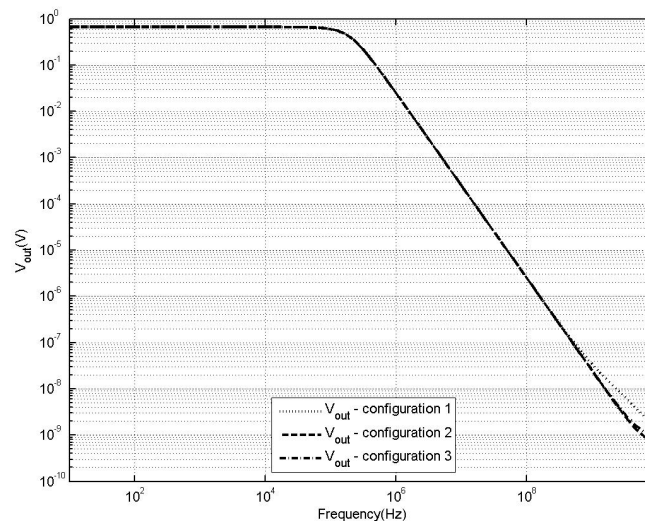
(b)

Fig. 3.10: (a) The input voltage and (b) the output voltage response of the three configurations shown in Fig. 3.9
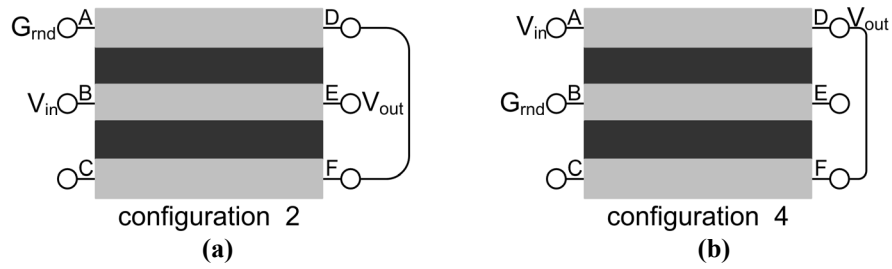
Fig. 3.11: Two configurations that have the same voltage response even though the placement of the I/O connections is slightly different

(a)

(b)
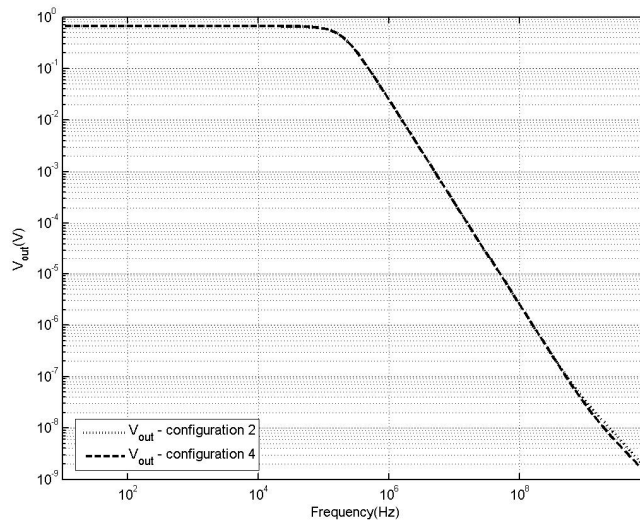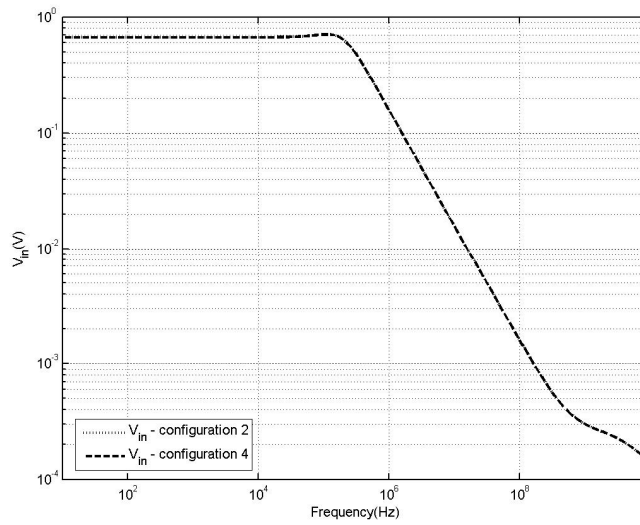
Fig. 3.12: (a) The input voltage and (b) the output voltage response of the two configurations shown in Fig. 3.11

3.1.2 Influence of the relative placement of I/O connections upon voltage gradients

When the input and output I/O connections are placed as shown in Fig. 3.13, a zero voltage gradient will be realised across the IPPM. This can be explained by considering the path of the displacement current as indicated in the figure. The current is seen to flow in opposite directions through the two conductive layers to which V_{in} and V_{out} are connected. As a result there will be no net flux linking these two layers together. Consequently the voltage gradient across the conductors will be forced to zero and the inductance of the structure will become negligibly small.
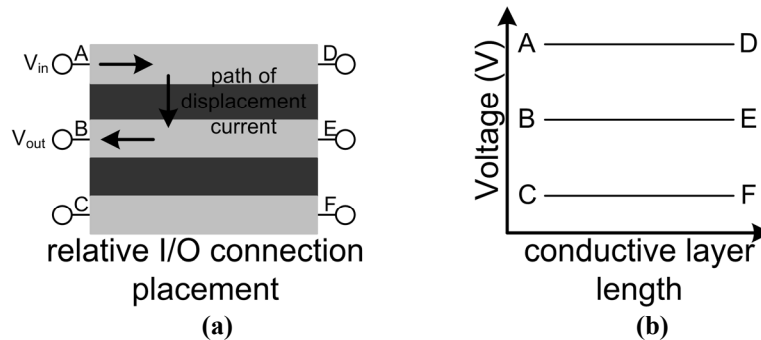
Fig. 3.13: (a) An example of the relative placement of I/O connections and (b) the influence on the voltage gradients

3.2 Manipulation of IPPMs

Through comparison of various configurations examined during the exhaustive search it was seen that configurations that were similar to one another also yielded similar results. From this it was discovered that the layers of the IPPMs could be manipulated in certain ways in order to predictably alter the behaviour of the configuration.

3.2.1 Floating layers
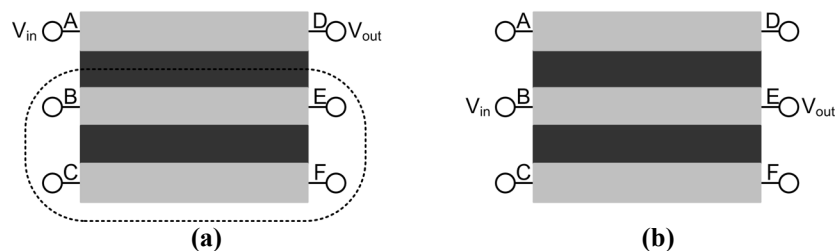
Fig. 3.14: (a) A configuration with a floating section (b) The new configuration realised by moving the I/O connections to terminals found in the floating section

A floating layer was defined as follows:

Floating layer
A layer of the IPPM whose terminals were not connected in any way.

Such layers can be found in the demarcated area of the IPPM shown in Fig. 3.14(a). The two terminals A and D connected to the I/O connections have their potentials held at a certain absolute value. In the floating layer section there will not be a

movement of charge across the boundary line as there are no paths along which the charge can move. Consequently the absolute potentials of the terminals in the floating section were not fixed. The voltage gradient across the floating layers still reflects the behaviour of the voltage gradient in the top layer. Due to this fact the I/O connections can be moved to any of the floating layers, provided that the placement of the connections relative to one another remains the same. This is shown in Fig. 3.14(b) where the I/O connections were moved from terminals A and D to terminals B and E. This was seen to have no effect on the frequency response of the structures, as is shown for the configurations of Fig. 3.14 in Fig. 3.15.

The preceding discussion investigated the concept of floating layers as applied to single-port network configurations. The same concept can be applied to the two-port network configurations as well. However, the placement of the I/O connections relative to one another must be maintained.

(a)

(b)
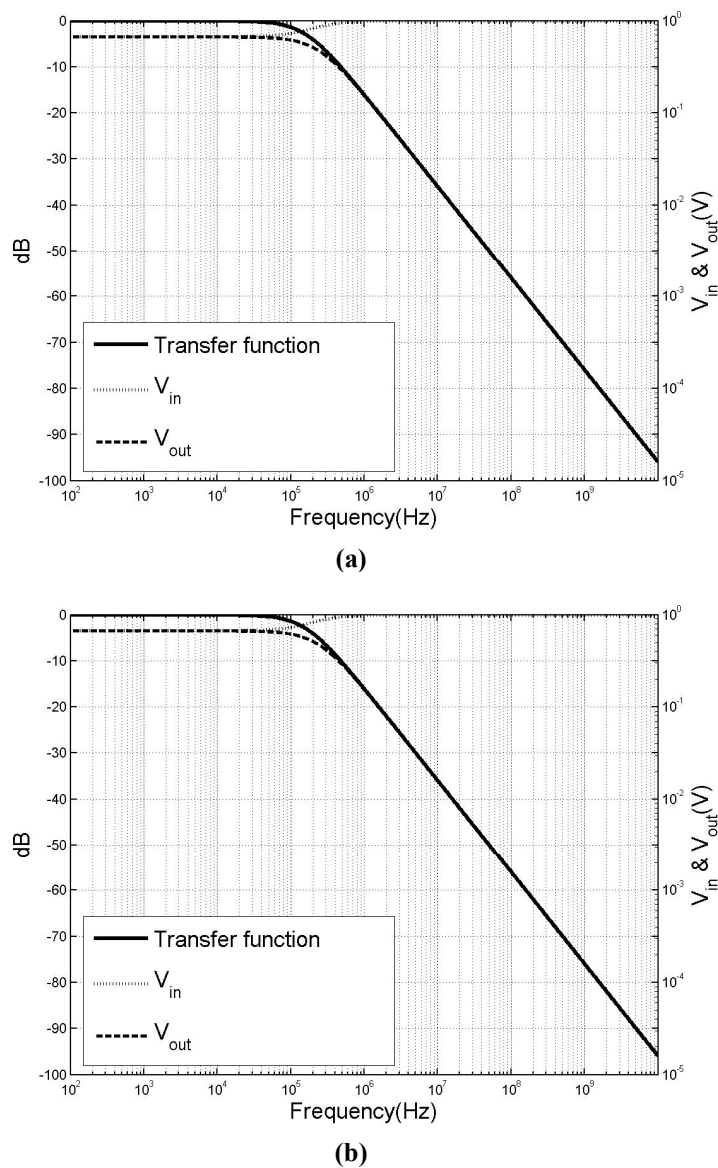
Fig. 3.15: The transfer function, input and output frequency responses of the configurations shown in (a) Fig. 3.14(a) and (b) Fig. 3.14(b)
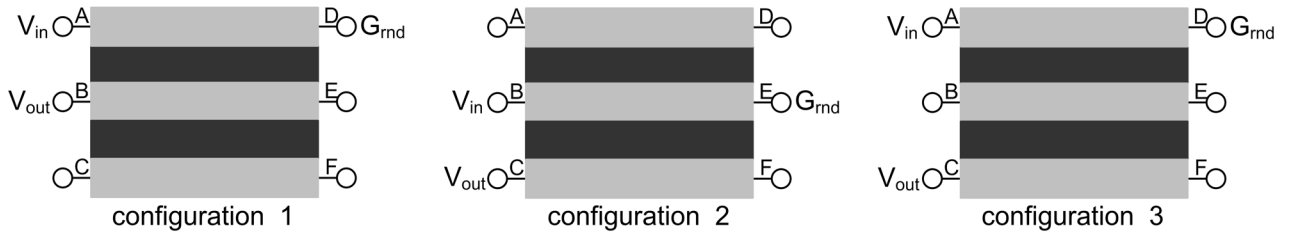
Fig. 3.16: Movement of the I/O connections of two-port network configurations to the terminals of floating layers

(a)

(b)
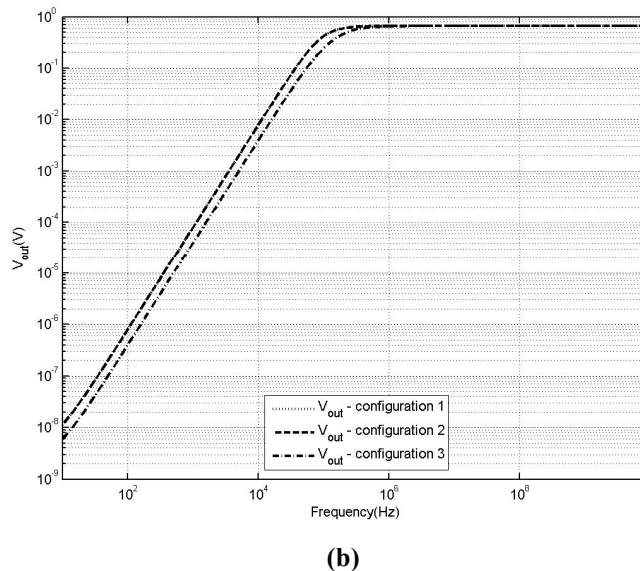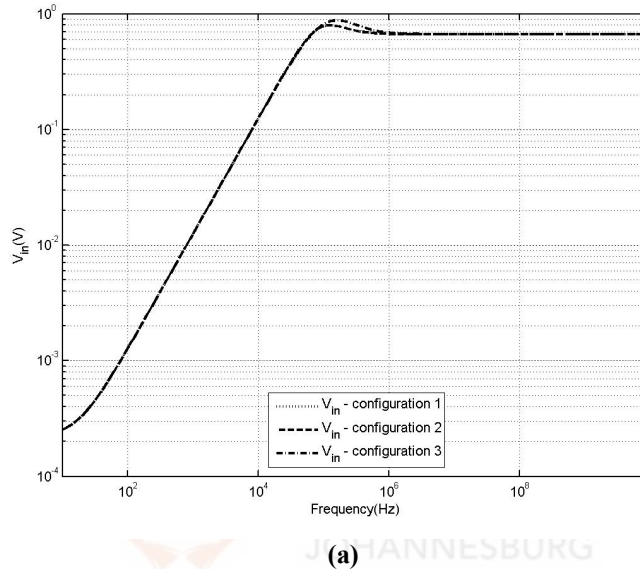
Fig. 3.17: (a) The input voltage response and (b) the output voltage response of the three configurations shown in Fig. 3.16

This is seen by considering the three configurations shown in Fig. 3.16. The second configuration is essentially the first configuration except for a shift in the placement of all the I/O connections. In the third configuration only the placement of the output voltage terminal was shifted. The input and output voltage responses of the three configurations are shown in Fig. 3.17. From this figure it be seen that the output re-

sponses of the first two configurations overlap exactly, but differ from that of the third configuration. As in the case of the vertical-connections, the shift in cut-off frequency of the third configuration's output response, relative to that of the other two configurations, can be explained by a difference in the utilisation of the dielectric. This is shown diagrammatically in Fig. 3.18, where the dielectric layers of the third configuration are effectively connected in series with one another. Due to this fact the definition of a floating layer, specifically in the case of two-port network configurations, was expanded.

Floating layers
Floating layers within an IPPM are layers that don't have any of their terminals connected to an interconnection or an I/O connection and are not situated between layers that do have these sorts of connections on their terminals.
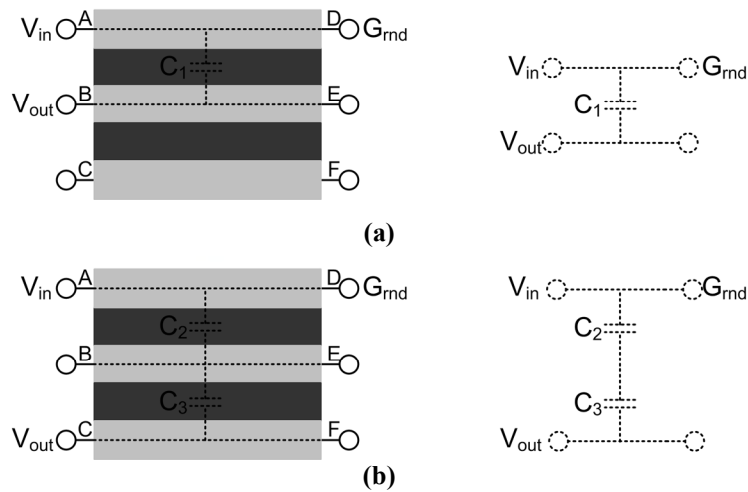
Fig. 3.18: The effective capacitance realised by the configurations shown in Fig. 3.16 (a) The effective capacitance realised by the first two configurations. (b) The effective capacitance realised by the third configuration

3.2.2 Repositioning of layers

It was found that the position of any given layer, namely that of the top layer, middle layer or bottom layer, can be interchanged with the position of other layers in the IPPM as long as the interconnections between the various terminals are not broken. The configuration was then considered to be unfolded. This process is shown diagrammatically in Fig. 3.19. The configuration in Fig. 3.19(a) is unfolded to yield two different configurations given in Fig. 3.19(b) and (c).
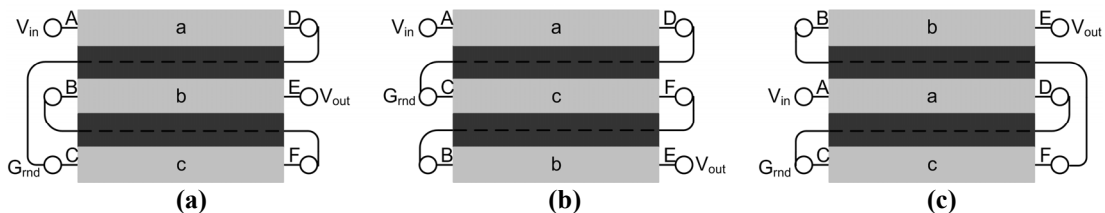
Fig. 3.19: (a) The original folded configuration, (b) the first unfolded case and (c) the second unfolded case considered
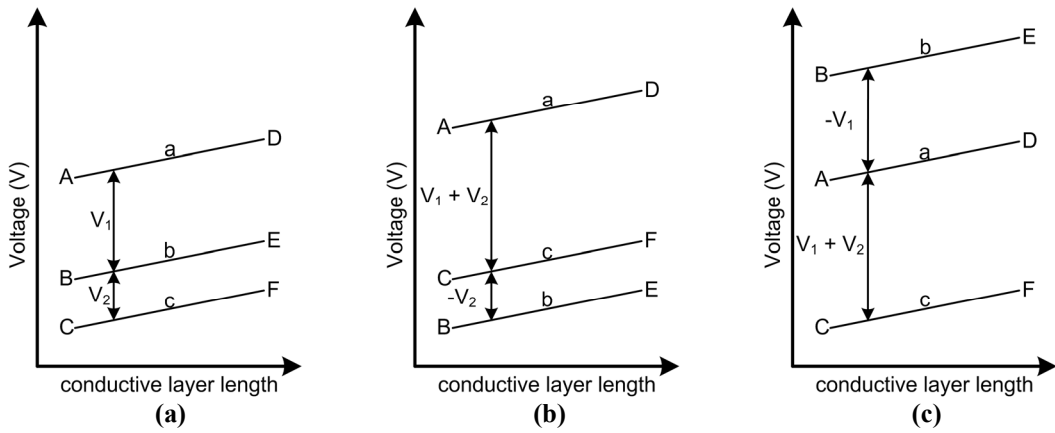
Fig. 3.20: The voltage gradients of (a) the original configuration, (b) the first unfolded case and (c) the second unfolded case
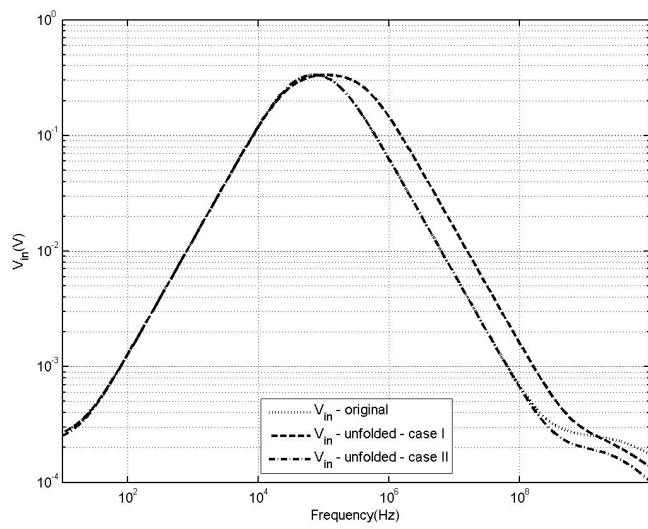
(a)
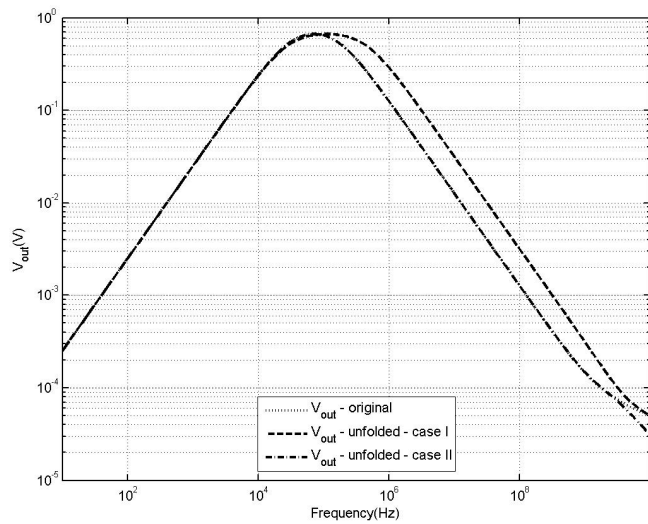
(b)

Fig. 3.21: (a) The input voltage response and (b) the output voltage response of the three configurations considered

50

This process can be better understood by considering the voltage gradient across each layer as well as the voltage difference between the layers for all three configurations, as shown in Fig. 3.20. The boundary conditions of the structure are defined by the interconnections and I/O connections. By not breaking any of the interconnections during the unfolding process the boundary conditions essentially remain the same. However, when considering the internal workings of the IPPM, the potential drop across the dielectric layers is seen to change. This results in a variation in the utilisation of the various dielectric layers, which manifests as a shift in cut-off frequency of the input and output voltage responses.

The voltage responses of the three configurations can be found in Fig. 3.21. Here it can clearly be seen that the general form of the responses of the three configurations is the same. The unfolded configurations of Fig. 3.19(b) and (c), show the shift in cut-off frequency as compared to the frequency responses of the original "folded" configuration of Fig. 3.19(a).

3.2.3 Combining of layers

Certain configurations could be reduced to equivalent single-layer IPPM or two-layer IPPM configurations. The ability to perform such an action was dependent on the presence of certain vertical-connections or floating layers within the configuration.

The importance of this concept is clearly seen when designing a configuration for a particular IPPM. In this circumstance care must be taken to avoid the situation where combination of layers is valid. If the concept is valid the configuration design will not be optimal as the same response could be obtained with a different IPPM with fewer layers.

Vertical-connections and the combination of layers

The presence of a vertical-connection on vertically adjacent layers indicated that the two layers in question could be combined into a single layer by eliminating the dielectric that originally separated the layers. This claim is based on the fact that the voltage difference over the dielectric layer is zero due to the identical voltage gradients found across the layers. As a result the dielectric layer would not be utilised and can be removed. Consequently the three-layer IPPM can be reduced to an equivalent reduced IPPM consisting of either one or two conductive layers. The process of combining layers is illustrated with the configurations of Fig. 3.22.
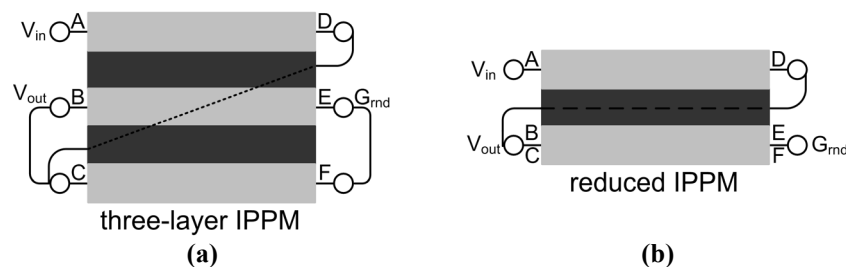
Fig. 3.22: (a) An arbitrary configuration with a vertical-connection between two vertically adjacent layers and (b) its equivalent reduced IPPM configuration

In the figure it can be seen that any interconnection or I/O connections present on the terminals of the three-layer IPPM were merely mapped to corresponding terminals in the reduced IPPM.

The reduced IPPM was modelled using a two-layer version of the quasi-distributed model and simulated as for the three-layer case. The voltage responses for both the two-layer and three-layer IPPMs are shown in Fig. 3.23 and are seen to correspond exactly.

Floating layers and the combination of layers

It has already been shown that when a floating layer is present in a configuration, the I/O connections can be shifted to the floating layers without altering the behaviour of the configuration in any way. This implies that the dielectric layer associated with the floating layer is not utilised. As a result the concept of the combination of layers was extended to include floating layers as well as vertical-connections.

(a)

(b)
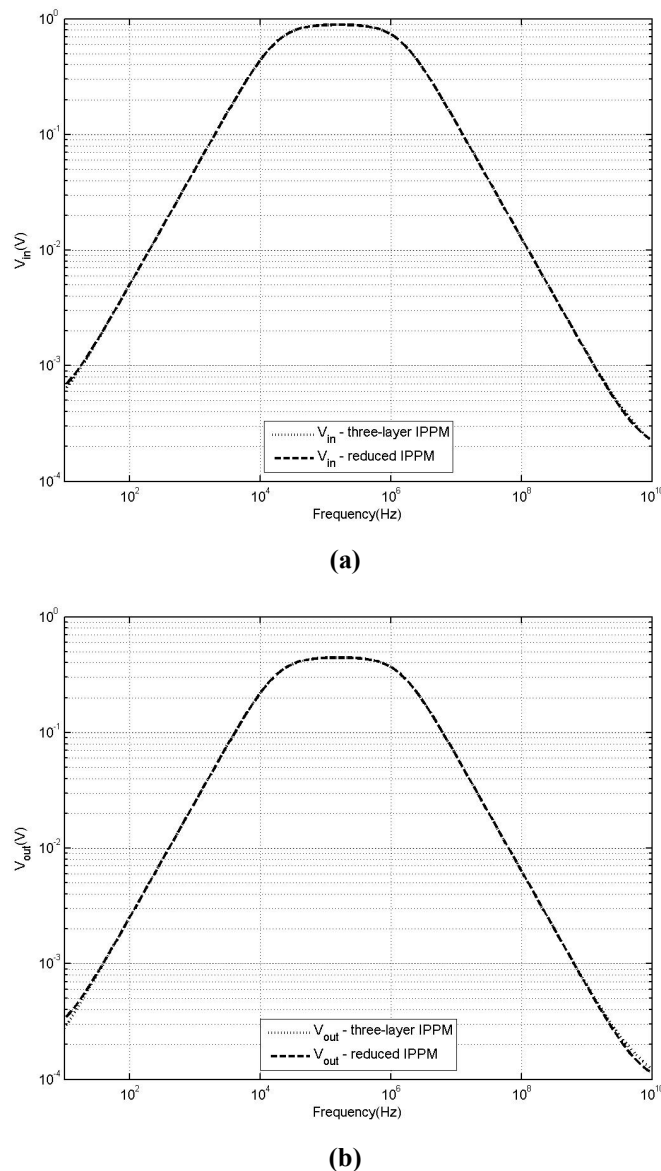
Fig. 3.23: (a) The input voltage response and (b) the output voltage response of the three-layer and reduced IPPM configurations
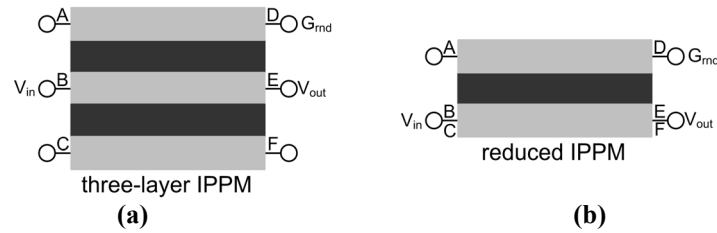
Fig. 3.24: (a) An arbitrary configuration with a floating layer present and (b) its equivalent reduced IPPM configuration

Fig. 3.24 shows a three-layer IPPM configuration where a floating layer was present. This configuration could be reduced to an equivalent two-layer IPPM configuration as shown. Once again a two-layer version of the quasi-distributed model was used to find the input and output voltage frequency responses of the reduced IPPM. The results of this investigation were compared to those of the three-layer IPPM voltage responses as shown in Fig. 3.25. As in the case of the vertical-connections, the three-layer IPPM and reduced IPPM configurations were seen to perform identically.

(a)

(b)
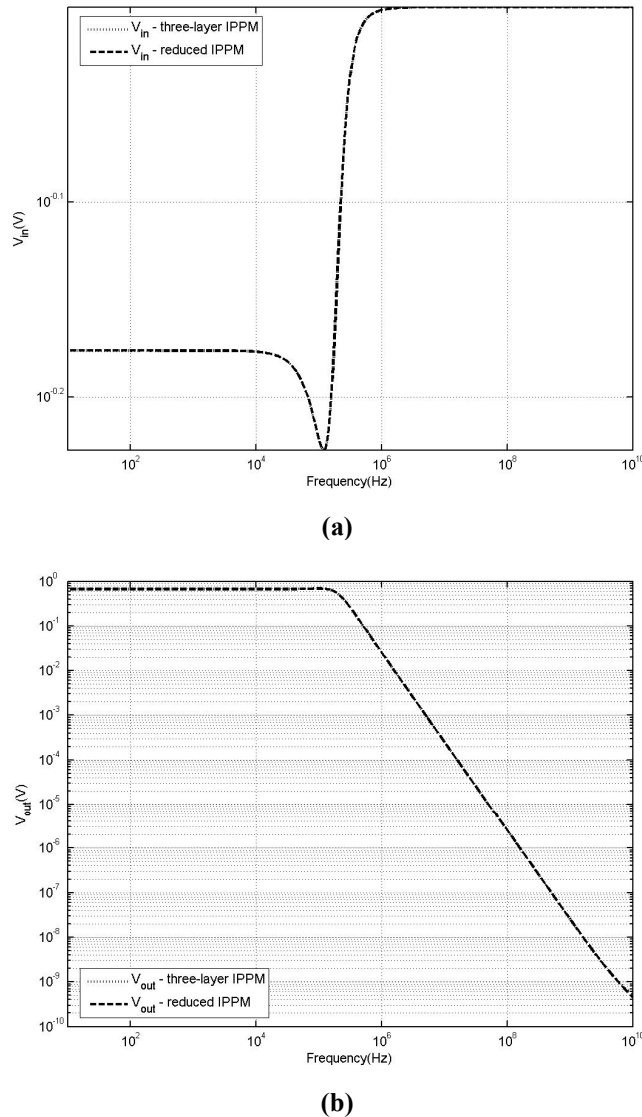
Fig. 3.25: (a) The input voltage response and (b) the output voltage response of the three-layer and reduced IPPM configurations

3.3 Dominant configurations

When analysing the exhaustive search results of the single-port network configurations it was seen that a so-called dominant configuration was found to exist within the set of configurations in each subgroup.

The dominant configuration referred to a commonality that was seen between the configurations. This commonality took the form of the presence of a particular interconnection and/or the placement of the I/O connections relative to one another. Most of the time the commonality/dominant configuration was seen to be explicitly present in the configurations. However, certain configurations had to be manipulated to obtain the dominant configuration. The manipulation involved applying either one or both of two concepts. Firstly the principle of the combination of layers was applied. Secondly the absolute potential of certain terminals was considered in the presence of shorting-connections and/or vertical-connections.

As previously mentioned the configurations within a subgroup yielded virtually identical transfer functions. This fact, combined with the fact that a dominant configuration was seen to exist in all the configurations, suggested that the utilisation of the inductance and capacitance within an IPPM was governed by the dominant configuration. The extent to which this statement is valid needs further investigation but is outside the scope of this study. The dominant configuration concept is explored here merely as a means of indicating a future research direction. If this concept can be better defined it may prove beneficial for the development of generalised guidelines for the design of IPPM configurations.

Only the single-port network configurations were considered in this section. In the case of the two-port networks it was not possible to divide the configurations into subgroups as was done in the case of single-port networks. The configurations themselves also became more complicated, due to the presence of the ground terminal, and did not readily lend themselves to the dominant configuration concept.

Each of the filter types found for the single-port network configurations and their respective subgroups are considered again here with reference to their dominant configurations.

3.3.1 Low pass filter

Table 3-I: Dominant configurations for the subgroups of the LPF category

Subgroup	Dominant configuration
1	V_{in} O—▭—OV_{out}

The dominant configuration was easily identified for most of the configurations in the subgroup, as V_{in} and V_{out} were connected on adjacent terminals. In certain configurations however, as shown in Fig. 3.26 the dominant configuration was found through application of the principle of combining layers due to the presence of vertical-connections.

As discussed in Chapter 2 it was seen that all the LPFs had a 20dB/dec drop-off and a cut-off frequency corresponding with that of the standard RL circuit. This was supported by the fact that the dominant configuration of the LPFs was seen to be a single conductive layer which realised an inductance.

(a)   (b)
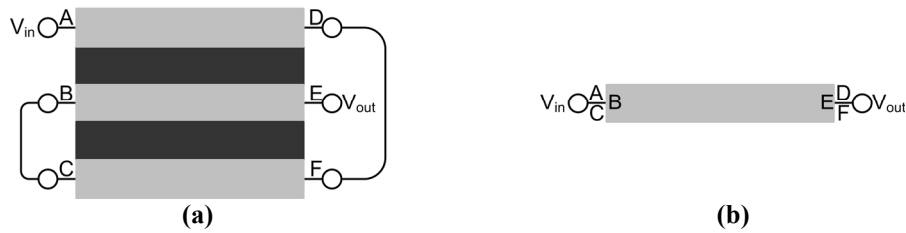
Fig. 3.26: (a) One of the single-port network configurations, with vertical-connections, that realised a LPF (b) The same configuration as in (a) after combining layers to find the dominant configuration

3.3.2 High pass filter

The cut-off frequency of a standard RC circuit is given in equation (3.2). This equation was used to numerically determine the cut-off frequency of the first four subgroups.

$$\omega_c = \frac{1}{RC} \tag{3.2}$$

A slight deviation in the determination of the cut-off frequency using equation (3.2), as compared to the value extracted from the simulation, is most likely due to a slight inaccuracy in the determination of the value of C.

Table 3-II: Dominant configurations for the subgroups of the HPF category

Subgroup	Dominant configuration	Subgroup	Dominant configuration
1		5	
2		6	
3		7	
4		8	

55

Subgroup 1

The dominant configuration was seen to be a two-layer IPPM with V_{in} and V_{out} connected to same-side terminals. The placement of V_{in} and V_{out} caused a zero voltage gradient as shown in Fig. 3.13. As a result only the dielectric layer was utilised.

The cut-off frequency of such a configuration can be found by substituting the load resistance, R_l, and the overall capacitance of the structure, $10C_1$, into equation (3.2). The values of R_l and C_1 correspond with those used in the quasi-distributed model. From this procedure a cut-off frequency of 159kHz was obtained which is close to the simulated cut-off frequency of 162kHz presented in Table 2-VI.

Subgroup 2

The configurations of subgroup 2 were found to have two dielectric layers separating V_{in} and V_{out}. The capacitive coupling between the input and output terminals could consequently be thought of as two capacitors connected in series, similar to the concept shown in Fig. 3.18. As a result the cut-off frequency was calculated by substituting R_l and the overall capacitance of the dominant configuration, $5C_1$, into equation (3.2). This yielded a cut-off frequency of 318kHz as compared to the simulated cut-off frequency of 331kHz.

Subgroup 3

The dominant configuration of subgroup 3 was seen to be the same as that of subgroup 1. Further investigation into the transfer functions of both subgroups indicated that, they could in actual fact, be combined into one subgroup. The configurations were placed in separate subgroups due to a slight deviation in the transfer functions at the lower frequencies that exceeded the criterion used to sort the configurations into the respective subgroups. This deviation is most likely due to convergence issues in the simulations. The simulation cut-off frequency of the configurations in this subgroup was also seen to be 162kHz.

The configurations within this subgroup were found to have a zero voltage gradient across the IPPM structure. This was attributed to one of two possible reasons: firstly due to the absence of net flux in the structure, as discussed in section 3.1.2; or secondly, through the presence of a shorting-connection in the configurations.

Subgroup 4

All the configurations in subgroup 4 utilised both dielectric layers. The dominant configuration realised an effective parallel connection of the dielectric layers similar to that shown in Fig. 3.8. Once again the cut-off frequency was determined by substituting R_l and the overall capacitance, $20C_1$, into equation (3.2) to yield 80kHz as compared to the simulated value of 81kHz.

It was also found that all the configurations in subgroup 4 had a zero voltage gradient. Once again this was attributed to either no net flux or a shorting-connection in the configuration.

Subgroups 5 through 8

In subgroups five through eight, it was found that the transfer function was not that of a pure HPF. Instead the transfer functions appeared as the combination of conventional BSF and HPF transfer functions. This seems to imply that, although the drop-off of the subgroups was still only 20dB/dec, both the inductance and the capacitance of the IPPM was utilised. Fig. 3.27 shows an example of such a transfer function for a configuration found in subgroup eight. The input and output voltage frequency responses are also shown.

The dominant configuration of all these subgroups had a cross-connection present similar to that found in the parallel resonant configuration discussed in Chapter 1. Another aspect that was noted was the fact that none of these configurations had zero voltage gradients.
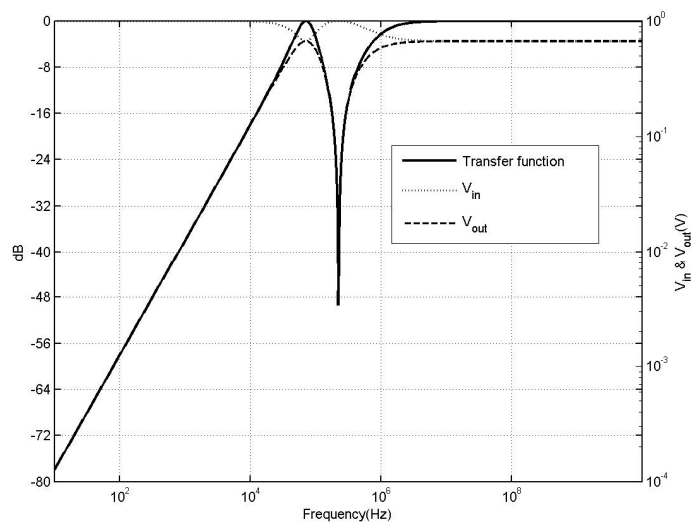
Fig. 3.27: The frequency response of an arbitrary configuration found in subgroup 8

3.3.3 Band pass filter

It should be noted that subgroups one and three should in actual fact be combined into a single subgroup as can be seen by the identical dominant configurations. This fact was confirmed through visual inspection of the transfer functions associated with the configurations in the two subgroups. To the naked eye the transfer functions are identical, even though a slight deviation must exist that fell short of the criterion used to sort the configurations into the respective subgroups.

In all four subgroups the dominant configuration was seen to be similar to the series resonant configuration discussed in Chapter 1. However, the number of dielectric layers and the effective parallel or series connection of these layers was seen to differ between the dominant configurations. This would imply that the overall capacitance realised by the dominant configurations differed, resulting in the shift in cut-off frequencies seen in Table 2-VII.

57

Table 3-III: Dominant configurations for the subgroups of the BPF category

Subgroup	Dominant configuration	Subgroup	Dominant configuration
1		3	
2		4	

3.3.4 Band stop filter

Table 3-IV: Dominant configurations for the subgroups of the BSF category

Subgroup	Dominant configuration	Subgroup	Dominant configuration
1		6	
2		7	
3		8	
4		9	
5		10	

All of the dominant configurations had cross-connections present that were similarly placed to those of the parallel resonant configuration discussed in Chapter 1. The configurations in the BSF category were more complex than those of the other filter categories. As a result it became more difficult to isolate the dominant configuration. This aspect could possible be addressed if this concept is to be further investigated in another study.

3.4 Conclusion

During the exhaustive search a number of features were found that aided in developing an understanding of the functionality of a three-layer IPPM. These features indicated the influence that certain interconnections and/or the relative placement of I/O connections would have on the behaviour of the IPPM. Knowledge of these features could prove beneficial when designing configurations to use in an application. Such knowledge would allow the designer to either use these features to his benefit or avoid using them if they prove to be an inefficient utilisation of the IPPM.

Specifically, it was seen that both the voltage gradient found across the conductive layers of the IPPM as well as the absolute potentials at the terminals of these layers could be manipulated in a well-defined manner. The manner in which this was realised was through the use of interconnections such as cross-connections, shorting-connections, or vertical-connections.

The cross-connections were seen to force the absolute potential of various terminals to the same value. This was of particular importance when considering the shorting-connections, a specific type of cross-connection. The shorting-connection was seen to force the voltage gradient to zero. As a consequence adjacent terminals were forced to the same absolute potential. Finally the vertical-connection caused the absolute potential of two possibly unconnected terminals to take on the same value.

Further investigation of the vertical-connection showed that this connection directly influenced the utilisation of the dielectric layers. The placement of the connection about the y-axis was also considered and shown to not have any noticeable influence on the configuration behaviour.

Not only could the interconnections cause a zero voltage gradient, but it was also shown that the placement of the I/O connections in certain circumstances had the same effect.

Three ways in which the actual layers of the IPPM could be manipulated without changing the configuration behaviour were presented. These aspects were discussed in terms of the placement of I/O connections in the presence of floating layers; the repositioning of layers to obtain a shift in cut-off frequencies; and the combination of layers due to the presence of vertical-connections and floating layers. An awareness of the principles highlighted should prove beneficial during configuration design.

Lastly the concept of a dominant configuration was addressed. The dominant configuration referred to a commonality that was seen to exist between configurations that produced identical filter responses. This concept was not thoroughly investigated but could prove useful in a design procedure. To this end more research needs to be performed on the topic however, this is outside the scope of this dissertation.

CHAPTER 4

Integrated LPFs for both single-phase and three-phase application

In Chapter 2 all possible three-layer IPPM configurations were considered. In order to realise an EMI filter an IPPM implementation that behaved as a LPF was required. The configurations that met this requirement were identified during the exhaustive search and were further investigated in this chapter. Fig. 4.1 shows a hierarchical breakdown of the analysis procedure applied to these configurations.
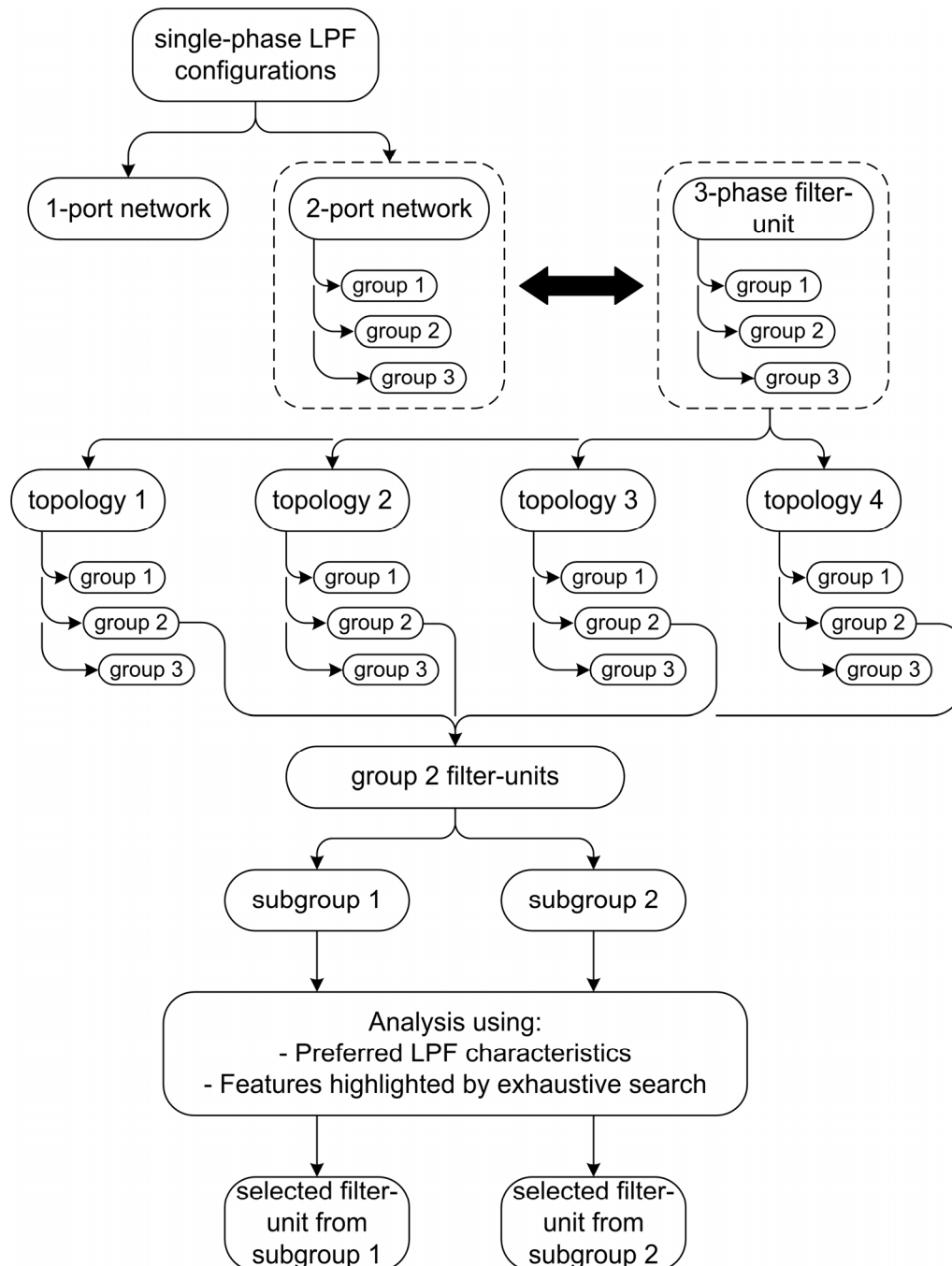
Fig. 4.1: Hierarchy tree of investigation performed on integrated LPFs

From the exhaustive search 43 single-port network configurations as well as 149 two-port network configurations were identified as yielding LPF behaviour. These configurations were analysed by finding the value of the drop-off in dB/dec as well as the pass-band value for each configuration. The transfer function of the single-port network configurations were used to find these values while the output voltage response was used for the two-port network configurations. From this analysis it was seen that the two-port network configurations could be divided into three groups according to the drop-off value.

The investigation thus far was only considering a single-phase application of the IPPMs. The final goal of the EMI filter required a three-phase application of these structures. A bridge between the two applications was created through the introduction of a filter-unit concept. Filter-units were various IPPM configurations that were used to realise a three-phase filter topology. In Fig. 4.1 the filter-units are shown as a direct mapping of the two-port network configurations, implying that 149 filter-units were considered. Each of these filter-units were then used to realise four different three-phase topologies. All four topologies were analysed by means of simulation. As in the single-phase case the drop-off and pass-band values of the output voltage response were extracted from the three-phase simulation. It was seen to still be possible to divide the topologies realised with the filter-units into the same three groups found for the single-phase configurations. Upon closer inspection of these results group 2 was seen to yield the best three-phase filter performance. Consequently, only the filter-units classified as group 2 were further investigated.

It was possible to classify the filter-units of group 2 into two subgroups according to the placement of the I/O connections within the filter-unit configurations. The filter-units in each of these subgroups were analysed through inspection of their associated cut-off frequencies. Further analysis was performed through the application of the various features discussed in Chapter 3. From this procedure it was possible to isolate two filter-units, one from each subgroup, that would be experimentally constructed and verified as discussed in Chapters 5 and 6.

4.1   Further analysis of the LPF configurations

As previously mentioned, a total of 192 configurations that behaved as LPFs were found through the exhaustive search. These configurations were then analysed in terms of drop-off and pass-band values. For the single-port network configurations these values had already been obtained by examination of the transfer function, as discussed in Chapter 2. However, in the two-port network case the transfer function was not used to investigate the responses of the configurations. Consequently the drop-off and pass-band values were determined through examination of the output voltage frequency response instead. To this end the output voltage response in dB was calculated as shown in equation (4.1).

$$V_{out-dB} = 20 \log |V_{out}| \qquad (4.1)$$

$$PB_r = \frac{|V_{out}|}{|V_{in}|} \qquad (4.2)$$

The drop-off in dB was found as the gradient of the slope obtained from a plot of $V_{out\text{-}dB}$. The pass-band ratio, PB_r, was defined as the value found from equation (4.2)

in the region of the pass-band, as seen in a plot of $V_{out\text{-}dB}$. A typical example of such a plot can be found in Fig. 4.2.

The results thus obtained for all 192 configurations are shown in Table 4-I. The numbering convention used to identify the various configurations merely reflected the order in which the LPF configurations were generated during the exhaustive search.

From the tabulated results it can be seen that all the configurations behave comparably in terms of pass-band values. This is due to the fact that a pass-band value of 0dB means the same as a PB_r of 1, namely that the value of V_{out} is equal to that of V_{in} in the pass-band. For both the single-port and two-port networks it was found that $V_{out} \approx 0.667V_s$ in the pass-band region.

The single-port networks were all seen to have a drop-off of -20dB/dec. In the two-port network case however, the majority of the drop-off values were seen to be either -20dB/dec or -40dB/dec. A few configurations were even seen to yield drop-off values of greater than -40dB/dec. In Table 4-I the two-port network configurations have been categorised into three groups according to these drop-off values.

Upon closer inspection of the configurations in group 3 it was seen that, although the gradient of the slope of $V_{out\text{-}dB}$ was steep, the output voltage levelled off at a steady state value at the higher frequencies. The value of $V_{out\text{-}dB}$ at this steady state was seen to be approximately the same as the final value of $V_{out\text{-}dB}$ found for a configuration with a drop-off of -20dB/dec. This can be seen by referring to Fig. 4.2 which shows the output voltage responses of configurations 53 and 95 respectively.
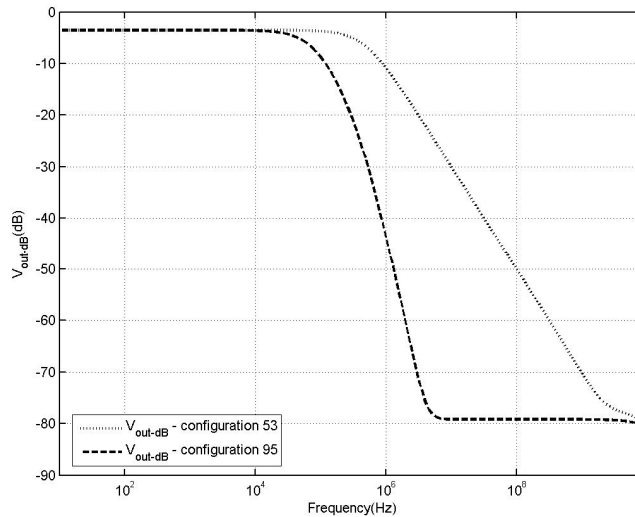
Fig. 4.2: Plots of $V_{out\text{-}dB}$ for configurations 53 and 95

The two-port network configurations were further analysed and a number of similarities between the configurations within each group were found:

- The configurations in group 1 all fell into the category "V_{in} low at high frequencies", as discussed in Chapter 2. All the configurations were also seen to have a HF path present between all three I/O connections V_{in}, V_{out} and G_{rnd}. This HF path was introduced due to the fact that all three I/O connections were found on same-side terminals or through the presence of a cross-connection in the configuration.

Table 4-I: Drop-off and pass-band values found for the LPF configurations

Single-port network configurations								
Configuration	Drop-off (dB/dec)	Pass-band(dB)	Configuration	Drop-off (dB/dec)	Pass-band(dB)	Configuration	Drop-off (dB/dec)	Pass-band(dB)
1	-20	0	16	-20	0	30	-20	0
2	-20	0	17	-20	0	31	-20	0
3	-20	0	18	-20	0	32	-20	0
4	-20	0	19	-20	0	33	-20	0
5	-20	0	20	-20	0	34	-20	0
6	-20	0	21	-20	0	35	-20	0
7	-20	0	22	-20	0	36	-20	0
8	-20	0	23	-20	0	37	-20	0
9	-20	0	24	-20	0	38	-20	0
10	-20	0	25	-20	0	39	-20	0
11	-20	0	26	-20	0	40	-20	0
12	-20	0	27	-20	0	41	-20	0
13	-20	0	28	-20	0	42	-20	0
14	-20	0	29	-20	0	43	-20	0
15	-20	0						

Two-port network configurations								
Configuration	Drop-off(dB/dec)	PB_r	Configuration	Drop-off(dB/dec)	PB_r	Configuration	Drop-off(dB/dec)	PB_r
Group 1						Group 2		
53	-20	1.000	133	-20	1.000	44	-40	1.000
56	-20	1.000	134	-20	1.000	45	-40	1.000
66	-20	1.000	135	-20	1.000	46	-40	1.000
77	-20	1.000	136	-20	1.000	47	-40	1.000
78	-20	1.000	137	-20	1.000	48	-40	1.000
79	-20	1.000	138	-20	1.000	49	-40	1.000
80	-20	1.000	139	-20	1.000	50	-40	1.000
81	-20	1.000	140	-20	1.000	51	-40	1.000
82	-20	1.000	141	-20	1.000	52	-40	1.000
83	-20	1.000	142	-20	1.000	54	-40	1.000
84	-20	1.000	143	-20	1.000	55	-40	1.000
85	-20	1.000	144	-20	1.000	57	-40	1.000
86	-20	1.000	145	-20	1.000	58	-40	1.000
87	-20	1.000	146	-20	1.000	59	-40	1.000
88	-20	1.000	147	-20	1.000	60	-40	1.000
89	-20	1.000	148	-20	1.000	61	-40	1.000
90	-20	1.000	149	-20	1.000	62	-40	1.000
91	-20	1.001	150	-20	0.999	63	-40	1.000
92	-20	1.000	151	-20	1.000	64	-40	1.000
93	-20	1.000	152	-20	1.000	65	-40	1.000
94	-20	0.999	153	-20	1.000	67	-40	1.000
96	-20	1.000	154	-20	1.000	68	-40	1.000
97	-20	1.000	155	-20	1.000	69	-40	1.000
98	-20	1.000	156	-20	1.000	70	-40	1.000
99	-20	1.000	157	-20	1.000	71	-40	1.000
100	-20	1.000	158	-20	1.000	72	-40	1.000
101	-20	1.000	159	-20	1.000	73	-40	1.000
102	-20	1.000	160	-20	1.000	74	-40	1.000
103	-20	1.000	161	-20	1.000	75	-40	1.000
105	-20	1.000	162	-20	1.000	76	-40	1.000
106	-20	1.000	163	-20	1.000	171	-40	1.000
107	-20	1.000	164	-20	0.999	172	-40	1.000
108	-20	1.000	165	-20	1.000	173	-40	1.000
109	-20	1.000	166	-20	1.000	174	-40	1.000
110	-20	1.000	167	-20	0.999	187	-40	1.000
111	-20	1.000	168	-20	1.000	188	-40	1.000
112	-20	1.000	169	-20	1.000	189	-40	1.000
113	-20	1.000	170	-20	1.000	190	-40	1.000
114	-20	1.000	175	-20	1.000	Group 3		
116	-20	1.000	176	-20	1.000	95	-49	1.000
117	-20	1.000	177	-20	1.000	104	-54	1.000
118	-20	1.000	178	-20	1.000	115	-59	1.000
119	-20	1.000	179	-20	1.000	120	-60	1.000
121	-20	1.000	180	-20	1.000	122	-59	1.000
123	-20	1.000	181	-20	1.000	125	-60	1.000
124	-20	1.000	182	-20	1.000			
126	-20	1.000	183	-20	1.000			
127	-20	1.000	184	-20	1.000			
128	-20	1.000	185	-20	1.000			
129	-20	1.000	186	-20	1.000			
130	-20	1.000	191	-20	1.000			
131	-20	1.000	192	-20	1.000			
132	-20	1.000						

- The configurations in group 2 fell into two categories: "V_{in} low at high frequencies" and "V_{in} consistently high". V_{in} and V_{out} were connected to opposite-side terminals in all of the configurations. A HF path was however found to be present between either V_{in} and G_{rnd}, or V_{out} and G_{rnd}. No cross-connections were present in any of the configurations.

- The configurations in group 3 all fell into the category "V_{in} low at high frequencies". As in the case of group 1, a HF path was found to be present between all three I/O connections due to the presence of a cross-connection in all of the configurations in this group.

From the analysis performed in this section it was seen that the configurations of group 2 were the most likely candidates to produce the best LPF performance. However, the analysis performed thus far was for single-phase applications of the IPPMs only. In order to realise a three-phase EMI filter the application of the IPPMs had to be expanded to a three-phase system.

4.2   Expansion of filter configurations from a single-phase application to a three-phase application

As a means of creating a bridge between the single-phase and three-phase application of the IPPMs the discrete component three-phase CM and DM EMI filters presented in Chapter 1 were considered.

(a)   (b)
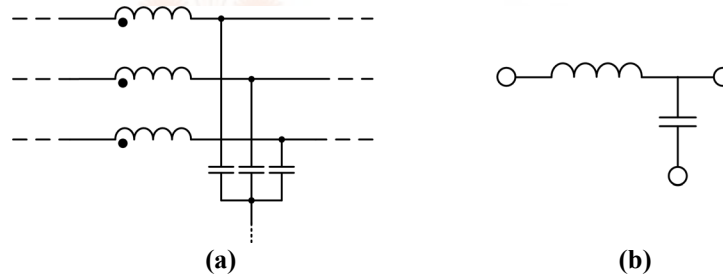
Fig. 4.3: (a) A standard topology used to realise a discrete component three-phase CM filter and (b) its constituent building block or filter-unit

Fig. 4.3(a) shows the standard topology used to realise such a CM filter. This filter can be seen to consist of three identical building blocks, referred to as filter-units. The filter-units in turn contain capacitive and inductive components and, in this particular case, correspond with the well known LC LPF configuration shown in Fig. 4.3(b). The same argument, using the same filter-unit, can be applied to the discrete component three-phase DM filter, shown in Fig. 1.2. The only differences between the two cases are the way in which the filter-units are interconnected and coupled with one another. In the former case the filter-units were connected in star formation and coupled with one another while delta formation with no coupling was used for the latter.

From this observation it is proposed that in order to realise a three-phase filter all that is required is a filter-unit, which itself can, but doesn't necessarily, serve as a LPF in a single-phase application. This is supported by the fact that it is reasonable to assume that a three-phase application, in a symmetrical three-phase system, can be reduced to an equivalent single-phase implementation. As a result the 192 differ-

ent three-layer configurations, discussed in the previous section, can each be considered to realise a filter-unit.

As already mentioned, in the case of the discrete filters it was seen that the filter-units could be connected in either star or delta formation. This concept can be expanded to the filter-units realised with the IPPMs as well. Consider the discrete LPF unit as shown in Fig. 4.4(a). It is seen to have three terminals, an input terminal, V_{in}, an output terminal, V_{out}, and a ground terminal, G_{rnd}. By comparing this to the two-port network filter-units, as represented by Fig. 4.4(b), a direct mapping can be seen to exist between the two types of filter-units in terms of terminal connections. It should be noted that the exact configuration of the two-port network IPPM filter-units does not need to be known.
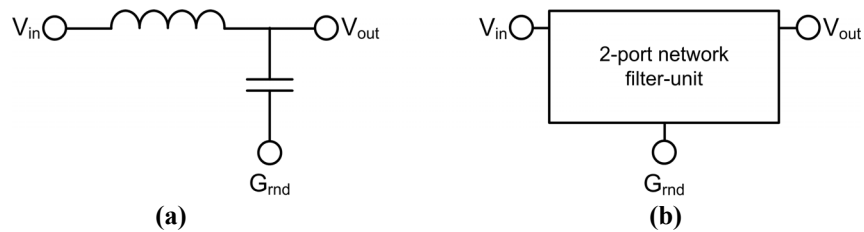
Fig. 4.4: The mapping of terminals that is seen to exist between (a) the discrete filter-unit and (b) the two-port network IPPM filter-unit

4.2.1 Realisation of star formation with IPPM filter-units

Fig. 4.5(a) shows a star formation realised with the discrete filter-unit. The connections between the three discrete filter-units can be mapped to three IPPM filter-units in order to realise a star formation as shown in Fig. 4.5(b).
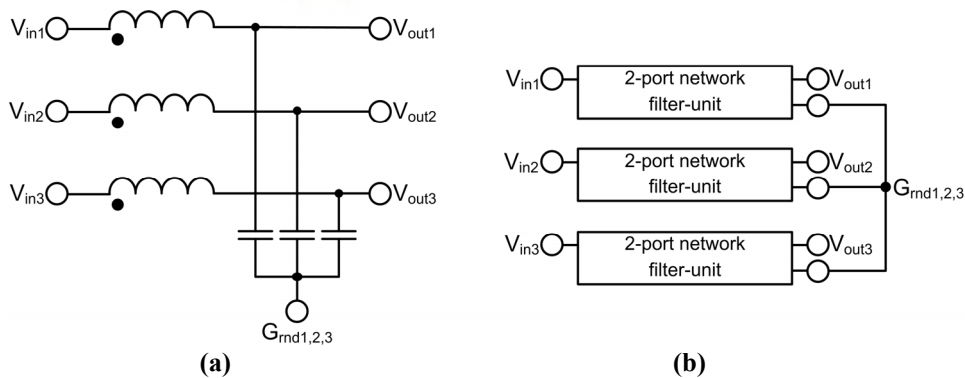
Fig. 4.5: A star formation realised with (a) the discrete filter-unit and (b) the two-port network IPPM filter-unit
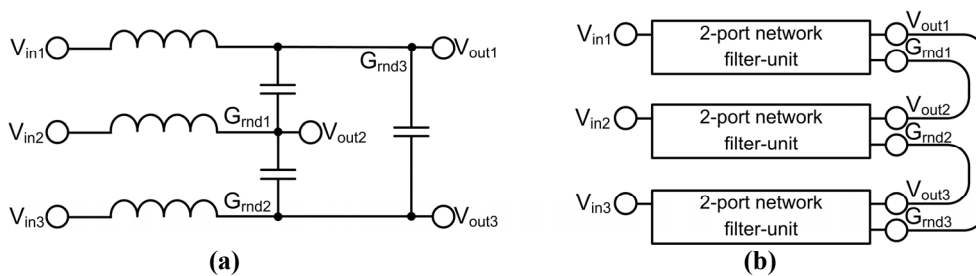
Fig. 4.6: A delta formation realised with (a) the discrete filter-unit and (b) the two-port network IPPM filter-unit

65

4.2.2 Realisation of delta formation with IPPM filter-units

As in the case of the star formation, a delta formation can be realised with three IPPM filter-units by connecting the terminals in the same fashion as for three discrete filter-units. This procedure is schematically shown in Fig. 4.6.

The single-port network filter-units cannot be connected in either star or delta formation. This is due to the fact that these filter-units do not have a ground terminal. It was also seen that the single-port network filter-units only realised first order filters, as seen by the -20dB/dec drop-off values. This implied that the dielectric utilisation realised by these filter-units was not necessarily as effective as that obtained by some of the two-port network filter-units. Taking these factors into account the single-port filter-units were considered to be an inefficient implementation of the IPPMs and were consequently excluded from further analysis.

4.3   Simulation of three-phase filters

The functionality of the three-phase filter was seen to be dependent on two main factors. Firstly, the interconnection of the three filter-units with one another, as either a star or a delta formation, aided in the realisation of either a CM or a DM filter. Secondly, the degree of magnetic coupling between the filter-units resulted in a high impedance seen by either the CM noise or the DM noise [11]. (Appendix B presents a more detailed discussion of this concept.) Bearing these aspects in mind four different three-phase filter topologies, which can be realised with any three filter-units, were considered:

- Topology 1: Star formation with magnetic coupling between filter-units.

- Topology 2: Star formation without magnetic coupling between filter-units.

- Topology 3: Delta formation with magnetic coupling between filter-units.

- Topology 4: Delta formation without magnetic coupling between filter-units.

By examining the standard discrete passive CM and DM filters discussed in Chapter 1 it can be seen that these filters are an implementation of topologies 1 and 4 respectively.

The implementation of a three-phase filter using IPPM filter-units was investigated through simulation of the four topologies.

4.3.1 Topology simulation setup

Each topology was realised in the simulation environment as is schematically shown for topology 1 in Fig. 4.7. In the figure topology 1 is explicitly shown to consist of three filter-units connected in star formation. The "dot" in the lower left hand corner of each filter-unit block represents the presence of magnetic coupling between the filter-units.

Identical filter-units were always used to realise any of the four topologies. This was to ensure that the overall three-phase filter would not introduce any imbalances into the three-phase system. Each filter-unit was modelled using the quasi-distributed

model, discussed in Chapter 2, consisting of only three cascaded cells. As mentioned in Chapter 2, the use of ten cells was more than sufficient in the single-phase simulations. Consequently, only three cells were used in the three-phase simulations without any loss in modelling accuracy over the frequency range of interest.
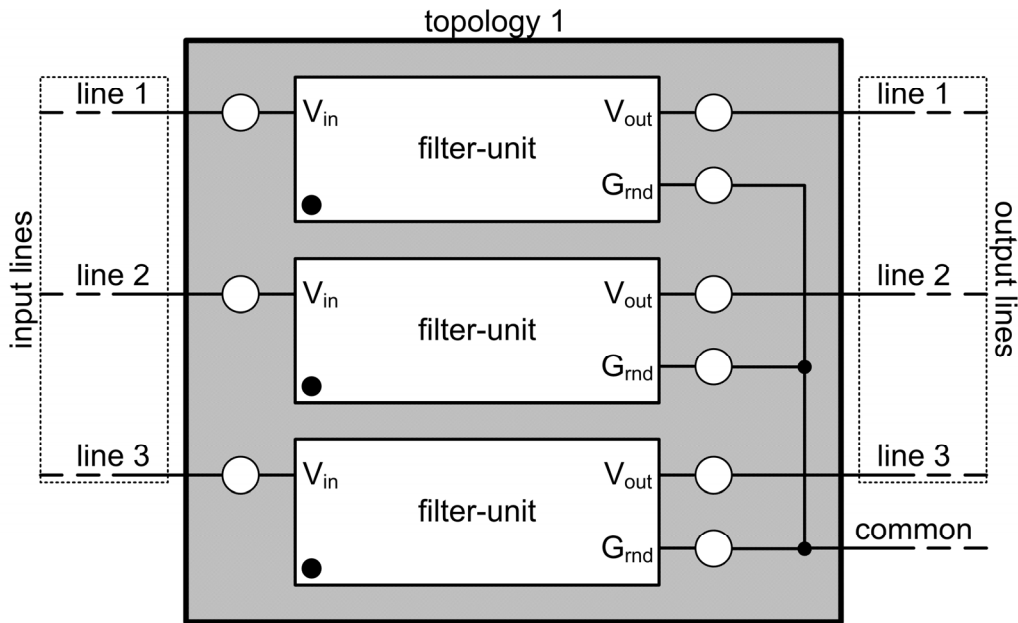
Fig. 4.7: The model used for topology 1 in the simulation environment

The coupling between the inductances found within each cell was unaffected by the choice in topology. The magnetic coupling between filter-units, as in topologies 1 and 3, was realised by introducing an additional coupling between the inductances found in coinciding cells of each filter-unit. (e.g. The inductors in the first cell of the first filter-unit were coupled together with one another and coupled to the inductors in the first cells of the remaining two filter-units.) The coupling coefficient between all three filter-units, C_{fu}, was set to unity, as in the single-phase simulations performed during the exhaustive search. In so doing a "best case scenario" for the three-phase filter behaviour obtained from topologies 1 and 3 was investigated.

As there was found to be 149 filter-units, 149 realisations of each topology were simulated. Further, the response of each topology realisation was obtained for both a CM and a DM stimulus. A sinusoidal voltage source was used to realise both stimuli. This could be justified by considering the fact that any CM or DM noise could be reduced, through Fourier analysis, to a system of sinusoids provided that the system remains linear. The simulation setup used for the two stimuli is shown schematically in Fig. 4.8.

(a)   (b)
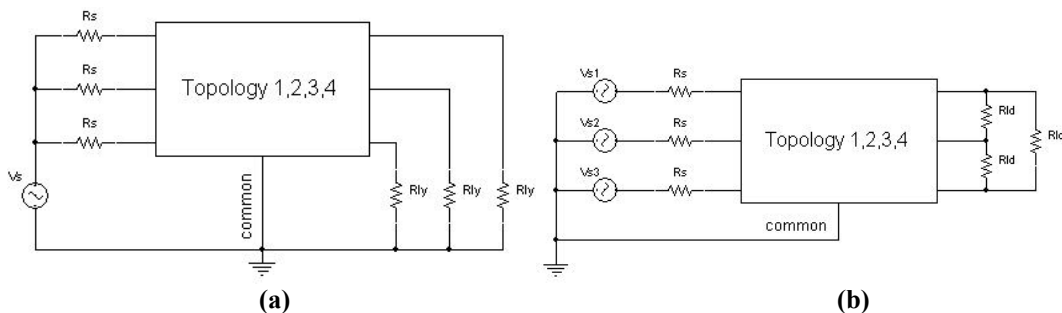
Fig. 4.8: The simulation setup used for all four topologies for (a) a CM stimulus and (b) a DM stimulus

For the CM stimulus the source voltage was common to all three lines of the topology, thereby ensuring the realisation of a CM current. The load resistors, R_{ly}, were connected in star formation to ensure that a CM path existed in the simulation. The value of the load resistors was calculated as in equation (4.3).

$$R_{ly} = \frac{R_l}{3} \qquad (4.3)$$

The variable R_l was calculated as discussed in Chapter 2, using the filter-unit model parameters.

A balanced, star connected three-phase voltage source was used for the DM stimulus to ensure the realisation of a DM current on each of the lines. Such a DM noise source implies a 120° phase shift between the DM noise signals found on the three lines, which is not necessarily the case in a practical setup. However, for purposes of simulation this method at least gave an indication as to whether or not a topology would be able to filter DM noise. The simulations utilising the CM stimulus would however, give an indication as to how the filter would respond to noise on the three lines that is not out of phase. Consequently both stimuli had to be simulated and the results to both observed for each topology. The load used for a DM stimulus was realised with resistors connected in delta formation. The value of each of these resistors was found using equation (4.4).

$$R_{ld} = 3R_{ly} = R_l \qquad (4.4)$$

The connection between the topologies and circuit ground, labelled *common*, was only present when simulating topologies 1 and 2, which were connected in star formation.

The values of the parameters used in the two simulation setups are listed in Table 4-II.

Table 4-II: The parameters and their respective values as used in the two simulation setups discussed

Parameter	Value
V_s	$1 \angle 0°$V
V_{s1}	$1 \angle 0°$V
V_{s2}	$1 \angle 120°$V
V_{s3}	$1 \angle -120°$V
R_s	50Ω
R_{ly}	33.33Ω
R_{ld}	100Ω
C_{fu}	1

4.3.2 Simulation results

From each of the topology simulations the input and output voltage responses for each filter-unit were found. It was seen that the responses obtained from all three filter-units were identical, within any filter topology realisation. This was expected due to the balanced nature of the three-phase filter simulations. Consequently, the simulation results discussed here were obtained from only one filter-unit.

It was also seen that when a DM stimulus was applied to the topology, the load configuration, either star or delta formation, had no effect on the voltage responses of the filter. However, in the case of the CM stimulus, the load had to be connected in star formation. If this was not the case there was no return path for the CM current

and as a result the voltage responses would have not been a true portrayal of the topologies behaviour in the presence of CM noise.

The output voltage responses from the simulations were analysed in the manner discussed in section 1, thereby finding the drop-off and pass-band ratio values. The results, for each topology are tabulated in Tables 4-III through 4-VI.

Table 4-III: Drop-off and pass-band values found for the three-phase filters realised with topology 1

Filter-unit	CM stimulus Drop-off (dB/dec)	PB_r	DM stimulus Drop-off (dB/dec)	PB_r	Filter-unit	CM stimulus Drop-off (dB/dec)	PB_r	DM stimulus Drop-off (dB/dec)	PB_r	Filter-unit	CM stimulus Drop-off (dB/dec)	PB_r	DM stimulus Drop-off (dB/dec)	PB_r
Group 1										Group 2				
53	-20	0.999	-20	0.999	139	-20	1.000	-20	1.000	44	-40	0.999	-20	0.999
56	-20	0.999	-20	0.999	141	-20	1.000	-20	1.000	45	-40	1.000	-20	1.000
66	-20	0.999	-20	0.999	142	-20	0.997	-20	1.000	46	-40	0.997	-20	1.000
77	-20	0.999	-20	1.000	144	-20	0.999	-20	1.000	47	-40	1.000	-20	1.000
78	-20	0.999	-20	1.000	145	-20	1.000	-20	1.000	48	-40	0.999	-20	1.000
79	-20	0.999	-20	1.000	147	-20	1.000	-20	0.999	49	-40	0.999	-20	0.999
80	-20	1.000	-20	1.000	148	-20	1.000	-20	0.999	50	-40	0.999	-20	1.000
81	-20	1.000	-20	1.000	149	-20	1.000	-20	1.000	51	-40	0.999	-20	1.000
82	-20	1.000	-20	1.000	150	-20	0.999	-20	0.999	52	-40	0.999	-20	1.000
84	-20	0.999	-20	1.000	151	-20	1.000	-20	1.000	54	-40	0.999	-20	1.000
86	-20	0.999	-20	1.000	153	-20	1.000	-20	0.999	55	-40	0.997	-20	1.000
87	-20	0.999	-20	1.000	154	-20	1.000	-20	0.999	57	-40	0.999	-20	1.000
88	-20	0.999	-20	1.000	155	-20	1.000	-20	1.000	58	-40	0.998	-20	1.000
89	-20	0.999	-20	1.000	156	-20	1.000	-20	1.000	59	-40	1.000	-20	1.000
90	-20	0.999	-20	1.000	158	-20	0.999	-20	0.999	60	-40	1.000	-20	1.000
91	-20	0.999	-20	1.000	160	-20	0.999	-20	0.999	61	-40	0.999	-20	1.000
92	-20	0.999	-20	1.000	161	-20	0.998	-20	1.000	62	-40	1.000	-20	1.000
93	-20	0.999	-20	1.000	162	-20	1.000	-20	1.000	63	-40	1.000	-20	1.000
94	-20	0.999	-20	0.999	163	-20	0.999	-20	1.000	64	-40	0.999	-20	1.000
96	-20	0.998	-20	1.000	164	-20	0.999	-20	0.999	65	-40	0.999	-20	1.000
97	-20	0.999	-20	1.000	165	-20	1.000	-20	1.000	67	-40	0.999	-20	1.000
98	-20	1.000	-20	1.000	166	-20	1.000	-20	1.000	68	-40	0.999	-20	1.000
99	-20	0.999	-20	1.000	167	-20	0.990	-20	0.999	69	-40	0.999	-20	1.000
100	-20	0.999	-20	1.000	168	-20	1.000	-20	1.000	70	-40	0.999	-20	1.000
101	-20	0.999	-20	1.000	169	-20	0.999	-20	0.999	71	-40	1.000	-20	1.000
102	-20	1.000	-20	1.000	170	-20	0.999	-20	0.999	72	-40	0.999	-20	0.999
103	-20	0.999	-20	0.999	175	-20	1.000	-20	0.999	73	-40	0.995	-20	1.000
105	-20	0.999	-20	1.000	176	-20	0.999	-20	1.000	74	-40	0.998	-20	1.000
106	-20	0.998	-20	1.000	177	-20	0.999	-20	1.000	75	-40	0.996	-20	1.000
107	-20	1.000	-20	0.999	178	-20	0.999	-20	0.999	76	-40	0.999	-20	1.000
108	-20	0.999	-20	1.000	181	-20	0.999	-20	1.000	171	-40	1.000	-20	1.000
110	-20	0.998	-20	1.000	183	-20	1.000	-20	0.999	172	-40	0.999	-20	0.999
112	-20	0.999	-20	0.999	184	-20	0.999	-20	0.999	173	-40	1.000	-20	1.000
113	-20	0.999	-20	1.000	185	-20	1.000	-20	0.999	174	-40	0.999	-20	1.000
114	-20	0.999	-20	1.000	186	-20	1.000	-20	1.000	187	-40	1.000	-20	1.000
116	-20	0.999	-20	1.000	191	-20	1.000	-20	1.000	189	-40	0.999	-20	1.000
117	-20	0.997	-20	0.999	192	-20	0.998	-20	0.999	188	-40	1.000	-20	1.000
118	-20	0.997	-20	0.999	85	-20	0.999	-20	0.999	190	-40	1.000	-20	0.999
119	-20	0.999	-20	1.000	109	-20	0.998	-20	0.999	Group 3				
121	-20	0.995	-20	1.000	157	-20	1.000	-20	1.000	95	-20	0.999	-20	0.999
123	-20	0.999	-20	1.000	83	-20	0.999	-20	0.999	104	-20	0.997	-20	0.999
124	-20	0.999	-20	1.000	111	-20	0.999	-20	1.000	115	-40	0.999	-20	1.000
127	-20	0.999	-20	1.000	159	-20	1.000	-20	1.000	120	-40	1.000	-20	1.000
128	-20	0.999	-20	0.999	126	-20	1.000	-20	1.000	125	-54	0.999	-20	1.000
129	-20	0.999	-20	1.000	130	-20	0.999	-20	1.000	122	-40	0.999	-20	1.000
131	-20	0.999	-20	1.000	143	-20	0.999	-20	0.999					
132	-20	0.999	-20	1.000	140	-20	0.999	-20	1.000					
133	-20	0.999	-20	1.000	146	-20	1.000	-20	1.000					
134	-20	0.999	-20	0.999	152	-20	1.000	-20	1.000					
135	-20	0.999	-20	0.999	180	-20	1.000	-20	1.000					
136	-20	1.000	-20	1.000	179	-20	0.999	-20	0.999					
137	-20	1.000	-20	1.000	182	-20	1.000	-20	1.000					
138	-20	1.000	-20	1.000										

Table 4-IV: Drop-off and pass-band values found for the three-phase filters realised with topology 2

Filter-unit	CM stimulus Drop-off (dB/dec)	PB_r	DM stimulus Drop-off (dB/dec)	PB_r	Filter-unit	CM stimulus Drop-off (dB/dec)	PB_r	DM stimulus Drop-off (dB/dec)	PB_r	Filter-unit	CM stimulus Drop-off (dB/dec)	PB_r	DM stimulus Drop-off (dB/dec)	PB_r
Group 1										Group 2				
53	-20	0.999	-20	0.999	139	-20	1.000	-20	1.000	44	-40	0.999	-40	1.000
56	-20	0.999	-20	0.999	141	-20	0.999	-20	0.999	45	-40	1.000	-40	1.000
66	-20	0.999	-20	0.999	142	-20	0.999	-20	0.999	46	-40	1.000	-40	1.000
77	-20	0.999	-20	0.999	144	-20	0.999	-20	0.999	47	-40	1.000	-40	1.000
78	-20	0.999	-20	0.999	145	-20	0.999	-20	0.999	48	-40	1.000	-40	1.000
79	-20	0.999	-20	0.999	147	-20	1.000	-20	1.000	49	-40	1.000	-40	1.000
80	-20	0.999	-20	0.999	148	-20	1.000	-20	1.000	50	-40	1.000	-40	1.000
81	-20	0.999	-20	0.999	149	-20	0.999	-20	0.999	51	-40	1.000	-40	1.000
82	-20	0.999	-20	0.999	150	-20	0.998	-20	0.998	52	-40	0.999	-40	1.000
84	-20	0.999	-20	0.999	151	-20	0.999	-20	0.999	54	-40	0.999	-40	1.000
86	-20	0.999	-20	0.999	153	-20	1.000	-20	1.000	55	-40	1.000	-40	1.000
87	-20	0.999	-20	0.999	154	-20	1.000	-20	1.000	57	-40	0.999	-40	1.000
88	-20	0.999	-20	0.999	155	-20	0.999	-20	0.999	58	-40	1.000	-40	1.000
89	-20	1.000	-20	1.000	156	-20	0.999	-20	0.999	59	-40	1.000	-40	1.000
90	-20	1.000	-20	1.000	158	-20	0.999	-20	0.999	60	-40	1.000	-40	1.000
91	-20	1.000	-20	1.000	160	-20	0.999	-20	0.999	61	-40	1.000	-40	1.000
92	-20	1.000	-20	1.000	161	-20	0.999	-20	0.999	62	-40	1.000	-40	1.000
93	-20	1.000	-20	1.000	162	-20	0.999	-20	0.999	63	-40	1.000	-40	1.000
94	-20	0.998	-20	0.999	163	-20	0.999	-20	0.999	64	-40	0.999	-40	1.000
96	-20	1.000	-20	1.000	164	-20	0.998	-20	0.998	65	-40	1.000	-40	1.000
97	-20	0.999	-20	1.000	165	-20	0.999	-20	0.999	67	-40	0.999	-40	1.000
98	-20	1.000	-20	1.000	166	-20	0.999	-20	0.999	68	-40	1.000	-40	1.000
99	-20	1.000	-20	0.999	167	-20	0.998	-20	0.998	69	-40	1.000	-40	1.000
100	-20	1.000	-20	1.000	168	-20	0.999	-20	0.999	70	-40	1.000	-40	1.000
101	-20	1.000	-20	1.000	169	-20	1.000	-20	1.000	71	-40	1.000	-40	1.000
102	-20	1.000	-20	1.000	170	-20	1.000	-20	1.000	72	-40	1.000	-40	1.000
103	-20	0.999	-20	0.999	175	-20	1.000	-20	1.000	73	-40	1.000	-40	1.000
105	-20	1.000	-20	1.000	176	-20	1.000	-20	1.000	74	-40	1.000	-40	0.997
106	-20	1.000	-20	1.000	177	-20	1.000	-20	1.000	75	-40	1.000	-40	0.999
107	-20	0.999	-20	0.999	178	-20	1.000	-20	1.000	76	-40	1.000	-40	1.000
108	-20	0.999	-20	0.999	181	-20	1.000	-20	1.000	171	-40	0.999	-40	1.000
110	-20	0.999	-20	0.999	183	-20	1.000	-20	1.000	172	-40	0.999	-40	1.000
112	-20	0.999	-20	0.999	184	-20	1.000	-20	1.000	173	-40	1.000	-40	1.000
113	-20	0.999	-20	0.999	185	-20	1.000	-20	1.000	174	-40	1.000	-40	1.000
114	-20	0.999	-20	0.999	186	-20	1.000	-20	1.000	187	-40	1.000	-40	1.000
116	-20	1.000	-20	1.000	191	-20	1.000	-20	1.000	189	-40	1.000	-40	1.000
117	-20	0.999	-20	0.999	192	-20	1.000	-20	1.000	188	-40	1.000	-40	1.000
118	-20	0.999	-20	0.999	85	-20	0.999	-20	0.999	190	-40	1.000	-40	1.000
119	-20	1.000	-20	1.000	109	-20	0.999	-20	0.999	Group 3				
121	-20	1.000	-20	1.000	157	-20	0.999	-20	0.999	95	-54	0.998	-54	0.999
123	-20	1.000	-20	0.999	83	-20	0.999	-20	0.999	104	-50	0.999	-51	0.999
124	-20	0.999	-20	1.000	111	-20	0.999	-20	0.999	115	-58	1.000	-58	1.000
127	-20	0.999	-20	0.999	159	-20	0.999	-20	0.999	120	-60	1.000	-58	1.000
128	-20	0.999	-20	0.999	126	-20	0.999	-20	0.999	125	-59	1.000	-59	1.000
129	-20	0.999	-20	0.999	130	-20	0.999	-20	0.999	122	-58	1.000	-58	1.000
131	-20	0.999	-20	0.999	143	-20	0.999	-20	0.999					
132	-20	0.999	-20	0.999	140	-20	0.999	-20	0.999					
133	-20	0.999	-20	0.999	146	-20	0.999	-20	0.999					
134	-20	1.000	-20	1.000	152	-20	0.999	-20	0.999					
135	-20	1.000	-20	1.000	180	-20	1.000	-20	1.000					
136	-20	1.000	-20	1.000	179	-20	1.000	-20	1.000					
137	-20	1.000	-20	1.000	182	-20	1.000	-20	1.000					
138	-20	1.000	-20	1.000										

Table 4-V: Drop-off and pass-band values found for the three-phase filters realised with topology 3

Filter-unit	CM stimulus Drop-off (dB/dec)	PB_r	DM stimulus Drop-off (dB/dec)	PB_r	Filter-unit	CM stimulus Drop-off (dB/dec)	PB_r	DM stimulus Drop-off (dB/dec)	PB_r	Filter-unit	CM stimulus Drop-off (dB/dec)	PB_r	DM stimulus Drop-off (dB/dec)	PB_r
Group 1										Group 2				
53	-	-	-20	0.998	139	-	-	-20	0.999	44	-	-	-20	0.999
56	-	-	-20	0.999	141	-	-	-20	0.999	45	-	-	-20	0.999
66	-	-	-20	0.999	142	-	-	-20	1.000	46	-20	0.998	-20	1.000
77	-	-	-20	0.999	144	-	-	-20	1.000	47	-20	0.998	-20	1.000
78	-	-	-20	0.999	145	-	-	-20	1.000	48	-	-	-20	1.000
79	-	-	-20	1.000	147	-	-	-20	0.999	49	-20	1.000	-20	0.999
80	-	-	-20	0.999	148	-	-	-20	0.999	50	-	-	-20	1.000
81	-	-	-20	0.999	149	-	-	-20	0.999	51	-	-	-20	0.999
82	-	-	-20	0.999	150	-	-	-20	0.999	52	-20	0.997	-20	0.999
84	-	-	-20	0.999	151	-	-	-20	1.000	54	-	-	-20	1.000
86	-	-	-20	0.999	153	-	-	-20	0.999	55	-20	1.000	-20	1.000
87	-	-	-20	0.997	154	-	-	-20	0.999	57	-	-	-20	0.999
88	-	-	-20	0.999	155	-	-	-20	1.000	58	-20	0.999	-20	1.000
89	-	-	-20	1.000	156	-	-	-20	1.000	59	-20	0.997	-20	1.000
90	-	-	-20	0.999	158	-	-	-20	0.999	60	-20	0.999	-20	1.000
91	-	-	-20	1.000	160	-	-	-20	0.999	61	-	-	-20	0.999
92	-	-	-20	0.999	161	-	-	-20	1.000	62	-20	1.000	-20	0.999
93	-	-	-20	1.000	162	-	-	-20	1.000	63	-	-	-20	1.000
94	-	-	-20	0.999	163	-	-	-20	1.000	64	-20	0.999	-20	0.999
96	-	-	-20	1.000	164	-	-	-20	0.999	65	-	-	-20	1.000
97	-	-	-20	1.000	165	-	-	-20	1.000	67	-	-	-20	1.000
98	-	-	-20	1.000	166	-	-	-20	1.000	68	-20	0.998	-20	1.000
99	-	-	-20	1.000	167	-	-	-20	0.999	69	-	-	-20	0.999
100	-	-	-20	1.000	168	-	-	-20	1.000	70	-20	0.999	-20	0.999
101	-	-	-20	0.999	169	-	-	-20	0.999	71	-20	0.999	-20	1.000
102	-	-	-20	1.000	170	-	-	-20	0.999	72	-	-	-20	1.000
103	-	-	-20	0.999	175	-	-	-20	1.000	73	-20	0.998	-20	0.999
105	-	-	-20	1.000	176	-	-	-20	1.000	74	-	-	-20	1.000
106	-	-	-20	0.999	177	-	-	-20	1.000	75	-20	0.996	-20	0.999
107	-	-	-20	1.000	178	-	-	-20	0.999	76	-	-	-20	0.996
108	-	-	-20	1.000	181	-	-	-20	1.000	171	-	-	-20	1.000
110	-	-	-20	0.999	183	-	-	-20	0.999	172	-20	1.000	-20	1.000
112	-	-	-20	1.000	184	-	-	-20	0.999	173	-	-	-20	1.000
113	-	-	-20	1.000	185	-	-	-20	0.999	174	-20	1.000	-20	1.000
114	-	-	-20	0.999	186	-	-	-20	1.000	187	-	-	-20	1.000
116	-	-	-20	1.000	191	-	-	-20	1.000	189	-	-	-20	1.000
117	-	-	-20	0.999	192	-	-	-20	0.999	188	-20	0.999	-20	1.000
118	-	-	-20	0.999	85	-	-	-20	0.999	190	-20	1.000	-20	1.000
119	-	-	-20	1.000	109	-	-	-20	1.000	Group 3				
121	-	-	-20	0.999	157	-	-	-20	0.999	95	-	-	-20	0.999
123	-	-	-20	1.000	83	-	-	-20	0.998	104	-	-	-20	0.999
124	-	-	-20	1.000	111	-	-	-20	1.000	115	-	-	-20	1.000
127	-	-	-20	0.999	159	-	-	-20	0.999	120	-	-	-20	1.000
128	-	-	-20	0.999	126	-	-	-20	0.999	125	-	-	-20	0.999
129	-	-	-20	0.999	130	-	-	-20	0.999	122	-	-	-20	1.000
131	-	-	-20	0.999	143	-	-	-20	0.998					
132	-	-	-20	0.999	140	-	-	-20	1.000					
133	-	-	-20	0.999	146	-	-	-20	1.000					
134	-	-	-20	0.999	152	-	-	-20	1.000					
135	-	-	-20	0.999	180	-	-	-20	1.000					
136	-	-	-20	1.000	179	-	-	-20	0.999					
137	-	-	-20	1.000	182	-	-	-20	1.000					
138	-	-	-20	1.000										

Table 4-VI: Drop-off and pass-band values found for the three-phase filters realised with topology 4

Filter-unit	CM stimulus Drop-off (dB/dec)	PB_r	DM stimulus Drop-off (dB/dec)	PB_r	Filter-unit	CM stimulus Drop-off (dB/dec)	PB_r	DM stimulus Drop-off (dB/dec)	PB_r	Filter-unit	CM stimulus Drop-off (dB/dec)	PB_r	DM stimulus Drop-off (dB/dec)	PB_r
Group 1										Group 2				
53	-	-	-20	0.999	139	-	-	-20	1.000	44	-	-	-	-
56	-	-	-20	0.999	141	-	-	-20	0.999	45	-	-	-	-
66	-	-	-20	0.999	142	-	-	-20	0.999	46	-20	1.000	-40	1.000
77	-	-	-20	0.999	144	-	-	-20	0.999	47	-20	0.999	-40	1.000
78	-	-	-20	0.999	145	-	-	-20	0.999	48	-	-	-	-
79	-	-	-20	0.999	147	-	-	-20	1.000	49	-20	0.997	-40	1.000
80	-	-	-20	0.999	148	-	-	-20	1.000	50	-	-	-	-
81	-	-	-20	0.999	149	-	-	-20	0.999	51	-	-	-	-
82	-	-	-20	0.999	150	-	-	-20	0.998	52	-20	0.996	-40	1.000
84	-	-	-20	0.999	151	-	-	-20	0.999	54	-	-	-	-
86	-	-	-20	0.999	153	-	-	-20	1.000	55	-20	0.999	-40	1.000
87	-	-	-20	0.999	154	-	-	-20	1.000	57	-	-	-	-
88	-	-	-20	0.999	155	-	-	-20	0.999	58	-20	0.999	-40	1.000
89	-	-	-20	1.000	156	-	-	-20	0.999	59	-20	0.998	-40	1.000
90	-	-	-20	1.000	158	-	-	-20	0.999	60	-20	1.000	-40	1.000
91	-	-	-20	1.000	160	-	-	-20	0.999	61	-	-	-	-
92	-	-	-20	1.000	161	-	-	-20	0.999	62	-20	1.000	-40	1.000
93	-	-	-20	0.999	162	-	-	-20	0.999	63	-	-	-	-
94	-	-	-20	0.999	163	-	-	-20	0.999	64	-20	0.998	-40	1.000
96	-	-	-20	1.000	164	-	-	-20	0.998	65	-	-	-	-
97	-	-	-20	0.999	165	-	-	-20	0.999	67	-	-	-	-
98	-	-	-20	1.000	166	-	-	-20	0.999	68	-20	0.996	-40	1.000
99	-	-	-20	1.000	167	-	-	-20	0.998	69	-	-	-	-
100	-	-	-20	1.000	168	-	-	-20	0.999	70	-20	0.998	-40	1.000
101	-	-	-20	1.000	169	-	-	-20	1.000	71	-20	0.999	-40	1.000
102	-	-	-20	1.000	170	-	-	-20	1.000	72	-	-	-	-
103	-	-	-20	0.999	175	-	-	-20	1.000	73	-20	0.999	-40	1.000
105	-	-	-20	1.000	176	-	-	-20	1.000	74	-	-	-	-
106	-	-	-20	1.000	177	-	-	-20	1.000	75	-20	0.999	-40	1.000
107	-	-	-20	0.999	178	-	-	-20	1.000	76	-	-	-	-
108	-	-	-20	0.999	181	-	-	-20	1.000	171	-	-	-	-
110	-	-	-20	0.999	183	-	-	-20	1.000	172	-20	1.000	-40	1.000
112	-	-	-20	0.999	184	-	-	-20	1.000	173	-	-	-	-
113	-	-	-20	0.999	185	-	-	-20	1.000	174	-20	1.000	-40	1.000
114	-	-	-20	0.999	186	-	-	-20	1.000	187	-	-	-	-
116	-	-	-20	1.000	191	-	-	-20	1.000	189	-	-	-	-
117	-	-	-20	0.999	192	-	-	-20	1.000	188	-20	0.999	-40	1.000
118	-	-	-20	0.999	85	-	-	-20	0.999	190	-20	0.999	-40	1.000
119	-	-	-20	1.000	109	-	-	-20	0.999	Group 3				
121	-	-	-20	1.000	157	-	-	-20	0.999	95	-	-	-20	0.999
123	-	-	-20	1.000	83	-	-	-20	0.999	104	-	-	-20	0.999
124	-	-	-20	1.000	111	-	-	-20	0.999	115	-	-	-20	1.000
127	-	-	-20	0.999	159	-	-	-20	0.999	120	-	-	-20	1.000
128	-	-	-20	0.999	126	-	-	-20	0.999	125	-	-	-20	1.000
129	-	-	-20	0.999	130	-	-	-20	0.999	122	-	-	-20	1.000
131	-	-	-20	0.999	143	-	-	-20	0.999					
132	-	-	-20	0.999	140	-	-	-20	0.999					
133	-	-	-20	0.999	146	-	-	-20	0.999					
134	-	-	-20	1.000	152	-	-	-20	0.999					
135	-	-	-20	1.000	180	-	-	-20	1.000					
136	-	-	-20	1.000	179	-	-	-20	1.000					
137	-	-	-20	1.000	182	-	-	-20	1.000					
138	-	-	-20	1.000										

As previously discussed in section 4.1 the two-port network configurations were divided into three groups. By sorting the three-phase results into the same three groups it was observed that, even in the three-phase application, the filter-units within each group were seen to yield similar results. This was found to be true for

all four topologies which led to further analysis of both the topologies and the filter-unit groups.

From inspection of the simulation results it was seen that not all of the filter-units realised a three-phase LPF for either one or both of the stimuli. This is indicated by the absence of data for a filter-unit in the tables, as is seen to be the case for topologies 3 and 4.

The PB_r in all four topologies was seen to be approximately 1 for all the filter-units where a functional three-phase LPF was realised. Further investigation showed that the relation $V_{out} \approx 0.4V_s$ held in the pass-band for all of the topologies.

Simulation results of topology 1

Group 1
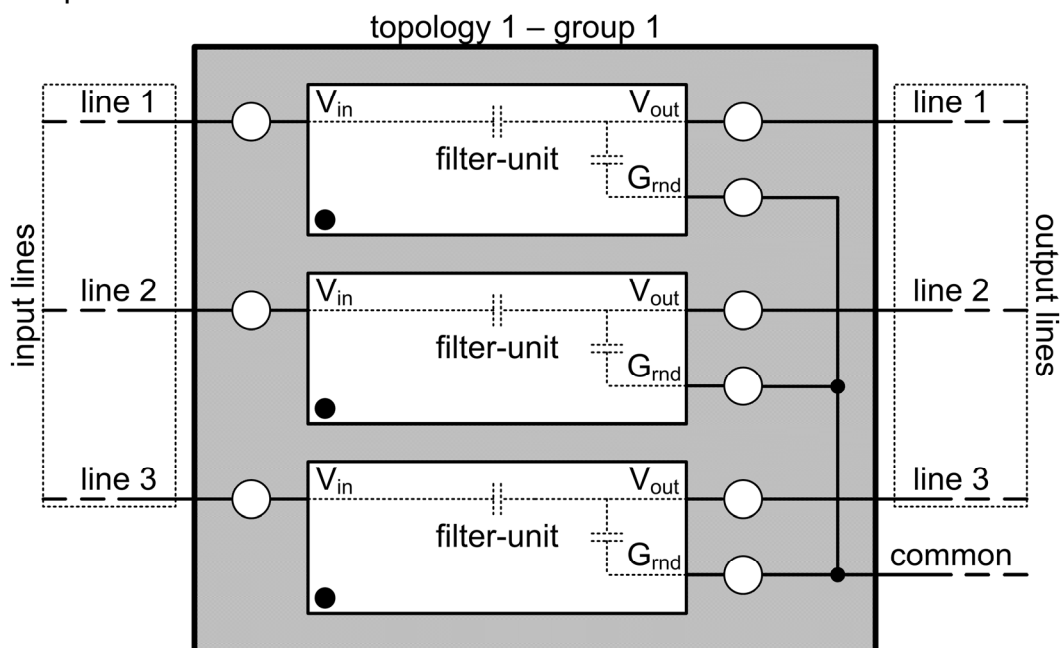
Fig. 4.9: A schematic representation of topology 1 as realised with the filter-units of group 1

By inspection of Table 4-III it was seen that all of the filter-units in group 1 realised three-phase LPFs, with a drop-off of -20dB/dec, for both the CM and DM stimuli. This can be explained by considering the filter-units and their interconnections as is shown in Fig. 4.9. In section 4.1 it was seen that all of the filter-units within group 1 were characterised by a HF signal path between all three I/O connections. In the figure the HF path is represented by the dashed capacitance. Due to the combination of these HF paths in the filter-units and the star formation, realised with the filter-units, the potential of the HF noise on both the input and output lines, of the topology, were pulled to the same potential as that of the common line. In the simulation the common line was connected to circuit ground, which resulted in an attenuation of the HF noise. The attenuation so realised was found to occur regardless of the type of noise stimulus. Consequently, a -20dB/dec drop-off was found for both stimuli used in the simulation. As this corresponds with the drop-off value obtained for the single-phase application of the filter-units, as shown in Table 4-I, the filter-units in this topology were considered to be performing at their best.

Fig. 4.10 shows the typical input and output voltage responses obtained for a filter-unit in group 1 due to both stimuli. From Fig. 4.10(a) it can be seen that the filter response due to the CM stimulus is not that of an ideal LPF. The voltage spike in the output voltage is probably due to a resonance attributed to the coupling between the filter-units. This conclusion was drawn because in the analysis of topologies 2 and 4, where there is no such coupling, it was seen that such a voltage spike did not typically occur in the presence of a CM stimulus.
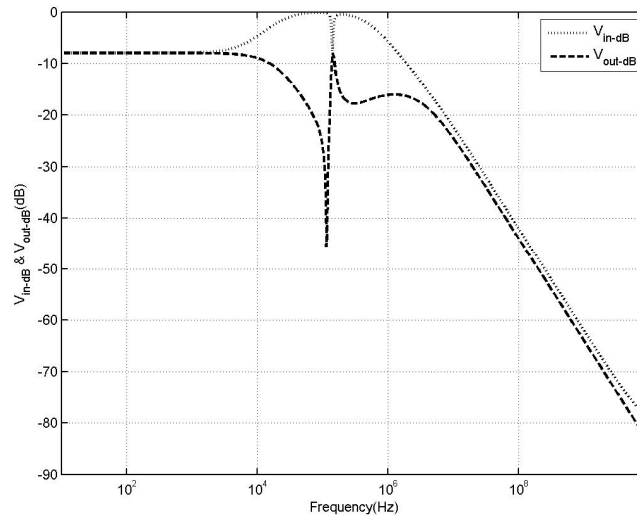
(a)
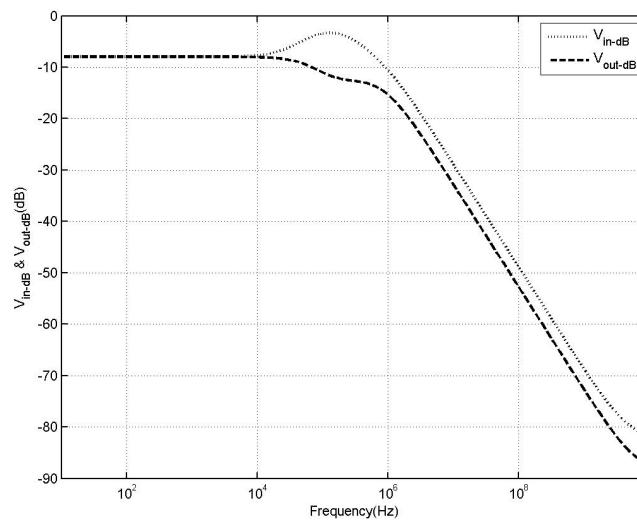
(b)

Fig. 4.10: The typical input and output voltage responses found for a filter-unit of group 1 due to (a) a CM and (b) a DM stimulus

Group 2

As in the case of group 1, all of the filter-units realised LPFs for both stimuli. The value of the drop-off however, was found to be -40dB/dec and -20dB/dec for the CM and DM stimuli respectively. Comparing these results to those shown in Table 4-I it was seen that the peak performance was obtained from the filter-units in the presence of CM noise but not for DM noise. This is probably due to the fact that the DM stimulus is not affected by the CM inductance. Consequently, only the capaci-

tive portion of the filter-units serves as a filter for the DM noise, resulting in the realisation of only a first order filter.

As mentioned in section 4.1 the filter-units in this group where characterised by different interconnections between the I/O connections. The filter-units could then be divided into two subgroups according to these attributes. In the first subgroup a HF path was present between V_{in} and G_{rnd} while in the second subgroup the HF path was found to be between V_{out} and G_{rnd}. Fig. 4.11 shows a schematic representation of the realisation of topology 1 using the filter-units from either subgroup.

(a)

(b)

Fig. 4.11: A schematic representation of topology 1 as realised with the filter-units of group 2 which were divided into (a) subgroup 1 and (b) subgroup 2

75

From these figures it can be seen that for the filter-units of subgroup 1 a HF path exists between the input lines and the common line. For subgroup 2 such a path is seen to exist between the output lines and the common line. Once again, the common line was connected to circuit ground in the simulation resulting in an attenuation of the HF noise on the output lines in both cases.

The typical input and output voltage responses for all of the filter-units of group 2 were seen to be similar to the responses found for group 1. The presence of a spike in the output voltage response was once again attributed to resonance.

Group 3

Initially some of the filter-units found in group 3 appeared to have a drop-off value greater than -20dB/dec in the presence of a CM stimulus. However, as in the single-phase application of these filter-units, the output voltage was seen to approach a steady state value at the higher frequencies. This steady state value was seen to be closer to the value of attenuation achieved with the filter-units of group 1, than with those of group 3. Fig. 4.12 shows a plot of the output voltage responses, for the CM stimulus, of the filters realised with filter-units 53, 44 and 125 of groups 1, 2 and 3 respectively. Consequently, the performance of the filter-units found in group 3 was considered to be similar to the performance of the filter-units of group 1.
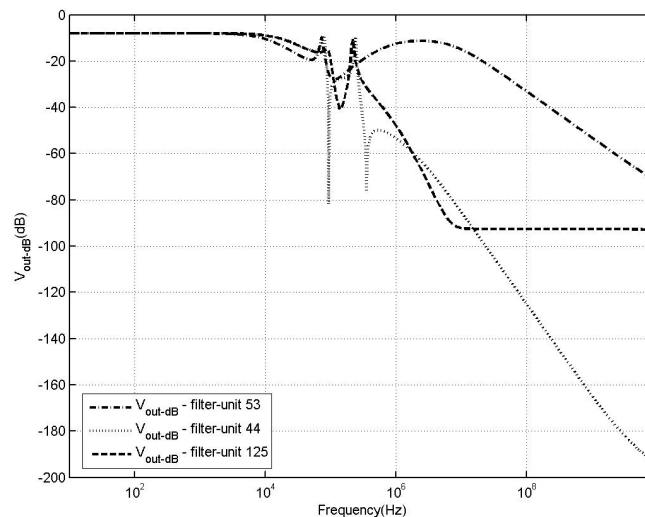
Fig. 4.12: Plots of $V_{out\text{-}dB}$ for the filters realised using topology 1 and filter-units 53, 44 and 125 in the presence of a CM stimulus

For a DM stimulus all the filter-units of group 3 had a drop-off of -20dB/dec as in the case of the filter-units of group 1. The similarity seen in the performance of the filter-units in groups 1 and 3 was considered to be due to the fact that, as in the case of group 1, the filter-units of group 3 had a HF path present between all three I/O connections of the filter-units.

Simulation results of topology 2

Group 1

In Table 4-IV it was seen that once again all of the filter-units in group 1 realised three-phase LPFs for both the CM and DM stimuli. This was explained using the same approach as was used for topology 1. As discussed previously the combination

of the HF paths in the filter-units and the star formation of the filter-units, resulted in attenuation of the HF noise. A -20dB/dec drop-off was found regardless of the type of stimulus used in the simulation. As before, this correspondence with the single-phase application was considered to indicate that the peak performance obtainable from the filter-units was being realised. This was seen to be the case for all three groups considered in this topology.
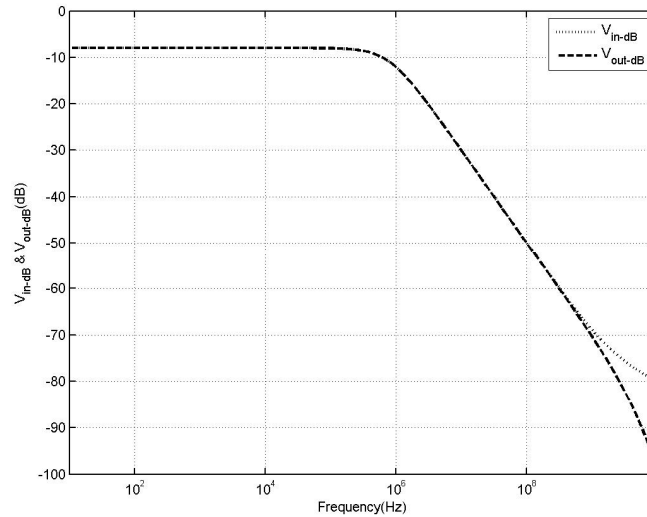
Fig. 4.13: The typical input and output voltage responses found for a filter-unit of group 1 due to both CM and DM stimuli

Fig. 4.13 shows the typical input and output voltage responses of the filter-units due to the CM stimulus. The response due to the DM stimulus is not shown as it was found to be identical to the CM stimulus response. This is due to the fact that the filter-units did not interact with one another in any way due to the absence of both a delta formation and magnetic coupling between the filter-units. Unlike in the case of topology 1, no voltage spike was seen to be present for either stimulus. As already mentioned, no coupling was present between the filter-units in topology 2. Consequently the resonance that caused the voltage spike in topology 1 played no role.

Group 2
All of the filter-units realised LPFs with a drop-off value of -40dB/dec for both stimuli, which corresponded with the drop-off value obtained in the single-phase case, for the respective filter-units.

Once again these filter-units were divided into two subgroups. The attenuation of the HF noise was attributed to the HF paths in, and the star formation realised with, the filter-units. In contrast with the results found for topology 1, the attenuation of the DM noise was seen to be -40dB/dec. This was attributed to the fact that there was no coupling between the filter-units. Consequently the inductance of the filter-units played a role in the filtering of this noise, as well as the capacitance.

The typical input and output voltage responses for both stimuli were similar to those of the filter-units of group 1. As in the previous group there was no voltage spike present and the responses due to either stimulus were identical.

Group 3

At first glance the filer units of subgroup 3 have high drop-off values. Once again this was shown to be misleading by considering Fig. 4.14. This figure shows a plot of the output voltage responses due to a CM stimulus, for the filters realised with filter-units 53 and 95. The response due to the DM stimulus was yet again found to be the same. From this it can be seen that the filter-units of group 3 behave comparably with the filter-units of group 1. This can once again be attributed to the fact that the filter-units of group 1 and 3 all have HF paths between all three of their I/O connections.
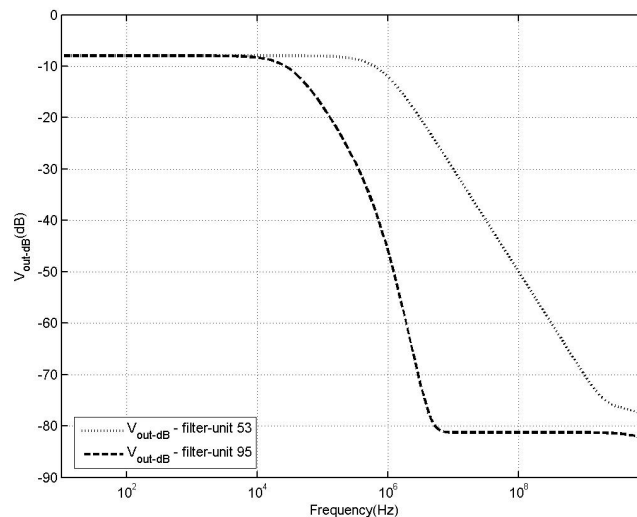
Fig. 4.14: Plots of $V_{out\text{-}dB}$ for the filters realised using topology 2 and filter-units 53 and 95 in the presence of a CM stimulus

Simulation results of topology 3

Group 1

Referring to Table 4-V it was seen that the filter-units only behaved as LPFs in the presence of the DM stimulus, with a drop-off of -20dB/dec. This can be explained with the aid of Fig. 4.15. From the figure it can be seen that the HF path, in conjunction with the delta formation of the filter-units, results in the propagation of HF signals between all three lines.

In the case of the CM stimulus the CM noise on input line 1, for instance, propagates through the filter-units to all three output lines. The same thing occurs to the CM noise found on input lines 2 and 3. The total noise seen on any one of the output lines is consequently of the same order of magnitude as the noise on the input line. As a result the filter-units were not seen to realise low pass three-phase filters for a CM stimulus.

The HF noise propagates between the lines in a similar fashion when the DM stimulus is applied to the topology. This noise, however, was cancelled out due to the fact that the DM noise on each of the input lines was modelled as three sinusoids that were 120° out of phase with one another. In a practical system this would most likely not be the case. The filter-units discussed here would consequently only realise a LPF for three-phase noise whose constituent parts were 120° out of phase. However, as previously discussed by comparing the results with those of Table 4-I,

it is seen that the peak performance of the filter-units is being obtained for a DM stimulus.

The typical input and output voltage responses of the filter-units to a DM stimulus are shown in Fig. 4.16.
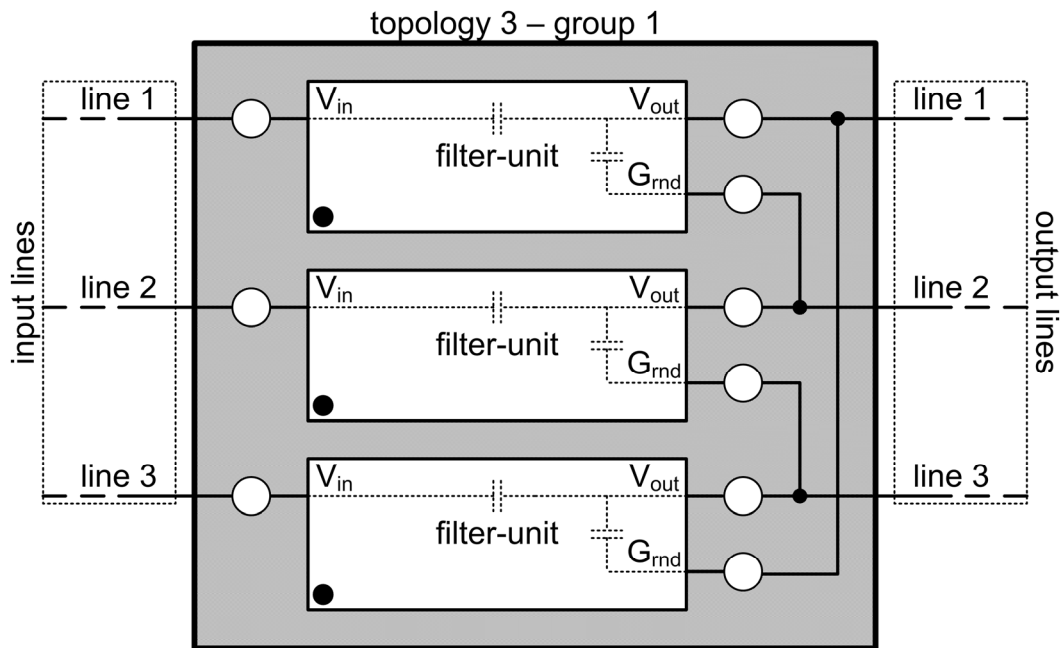
Fig. 4.15: A schematic representation of topology 3 as realised with the filter-units of group 1
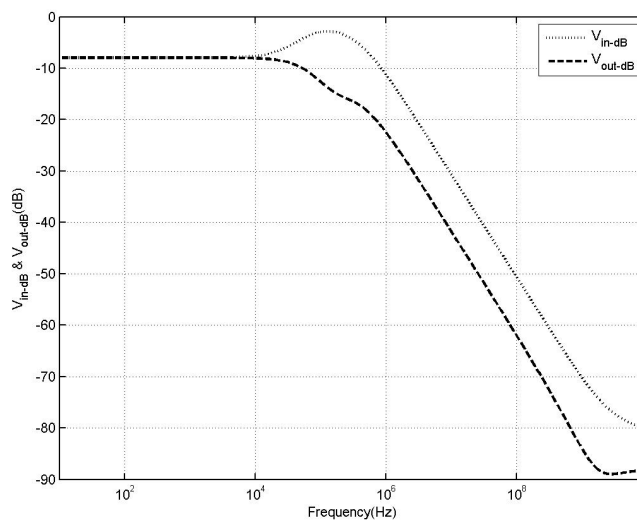
Fig. 4.16: The typical input and output voltage responses found for a filter-unit of group 1 due to a DM stimulus

Group 2

Further inspection of Table 4-V shows that some of the filter-units in group 2 did not behave as LPFs for either the CM or DM stimulus. This can be explained by considering the two subgroups that these filter-units could be subdivided into, as shown in Fig. 4.17. It was discovered that the filter-units that did not realise LPFs all belonged to subgroup 1 while the remaining filter-units belonged to subgroup 2.

Taking this fact into account it was seen that in the case of subgroup 1 the HF noise propagated from one line to another through the HF path of the filter-unit and by using the delta formation of the topology. As a result a LPF was not realised because the HF noise on the input lines was merely swapped to one of the output lines.
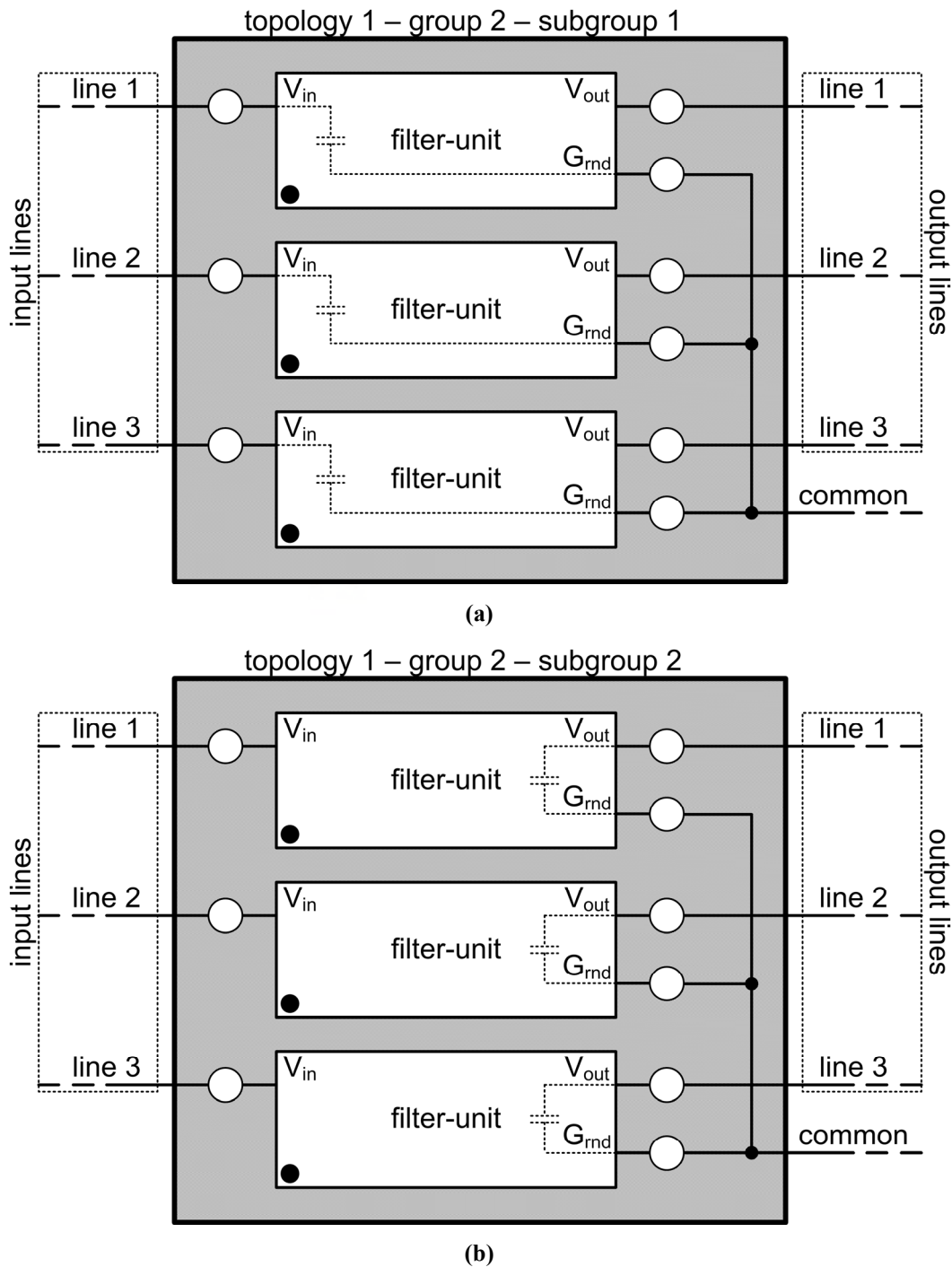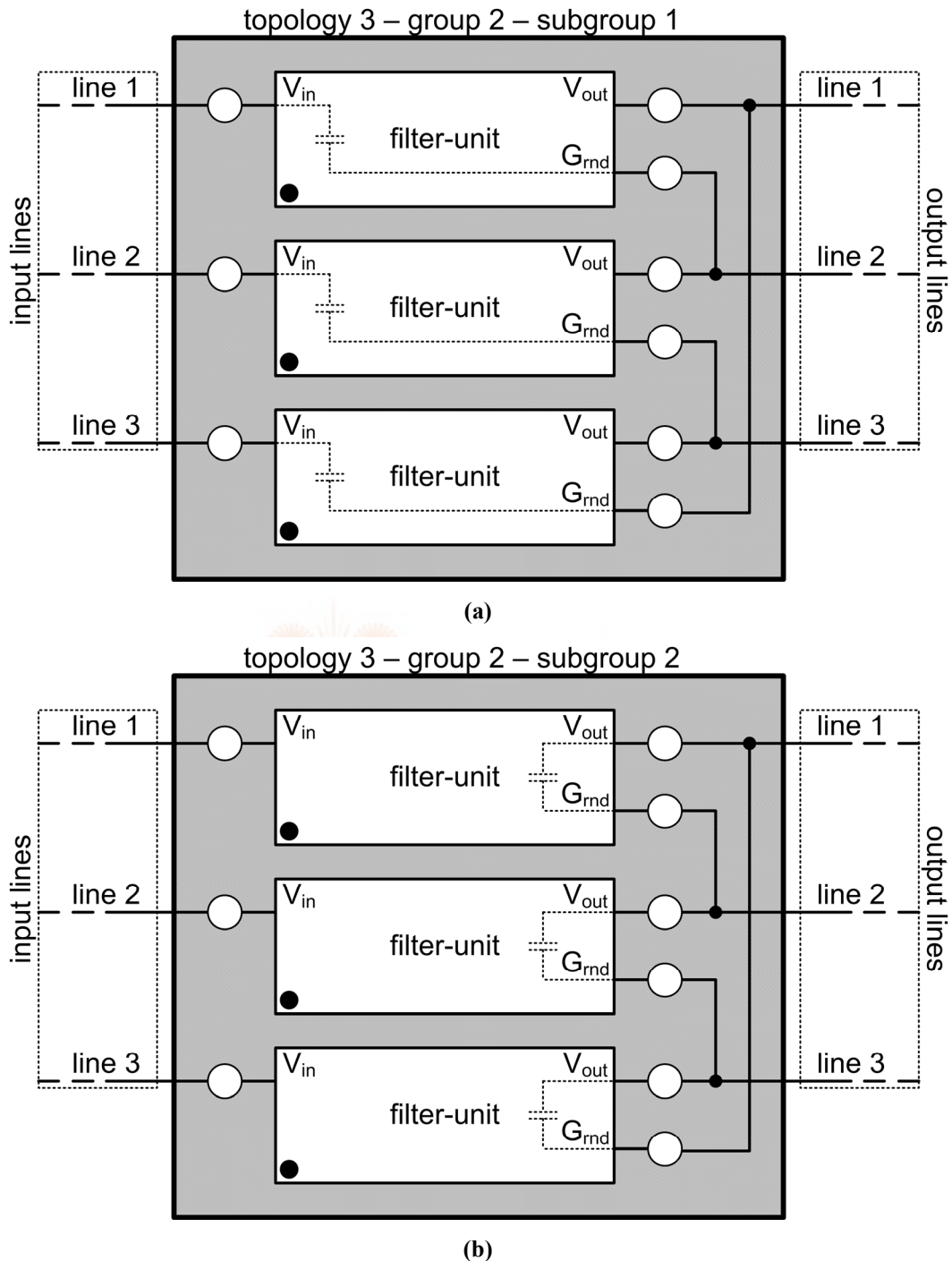

Fig. 4.17: A schematic representation of topology 3 as realised with the filter-units of group 2 which were divided into (a) subgroup 1 and (b) subgroup 2

In the case of subgroup 2 no such HF noise propagation was seen to occur between the lines, consequently the filter-units realised a three-phase LPF. Even though in a practical system the HF noise will not be perfectly out of phase, as in the simulation of the DM stimulus, the filters of subgroup 2 should realise a LPF. This can be said

due to the fact that the CM stimulus found on the three lines, which is in phase with one another, was also attenuated at the HFs.

The attenuation of the noise due to both stimuli, for the filter-units of subgroup 2, was only seen to be -20dB/dec. Comparison with the attenuation achieved in the single-phase case indicates that -20dB/dec was less than the optimal performance achievable with these filter-units. This was attributed to the fact that the capacitance realised by the delta formation of the filter-units allowed CM noise to propagate between the lines. As a result, only the inductance of the filter-units influenced the CM noise. For the DM stimulus, only the capacitive component of the filter-unit played a role in the filtering of the noise, as the DM noise was not influenced by a CM inductance.
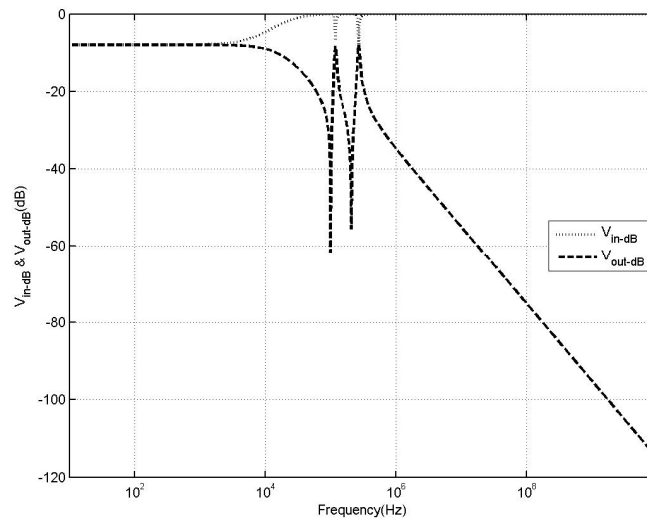
(a)
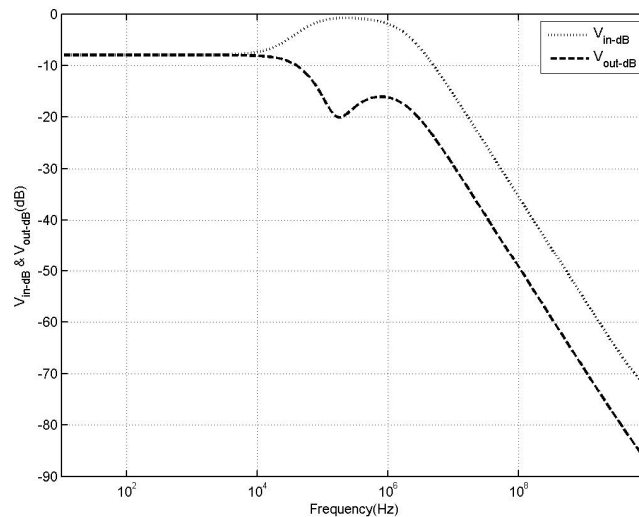
(b)

Fig. 4.18: The typical input and output voltage responses found for a filter-unit of group 2 due to (a) a CM and (b) a DM stimulus

Fig. 4.18 shows the typical input and output voltage responses due to both stimuli. As in the case of topology 1, the coupling between the filter-units was seen to intro-

duce a resonance that caused a voltage spike to occur in the output response due to a CM stimulus.

Group 3

The filter-units of group 3 were seen to behave similarly to those of group 1 in terms of drop-off value, and input and output voltage responses to both stimuli. This was due to the same reasons as discussed for topologies 1 and 2.

Simulation results of topology 4

Group 1

From Table 4-VI it was seen that none of the filter-units within group 1 realised a LPF when a CM stimulus was applied. In contrast, all of the filter-units were seen to yield a LPF with a drop-off of -20dB/dec for the DM stimulus, which corresponded with the peak performance obtainable from the filter-units. This was found to be due to the same reasons as discussed for group 1 of topology 3.
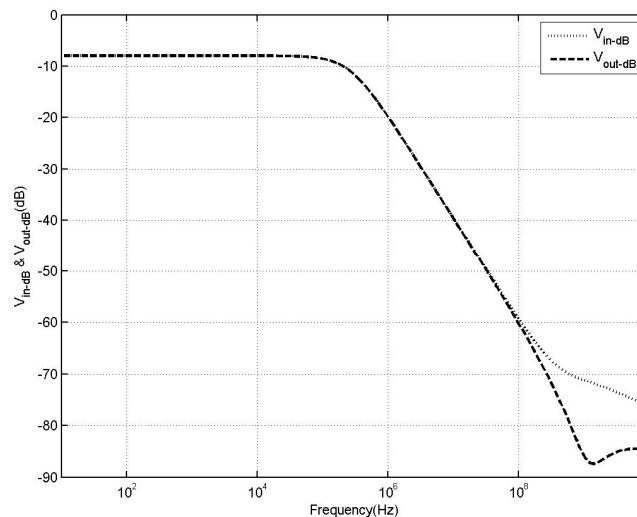
Fig. 4.19: The typical input and output voltage responses found for a filter-unit of group 1 due to a DM stimulus

Fig. 4.19 shows the typical input and output voltage response obtained for the filter-units due to a DM stimulus.

Group 2

As in topology 3, the filter-units in subgroup 1 did not realise LPFs while those of subgroup 2 did. This was again due to the presence of the HF path between the I/O connections of the filter-units within each subgroup.

For the filter-units of subgroup 2, the attenuation of the noise was however seen to be better in the case of a DM stimulus, with a drop-off of -40dB/dec, as compared to a drop-off of only -20dB/dec for the CM stimulus. This was attributed to the fact that both the inductive and capacitive components of the filter-units played a role in the filtering of the DM stimulus. Consequently, the peak performance of the filter-units was obtained for these cases. As discussed previously, only the inductive

component of the filter-unit influenced the filtering of the CM stimulus due to the presence of the delta formation between filter-units.

The typical voltage responses due to both stimuli are shown in Fig. 4.20. The voltage spike is seen to be absent, which corresponds with the fact that the filter-units of topology 4 are not coupled with one another. The noise seen in the higher frequencies of Fig. 4.20(b) is ascribed to numerical error from the simulation data.
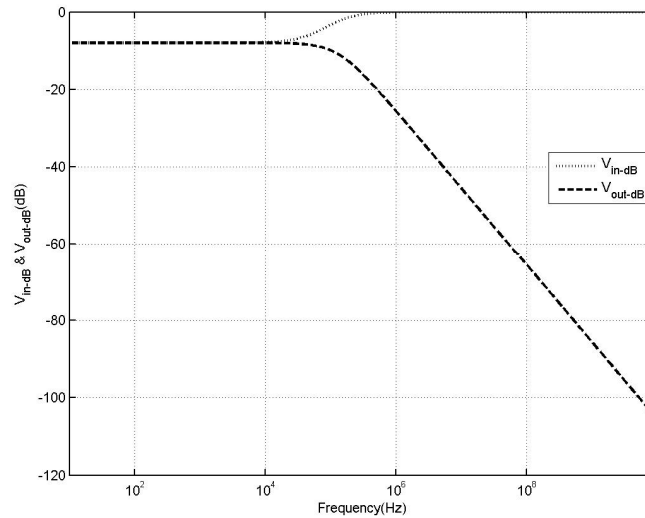
(a)
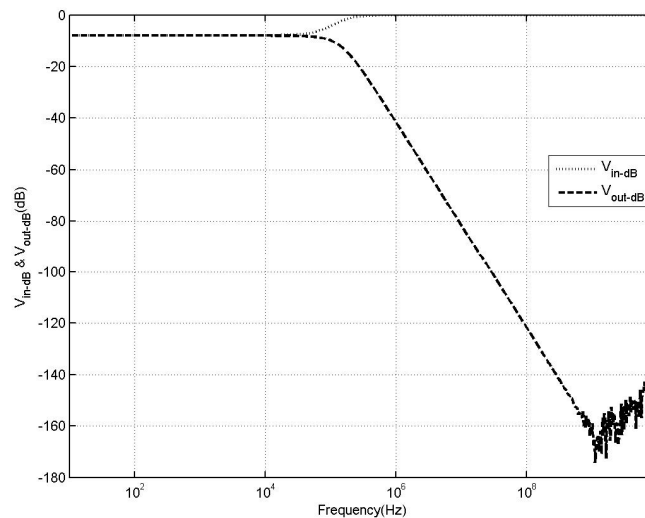
(b)

Fig. 4.20: The typical input and output voltage responses found for a filter-unit of group 2 due to (a) a CM and (b) a DM stimulus

Group 3

The filters of group 3 were seen to show the same results as those found for group 1. The reasons for the identical behaviour can be explained by the fact that, as in the case of the filter-units of group 1, the filter-units of group 3 all had a HF path present between V_{in}, V_{out} and G_{rnd}.

Comparison between the results of each topology

From the results discussed in the preceding sections it was seen that the realisation of a three-phase filter was dependent on the HF paths between the I/O connections of the filter-units, as well as whether or not the filter-units were connected in star or delta formation.

The presence or absence of magnetic coupling between the filter-units influenced two factors. Firstly, the performance of the filter-unit, in terms of the drop-off value, was seen to be at a peak when the value was the same as that found for the single-phase application of the filter-units. The magnetic coupling influenced this factor as the CM inductance of coupled filter-units was "not seen" by the DM noise. Secondly, the output responses were seen to have a voltage spike caused due to a resonance that was introduced when the filter-units were coupled together.

In topologies 1 and 2 the filter-units of group 2 were seen to yield the best results in terms of drop-off value for both the CM and DM stimuli. Further, the filter-units of group 2, subgroup 2, produced the best results for topologies 3 and 4. These filter-units were the only filter-units that realised LPFs for both stimuli in these two topologies. Table 4-VII summarises the drop-off values found for these filter-units, for each topology. From this table it can be seen that topologies 1 and 2 have comparable performance for CM noise, while topologies 2 and 4 behave comparably for DM noise. Topology 2, however, is seen to have the best overall response for both CM and DM noise. Nonetheless it was decided to experimentally construct all four topologies. In so doing various construction methods of the IPPMs could be investigated as well as the accuracy of the simulation predictions could be explored.

Table 4-VII: The drop-off values obtained for the specified filter-units for each topology

Topology	Filter-unit group	CM stimulus Drop-off(dB/dec)	DM stimulus Drop-off(dB/dec)
1	2	-40	-20
2	2	-40	-40
3	2, subgroup 2	-20	-20
4	2, subgroup 2	-20	-40

4.4   Analysis of group 2 filter-units

As the objective was still to realise a practical implementation of an integrated EMI filter using a three-layer IPPM, the filter-units that were to be used for this purpose had to be isolated. To this end, the performance of the filter-units found in group 2, for all the topologies, was seen to be superior to that of the other groups. Consequently, only these filter-units were considered as candidates for the EMI filter.

As a means to this end, the filter-units were further investigated in terms of their cut-off frequencies, ω_c. The cut-off frequencies shown in Table 4-VIII were obtained from the simulation of the single-phase application of these filter-units. The single-phase results were investigated instead of the three-phase results for two reasons. Firstly, the cut-off frequency was defined as the value of frequency where $V_{out\text{-}dB}$ had a value of -3dB below the pass-band value. In topologies 1 and 3 the typical output voltage response had noise introduced due to resonance. As a result, the cut-off frequency of these topologies would not be as well defined as in the case of topologies 2 and 4. Secondly, the single-phase application was used as a bench mark

for the best performance that could be obtained from the filter-units when considering drop-off voltage. This concept was now expanded to the obtainable cut-off frequency as well, implying that the cut-off frequency of the filter-units in a three-phase application would, at best, be the same as that found for the single-phase application.

Table 4-VIII: Cut-off frequencies found for the single-phase application of the filter-units found in group 2

Subgroup 1		Subgroup 2	
Filter-unit	ω_c (kHz)	Filter-unit	ω_c (kHz)
44	195	46	214
45	219	47	257
48	200	49	214
50	195	52	214
51	200	55	214
54	200	58	214
57	200	59	214
61	200	60	214
63	195	62	214
65	195	64	214
67	151	68	159
69	151	70	159
72	151	71	159
74	151	73	159
76	151	75	159
171	200	172	214
173	200	174	214
187	151	188	159
189	151	190	159

The filter-units were then further analysed by considering the actual configuration of the three-layer IPPM used to realise each filter-unit. These configurations can be found in Appendix C. From inspection of the actual configurations certain aspects were highlighted.

Firstly, filter-units 44, 48, 46 and 49 could in actual fact be reduced to two-layer IPPMs through the application of the principle of combining layers, due to the presence of floating layers in the configurations. Similarly, the presence of a vertical-connection between vertically adjacent layers in filter-units 50, 51, 54, 57, 61, 63, 65, 171, 173, 52, 55, 58, 59, 60, 62, 64, 172 and 174 implied that these filter-units could also be reduced to a two-layer IPPM. As this indicated that these filter-units did not efficiently utilise the available dielectric in the three-layer IPPM, they were eliminated from further analysis. Table 4-IX shows the set of remaining filter-units.

For a LPF, the cut-off frequency needs to be as low as possible. Bearing this in mind filter-units 45 and 47 were removed from consideration as their performance in terms of cut-off frequency was inferior to that of the other filter-units still remaining.

Upon closer inspection it was seen that filter-units 72 and 74, as well as filter-units 71 and 73 were in actual fact identical configurations. One of each of these pairs of filter-units should ideally have been eliminated in the search for unique configura-

tions discussed in Chapter 2. Consequently filter-units 73 and 74 were now eliminated from further consideration.

Table 4-IX: The set of remaining filter-units

Subgroup 1		Subgroup 2	
Filter-unit	ω_c (kHz)	Filter-unit	ω_c (kHz)
45	219	47	257
67	151	68	159
69	151	70	159
72	151	71	159
74	151	73	159
76	151	75	159
187	151	188	159
189	151	190	159

In Chapter 3 the discussion of vertical-connections indicated that the location of the vertical-connection, as well as the presence of a redundant vertical-connection did not influence the response of the structure. Using these facts it was possible to see that in subgroup 1 filter-units 67, 72 and 187 were identical in terms of the response obtained from each. The same conclusion was drawn for filter-units 69, 76 and 189. Consequently only one filter-unit from each set was retained, namely filter-units 67 and 69. For the case of subgroup 2, two similar sets of filter-units were also found. In the first set filter-units 68, 71 and 188 were found, while the second set consisted of filter-units 70, 75 and 190. In this instance only filter-units 68 and 70 were set aside for further analysis.

Of the four remaining filter-units it was seen that the placement of the I/O connections in each filter-unit, relative to the vertical-connection, was merely interchanged. In Chapter 3 it was shown that such configurations yielded identical responses. Consequently filter-unit 69 was eliminated from further investigation. The same principle was used to eliminate filter-unit 70 when compared to filter-unit 68.

Thus, the final set of filter-units that were to be practically realised in a three-phase EMI filter setup as shown in Table 4-X, consisted of only two filter-units.

Table 4-X: The final set of filter-units to be experimentally validated

Subgroup 1		Subgroup 2	
Filter-unit	ω_c (kHz)	Filter-unit	ω_c (kHz)
67	151	68	159

4.5 Conclusion

In this chapter a set of configurations were selected that realised LPFs. These configurations were analysed in terms of the drop-off value and pass-band ratio that was obtained from the simulated results. From this investigation it was seen that the single-port network configurations all realised LPFs with identical performance, while the two-port network configurations could be subdivided into three groups according to their performance.

The configurations considered thus far were seen to have application in a single-phase system. The idea of a filter-unit was then introduced that enabled the single-

phase concepts to be expanded to a three-phase system. The filter-unit concept was based on the assumption that in a symmetrical three-phase system the filter could be reduced to an equivalent single-phase implementation.

In the three-phase system the two-port network filter-units were used to realise four different topologies. These topologies were simulated using the quasi-distributed model, the results of which were tabulated.

Further investigation of these results showed that the filter-units could be classified into the same three groups used to categorise the single-phase two-port network configurations. It was seen that the filter-units within each group produced similar results. These filter-units were further investigated by taking into consideration the presence of HF signal paths between the V_{in}, V_{out} and G_{rnd} terminals of each filter-unit. The presence of such paths, in combination with the interconnections between the filter-units in the various topologies, enabled an explanation as to whether or not the filter-units realised a functional three-phase filter.

The presence of coupling between the filter-units, as required by topologies 1 and 3, was seen to influence the output voltage response of the three-phase filter. This influence normally manifested itself in the form of a voltage spike attributed to resonance.

The three-phase filters realised with each of the four topologies were also compared to the LPF response investigated for the single-phase configurations. In so doing it was assumed that the best performance that could be obtained from any given filter-unit was the same as the performance observed for its single-phase counterpart configuration. By means of this comparison it was possible to ascertain whether or not the filter-unit in any given topology was realising its peak performance.

Through this investigation it was determined that the filter-units that fell into the second group performed far better than any of the other filter-units in all four topologies. As a result only these filter-units were considered to be candidates for the practical realisation of a three-phase filter. However, at this stage there were still 38 filter-units to consider. These filter-units were analysed through application of the features discussed in Chapter 3. Through this process it was possible to eliminate a number of filter-units from any further investigation. The various features used to eliminate the filter-units were:

- Inefficient utilisation of the dielectric due to the presence of floating layers or vertical-connections on vertically adjacent layers.

- Identical frequency responses due to the location of the vertical-connection and/or the presence of a redundant interconnection.

- Identical frequency responses due to the placement of I/O connections relative to a vertical-connection.

A further two filter-units were also eliminated through inspection of the cut-off frequency realised by the single-phase configuration counterparts of the filter-units. Only the filter-units with the lowest possible cut-off frequency were retained.

Through this entire process the basic design of a three-phase EMI filter was laid out in terms of filter-units and topologies. It was also seen how 192 possible integrated LPF configurations were narrowed down to only 2 filter-unit configurations, which were to be used in a practical realisation of the three-phase EMI filters.

CHAPTER 5

Design and construction of the experimental test bench and the integrated filters

As discussed in Chapter 1, the final objective was to realise an integrated three-phase EMI filter that was located between the inverter, used for speed control, and the induction motor. Now that the filter-units and topologies that were to be used to realise this EMI filter had been identified, it was necessary to obtain a test bench and to design and construct the IPPMs.

The test bench was to consist of a PWM inverter and an induction motor. These test bench components are readily found in industry and can be purchased without much difficulty. The switching frequency of commercially available inverters is normally in the region just above 20kHz; while, the induction motors found in industry application are large machines with average voltage ratings in the region of 380V and up. These frequency and voltage specifications, of the inverter and induction motor, directly determine the frequency and voltage ratings required by an EMI filter.

The IPPMs that were to be used to realise the EMI filter were constructed from a material known as C-Ply. This material is specified as realising 5.7nF/in^2 capacitance with a relative permittivity of 16 and having a breakdown voltage of more than 100V [22]. However, the material has been successfully tested up to 600V without experiencing breakdown [23]. The exact value of the breakdown voltage was found to be dependent on the handling of the material during processing.

In order to err on the side of caution it was decided to implement the integrated filters in a low voltage application. The low capacitance value, that could be realised with these structures, was also a governing factor in the selection of the high frequency ratings of the integrated filters to be realised with the IPPMs. On account of these factors it was seen that the standard industry components of the test bench could not be used in this application. This issue was addressed through the design and construction of a low voltage, high frequency test bench setup instead. To this end a low voltage three-phase induction motor was obtained and a high frequency PWM inverter was constructed.

Even though the integrated EMI filters discussed here would not be sufficient for an industry application the integrated filter concept was still creditable. Through improved material processing procedures it is, in all likelihood, possible to use the C-Ply material in industry applications. Alternatively, other materials, normally incorporating ceramic dielectrics that inherently have higher breakdown voltages and greater dielectric relative permittivities, could be used. However, the processing techniques and equipment necessary for the development of such materials are more complicated than those required for C-Ply. An investigation into the feasibility of integrated three-phase filters, like the one considered in this study, does not justify the use of such complicated processing procedures required for such materials.

In this chapter the exact requirements of the test bench were identified through an investigation into the material properties of C-Ply. The design and construction of the low voltage, high frequency test bench was addressed. Finally the design and construction of the IPPMs, using the C-Ply material was presented.

5.1 Material used to realise the integrated filters

Before the test bench could be constructed it was seen to be necessary to do an investigation into the material that was to be used to realise the integrated, three-phase filters.

The IPPMs thus far have been described as dielectric layers sandwiched between conductive layers. It was seen that Printed Wiring Board (PWB) inherently realised this required structure.

PWB is often used as a surface on which to mount and connect components so as to realise an electronic circuit [24]. Typically a PWB comprises of a non-conductive substrate mounted to a conductive layer. These boards can be single-layered (one substrate and one conductive layer), double-layered (one substrate sandwiched between two conductive layers) or multi-layered (many substrate layers sandwiched between consecutive conductive layers) [24].

A spin-off of the PWB material, which is sometimes used for power supply decoupling [25], is known as embedded capacitor material. This material differs from the standard PWB by the fact that the substrate material has a relative permittivity high enough for it to be used as a dielectric in a capacitance application.

Such material, known as *C-ply*, that is commercially available was obtained from 3M Manufacturers. C-ply is a double-layered PWB, with a barium-titanate embedded substrate found between the two conductive layers. It is used in industry as a decoupling capacitor on HF digital boards [23]. The properties of the material, as specified in the datasheet provided by 3M Manufacturers [22], are shown in Table 5-I.

Table 5-I: General properties of C-Ply material [22]

Attribute	Value
Dielectric Thickness	$16\mu m$
Capacitance/Area	$5.7nF/in^2$
Dielectric Constant	16
Freq., Voltage, Temperature	Meets X7R
Dielectric Strength	$\sim130V/\mu m$
Breakdown Voltage	>100V
Copper Thickness	$35\mu m$
Flammability Rating	94V-0

In its native form C-ply only realises a two-layer IPPM. In order to construct a three-layer IPPM with this material, it was necessary for it to be processed. Consequently, the affect that this material processing would have on the material's properties needed to be investigated. This investigation was broken into two parts. The first part investigated the physical properties of the material, while the second part looked at the electrical properties.

5.1.1 Physical properties

A sample of C-Ply was prepared and examined using both an optical and an electron microscope. From this the dielectric thickness and material composition were investigated, the details of which can be found in Appendix D.
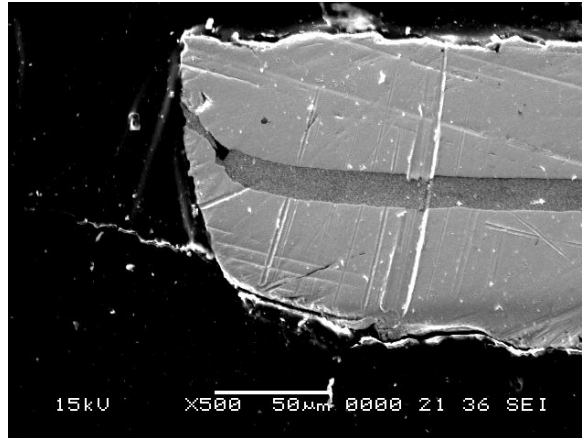
Fig. 5.1: Side-on view of a C-Ply sample at 500× magnification as seen under the electron microscope

Fig. 5.1 shows a side-on view of the C-Ply sample at one of the ends of the material, as seen under the electron microscope at 500× magnification. From this image it can be seen that the process of cutting the C-Ply damages both the dielectric and the copper at the point where the material was cut. This scenario is detrimental as it could introduce a direct short between the two conductive layers. Even in the absence of such a short, the breakdown voltage of the material would be considerably reduced through such an edge due to the close proximity of the two copper layers. In order to avoid both of these possibilities it was seen to be necessary to account for this through the etching process used in the integrated filter manufacture. This can best be explained with reference to Fig. 5.2, where a schematic representation of the C-Ply material is shown. In Fig. 5.2(a) the clearance between the two conductive layers at the material edge is shown to be equal to the thickness of the dielectric, provided damage has not occurred as in Fig. 5.1. Furthermore, consider a section of the bottom conductive layer to be extended, as shown in the figure. In so doing a contact surface would be created as a realisation of the terminals of the IPPM structure. Once again the clearance, at the corner of the contact surface, is seen to be equivalent to the thickness of the dielectric. It was found that the dielectric was not mechanically strong enough to support itself if the conductive layer on both sides of the dielectric was removed during etching. As a result one of the conductive layers had to be etched further back from the edge of the material as shown in Fig. 5.2(b). Not only is the clearance between the two conductive layers considerably increased, but the bottom conductive layer gives mechanical support to the dielectric. By increasing the clearance as discussed here, a drop in the value of the breakdown voltage of the material was avoided.

As already mentioned earlier, the C-Ply was a double-layered embedded capacitor material. In order to realise a three-layer IPPM, two pieces of C-Ply had to be utilised. This was done by stacking two pieces of C-Ply on top of one another and by using two pieces of FR4 pre-preg and PC board, as shown in Fig. 5.3. The entire structure was then set under high temperature and high pressure to form a rigid three-layer IPPM. In this procedure there was no actual bond formed between the

conductive layers of the two pieces of C-Ply at the point where they made contact. It was possible that voids might be present in the structure between these layers. However, these voids would be encapsulated by two equipotential conductive layers. As a result, the electric field found within the voids would be at zero. Hence, the voids would not influence the functionality of the structures [23].

(a)   (b)
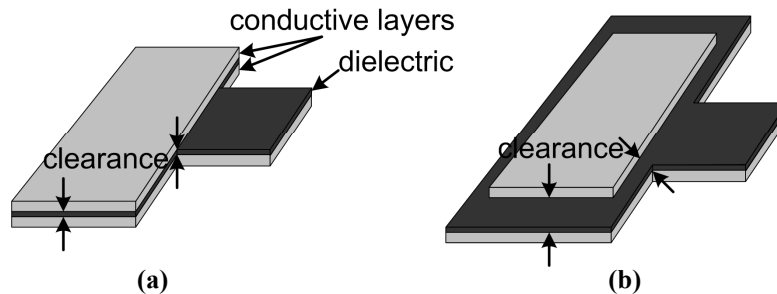
Fig. 5.2: Schematic representation of the C-Ply showing the clearance found between the two conductive layers at the edge of the material (a) before [23] and (b) after etching
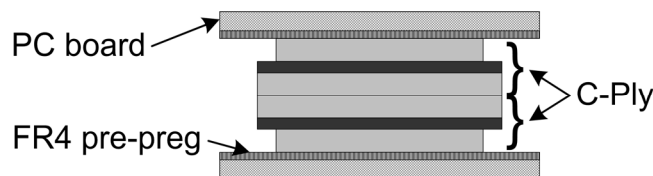
Fig. 5.3: Schematic representation of a three-layer IPPM realised with two pieces of C-Ply

5.1.2 Electrical properties

In order to study the electrical characteristics of the C-Ply, a number of parallel plate capacitors were made from the material. To this end a number of rectangular pieces of C-Ply were cut. The top conductive layer was then etched back from the edge of the material to form parallel plate capacitors with unequal plate sizes. A schematic representation is shown in Fig. 5.4. These capacitors were used to investigate the relative permittivity of the dielectric and the capacitance per unit area of the material. The details of this investigation can be found in Appendix D. From this investigation it was found that the capacitance per unit area of the material was on average 8.70pF/mm^2. This equates to 5.61nF/in^2 which is comparable to the per square inch rating given in the datasheet.
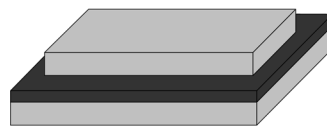
Fig. 5.4: Schematic representation of the parallel plate capacitor constructed from C-Ply

Another aspect that was also looked at was the influence that compressing the material had on the capacitance, the details of which can be found in Appendix D. Such a compression was found to have no noticeable influence.

The breakdown voltage of the material was investigated by placing the capacitors in series with a current limiting resistor and a DC voltage source. The dielectric was seen to experience breakdown when an arc occurred, through the dielectric, between the two plates of the capacitors. The voltage at which this phenomenon was observed was measured and defined as the breakdown voltage of the material. These arcs were however, intermittent and occurred at different voltages for each of the

capacitors. Consequently, further investigation was performed with more test samples of various shapes [23]. The only factor that seemed to influence the value of the breakdown voltage was damage sustained by the dielectric (e.g. folds or indentations) during the manufacturing process [23]. On average the breakdown voltage was seen to be higher than the specified value of 100V, unless the dielectric had been damaged. In this event, the lowest breakdown voltage observed was 45V. A graph showing the relative frequency of dielectric breakdown at various voltages can be found in Appendix D.

5.2 The test bench

As mentioned earlier, the test bench necessary for the experimental measurements consisted of an induction motor and a PWM inverter. The choice of induction motor and inverter were dependent on the breakdown voltage and capacitance per unit area realisable with the C-Ply.

The breakdown voltage was, at worst, seen to be 45V. Due to the influence of the manufacturing process on this value it was not possible to guarantee that the IPPMs constructed would have a breakdown voltage greater than the worst case scenario. As a result it was seen to be necessary to experimentally test the integrated filters in a low voltage application, preferably below 45V.

In the construction of these EMI filters it was planned to use an E64 core. Such a large core was selected to ease the manufacture of the prototype filter. However, even with such a large core, the area of the filter-units would be limited. As a consequence, the capacitance that would be realised with the structures would only be on the order of a few hundred nF.

The inductance of the IPPMs could be increased by realising a multi-turn structure. However, the quasi-distributed model used in the analysis of the IPPMs was only meant for single-turn applications. Further, increasing the number of turns drastically increases the complexity of the manufacturing process. Due to both of these factors only single-turn IPPM structures were considered, the inductance of which would be limited to be in the order of a few tens of μH.

As a consequence of the values of passive component energy storage that could be practically realised with the C-Ply material, a high switching frequency, in the order of a few hundred kHz, had to be used in the inverter.

5.2.1 The induction motor

Due to the low breakdown voltage of the C-Ply a low voltage three-phase induction motor was required. Such a motor was obtained, the nameplate ratings of which are given in Table 5-II [26].

Table 5-II: Nameplate ratings of the induction motor used in the test bench

Low voltage induction motor nameplate ratings	
Output Power	105W
Slip at full-load	0.12
Line-to-line voltage	15V
Line Current	6.1A

The required bus voltage for an inverter used to drive this motor at full power was calculated as 37V. The method used to determine this value can be found in Appendix D. The magnitude of the bus voltage was within the worst case scenario limit of the C-Ply breakdown voltage, namely 45V.

5.2.2 The PWM inverter

As discussed, the realisable cut-off frequency of the IPPM was in the order of a few hundred kHz. So as to be able to noticeably measure the filtering influence that the IPPMs have on HF noise it was necessary for the switching frequency of the inverter to be high. This meant that the commercially available inverters could not be used, as not only did the inverter have to be low voltage, but also HF in nature. Consequently, a HF, low voltage inverter was designed and constructed.

The details of the design and construction of the inverter are not pertinent to the study being discussed here and hence can be found in Appendix D. It should be noted however that the switching frequency of the inverter was arbitrarily selected as 200kHz.

5.3 Practical realisation of integrated three-phase EMI filters

Now that the configuration of the various filter-units had been decided on; the material used to realise the IPPMs had been characterised; and the test bench had been constructed; it was eventually possible to actually build the integrated three-phase filters and experimentally validate the concept.

As stated earlier, it was decided to use an E64 core in the construction of the IPPMs. The dimensions of this core [27], that in turn determined the IPPM dimensions, can be found in Appendix D.

Next, by examination of the four topologies to be realised it was seen that two main factors had to be addressed during the construction of the IPPMs. Firstly, it was necessary to be able to configure the IPPMs in a number of ways, so as to realise the various filter-units. Specifically, the filter-units had to be able to realise star and delta formations as well as different interconnections. To this end the IPPMs had to be constructed in such a way that all six terminals could be utilised independently. This implied that the interconnections of the filter-units could not be inherently realised in the manufacturing process. However, this would be an avenue to explore in future application of the IPPMs where a particular filter-unit configuration is being utilised. In this study this notion was touched upon with the realisation of IPPMs that inherently realised a star formation, as discussed later.

Secondly, the three filter-units had to be magnetically coupled together in order to realise topologies 1 and 3, while no such coupling was required for topologies 2 and 4. This coupling was practically realised by designing the IPPMs in such a way that three individual IPPMs would share a common core. The coupling was reduced by using three individual cores for each of the three IPPMs. As a result, different IPPMs had to be designed and constructed to realise topologies 1 and 3 from those required to realise topologies 2 and 4.

The IPPMs built for either case are listed in Table 5-III and are discussed in more detail in the following sections.

Table 5-III: List of the IPPMs that were designed and constructed

No magnetic coupling between filter-units		
IPPM	Description	Topology
1	3-layer IPPMs	2, 4
Magnetic coupling between filter-units		
IPPM	Description	Topology
2	Vertically stacked IPPMs	1, 3
3	Horizontally stacked IPPMs	1, 3
4	Inherent star formation	1

5.3.1 No magnetic coupling between filter-units

For topologies 2 and 4 it was required that there be no magnetic coupling between the three filter-units. In the practical realisation of the filter-units this ideal case was achieved to some degree by stacking the three units on top of each other and separating them with a piece of ferrite, as shown in Fig. 5.5.
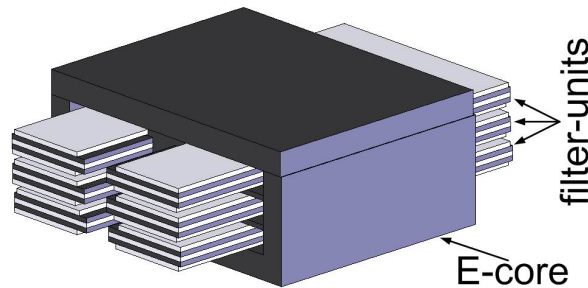
Fig. 5.5: The three filter-units stacked on top of one another to limit the coupling between the respective units

(a)   (b)   (c)
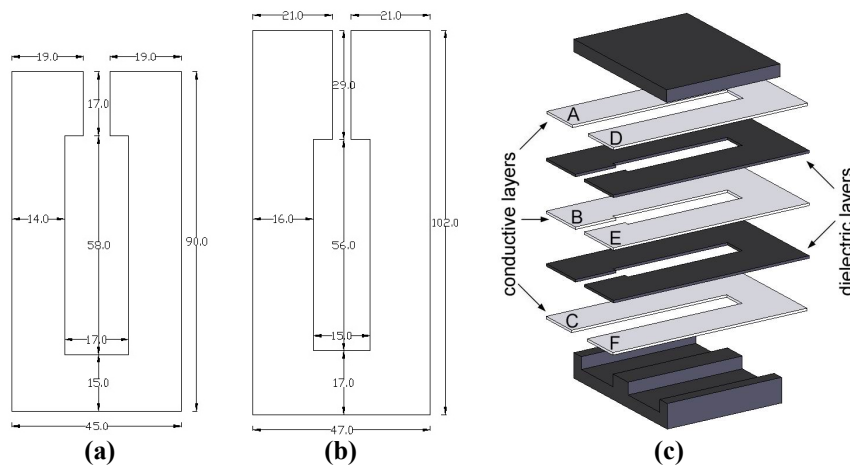
Fig. 5.6: The dimensions, in mm, of (a) the top and bottom conductive layers and (b) the middle conductive layer of the IPPMs (c) Pictorial exploded view of the three-layer IPPM used for single-phase application and as a filter-unit in three-phase application

In this application each filter-unit was realised with a separate three-layer IPPM. The three IPPMs were however, identical to one another. The etching pattern, and dimensions used to realise a single such IPPM are shown in Fig. 5.6(a) and (b).

Only the top and middle layers of the IPPM are shown, as the top and bottom layers
were identical in size and shape. An exploded view of a single IPPM, to be used to
realise a single filter-unit, is shown in Fig. 5.6(c), with labels on each of the termi-
nals that correspond with the terminals of the IPPM schematic representation shown
in Fig. 2.2.

In Chapter 2 a practical realisation of a single-phase IPPM was used to measure the
transfer function of various configurations on a network analyser. One of the filter-
units discussed here was used for that purpose. All three filter-units were required to
be stacked together, as shown in Fig. 5.5, to extend their use to three-phase applica-
tion.

Fig. 5.7 shows the final product, with all three-filter-units stacked on top of one an-
other.
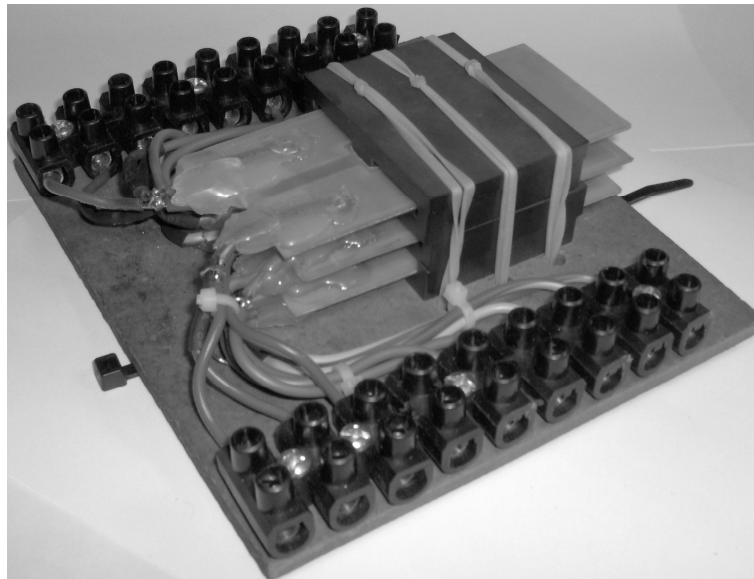
Fig. 5.7: Photograph of the three filter-units stacked on top of one another

5.3.2 Magnetic coupling between filter-units

For topologies 1 and 3 the filter-units had to be magnetically coupled together. This
was achieved by ensuring that the filter-units shared a common core. In order to re-
alise as large a coupling coefficient as possible the IPPMs were designed and con-
structed so that the filter-units were placed as close to one another as possible. This
was achieved through two different methods. In the first method, the filter-units
were stacked on top of one another, while in the second method the filter-units were
placed adjacent to one another.

Vertically stacked IPPMs

The structure realised here was an extension of the three separate filter-units dis-
cussed in section 5.3.1. The main difference was that the filter-units were no longer
separated by a piece of ferrite but were instead stacked directly on top of one an-
other, with only a piece of PC board and pre-preg to separate the three units. A
schematic representation of the structure is shown in Fig. 5.8. In the figure the six

terminals of the three filter-units are shown. The subscripts refer to the filter-unit that any given terminal is associated with.
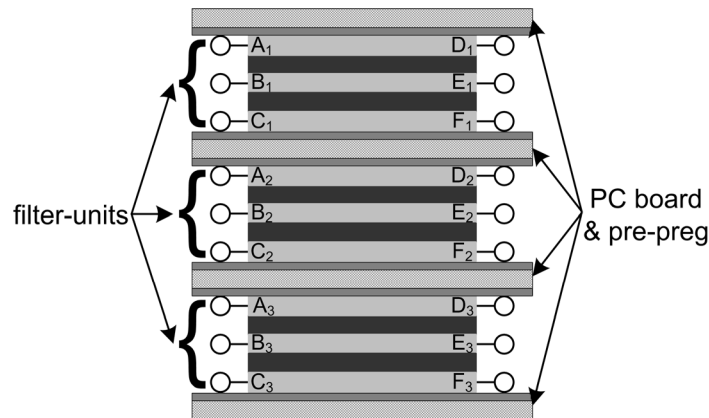
Fig. 5.8: Schematic representation of the vertically stacked IPPMs used to realise coupling between the filter-units

It should be noted that the capacitive coupling that would occur between filter-units was considered to be negligible as compared to the capacitive coupling between conductive layers within a filter-unit. This was due to the fact that the thickness of the dielectric layer was considerably smaller than the thickness of the PC board and pre-preg combination; 16μm as compared to 500μm of PC board and two layers of 64μm pre-preg. Furthermore, the relative permittivity of the PC board and pre-preg would be far less that that of the dielectric layer; 16 as compared to a relative permittivity of 4.7 for both the PC board and the pre-preg. Both of these factors reduced the capacitive coupling between the filter-units as compared to the capacitive coupling between the conductive layers.
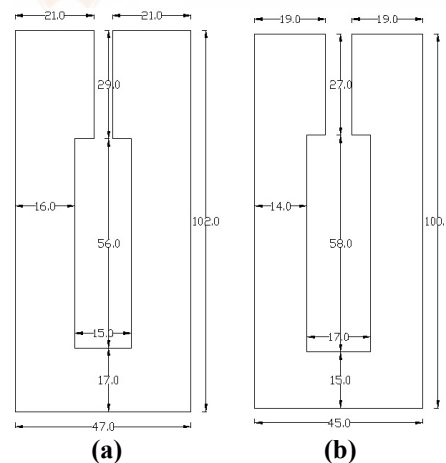
Fig. 5.9: The dimensions, in mm, of (a) the top and bottom conductive layers and (b) the middle conductive layer of the IPPMs

Once again, the three filter-units were identical to one another. Fig. 5.9 shows the dimension of the top and middle layers of the IPPMs. The top and bottom layers were identical. The similarity between the etching patterns of these filter-units and those in section 5.3.1 can be seen.

Fig. 5.10 shows a photograph of the vertically stacked IPPM structure. Comparison of this figure with Fig. 5.7 indicates that the magnetically coupled IPPMs used considerably less magnetic material as well as occupying less space than the uncoupled structures.
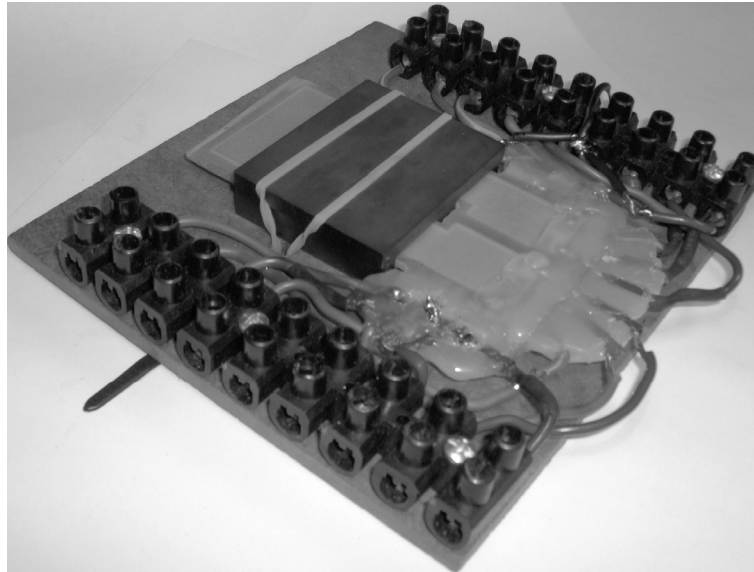
Fig. 5.10: Photograph of the vertically stacked IPPM structure

Horizontally stacked IPPMs

When realising the vertically stacked IPPMs, each filter-unit had to be realised as a separate unit and combined during the pressing stage of the manufacturing process. This meant that enough C-Ply material was used to realise three IPPMs. In an attempt to use less material and thereby decrease the space utilised by the IPPM the three IPPMs were stacked horizontally instead of vertically. This could be achieved by etching a single layer of C-Ply so as to realise three IPPMs. In so doing, only a third of the material used in the vertically stacked IPPM structure was used for the horizontally stacked IPPMs. It was also no longer necessary to separate the IPPMs with PC board, resulting in even more material savings.

The possible disadvantage of this placement of the IPPMs relative to one another was that the magnetic coupling between filter-units might be decreased. In order to investigate if this was the case, the filter-units were constructed using the etching patterns shown in Fig. 5.11(a) and (b). As before, the top and bottom conductive layers were identical to one another.

| (a) | (b) | (c) |
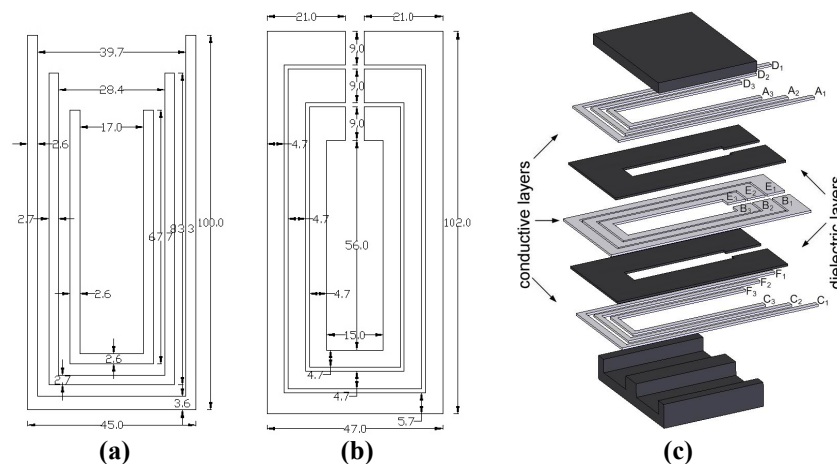
Fig. 5.11: The dimensions, in mm, of (a) the top and bottom conductive layers and (b) the middle conductive layer of all three IPPMs (c) Pictorial exploded view showing the placement of the three IPPMs adjacent to one another

Fig. 5.11(c) shows an exploded view of the final structure. The terminals of the three IPPMs are labelled; the subscripts corresponding with the filter-unit that any given terminal is associated with.
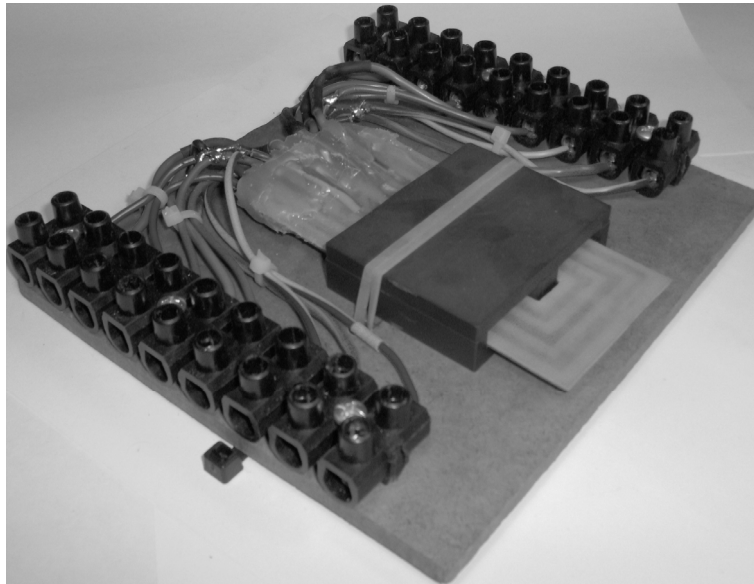
Fig. 5.12: Photograph of the horizontally stacked IPPM structure

Fig. 5.12 shows a photograph of the horizontally stacked IPPM structure. Less C-Ply, pre-preg and PC board material were used in the construction of this structure as compared to that used to realise the filter of Fig. 5.10.

Inherent star formation

In Chapter 6 it was seen that the vertically and horizontally stacked IPPMs yielded similar results. From this fact it was concluded that the coupling between the filter-units in both structures was comparable. As a result further consideration was given to the horizontally stacked IPPM structure in terms of inherently realising connections within the design. The purpose of this investigation was to determine if it was feasible to consider inherently realising connections, especially as doing so often lent itself towards simplifying the manufacturing process.

To this end the configurations of the two filter-units, identified in Chapter 4 for application in the three-phase EMI filter, were further examined. The filter-units are shown in Fig. 5.13 for ease of reference. From this figure it can be seen that both filter-units 67 and 68 have a ground terminal present on the middle conductive layer. For the realisation of topologies 1 and 2 the three filter-units were to be connected in star formation. This implies that the three ground terminals of three identical filter-units were to be connected together.

It was possible to inherently realise this formation by modifying the horizontally stacked IPPM design. The layers on which the ground terminals were found were used to realise a ground plane, achieved through the combination of the three individual windings into one large winding. This meant that the middle conductive layer was used to form the ground plane.

The etching patterns used to realise this structure are shown in Fig. 5.14. The top and bottom layers of the IPPMs were no longer identical to facilitate the connections required to each of the windings.
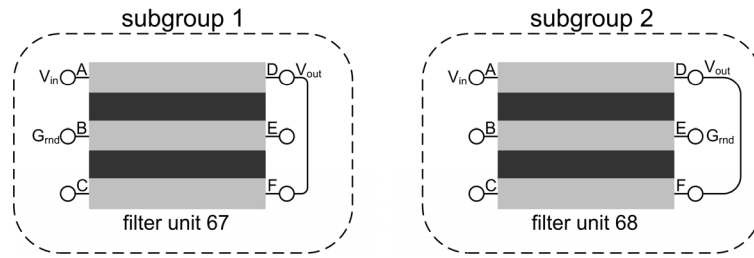
Fig. 5.13: The two filter-units to be experimentally investigated

(a)   (b)   (c)
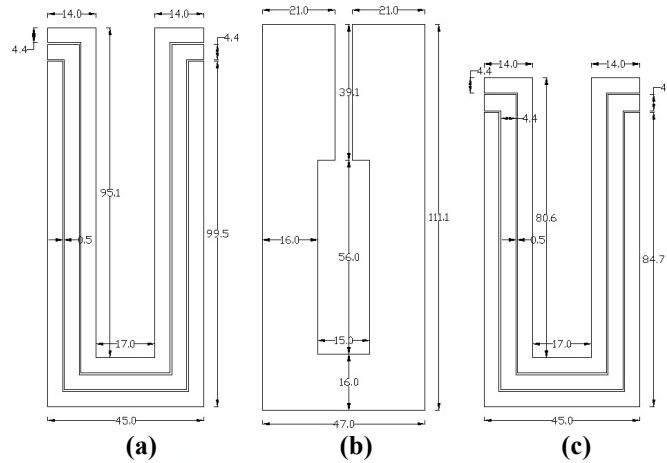
Fig. 5.14: The etching patterns and dimensions, in mm, of (a) the top, (b) the middle and (c) the bottom conductive layers used for filter-units 67 and 68

Due to the inherent presence of magnetic coupling between the filter-units in the inherent star formation IPPM only topology 1 could be realised with these structures.

Fig. 5.15 shows a photograph of the final product. Fewer connections protruding from the structure can be seen than those present in the Fig. 5.12.
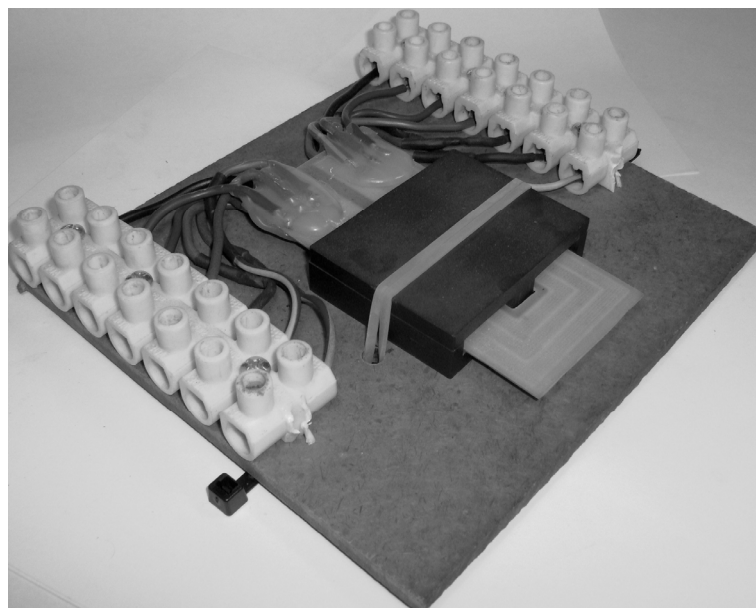
Fig. 5.15: Photograph of the inherent star formation IPPM structure

5.4 Conclusion

The IPPMs, considered thus far in simulation, were physically realised for purposes of experimental verification of the theory. To this end material had to be found that could be used to manufacture the IPPMs. The material obtained, C-Ply, was seen to have a relatively low breakdown voltage and a capacitance per unit area of approximately $8.70pF/mm^2$. These values were experimentally validated so as to investigate the influence of the manufacturing process on the electrical properties of the material. Due to the results of this investigation it was discovered that the test bench required for the filters had to be low voltage and HF in nature. Consequently, a test bench was designed and constructed to meet these criteria.

Industrial inverters and motors were not used in the test bench as the EMI filter required in an industrial application is high voltage and LF in nature. However, the approach in this study was merely to verify the simulation predictions and not to realise an industrial-grade EMI filter. Nonetheless, with more complex manufacturing procedures and the utilisation of ceramic dielectrics it should be possible to manufacture an integrated three-phase EMI filter for industrial applications.

The design of the IPPMs to be investigated with the test bench was considered in two main categories. Firstly IPPMs that were not magnetically coupled together were considered for the realisation of topologies 2 and 4. Secondly IPPMs that were magnetically coupled together were necessary for the practical implementation of topologies 1 and 3. In order to realise these two categories, the construction of the IPPMs had to be approached differently.

The non-magnetically coupled IPPMs were constructed as three individual three-layer IPPMs. These structures were then placed on top of one another, separated by a piece of ferrite. In so doing the presence of magnetic coupling between the three filter-units was discouraged.

The magnetically coupled IPPMs were realised with two different structures. In the first structure the filter-units were stacked on top of one another, while the same filter-units were stacked adjacent to one another in the second structure. A third structure, the filter-units of which were also magnetically coupled together, was also realised. In this structure a star formation between the filter-units was inherently realised through the introduction of a ground plane into the structure. Only topology 1 could be physically realised with this structure.

The etching patterns for all of these IPPMs were designed according to the size limitations of the E64 core to be used in the experimental setup. These etching patterns, along with the actual dimensions used, are given in this chapter.

Through the implementation of these IPPMs in an experimental setup a number of design concepts, such as vertical and horizontal stacking of filter-units and inherent connections, were investigated that are further discussed in Chapter 6.

CHAPTER 6

Experimental setup, measurement procedure and results

The IPPMs, discussed in Chapter 5, were used to practically realise the three-phase filters presented in Chapter 4. An evaluation of the performance of these filters under operating conditions was executed with the aid of the test bench. In this manner a number of concepts relating to the IPPMs were investigated:

- The behaviour of the IPPMs as predicted by means of simulation was practically verified.

- The realisation of the same filter, with different IPPM structures i.e. vertically stacked IPPMs as compared to horizontally stacked IPPMs, was explored.

- The feasibility of inherently realising interconnections during the manufacturing process of the IPPMs was also considered.

Through this investigation it was shown to indeed be feasible to integrate a three-phase EMI filter. This conclusion was drawn through an evaluation of the performance of the integrated filters. The performance of the filter was ascertained through the use of comparative measurements, namely CM and DM current measurements with and without the filters present in the test bench. With the aid of these results it was seen that the filters suppressed both CM and DM currents. However, in order for these measurements to be reliable, repeatable and instil a certain amount of confidence, care had to be taken with the experimental setup and the measurement procedure.

To this end careful consideration of the grounding of the measurement equipment and the experimental apparatus was imperative. Such a well-defined ground plane was achieved by performing the measurements in a Faraday cage, although the advantages of radiation shielding by the Faraday cage were not utilised. The placement and interconnection of all the components of the experimental setup were considered and documented.

Once the exact setup had been clarified it was still necessary to put some thought into the measurement procedure used to evaluate the CM and DM currents. In so doing not only would confidence in the measurements be gained but a deeper understanding of the meaning of the measurement results could be developed. For this purpose the instantaneous currents within a three-phase system were considered in terms of both CM and DM currents.

The measurement procedures discussed were used to characterise the test bench when no filters were present in the setup. These measurements were compared with the noise floor of the experimental setup so as to establish a reference bench mark used to interpret the filter measurements.

6.1 Experimental setup

The basic experimental setup consisted of the inverter, the EMI filter and the induction motor, connected as shown in Fig. 6.1. In the figure, the motor case and the midpoint of the DC bus are shown to be connected to earth. The connection of the EMI filter to this earth was dependent on whether or not the topology used to realise the filter was connected in star or delta formation, only the former requiring such a connection.
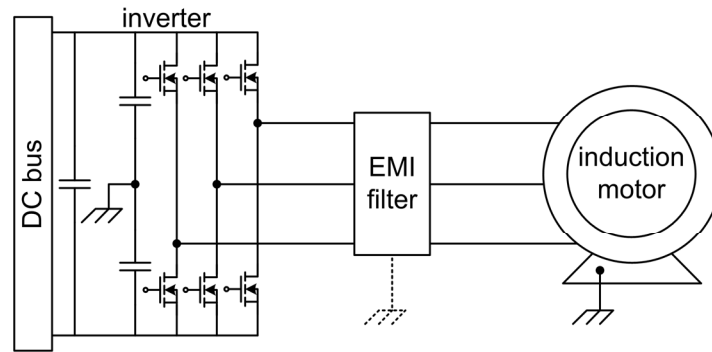
Fig. 6.1: The basic experimental setup used to test the integrated filters

However, even though the basic setup to be realised was known, more care had to be taken into the exact realisation of this setup. This was due to the fact that EMI measurements were to be performed. Normally when taking such measurements they are performed to verify whether or not a device adheres to a particular EMI standard. These standards consequently have a set of guidelines for the experimental setup and the measurement procedure. In order to see if the device performs within the acceptable limitations of the standard these guidelines must be adhered to precisely. In the experimental setup described here no such guidelines were followed. This was due to the fact that the measurements were comparative in nature so as to determine the functionality of the filters and not as a performance evaluation for industry application [28]. Even though this was the case, care still had to be taken in the experimental setup so that the measurements would be repeatable and could be comparatively analysed with a degree of confidence.

As discussed in Chapter 1, the EMI to be measured was classified as conducted EMI, which is known to consist of CM and DM noise. Especially in the case of CM noise, the EMI is found to manifest in the ground paths of the experimental setup. As a result the grounding of the experimental setup, in terms of the device under test (DUT) and the measurement equipment, had to be carefully scrutinised.

In order to ensure such a well-defined setup, the measurements were performed in a Faraday cage. This allowed all the experimental equipment to be easily grounded to a physical earth that had a well defined ground reference plain [28]. It should be noted that the benefits of radiation shielding, normally the driving factor as to why a Faraday cage is utilised, were not used. This was attributed to the fact that the EMI of interest was conducted EMI and not radiated EMI.

A schematic representation of the complete experimental setup showing the placement of the equipment used, relative to one another, is shown in Fig. 6.2.
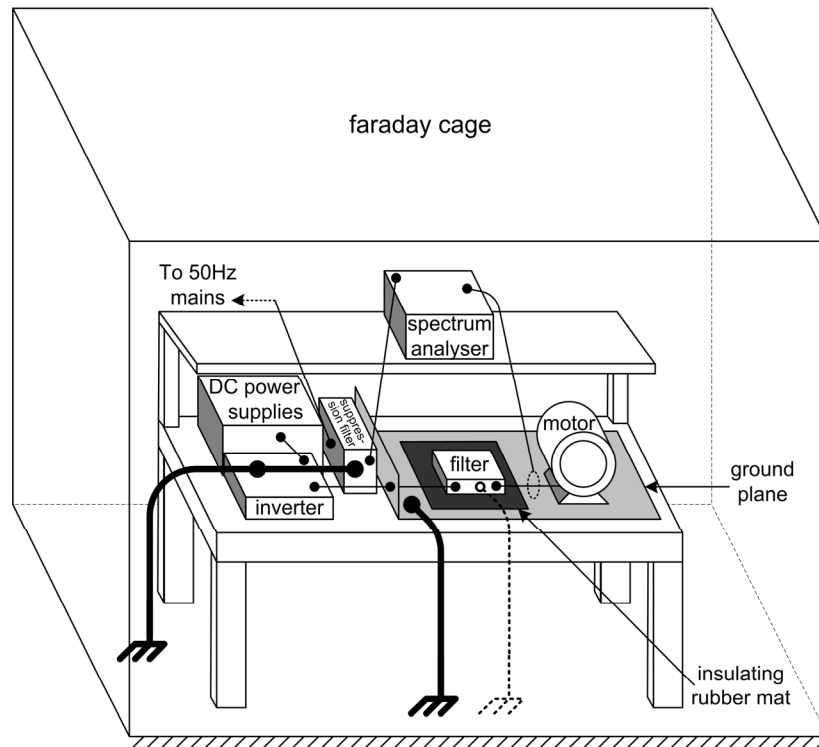
Fig. 6.2: Schematic representation of the experimental setup [28]

From the figure it can be seen that the motor and the filter were placed on a ground plane that was connected to physical earth. The filter however, was insulated from the ground plane by means of an insulating mat. In so doing the grounding of the filter could be controlled to only be realised for a star formation.

The DC power supplies and the inverter were placed separate from the filter and motor setup as, although necessary for the investigation, they were not an essential part of the investigation.

A mains suppression filter with surge protection was placed between the 50Hz mains supply and the measurement equipment. This was to ensure that any noise present on the mains did not interfere with the measurement.
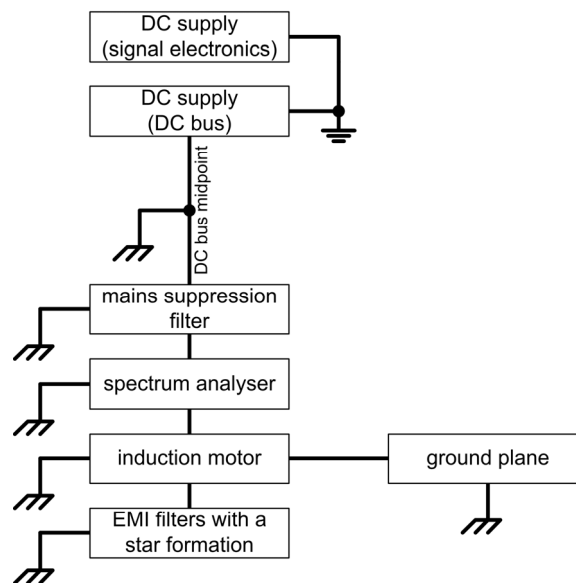
Fig. 6.3: A grounding map of the experimental equipment [28]

Fig. 6.3 shows a ground map of the experimental setup. The ground map indicates the connection of the experimental equipment to ground reference points and the existence of ground paths between the equipment [28]. From the figure it can be seen that the two DC power supplies used in the setup were not connected to earth and were in actual fact floating. The circuit grounds of the two supplies were however connected to the same reference point. The power supply used as the DC bus was grounded to earth through a connection to the midpoint of the DC bus, as shown in Fig. 6.1. It was necessary to connect the DC power supplies in this fashion to facilitate a well-defined path for the flow of CM current in the setup. The path was considered to be through the cables connecting the motor to the inverter, into the ground plane and back to the cables through the midpoint of the DC bus.

6.2 Measurement procedure

A spectrum analyser was used to take frequency domain measurements of the currents in the setup so as to investigate the EMI. The current was measured as the conducted EMI noise in this investigation manifested itself as CM and DM currents. Only the frequency domain was considered as the PWM scheme of the inverter was carrier-based PWM, with the carrier frequency being defined as the switching frequency of the inverter. In [6] the harmonic spectrum of such an inverter is defined as "pairs of salient sidebands, centred around the carrier frequency and additional frequency bands located on either side around integral multiples of the carrier frequency". This definition implied that the distribution of the noise would be over a frequency range and not centralised at a specific frequency. Consequently, a frequency domain measurement would prove to be more informative than a time domain measurement.

The measurements were taken between the range 100kHz to 30MHz with a HP8591E spectrum analyser. The frequency range was selected according to common measurement practice associated with conducted EMI.

The spectrum analyser was used in conjunction with a Tektronix P6021 high bandwidth alternating current probe. It should be noted that the measurements taken with this current probe had a scaling factor of 10mA/mV and a further 10dB of attenuation due to the presence of an HP11947A transient limiter.

Generally, quasi-peak detectors are used for EMI measurements [28]. However, the current measurements presented in this chapter are peak measurements. This was due to the fact that the spectrum analyser used to perform the measurements was not capable of taking quasi-peak measurements. This is slightly disadvantageous as a peak measurement shows the maximum amplitude measured over the range of frequencies during some time period. The measurement thus obtained effectively shows the worst possible noise signal found at any given frequency. However, EMI is not normally fixed in amplitude and often consists of low pulse repetition frequency emissions [28]. This is the main motivation for using quasi-peak detectors for EMI measurements instead of peak measurements, as the peak measurements will show certain emissions more severely than quasi-peak measurements. However, as the measurements taken here are comparative in nature, the use of peak measurements instead of quasi-peak measurements is not necessarily catastrophic to the results obtained. The main aspect to bear in mind is that the absolute values of the measured currents correspond with the maximum current measured at any given

frequency during the time taken to perform the measurement. The general trend depicted in the measurements, namely whether or not the filter manages to suppress the HF noise, will still be shown.

Before the measurements could be taken, the measurement procedure still needed to be examined. This was necessary so that the correct interpretation could be applied to the measured results. To this end it was necessary to investigate the paths along which CM and DM currents would flow in a three-phase system.

As a starting point the well defined paths of CM and DM currents in a single-phase system [8] were considered, as shown in Fig. 6.4. The DM currents, I_{dm1} and I_{dm2}, are defined as being equal in magnitude, but oppositely directed. These are termed the desired or functional currents in the system. The CM currents, I_{cm1} and I_{cm2}, while also being equal in magnitude, flow in the same direction DM the two lines, normally using the ground path as a return path. These currents are not supposed to be present in the system. In the event that the CM current, is not evenly distributed between the two lines, the unbalanced part of the CM current is incorporated into the DM current [13]. Consequently, the CM currents will always have equal magnitude in a single-phase application.
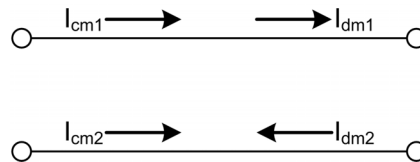
Fig. 6.4: Flow of CM and DM currents in a single-phase application [8]

However, in a three-phase application the flow of CM and DM currents is not as well defined. In Chapter 1 a general definition for three-phase CM and DM noise was mentioned as "ground-loop noise" and "line-to-line noise" respectively. Keeping this definition in mind, expanding the single-phase definitions presented here and through use of an approximation of the paths of conducted EMI currents as used for three-phase filter design in [11], the subsequent analysis of instantaneous currents was used to define both CM and DM current measurement procedures.

6.2.1 Instantaneous three-phase currents
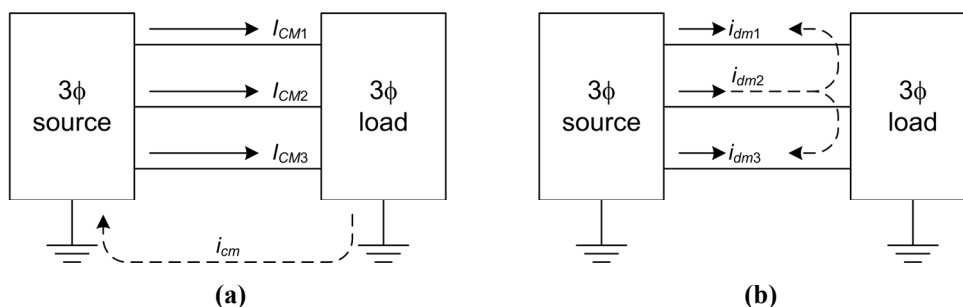
Fig. 6.5: Schematic representation of the flow of (a) CM current and (b) DM current in an arbitrary three-phase system

In an arbitrary three-phase system the total CM current, i_{cm}, found in the ground plane is seen to split between the three lines of the three-phase system into three CM current components, I_{CM1}, I_{CM2} and I_{CM3}. This is shown schematically in Fig. 6.5 (a). From this definition the following relation can be found at an instant in time.

$$i_{cm} = I_{CM1} + I_{CM2} + I_{CM3} \tag{6.1}$$

Using equation (6.1) the three CM current components can be written in terms of the total CM current found in the return path as shown in equation (6.2).

$$
\begin{aligned}
I_{CM1} &= ai_{cm} \\
I_{CM2} &= bi_{cm} \\
I_{CM3} &= \left(1-(a+b)\right)i_{cm}
\end{aligned}
\tag{6.2}
$$

The variables *a* and *b* are dimensionless and have values that satisfy all three of the conditions $0 \le a \le 1$, $0 \le b \le 1$ and $0 \le a+b \le 1$. This gives a mathematical representation of the portion of total CM current found on each line at an instant in time. If the three-phase system is balanced the CM current components are given as follows:

$$
\begin{aligned}
a = b &= \tfrac{1}{3} \\
\therefore I_{CM1} &= \tfrac{1}{3}i_{cm} \\
\therefore I_{CM2} &= \tfrac{1}{3}i_{cm} \\
\therefore I_{CM3} &= \tfrac{1}{3}i_{cm}
\end{aligned}
\tag{6.3}
$$

However, in practice imbalances in a three-phase system can occur. Further, considering the fact that, unlike in the single-phase case where an imbalance in the CM current between the lines translates into DM current, the same cannot be said for a three-phase system [13]. Consequently it is necessary to consider the CM current components in the form given in equation (6.2).

Fig. 6.5 (b) shows a schematic representation of the paths along which the DM current flows in a three-phase system. The DM current inherent to lines 1, 2 and 3 is represented by i_{dm1}, i_{dm2} and i_{dm3} respectively. These currents are seen to use the other two lines as a return path. This is explicitly shown for i_{dm2} in the figure. From this interpretation, the total DM current, or the DM current component, I_{DM1}, I_{DM2} and I_{DM3}, found on lines 1, 2 and 3 respectively, is seen to be a combination of the DM current inherent to the line, and a portion of the DM currents inherent to the other two lines of the system. This is shown in equation (6.4) through application of the variables α, β and γ. As in the CM current case, α, β and γ represent the portion of the inherent DM current found on the return lines. These variables are also dimensionless and satisfy the conditions $0 \le \alpha \le 1$, $0 \le \beta \le 1$ and $0 \le \gamma \le 1$. The DM current components for each line can then be written as:

$$
\begin{aligned}
I_{DM1} &= i_{dm1} - \beta i_{dm2} - \gamma i_{dm3} \\
I_{DM2} &= i_{dm2} - \alpha i_{dm1} - (1-\gamma)i_{dm3} \\
I_{DM3} &= i_{dm3} - (1-\alpha)i_{dm1} - (1-\beta)i_{dm2}
\end{aligned}
\tag{6.4}
$$

Once again this definition, for a balanced three-phase system, reduces to:

$$
\begin{aligned}
\alpha = \beta = \gamma &= \tfrac{1}{2} \\
\therefore I_{DM1} &= i_{dm1} - \tfrac{1}{2}i_{dm2} - \tfrac{1}{2}i_{dm3} \\
\therefore I_{DM2} &= i_{dm2} - \tfrac{1}{2}i_{dm1} - \tfrac{1}{2}i_{dm3} \\
\therefore I_{DM3} &= i_{dm3} - \tfrac{1}{2}i_{dm1} - \tfrac{1}{2}i_{dm2}
\end{aligned}
\tag{6.5}
$$

Equations (6.2) and (6.4) can be combined to find the total line currents, I_1, I_2, and I_3.

$$I_1 = I_{CM1} + I_{DM1} = ai_{cm} + i_{dm1} - \beta i_{dm2} - \gamma i_{dm3}$$

$$I_2 = I_{CM2} + I_{DM2} = bi_{cm} + i_{dm2} - \alpha i_{dm1} - (1-\gamma) i_{dm3} \qquad (6.6)$$

$$I_3 = I_{CM3} + I_{DM3} = (1-(a+b)) i_{cm} + i_{dm3} - (1-\alpha) i_{dm1} - (1-\beta) i_{dm2}$$

The mathematical definition of these line currents was used to substantiate measurement procedures for both CM and DM currents.

6.2.2 CM current measurement

The CM current measurement was taken by feeding all three lines through the current probe simultaneously, as shown in Fig. 6.6. The current so measured, $I_{cm-meas}$, is equivalent to measuring the sum of the three line currents. As shown by considering equation (6.6) and (6.7), such a summation reduces to the total CM current of the system due to the fact that the DM current components cancel one another out.

$$I_{cm-meas} = I_1 + I_2 + I_3 = i_{cm} \qquad (6.7)$$

This result is obtained regardless as to whether or not the system is balanced.
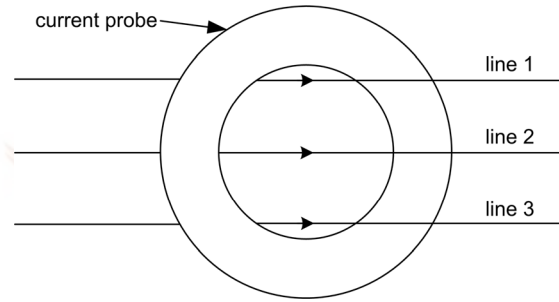
Fig. 6.6: Schematic representation of the measurement procedure used to measure CM current

6.2.3 DM current measurement

As shown in equation (6.6), the line currents constitute a CM current component and a DM current component. Various techniques exist to separate these components for the purposes of measurement in a three-phase system [29]. However, many of these methods require numerical treatment of the measured data, detailed models of the system and/or the construction of either active or passive separator circuits to be introduced into the system. Generally these techniques have been developed to produce well-defined CM and DM current measurements for the purposes of evaluating devices for EMI emissions, according to the EMI standards. As in the case of the experimental setup, the comparative nature of the measurements did not justify going to great lengths to obtain such a DM current measurement. Instead, a measurement procedure to obtain an indication of the DM current components was developed that merely involved looping the various lines of the system through the current probe in a particular order.

Fig. 6.7 shows the measurement procedure used to obtain a measurement of the DM current component in line 1. The justification of this measurement procedure can best be shown by considering a balanced system, where the CM and DM current

components are given by equations (6.3) and (6.5) respectively. In such a case, the current measured using the setup of Fig. 6.6 is given by equation (6.8).
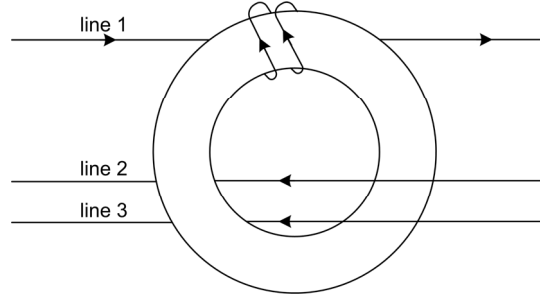
Fig. 6.7: Schematic representation of the measurement procedure used to measure DM current in line 1

$$
\begin{aligned}
I_{dm-meas1} &= 2I_1 - I_2 - I_3 \\
&= 3i_{dm1} - \frac{3}{2}i_{dm2} - \frac{3}{2}i_{dm2} \\
&= 3I_{DM1}
\end{aligned}
\tag{6.8}
$$

The CM current component is seen to be eliminated entirely from the measurement. The DM current can then be obtained from the measured result through a simple scaling in amplitude. Similarly, a measurement of the DM current components for lines 2 and 3 can also be obtained.

However, as mentioned earlier, in a practical setup, there are usually asymmetries present that cause an imbalance in the system. The measurements obtained, for each of the three lines, in the event of an unbalanced system, are given in equations (6.9) through (6.11), as found using equation (6.6).

$$
\begin{aligned}
I_{dm-meas1} &= 2I_1 - I_2 - I_3 \\
&= (3a-1)i_{cm} + 3(i_{dm1} - \beta i_{dm2} - \gamma i_{dm3}) \\
&= (3a-1)i_{cm} + 3I_{DM1}
\end{aligned}
\tag{6.9}
$$

$$
\begin{aligned}
I_{dm-meas2} &= 2I_2 - I_1 - I_3 \\
&= (3b-1)i_{cm} + 3(i_{dm2} - \alpha i_{dm1} - (1-\gamma)i_{dm3}) \\
&= (3b-1)i_{cm} + 3I_{DM2}
\end{aligned}
\tag{6.10}
$$

$$
\begin{aligned}
I_{dm-meas3} &= 2I_3 - I_1 - I_2 \\
&= (2-3(a+b))i_{cm} + 3(i_{dm3} - (1-\alpha)i_{dm1} - (1-\beta)i_{dm2}) \\
&= (2-3(a+b))i_{cm} + 3I_{DM3}
\end{aligned}
\tag{6.11}
$$

From the above equations it can be seen that the DM current measurement, for each line, reduces to the DM current component of the respective line combined with a portion of the CM current. In the event that the system is not balanced, this measurement procedure may not produce a true DM current measurement. Consequently, the system itself had to be further investigated to validate the use of this measurement procedure.

6.3   Experimental results

Before the integrated filter performance could be evaluated it was first necessary to characterise the test bench through a series of measurements. The experimental setup used for this purpose was identical, to the setup used for the filters, in every way except one. This difference was the omission of the filters from the setup. Instead, the inverter was connected directly to the motor.

6.3.1 Test bench characterisation

The CM current was first measured relative to the noise floor. The noise floor was defined as the current measurement when both the inverter and the DC bus were turned off. In so doing, the noise spectrum that was to be suppressed by the filter was clearly seen. The measured result is shown in Fig. 6.8.
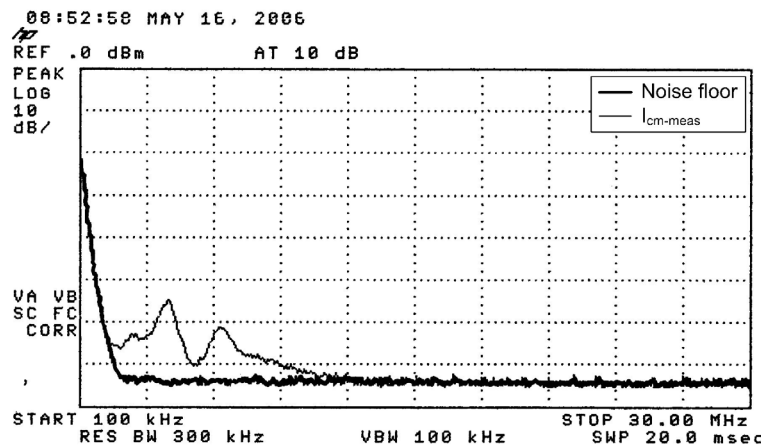
Fig. 6.8: CM current measurement performed in the absence of a filter, as compared to the noise floor

As already mentioned, the DM current measurement procedure proposed in section 6.2.3, yields a true measurement of the DM current in the event that the system is balanced. However, this is generally not the case with a PWM source. Consequently the test bench was further investigated to determine whether or not this measurement procedure could be used in the filter performance analysis.

To this end the DM current was measured for all three lines of the setup, using the described measurement procedure, as compared to the noise floor. The results are shown in Fig. 6.9. From these figures it can be seen that the DM current measurement on all three lines yielded nearly identical results. This however, was not an indication of a symmetric system. It is possible that values of a, b, α, β and γ, might exist such that the three measurements of equations (6.9) through (6.11) yield identical results, even though the system is not symmetric. However, if these measurements did not yield identical results, it would unarguably indicate that the system was asymmetric. Fortunately, this is was not found to be the case.

As a result the test bench had to be further investigated. This was done by comparing the DM current component measurements already obtained with a line current measurement. The line current measurement was performed by passing the relevant line through the current probe three times, in the same direction. The measurement thus obtained, as applied to line 1, is mathematically represented by equation (6.12).
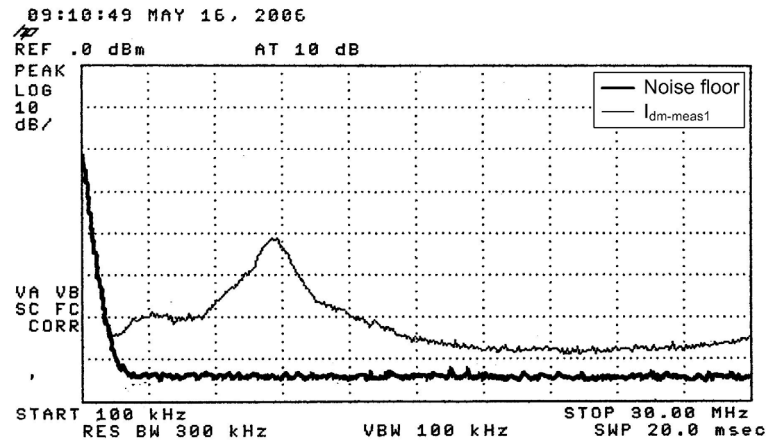
(a)
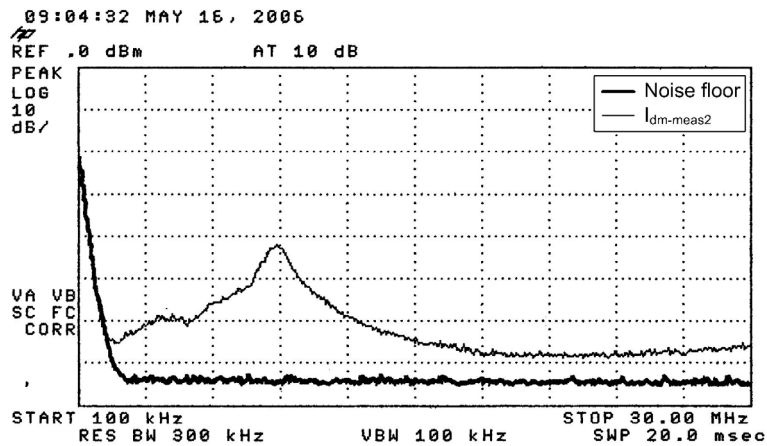
(b)
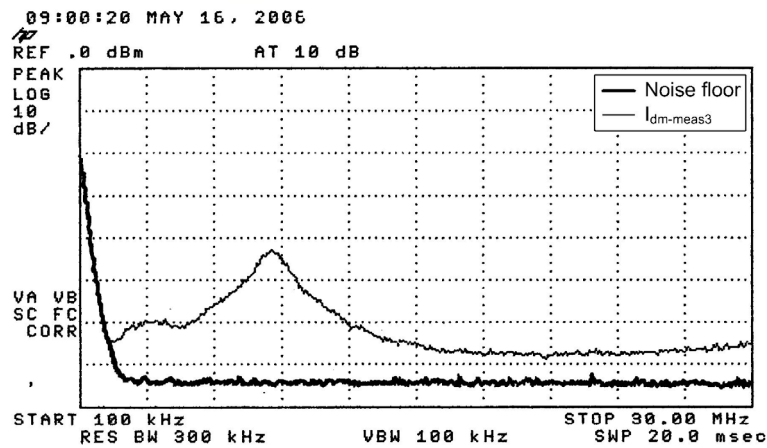
(c)

Fig. 6.9: DM current measurement performed in the absence of a filter, as compared to the noise floor, for (a) line 1, (b) line 2 and (c) line 3

$$I_{1-meas} = 3I_{CM1} + 3I_{DM1} = 3I_1 \qquad (6.12)$$

These measured results for all three lines can be found in Fig. 6.10. From the figures it can be seen that, by using the DM current measurement discussed in section 6.2.3, a current peak is eliminated, that is present in the line current measurement. Further examination of this peak shows it to occur at the same frequency as the first peak of the CM current shown in Fig. 6.8. This was seen to be the case for all three lines.

110

(a)

(b)

(c)
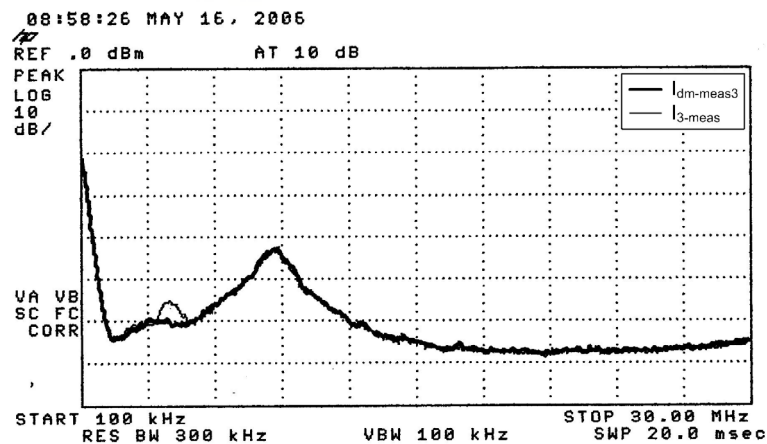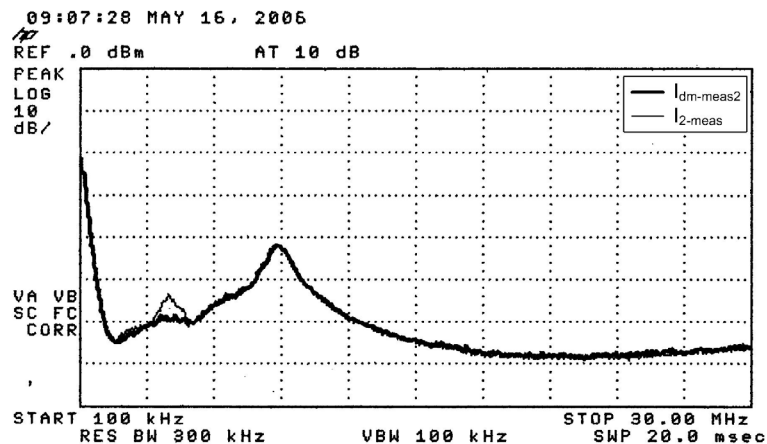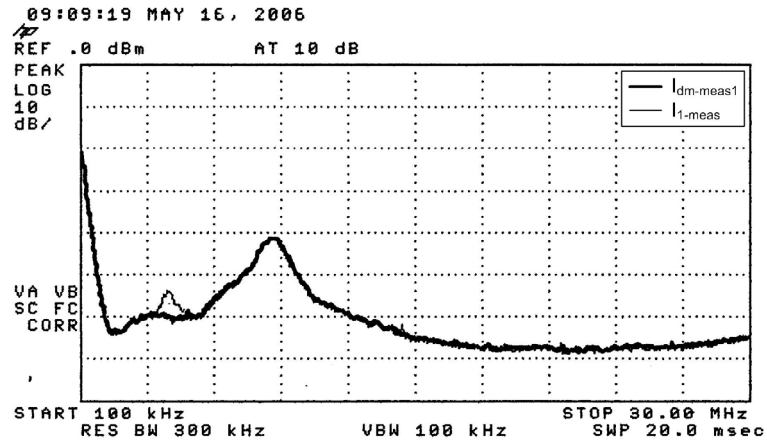
Fig. 6.10: DM current measurement performed in the absence of a filter, as compared to the line current measurement, for (a) line 1, (b) line 2 and (c) line 3

From these observations it was concluded that although it was not known whether or not the system was symmetrical, the DM current measurement eliminated at least some of the CM current, as seen through the suppression of the current peak. As a result, the measured current spectrum was taken as a measurement of predominantly DM current. Due to the comparative nature of the results later obtained, this was seen to be an adequate measurement procedure for the determination of the filter performance in the presence of DM noise.

The measurements discussed here were taken when the filter was omitted from the experimental setup. Through the introduction of the filter into the setup it is possible that asymmetries, which were not previously present in the three-phase system, could be introduced. However, due to the geometrical symmetry of the IPPMs used to realise the filters, the introduction of any such asymmetries was expected to be limited. In most of the measured results, with the filters present, the CM and DM currents were seen to be suppressed. Hence, even if asymmetries were introduced, the presence of the filters was still seen to lessen the HF noise seen by the motor when the filters were absent.

6.3.2 Integrated three-phase EMI filter results

The single-turn IPPMs discussed in Chapter 5 were used to realise the two filter-units found at the end of Chapter 4, which are shown again in Fig. 6.11 for ease of reference. These filter-units were each used to realise four EMI filters through implementation of the topologies discussed in Chapter 4. The filter performance was investigated through comparative measurements of both the CM and DM currents.

Only the measured results of the DM current as found on one of the lines in the three-phase system is presented. DM current measurements were taken for all three lines but were seen to yield virtually identical results. In a few cases a slight deviation in peak values between the three measurements was seen, but this was attributed to the fact that peak measurements were taken instead of quasi-peak.
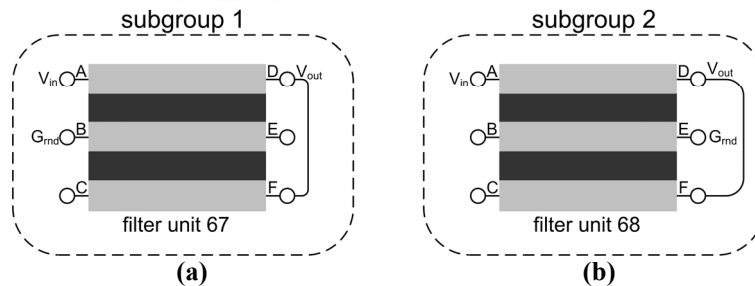
Fig. 6.11: The two filter-units to be experimentally investigated

Topology 1

Topology 1 was characterised by a star formation and the presence of magnetic coupling between the three filter-units. Table 6-I repeats the simulation results presented in Chapter 4, for ease of reference.

It was possible to implement topology 1 with three of the IPPMs discussed in Chapter 5, namely the vertically stacked, horizontally stacked and inherent star formation IPPMs. All three of these IPPMs were used to physically realise the EMI filters for both filter-units. The measured results for filter-unit 67 are tabulated in Table 6-II.

Table 6-I: Simulated results obtained for topology 1

Filter-unit	Common mode stimulus		Differential mode stimulus	
	Drop-off(dB/dec)	PB_r	Drop-off(dB/dec)	PB_r
67	-40	0.999	-20	1.000
68	-40	0.999	-20	1.000

Table 6-II: Measured results obtained for the physical realisation of topology 1

Filter-unit	CM current measurement	DM current measurement for line 1
67		
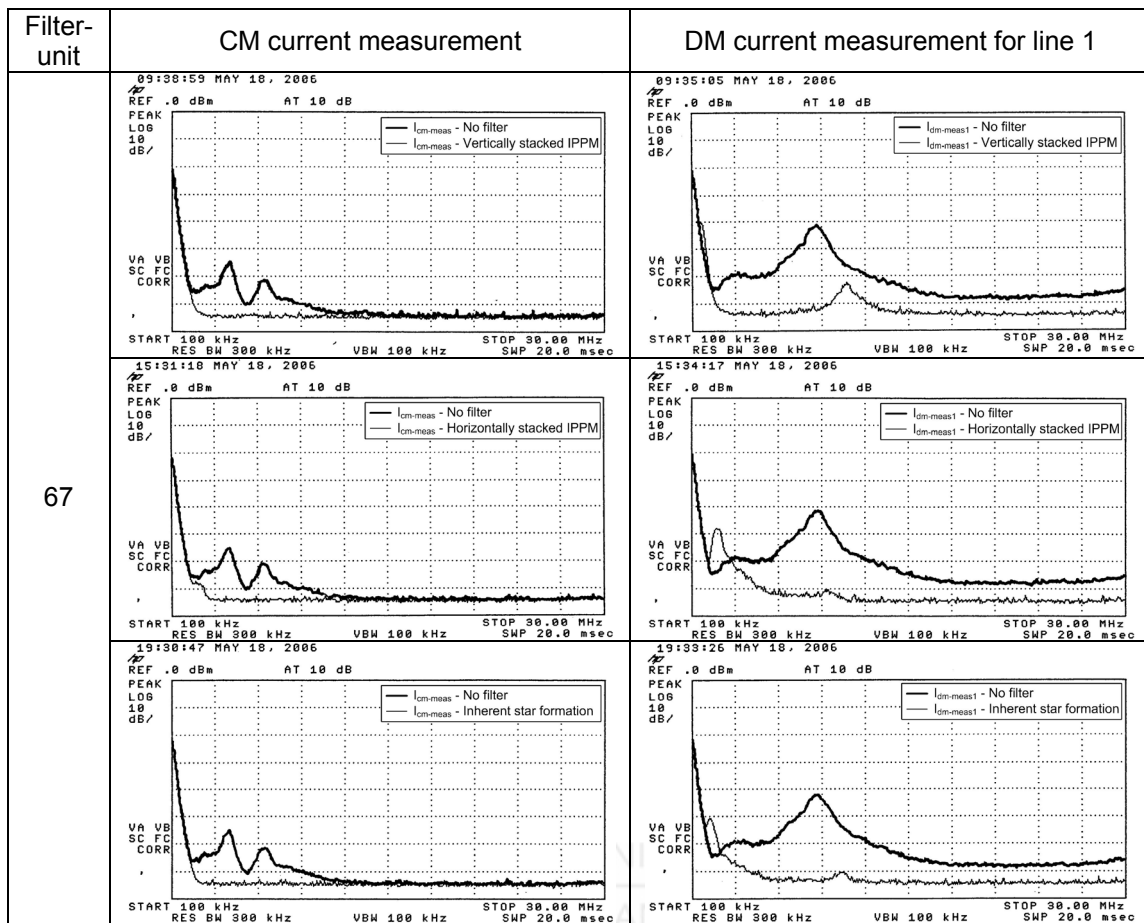
Earlier in this chapter a great deal of attention was given to the experimental setup, particularly in terms of grounding. Fig. 6.12 shows the DM current measurements for EMI filters realised with filter-unit 67 and either the vertically stacked IPPM or the inherent star formation IPPM. The only difference in the setup used for these measurements, and the measurements presented in Table 6-II, was the connection to ground from the filter-units. This connection could be considered to consist of two parts, firstly a connection between the filter-units to a common point used to realise a star formation, and secondly, a connection from the common point to the ground plane.

When considering the results obtained for the vertically stacked filter, the result of Fig. 6.12(a) and the tabulated result are seen to deviate greatly from one another. In the poor grounding case the length of the first part of the ground connection, to a common point, was considerably long. This was also true for the connection from the common point to the ground plane.

In Fig. 6.12(b) the deviation, between the poor grounding case with the inherent star formation IPPM and the tabulated result, is not as great as in the vertically stacked IPPM case. This can be attributed to the fact that the length of the interconnection from the filter-units to a common point was the shortest possible length that could be realised. However, some deviation still existed due to the length of the wire connecting this common point to the ground plane.

113

From these observations it can be seen that it was necessary to keep both parts of the ground connections as short as possible. If the length of the wire used for either of these connections was too long the voltage drop over the wire became significant enough to influence the measurements.

When considering topologies that realised a delta formation the same principle, where the interconnections between filter-units were kept as short as possible, was also applied. In so doing confidence was gained that the measured results were a true representation of the filters' performance. This principle was further extended to the interconnections within the filter-unit configurations as well.

These observations highlighted one of the benefits of inherently realising connections during the manufacturing stage of the IPPMs; namely the fact that the length of interconnections will be the shortest possible length that can be practically realised.
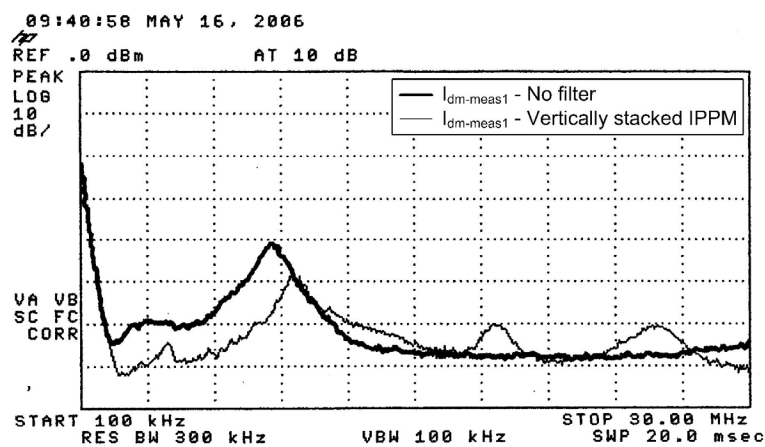
(a)
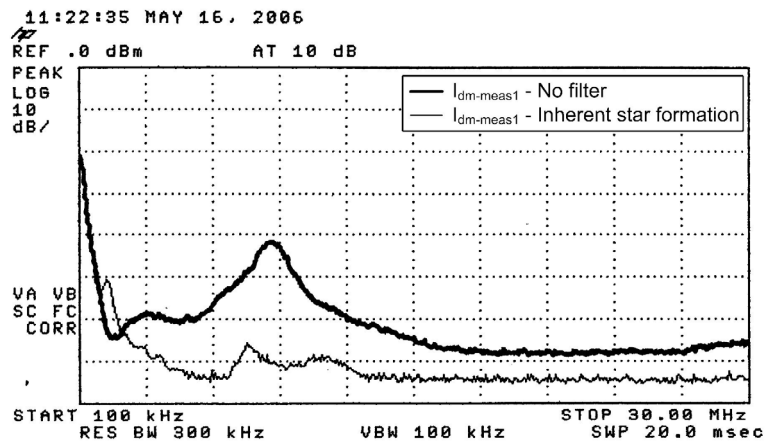
(b)

Fig. 6.12: DM current measurement taken with poor grounding technique for an EMI filter realisation utilising (a) the vertically stacked IPPM and (b) the inherent star formation IPPM

As already mentioned, only the measured results of filter-unit 67 are shown in Table 6-II. This is due to the fact that filter-unit 68 was found to yield similar results, which are included in Appendix E. This similarity in practical measurements corresponded with the simulation prediction where filter-units 67 and 68 had the same drop-off and pass-band values for both CM and DM stimuli. Further comparison between the measured and simulated results also indicated that the quasi-distributed

114

model did correctly predict the fact that these filter-units could be used to realise a three-phase EMI filter.

When considering only the CM current measurements it was seen that the filters suppressed virtually all of the CM current. Not only this, but virtually identical performance was achieved using the three different IPPMs.

In the case of the DM current most of the noise was suppressed. When the coupling between the filter-units is ideal, the DM signals will not see the CM inductance. However, in a practical setup the coupling between the filter-units would not be ideal. Consequently, the leakage inductance would serve as DM inductance that contributed to the suppression of the DM current.

Some deviation between the results obtained with the three different IPPMs was seen for the DM current measurements. This can be seen through the introduction of a resonant peak at the lower frequencies in the results obtained with the horizontally stacked and the inherent star formation IPPMs. In contrast, this peak was not present in the results of the vertically stacked IPPM. Most likely this peak was related to the capacitive coupling between the filter-units. This coupling would vary between the three IPPMs due to the difference in geometric placement of the filter-units with respect to one another.

From this investigation it was seen that a number of different practical implementations could be used to realise the same EMI filter. The results of each of these implementations would vary depending on the capacitive and magnetic couplings realised within the structures. However, the general trend, as to whether or not the EMI filter would indeed suppress the conducted EMI noise was the same.

Lastly, a comparison of the results obtained with the horizontally stacked IPPM and the inherent star formation IPPM shows that the two structures yielded near identical results. As the latter structure was considerably easier to manufacture it would seem that further investigation into the inherent realisation of connections, during the manufacturing of the IPPMs, is a feasible research direction.

Topology 2

Topology 2 consisted of a star formation and no coupling between the filter-units. Once again the simulated results are repeated in Table 6-III. For the practical implementation of these filters only the single 3-layer IPPMs could be used. The relevant filter performance measurements for filter-unit 67 can be found in Table 6-IV.

Table 6-III: Simulated results obtained for topology 2

Filter-unit	Common mode stimulus		Differential mode stimulus	
	Drop-off(dB/dec)	PB_r	Drop-off(dB/dec)	PB_r
67	-40	0.999	-40	1.000
68	-40	1.000	-40	1.000

Table 6-IV: Measured results obtained for the physical realisation of topology 2

Filter-unit	CM current measurement	DM current measurement for line 1
67		
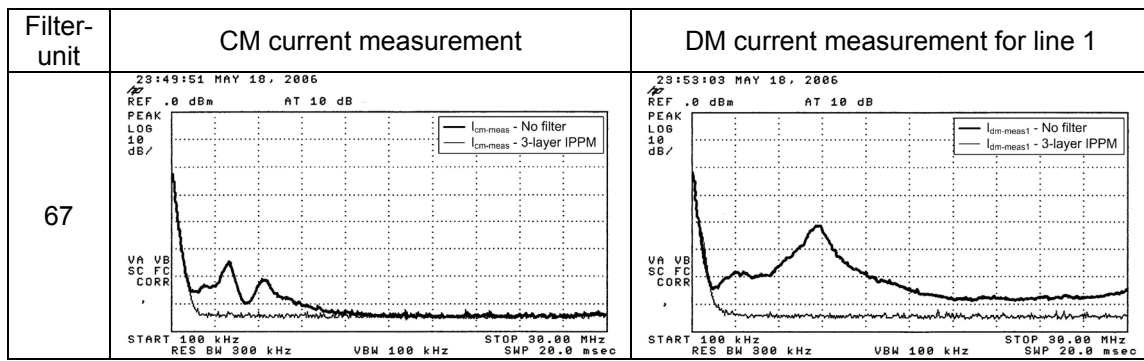
As in the previous section, only the results of filter-unit 67 are shown. This is due to the fact that, as predicted by the simulation, the results obtained by the two filter-units were comparable. The measurement results of filter-unit 68 can be found in Appendix E. The simulation results were once again seen to correctly predict the realisation of an EMI filter.

Significant suppression of both the CM and DM currents was seen.

Even though the filter-units of this topology were not supposed to be coupled with one another, some degree of coupling would exist in a practical setup. This coupling would lend itself to the suppression of the CM current as the coupling would manifest itself in the formation of CM inductance. Furthermore, CM signals do see impedance due to DM inductance, albeit the magnitude of this impedance is less than that seen by DM signals. (A discussion of CM and DM impedance can be found in Appendix B.) The excellent suppression of the CM current can be attributed to the CM impedance realised in the presence and absence of coupling, as well as the capacitance of the filter-units.

In the case of the DM current virtually all of the noise was suppressed and no resonant peaks were introduced.

Topology 3

The filter-units of topology 3 were connected in delta formation and magnetically together. The simulated results of this topology can be found in Table 6-V and the results of the practical setup, realised with both the vertically stacked and horizontally stacked IPPMs, are shown in Table 6-VI.

Table 6-V: Simulated results obtained for topology 3

Filter-unit	Common mode stimulus		Differential mode stimulus	
	Drop-off(dB/dec)	PB_r	Drop-off(dB/dec)	PB_r
67	-	-	-20	1.000
68	-20	0.998	-20	1.000

Table 6-VI: Measured results obtained for the physical realisation of topology 3

Filter-unit	CM current measurement	DM current measurement for line 1
67		
68		
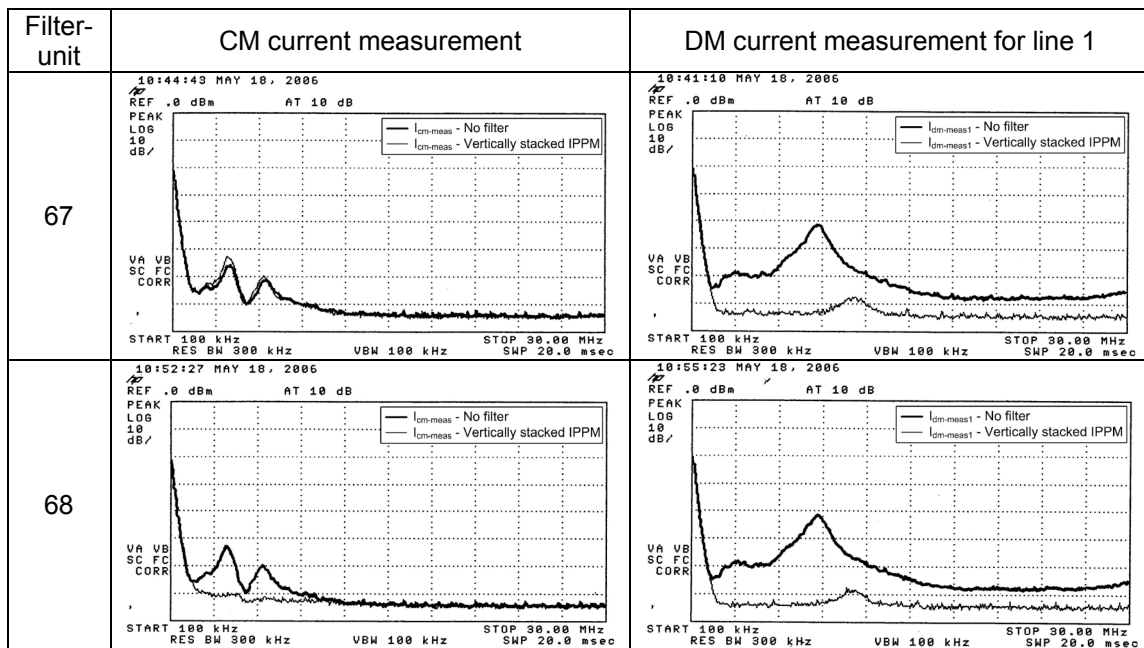
Inspection of Table 6-VI shows the presence of results for both filter-units. This corresponds with the fact that the simulated results for a CM stimulus were different for the two filter-units. Once again, the simulation was seen to be an accurate interpretation as to whether or not the topology realisation with a particular filter-unit was possible.

For filter-unit 67 the simulation results indicated that an EMI filter constructed using topology 3 would suppress DM noise but not CM noise. This fact was reflected in the experimental measurements where the DM current was greatly reduced by the presence of the filter, but no influence was seen on the CM current. These results were found using the vertically stacked IPPM. The results obtained with the aid of the horizontally stacked IPPM were similar and can be found in Appendix E.

The results of filter-unit 68 also showed an agreement with the simulation predictions. Once again similar results were obtained for both IPPM structures and as a result the measurements taken with the horizontally stacked IPPM have been moved to Appendix E.

As in the case of topology 1, it can be seen that different practical realisations of the same EMI filter are possible. Further comparison, between the DM current measurements of topologies 1 and 3, show that no resonant peaks were introduced by the filters realised with the horizontally stacked IPPM. The only difference between the two realisations of the EMI filters was the interconnection of the filter-units in either star or delta formation. This indicates that a manipulation of the capacitive coupling between the filter-units may be achieved by altering external connections. Furthermore, the variation in interconnections resulted in a change in the inductance of the interconnections. Consequently any coupling between the filter-units can be considered to have a dependence on both the geometric construction of the filter-units as well as the interconnections between the filter-units.

Topology 4

Topology 4 was characterised by a delta formation between the filter-units in the absence of magnetic coupling. Table 6-VII provides the simulation predictions for filter-units 67 and 68. As in the case of topology 2, only the 3-layer IPPMs could be used to physically realise the filters of topology 4. The measured results are shown in Table 6-VIII.

Table 6-VII: Simulated results obtained for topology 4

Filter-unit	Common mode stimulus		Differential mode stimulus	
	Drop-off(dB/dec)	PB_r	Drop-off(dB/dec)	PB_r
67	-	-	-	-
68	-20	0.996	-40	1.000

Table 6-VIII: Measured results obtained for the physical realisation of topology 4
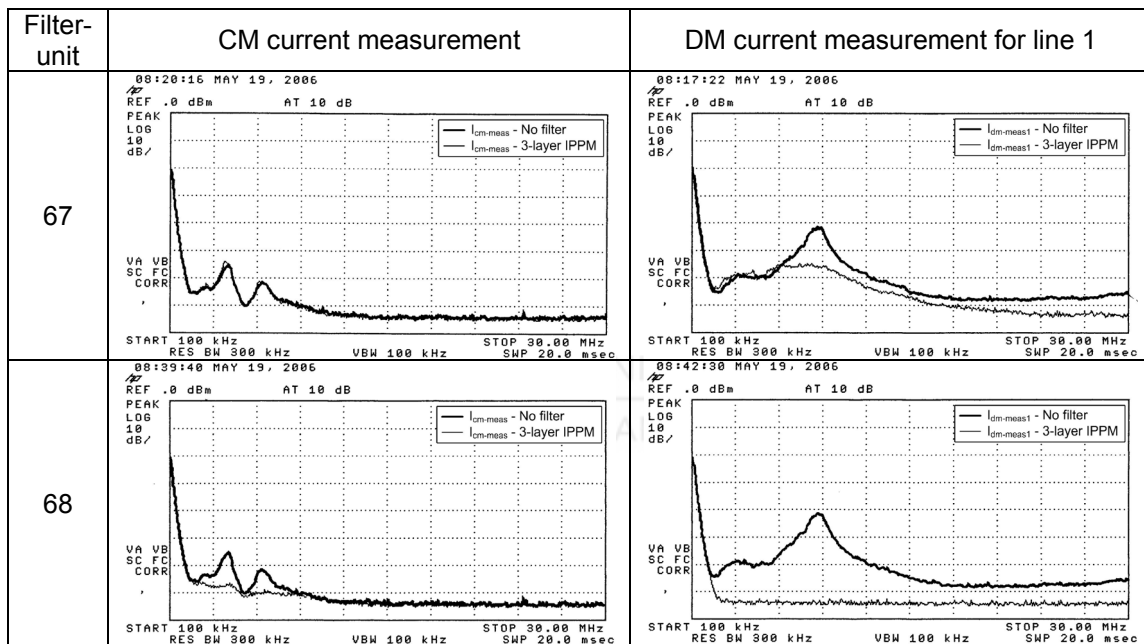
Once again the simulation was seen to correctly predict the behaviour of the EMI filter. The measured results of filter-unit 67 showed no suppression of the CM current and little suppression of the DM current. In contrast filter-unit 68 was seen to suppress both currents. However, even though the CM current was suppressed by filter-unit 68, better results were seen in CM current measurements of topologies 1 and 2.

The results presented in this section show that an integrated EMI filter is plausible. The filters presented here were only prototypes to prove the feasibility of the concept. However, through further research into the design of these structures it should be possible to realise integrated three-phase EMI filters for industrial applications.

6.4   Conclusion

The performance of the integrated filters was evaluated through comparative measurements of the CM and DM currents of the three-phase system, with and without the filters present. It was seen that for these measurements to be informative and repeatable care had to be taken in terms of how the experimental setup was realised and the actual measurement procedure.

The experimental setup made use of a Faraday cage in order to obtain a well-defined ground reference plane. Careful consideration was then given as to the grounding of both the experimental test bench and the measurement equipment. This was necessary as the return path of the CM current was through the ground plane.

In order to measure both CM and DM currents, the flow of these currents in a three-phase system was investigated. Two measurement procedures, one for CM current and another for DM current, were then discussed using the mathematical model developed for the two currents.

The test bench was characterised using these two measurement procedures to determine the CM and DM currents present in the system when the filters were absent from the setup. From this it was seen that the CM current could readily be measured. However, the exact interpretation of the measurement obtained by means of the DM current measurement procedure, was investigated. In the three-phase system, used for the experimental results of this study, it was seen that the measurement presented here was sufficient to use as an indication as to whether or not the integrated filters suppressed the DM current.

The topologies discussed in Chapter 4 were then physically realised using the IPPMs discussed in Chapter 5. The performance of these filters, as realised with two different filter-units, was evaluated by means of a CM and DM current measurement.

Through this investigation a number of features were highlighted. Firstly, the necessity for good grounding practice in the filter construction was shown. Poor grounding techniques led to incorrect and normally non-repeatable results.

It was also shown that it is indeed possible to integrate a three-phase EMI filter. The basic design of such a filter is possible with the quasi-distributed model discussed in this dissertation. This model was seen to give reliable predictions as to whether or not a particular filter-unit would indeed function as a three-phase EMI filter. However, no direct correlation, between the predicted drop-off value of the simulated filter and the suppression achieved with the practical instantiation of the filter, was observed. This could be attributed to a combination of a number of factors:

- In the simulation the frequency scale was logarithmic while a linear frequency scale was used in the measurements. Consequently, if the filters did respond differently, according to their predicted drop-off values, this difference would still have been almost indiscernible in the practical results.

- The measurement equipment had a noise floor that the measured results eventually levelled off at. The attenuation of the simulation results, however, continued indefinitely. This implies that in the practical measurements, the drop-off value of the filter response would only be valid for a small fre-

quency range. As a further consequence of the linear frequency scale it would be difficult to identify this frequency band.

- The drop-off value of the filters could be incorrectly predicted by the simulation. Most likely this fact would be a direct result of the omission of losses in the quasi-distributed model.

- A deviation from ideal magnetic coupling, between the filter-units and between the conductive layers of the filter-units, in a practical filter would probably influence the drop-off values as well.

In the discrete passive component filter introduced in Chapter 1 the CM and DM filters were two separate entities. Hybrids of these two filters have been investigated as in [11]. In this chapter all four topologies were shown to suppress both CM and DM currents with at least one of the two filter-units investigated. Consequently the EMI filters presented here can be considered an integration of passive components as well as CM and DM filters.

It was shown that the practical construction of these filters could be realised in a number of different ways. For instance, the vertically stacked and horizontally stacked IPPMs were in essence different realisations of the same thing. Through further investigation this fact could be exploited during the manufacturing process. In so doing, the cheapest, most efficient filter can be developed.

From the results presented in the previous section it can be seen that the filters realised with topology 2 yielded the best performance for both CM and DM currents. However, due to the non-coupled nature of this topology it is also one of the filters that use the most magnetic material. It would be beneficial to further investigate the filters realised with topology 1, as the results obtained for these filters were a close second to those of topology 2. Further advantages of realising filters with topology 1 include the utilisation of less magnetic material and ease of inherently realising connections such as the star formation.

CHAPTER 7

Conclusion and future work

The body of work presented in this dissertation could be divided into two main parts. These parts were seen to correspond with the investigation objectives presented in Chapter 1, namely:

- An investigation into the various configurations that can be realised with IPPMs and the resultant behavioural response obtained from these configurations.

- The design and construction of an integrated three-phase EMI filter. The practical analysis of such a structure served as an investigation into the feasibility of the integrated three-phase filter concept and, as a practical validation of the insight gained through the investigation of the first objective.

In this chapter, the conclusions drawn from each of the previous chapters are revisited. These conclusions are presented in context of the main dissertation objectives. At the end of the chapter possible future avenues of research of the integrated structures, which were brought to light through this study, are mentioned.

7.1   Conclusion

7.1.1 IPPM configuration investigation

To date, the use of IPPMs in any application has been based on the designers' past experience with the modules. No generalised theory or synthesis guidelines exist to aid the selection of configurations to be used for an application. Such guidelines would prove invaluable for a designer. Not only would it indicate the best direction to follow in the design process, but it would also lend itself towards a deeper understanding of the functionality of the IPPMs. Through this approach the possibilities as well as the limitations as to what is realisable with these structures should be readily identified.

In an attempt to build the foundations for such a set of guidelines, an exhaustive search of all possible configurations to be realised with an IPPM was performed. However, there are almost limitless possibilities in the nature and shape of the IPPMs. Consequently it was necessary to limit the scope of the investigation to a single IPPM structure. For this purpose a three-layer IPPM was decided upon.

In Chapter 2 the procedure used to perform the exhaustive search was discussed in detail. The first step was to identify the set of all possible configurations. Once the set of configurations was known, each configuration had to be simulated using a Spice type circuit simulation. The results obtained from these simulations were used in the analysis of the configuration behaviour.

In order to identify the set of all possible configurations it was first necessary to find a concise manner to hold the information about each configuration. Unfortunately, no such method was found through investigation into previous work on IPPMs. As a

result, a method to represent each configuration was developed using two matrices. These matrices were used to numerically generate the set of all configurations that it was possible for them to represent. However, in this set a number of the configurations were not of any value in a practical realisation of the IPPMs. As a result the IPPM structure and various configurations were further considered. In so doing criteria used to eliminate these impractical configurations were identified. This procedure was used to identify the set of all configurations for single-port and two-port networks.

A Spice type circuit simulation of each of these configurations was performed using a quasi-distributed model. From these simulations the frequency response of each configuration was extracted.

When considering the behaviour of a configuration it was seen that the transfer function concept could yield misleading results. Analysis of the simulation setup for each of the networks determined whether or not the transfer function was indeed misleading. As a result of this observation it was seen to be necessary to employ a different approach to the analysis of the single-port and two-port network results. However, regardless of the approach both networks were seen to realise LPFs, HPFs, BPFs, BSFs and a miscellaneous group of filter responses. From analysis of the configurations within each filter category general trends between the placement of the I/O connections and the filter response were highlighted. Specifically, HF and LF signal paths were seen to be inherent between the terminals of the IPPM. The placement of the I/O connections using these terminals was seen to utilise one, both or neither of these signal paths. These general trends will hopefully form the basis of the design guidelines that this research was attempting to uncover.

Chapter 3 dealt with a number of aspects of the integrated structures that the exhaustive search brought to light. These aspects contribute towards a better understanding of the functionality of the IPPMs as they often indicated the manner in which the dielectric layers of the IPPM were utilised.

It was seen to be possible to manipulate the voltage gradient across a conductive layer of the IPPM. As a direct consequence of the magnetic coupling between the various layers, any alteration made in the voltage gradient of one conductive layer was reflected in all conductive layers. A few types of interconnections: cross-connections, shorting-connections and vertical-connections, were identified. The influences that these connections have, on the voltage gradient across an IPPM and the absolute potential of the terminals, were illustrated. Specifically, the cross-connection was seen to cause two opposite-side terminals to take on the same absolute potential. The shorting-connection performed the same function as the cross-connection as well as forcing the voltage gradient to zero. Lastly, the vertical-connection influenced the absolute potential of two same-side terminals causing them to take on the same value. These connections were seen to be responsible for the type of filter behaviour obtained from certain configurations.

Particular attention was paid to the vertical-connection. The manner in which this connection influenced the utilisation of the dielectric was discussed. Depending on the exact placement of the vertical-connection the dielectric layers were either underutilised or efficiently utilised. The former case was achieved when the vertical-connection was placed on vertically adjacent layers, while the interconnection of

vertically non-adjacent layers with a vertical-connection was seen to realise the latter case. The exact location of the vertical-connection, in terms of which side of the IPPM structure the connection was placed, was found to be irrelevant.

A number of methods to manipulate the configurations, without causing a change in the behaviour of the configuration were presented. These methods included the repositioning of layers, without breaking any of the interconnections of the configurations. Such a procedure caused a shift in the cut-off frequency of the filter behaviour. The relocation of I/O connections in the presence of floating layers was also seen to have no influence on the behaviour of the configuration. Lastly it was seen that an IPPM structure with less layers could be used to realise the same response if the dielectric layers of the original structure were not utilised.

A final aspect, namely that of the dominant configuration, was considered as a means of highlighting a trend that was seen during the exhaustive search. However, other than the fact that the existence of this trend was evident, not much more can currently be said about it without further research.

All of the aspects that were dealt with did not necessarily point to a single design solution when considered separately. However, in the context of configuration design and implementation, knowledge of these aspects should aid the decisions of the designer. Some of these aspects would indicate a preferable path for the design to follow while others indicate paths to avoid.

7.1.2 Integrated three-phase EMI filter

Previous research and implementations of integrated passive technologies have been single-phase in nature. In any field of research it is always necessary to identify and investigate previously unexplored research directions. To this end it was decided to investigate the design and implementation of an integrated passive in a three-phase system. Consequently a passive three-phase EMI filter, used in a variable speed induction motor drive application, was selected as a candidate for integration.

The design process, discussed in this dissertation, which was used to realise the filter was based on the results of the exhaustive search.

In Chapter 4 the configurations identified in Chapter 2 as LPF configurations were isolated and further investigated. However, the configurations considered here were single-phase applications of the IPPM structures. In order to realise a three-phase integrated structure it was necessary to form a bridge by which the single-phase applications could be incorporated into a three-phase system.

The approach used in this dissertation involved the introduction of the concept of a filter-unit. Due to the symmetry of the three-phase application it was reasonable to assume that a three-phase application could be reduced to an equivalent single-phase implementation. The filter-unit concept was based on this assumption where the single-phase application was merely expanded to the three-phase application. It is possible that different approaches may be used whereby the integrated structures are considered as a three-phase entity without having a single-phase counterpart. Such an approach, however, is left for future work.

In this study a set of three identical filter-units were interconnected in one of four possible topologies. In so doing a three-phase filter implementation of the IPPMs was realised. Each of the three-phase filters was simulated and the results further analysed. As in the single-phase case presented in the exhaustive search, the behaviour of the three-phase filters could be attributed to the presence of HF and LF signal paths. However, these paths were now not only present within the IPPM structures, but between the filter-units as well. The observed filter behaviour in response to CM and DM stimuli was seen to be dependent on these paths.

A group of filter-units, that was seen to correspond with one of the groups of two-port network LPF configurations, was identified as yielding the most promising three-phase filter results. The configurations of these filter-units were investigated. Through application of many of the aspects highlighted by the exhaustive search, it was possible to isolate two filter-units from this group that were to be used in the practical realisation of an integrated three-phase EMI filter.

The integrated three-phase filter designed in Chapter 4 was practically constructed. Such a realisation of the filter would allow the feasibility of actually implementing such a structure to be investigated. Through this investigation the results of the exhaustive search could be practically validated. However, in order to perform such an analysis it was necessary to obtain a test bench for the three-phase filters. The voltage and frequency rating of such a test bench were determined by the materials used to realise the integrated filters.

In Chapter 5 the material limitations of the embedded capacitor material, C-Ply, that was used in the construction of the filters, was discussed. It was found that the breakdown voltage of the material was unpredictably low, depending on how the material was handled during processing. So as to avoid any complications introduced, through the material experiencing breakdown under operating conditions, it was decided to implement a low voltage application of the filters. Furthermore, the energy storage capability of the C-Ply material was limited. This implied that the cut-off frequency of the filters would be in the order of a few hundred kHz. Due to these specifications the test bench could not be constructed using commercially available inverters and motors. Consequently a low voltage induction motor was obtained and a HF inverter was designed and constructed. In the event that the integrated three-phase filters are to be used in an industrial application, the required voltage and frequency rating could be obtained through a combination of, improved processing techniques and, the use of materials with a higher relative permittivity.

A number of IPPMs were constructed to be used in the realisation of the three-phase filters. The design of the IPPMs was dependent on the topology of the final three-phase filter. Furthermore, all of these IPPMs were single-turn in nature due to the fact that the quasi-distributed model used to simulate the IPPMs was only applicable to a single-turn realisation of the modules.

Once the test bench and the three-phase filters had been constructed, it was still necessary to give careful consideration to the experimental setup and the measurement procedure to be used during the investigation. This was necessary to ensure that the measurements were well-defined, repeatable and correctly interpreted. Chapter 6 gives careful consideration to these points.

Care was taken during the layout of the experimental setup with respect to ground connections. This was necessary as CM currents are known to use the ground path as a return path.

The measurement procedure of both CM and DM currents was investigated with the aid of a mathematical model of the instantaneous currents. The procedure described for the CM current was seen to yield good results regardless as to whether or not the three-phase system was balanced. In contrast, the measurement procedure proposed for DM currents yielded good results for a balanced system. As a PWM inverter is normally not balanced the test bench was characterised using the measurement procedures. From this characterisation it was seen that the DM current measurement gave a good indication of the DM current in the system.

Comparative measurements of the CM and DM currents present in the three-phase system, with and without the presence of the filters, were then used to evaluate the filter performance.

From these measurements it was seen that the quasi-distributed model correctly predicted the behaviour of the three-phase filters in the presence of both CM and DM noise. Namely, if the model suggested that the filter-unit and topology combination would not yield a functional three-phase EMI filter, the measurements showed the failure of the filter to suppress the relevant EMI noise. Conversely, if the simulation predicted that the noise would be suppressed, the measured results indicated a substantial drop in the noise.

The various IPPM structures, which had been developed for the magnetically coupled filter-units, illustrated that it was possible to realise the integrated filters in a number of different ways. Only slight differences were observed in the measured responses. It was also seen that the inherent realisation of connections during the IPPM design stage was not only feasible, but preferable. Such connections limited problems introduced through poor grounding and interconnection inductance attributed to the length of the interconnection wires.

Through these results it was shown that the concept of an integrated three-phase EMI filter was indeed feasible. Furthermore, the fact that the measured filter responses corresponded with the simulation predictions served as validation of the design procedure. This procedure was a direct result of the exhaustive search, in terms of the identification of LPF configurations and the IPPM aspects highlighted by the exhaustive search.

7.2 Future work

During the course of this investigation a number of aspects were brought to light that would benefit from further research. These aspects can be discussed in three separate sections: simulation of IPPMs; IPPM theory development; and practical implementation of IPPMs.

7.2.1 Simulation of IPPMs

The quasi-distributed model considered in this study was limited to a single-turn application of the IPPMs. However, it is intuitive that the inductance of these struc-

tures can be greatly increased through the realisation of multi-turn IPPM structures. Such an increase in inductance would be advantageous in filter design as it would result in a reduction of the cut-off frequency. To this end the development of a multi-turn, multi-layer IPPM models would be beneficial in the construction of such filters.

The current model, as well as any multi-turn models set aside for future work, would themselves benefit from the incorporation of losses into the model. A number of losses occur within the IPPM structures, such as:

- HF losses due to skin and proximity effects within the IPPM structure.

- Hysterisis losses in the E-core.

- Losses attributed to saturation of the E-core.

7.2.2 IPPM theory development

As already mentioned, no general configuration design guidelines for IPPM structures exist. The results of the exhaustive search performed in this study could serve as a foundation for the development of just such a set of guidelines. To this end the general trends noted in Chapters 2 and 3, as well as the dominant configuration concept, would need to be further explored and presented in a structured guideline format. A result of such a set of guidelines would enable future configuration design to be performed, without the aid of previous experience with the structures, or the necessity of an exhaustive investigation.

Any guidelines developed on the basis of the exhaustive search presented in this study would be specific to a three-layer IPPM structure. The extrapolation of these guidelines to multi-layered IPPM structures would result in a more complete integrated passive theory.

Furthermore, the exhaustive search was performed on single-phase applications of the IPPMs. It was however shown that the single-phase applications could be expanded to a three-phase application with the aid of the filter-unit concept. This implies some sort of correlation between single-phase and three-phase IPPM implementations. Further investigation into the exact nature of this correlation, particularly from the perspective of design principles or guidelines, would be beneficial. This may in turn result in a various three-phase implementations of the IPPMs without the filter-unit concept.

The design guidelines, suggested thus far for either single-phase or three-phase applications, have been based on the observation of general trends that the configurations were seen to display. A more in depth analysis of the IPPMs in terms of their actual electromagnetic structure and behaviour is still needed. Such a study would be of great benefit in the three-phase implementation of the IPPM structures.

Fig. 7.1 shows the simulated output voltage response to a CM stimulus when filter-units 67 and 68 were used to realise topology 1. Although the drop-off and pass-band values of the two filters were found to be identical their behaviour was seen to deviate somewhat. The reasons for this sort of behavioural deviation most likely lie hidden in the electromagnetic nature of the structures.
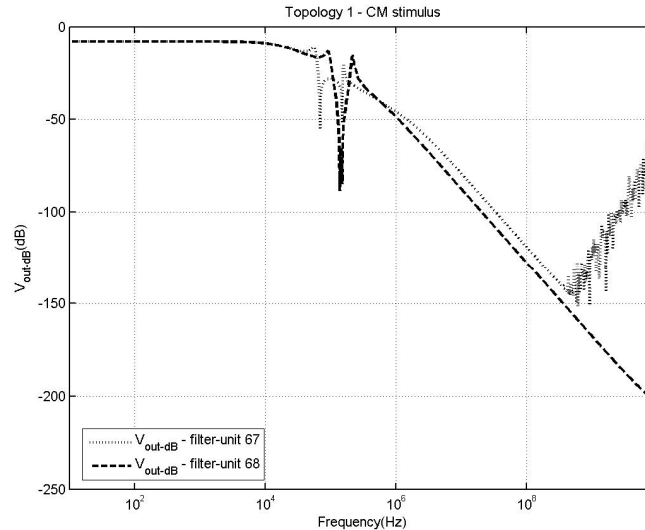
Fig. 7.1: Output voltage response of topology 1, as realised with filter-units 67 and 68, due to a CM stimulus

7.2.3 Practical implementation of IPPMs

In order to harness any advancement in the theory behind integrated structures, a practical implementation of these structures must be realised. Consequently research performed into the technology behind the construction of the IPPMs would be beneficial to the field. To this end a number of factors stand out that require attention.

Firstly, the actual construction process used for the IPPMs needs to be better refined. This would involve the development of better manufacturing techniques in terms of actually building a multi-layered structure. Present techniques are cumbersome and do not readily lend themselves to the realisation of structures with more than three conductive layers. Further complications are introduced if multi-turn structures are to be developed.

Secondly, a well-defined, easily implemented, reliable method of introducing contacts onto the terminals of the IPPMs also needs much consideration. This would be closely related to the inherent realisation of connections within the IPPMs. Both these factors would be beneficial as the robustness of the IPPM structures would hopefully be improved as compared to its current state.

Beyond the manufacturing procedures, the actual geometric design of the structures needs further investigation. Through small alterations of this design the magnetic and capacitive coupling between multiple IPPMs, as in the case of the filter-units, can be changed. The type of geometric differences that are responsible for certain changes need to be identified. In so doing it may be possible to manipulate features such as the degree of magnetic or capacitive coupling present between filter-units. This would have a direct influence on the response of the filters. If the nature of this influence can be predicted it would eventually result in the improvement of filter performance.

APPENDIX A

Interpretation of transfer functions through the use of circuit analysis
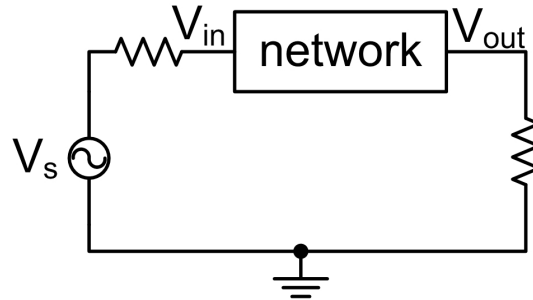
Fig. A.1: Conventional layout of a network used to determine a transfer function

When considering a standard network, as shown in Fig. A.1, the traditional transfer function is defined as the ratio given in equation (A.1).

$$H(\omega) = \frac{V_{out}}{V_{in}} \tag{A.1}$$

This transfer function describes the behaviour of only the network in the frequency domain. No consideration is given to the source driving the network. However, the definition of the traditional transfer function can be slightly modified to include the influence of the network on the source voltage seen at its input terminal. This gives rise to a system transfer function given in equation (A.2).

$$H_{sys}(\omega) = \frac{V_{out}}{V_s} \tag{A.2}$$

It should be noted that the source seen by the network in Fig. A.1 was a non-ideal source due to the presence of the source impedance. This impedance was considered to be purely resistive for simplicity.

Circuit analysis methods can be applied to a network to obtain a closed form solution of $H(\omega)$ and $H_{sys}(\omega)$. In the event that the magnitude of V_{in} varies, the two transfer functions will yield vastly different results. However, if the two transfer functions yield similar results the source is not greatly influenced by the network. This implies that the chances of a misleading transfer function interpretation are limited. These concepts were illustrated by means of a case study.

A.1 Case study

This procedure was applied to the arbitrary two-port network configuration shown in Fig. 2.16 of Chapter 2.

The quasi-distributed model of the configuration was simplified so that circuit analysis could be utilised. The simplified model was based on a single cell of the original model and is shown in Fig. A.2.
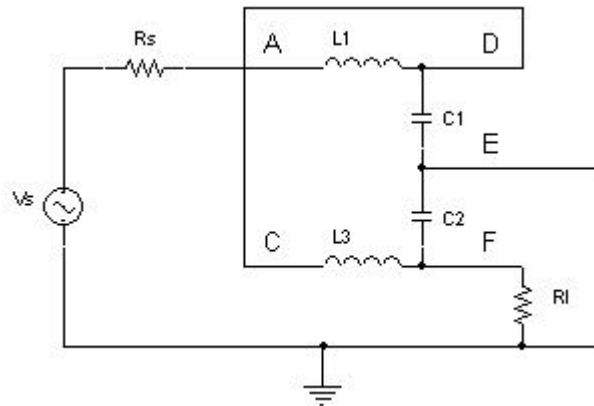
Fig. A.2: Simplified quasi-distributed model used for circuit analysis

In the simplified model, all the resistors of the cell were removed. This would not influence the behaviour of the configuration to any great degree as these resistors were only used to ensure the convergence of the numerical methods utilised in the simulation. Inductors L_1 and L_3 were kept, while inductor L_2 was omitted. The justification for such a step was due to the fact the middle conductive layer of the configuration was only connected at one terminal, i.e. terminal E. The absolute value on terminal B was consequently floating and did not influence the behaviour of the IPPM; rather, the behaviour of the IPPM would determine the absolute voltage seen at terminal B. The coupling between the two remaining inductors was given by the coupling coefficient C_o. The inductors were taken to have a mutual inductance, M, such that:

$$M = C_o L \qquad\qquad (A.3)$$

The variable, L, represents the self inductance of the two inductors. The inductance of L_1 and L_3, was considered to be the same due to the fact that in a physical realisation of this IPPM, the geometries of all three conductive layers would be identical. As a result, the inductance of each layer would be the same. Circuit analysis was then performed on the simplified model to find the closed form solutions of the transfer functions. Fig. A.3 shows the simplified model of Fig. A.2 as was used during the circuit analysis for both transfer functions. The only difference between the two figures is that the layout of the circuit was slightly altered in the latter case.
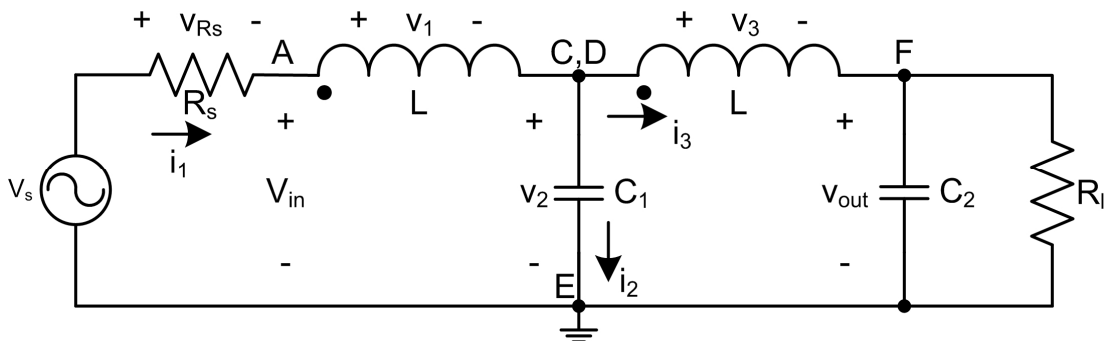
Fig. A.3: The simplified model of Fig. A.2 redrawn with a different layout

A.2 Derivation of the traditional transfer function, $H(\omega)$

The closed form solution of the transfer function was used through application of Laplace analysis of the circuit.

Firstly, the Laplace transformation of the capacitive impedances in the circuit was found:

$$Z_{C_1} = \frac{1}{sC_1} \tag{A.4}$$

$$Z_{C_2} = \frac{1}{sC_2} \tag{A.5}$$

The equivalent impedance of the parallel combination of C_2 and R_l was then found:

$$Z_{R_l // C_2} = \frac{R_l\left(\dfrac{1}{sC_2}\right)}{R_l + \dfrac{1}{sC_2}} = \frac{R_l}{R_l C_2 s + 1} \tag{A.6}$$

Using Ohm's law the current $i_3(s)$ was found.

$$i_3(s) = \frac{V_{out}(s)}{Z_{R_l // C_2}} = \frac{V_{out}(s)}{R_l}\left(R_l C_2 s + 1\right) \tag{A.7}$$

Using first principles, the voltage drops, $v_1(t)$ and $v_3(t)$, across the inductors could be determined.

$$v_1(t) = L\frac{di_1(t)}{dt} + M\frac{di_3(t)}{dt} \tag{A.8}$$

$$v_3(t) = L\frac{di_3(t)}{dt} + M\frac{di_1(t)}{dt} \tag{A.9}$$

Taking the Laplace transform of equations (A.8) and (A.9) yields:

$$v_1(s) = s\left(Li_1(s) + Mi_3(s)\right) \tag{A.10}$$

$$v_3(s) = s\left(Li_3(s) + Mi_1(s)\right) \tag{A.11}$$

Applying Kirchoff's Voltage Law (KVL) to the circuit gives the following relation:

$$V_s(s) = v_{R_s}(s) + v_1(s) + v_3(s) + V_{out}(s) \tag{A.12}$$

However, it is possible to express the value of v_{R_s} in terms of V_s and V_{in}.

$$v_{R_s}(s) = V_s(s) - V_{in}(s) \tag{A.13}$$

Substituting equation (A.13) into equation (A.12) yields:

$$V_{in}(s) = v_1(s) + v_3(s) + V_{out}(s) \tag{A.14}$$

Equations (A.10) and (A.11) are then substituted into equation (A.14). The result is rearranged to find i_1.

$$i_1(s) = \frac{V_{in}(s) - V_{out}(s)}{(L+M)s} - i_3(s) \tag{A.15}$$

Equation (A.7) is substituted into equation (A.15):

$$i_1(s) = \frac{R_l V_{in}(s) - \left[(L+M)(R_l C_2 s + 1)s + R_l\right] V_{out}(s)}{R_l(L+M)s} \tag{A.16}$$

From Kirchoff's Current Law (KCL) the currents in the circuit can be related as:

$$i_2(s) = i_1(s) - i_3(s) \tag{A.17}$$

Substituting equations (A.7) and (A.16) into equation (A.17) yields:

$$i_2(s) = \frac{R_l V_{in}(s) - \left[2 R_l C_2 (L+M)s^2 + 2(L+M)s + R_l\right] V_{out}(s)}{R_l(L+M)s} \tag{A.18}$$

Through application of Ohm's law it is found that:

$$v_2(s) = i_2(s) Z_{C_1} = \frac{i_2(s)}{sC_1} \tag{A.19}$$

Using KVL it can be seen that:

$$v_2(s) = v_3(s) + V_{out}(s) \tag{A.20}$$

By equating equations (A.19) and (A.20) and substituting equation (A.11) the following relation is obtained:

$$\frac{i_2(s)}{sC_1} = sLi_3(s) + sMi_1(s) + V_{out}(s) \tag{A.21}$$

Substitution of equations (A.7), (A.16) and (A.18) into equation (A.21) and manipulating this result, so as to make $\frac{V_{out}(s)}{V_{in}(s)}$ the subject, results in the Laplace transformation of the traditional transfer function:

$$\frac{V_{out}(s)}{V_{in}(s)} = \frac{R_l(MC_1 s^2 - 1)}{R_l C_1 C_2 (M^2 - L^2)s^4 + C_1(M^2 - L^2)s^3 - R_l\left[C_1 L + 2C_2(L+M)\right]s^2 - 2(L+M)s - R_l} \tag{A.22}$$

The transfer function in the frequency domain is found by making the substitution $s = j\omega$. The dependence of the transfer function on the coupling coefficient of the two inductors is explicitly shown by substitution of equation (A.3). The transfer function, obtained by making these two substitutions had the form shown in equation (A.23).

$$H(\omega) = \frac{V_{out}(\omega)}{V_{in}(\omega)} = \frac{x}{y + jz} \tag{A.23}$$

The variables, x, y and z are given in equation (A.24).

$$\begin{aligned} x &= -R_l\left(C_1 C_o L\omega^2 + 1\right) \\ y &= R_l C_1 C_2 L^2 \left(C_o^2 - 1\right)\omega^4 + R_l L\left[C_1 + 2C_2(C_o + 1)\right]\omega^2 - R_l \\ z &= -\left[C_1 L^2 \left(C_o^2 - 1\right)\omega^3 + 2L(C_o + 1)\omega\right] \end{aligned} \tag{A.24}$$

The transfer function of the system, for ideal coupling, was found by setting the value of C_o to unity. The magnitude of the transfer function in such a case is shown in equation (A.25).

$$\left|H_{ideal}(\omega)\right| = \frac{R_l\left(C_1L\omega^2+1\right)}{\sqrt{\left[R_lL\left[C_1+4C_2\right]\omega^2-R_l\right]^2+16L^2\omega^2}} \tag{A.25}$$

A.3 Derivation of the system transfer function, $H_{sys}(\omega)$

The system transfer function was found through using the relation for $V_{in}(s)$, given in equation (A.26).

$$V_{in}(s)=V_s(s)-v_{R_s}(s)=V_s(s)-i_1(s)R_s \tag{A.26}$$

Equations (A.3) and (A.16) were substituted into equation (A.26), and used to find an expression for V_{in} as follows:

$$V_{in}(s)=\frac{R_lL\left(C_o+1\right)sV_s(s)+R_s\left[R_lC_2L\left(C_o+1\right)s^2+L\left(C_o+1\right)s+R_l\right]V_{out}(s)}{R_l\left[L\left(C_o+1\right)s+R_s\right]} \tag{A.27}$$

The result was substituted into equation (A.22) and manipulated so as to make $\dfrac{V_{out}(s)}{V_s(s)}$ the subject. The form of the resultant system transfer function is shown in equation (A.28). The variables r, t, u, v and w are presented in equation (A.29).

$$\frac{V_{out}(s)}{V_s(s)}=\frac{R_l\left(C_1Ms^2-1\right)}{rs^4+ts^3+us^2+vs+w} \tag{A.28}$$

$$r=R_lC_1C_2L^2\left(C_o^2-1\right)s^4$$
$$t=C_1\left[L^2\left(C_o^2-1\right)-R_lR_sC_2L\right]$$
$$u=-C_1L\left(R_l+R_s\right)-2R_lC_2L\left(C_o+1\right) \tag{A.29}$$
$$v=-R_lR_s\left(C_1+C_2\right)-2L\left(C_o+1\right)$$
$$w=-R_l-R_s$$

The frequency domain representation of the system transfer function was found by making the substitution $s=j\omega$. The form of the transfer function is shown in equation (A.30). The variables m, o and q can be found in equation (A.31).

$$H_{sys}(\omega)=\frac{V_{out}(\omega)}{V_{in}(\omega)}=\frac{m}{o+jq} \tag{A.30}$$

$$m=-R_l\left(C_1C_oL\omega^2+1\right)$$
$$o=R_lC_1C_2L^2\left(C_o^2-1\right)\omega^4+\left[C_1L\left(R_l+R_s\right)+2R_lC_2L\left(C_o+1\right)\right]\omega^2-\left(R_l+R_s\right) \tag{A.31}$$
$$q=\left[R_lR_sC_1C_2L-C_1L^2\left(C_o^2-1\right)\right]\omega^3-\left[R_lR_s\left(C_1+C_2\right)+2L\left(C_o+1\right)\right]\omega$$

As before, the system transfer function with ideal coupling between L_1 and L_3 was found, the magnitude of which is given by equations (A.32) and (A.33).

$$\left|H_{sys-ideal}(\omega)\right|=\frac{R_l\left(C_1L\omega^2+1\right)}{\sqrt{k^2+l^2}} \tag{A.32}$$

$$k = L\left[C_1\left(R_l + R_s\right) + 4R_lC_2\right]\omega^2 - \left(R_l + R_s\right)$$

$$l = \left[R_lR_s\left(C_1 + C_2\right) + 4L\right]\omega - R_lR_sC_1C_2L\omega^3$$

(A.33)

A.4 Analysis of closed form transfer function solutions

(a)
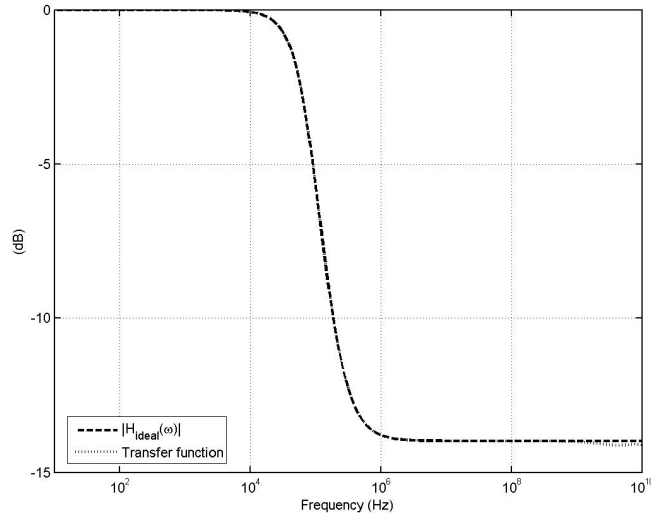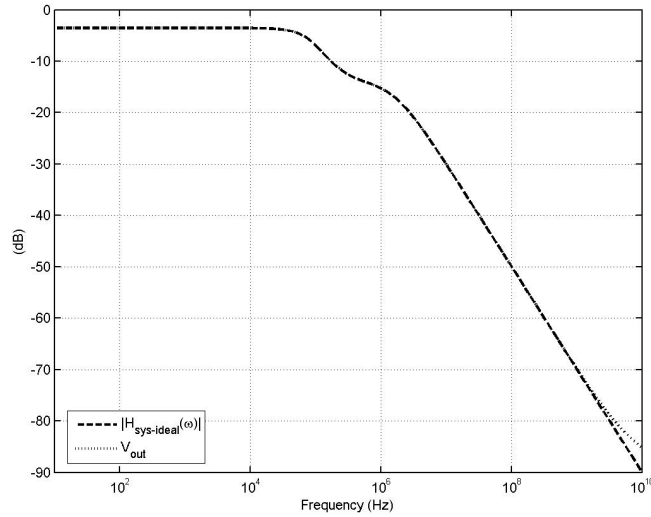
(b)

Fig. A.4: (a) $\left|H_{ideal}(\omega)\right|$ **compared to the transfer function obtained from the simulation. (b)** $\left|H_{sys-ideal}(\omega)\right|$ **compared to the output voltage response obtained from the simulation**

The case study configuration was also simulated using the quasi-distributed model and simulation setup described in Chapter 2. The input and output voltage frequency responses as well as the transfer function were obtained from the simulation.

Equations (A.25) and (A.32) were then used to find the traditional and system transfer function magnitudes of the configuration, using parameter values determined by

those of the simulation. The component values, R_l and R_s were identical to those used in the simulation. However, the values of C_1, C_2, and L were set to values ten times greater than the values used in each cell of the simulation. This was to ensure that the overall inductance and capacitance realised in the simulation was comparable to that of the simplified circuit even though ten cells were used in the simulation model.

Fig. A.4(a) and (b) shows the results obtained for the two transfer functions. Clearly the results differ greatly implying that the magnitude of the source voltage, seen at the input terminal of the IPPM, is influenced. These results were also compared to the transfer function and output voltage frequency response (both in dB) obtained from the simulation. Fig. A.4(a) shows excellent correlation between $\left|H_{ideal}(\omega)\right|$ and the simulation transfer function. The same is seen to be true for $\left|H_{sys-ideal}(\omega)\right|$ and the output voltage frequency response of the simulation as shown in Fig. A.4(b). From this it can be seen that the behaviour of the configuration can be investigated through examination of the output voltage frequency response in the event that the traditional transfer function is shown to be misleading.

APPENDIX B

Coupled inductors
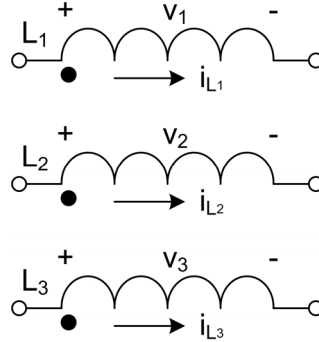
Fig. B.1: Three coupled inductors

Fig. B.1 shows a set of three coupled inductors. Each of the inductors has a self-inductance L and is coupled together with the other inductors with a coupling coefficient C_o. The mutual inductance between any two inductors can then be found with equation (B.1).

$$M = C_o L \qquad (B.1)$$

The voltage drop across each conductor can be expressed using first principles in the Laplace domain, as shown in equation (B.2).

$$v_1(s) = s\left[Li_{L_1}(s) + M\left(i_{L_2}(s) + i_{L_3}(s)\right)\right]$$

$$v_2(s) = s\left[Li_{L_2}(s) + M\left(i_{L_1}(s) + i_{L_3}(s)\right)\right] \qquad (B.2)$$

$$v_3(s) = s\left[Li_{L_3}(s) + M\left(i_{L_1}(s) + i_{L_2}(s)\right)\right]$$

In this form the voltage drop across each inductor can be used to explain a few topics relating to coupled inductors.

B.1 Voltage gradient

In the event that the coupling is ideal the magnitude of the mutual inductance becomes equivalent to that of the self inductance. This causes the voltage drop across each inductor to also become equivalent in magnitude:

$$v_1(s) = v_2(s) = v_3(s) = sL\left(i_{L_1}(s) + i_{L_2}(s) + i_{L_3}(s)\right) \qquad (B.3)$$

This fact can be used when considering the voltage gradient found along the length of an inductor or conductive layer. The conductive layers of the three-layer IPPMs, discussed in this dissertation, have already been modelled as a number of equally sized inductors connected in cascade, a so-called inductor string. These inductors would be coupled together as indicated in Fig. B.2. As previously shown, the magnitude of the voltage drop across the coupled inductors would be identical, represented by v_a, v_b and v_c in the figure.
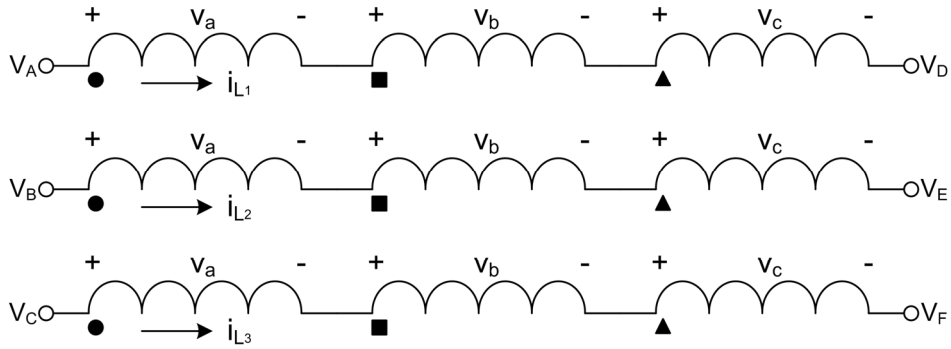
Fig. B.2: Three inductor strings consisting of coupled inductors

Fig. B.3 shows a plot of the typical voltage gradient that would be found along any one of the three inductor strings. The value of the voltage gradient would be identical for all three inductor strings even if the absolute potentials at the terminals, V_A through V_F, were different from one another, as represented by the arbitrary values of V_x and V_y in the figure.
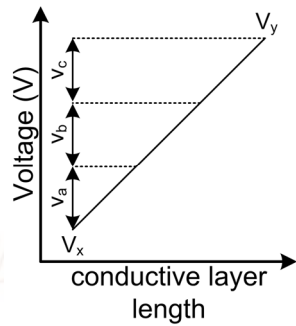
Fig. B.3: Typical plot of voltage vs. conductor length

B.2 CM impedance

Fig. B.4: Inductors used to determine CM impedance

CM impedance refers to the impedance seen by CM currents flowing through a set of inductors. Due to the three-phase nature of the investigation, presented in this dissertation, the CM impedance for three inductors, as shown in Fig. B.4, was considered. The terminals of the three inductors were connected together. In so doing an approximation of balanced CM currents found in a balanced three-phase system was obtained. Due to this balance the currents were related as in equation (B.4).

$$i_{L_1}(t) = i_{L_2}(t) = i_{L_3}(t) \tag{B.4}$$

The CM impedance, Z_{cm}, of the structure was seen to be given by equation (B.5).

$$Z_{cm} = \frac{V_{GH}}{3i_{L_1}(t)} \tag{B.5}$$

From the figure, it is clear that $V_{GH} = v_1(t)$. This fact was used to substitute the Fourier domain representation of equation (B.3) into equation (B.5):

$$Z_{cm} = \frac{j\omega[L+2M]i_{L_1}(t)}{3i_{L_1}(t)} = j\frac{\omega}{3}[L+2M] \tag{B.6}$$

The value of Z_{cm} has a dependence on the value of the mutual coupling. In the event that the three inductors are ideally coupled together to form a CM inductance, the CM impedance is given by equation (B.7).

$$Z_{cm}\big|_{C_o=1} = j\omega L \tag{B.7}$$

Alternatively, if there is no coupling between the inductors, so as to form a DM inductance, the CM currents still see some CM impedance, as shown in equation (B.8)
.

$$Z_{cm}\big|_{C_o=0} = j\frac{\omega L}{3} \tag{B.8}$$

In the event that the system is not balanced, the value of Z_{cm} would differ from that of equation (B.6). However, the CM currents would still see an impedance regardless as to whether or not the inductors were coupled together.
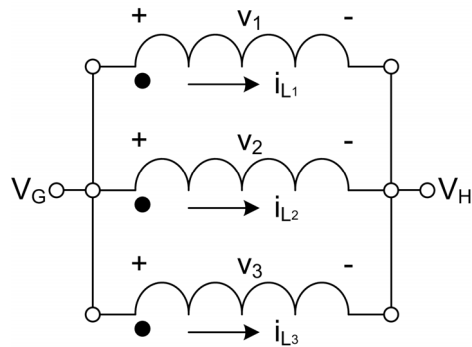
B.3 DM impedance
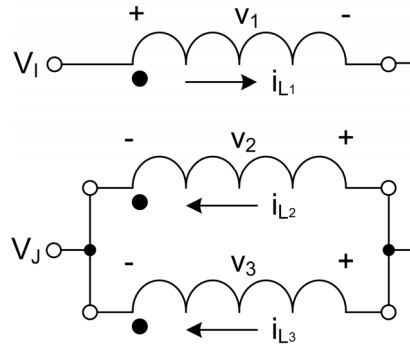
Fig. B.5: Inductors used to determine DM impedance

DM impedance refers to the impedance seen by DM currents flowing through a set of inductors. In a three-phase system the DM current on one line uses the remaining two lines as a return path, as shown in Fig. B.5. The Laplace domain representation of the voltage across each inductor is then given as in equation (B.9).

$$\begin{aligned}
v_1(s) &= s\left[Li_{L_1}(s) - M\left(i_{L_2}(s) + i_{L_3}(s)\right)\right] \\
v_2(s) &= s\left[Li_{L_2}(s) + M\left(i_{L_3}(s) - i_{L_1}(s)\right)\right] \\
v_3(s) &= s\left[Li_{L_3}(s) + M\left(i_{L_2}(s) - i_{L_3}(s)\right)\right]
\end{aligned} \tag{B.9}$$

In a balanced system, the DM current would split evenly between the two lines used as a return path. Consequently, the magnitude of the three currents is related as in equation (B.10).

$$\left| i_{L_2}(t) \right| = \left| i_{L_3}(t) \right| = \frac{1}{2} \left| i_{L_1}(t) \right| \tag{B.10}$$

The DM impedance, Z_{dm}, can be defined as in equation (B.11).

$$Z_{dm} = \frac{V_{IJ}}{i_{L_1}(t)} \tag{B.11}$$

From the figure it can be seen that $V_{IJ} = v_1(t) + v_2(t)$. Using this relation and substituting the Fourier domain representation of equation (B.9) into equation (B.11) yields:

$$Z_{dm} = \frac{j\omega\left[L - M\right] i_{L_1}(t) + j\omega\left[\dfrac{L}{2} - \dfrac{M}{2}\right] i_{L_1}(t)}{i_{L_1}(t)} = j\frac{3\omega}{2}\left[L - M\right] \tag{B.12}$$

Once again the value of the impedance is dependent on the magnitude of the mutual inductance. In the event that the coupling between the inductors is ideal, the magnitude of the DM impedance reduces to zero.

$$Z_{dm}\big|_{C_o=1} = 0 \tag{B.13}$$

However, if no coupling is present between the inductors, the value of Z_{dm} is given by equation (B.14).

$$Z_{dm}\big|_{C_o=0} = j\frac{3\omega L}{2} \tag{B.14}$$

If an imbalance were to exist in the system, the value of the DM impedance seen by the DM current inherent to each of the three lines would differ. However, in all three cases the DM impedance for ideally coupled inductors would still reduce to zero.

APPENDIX C

Filter-unit configurations for the filter-units of group 2
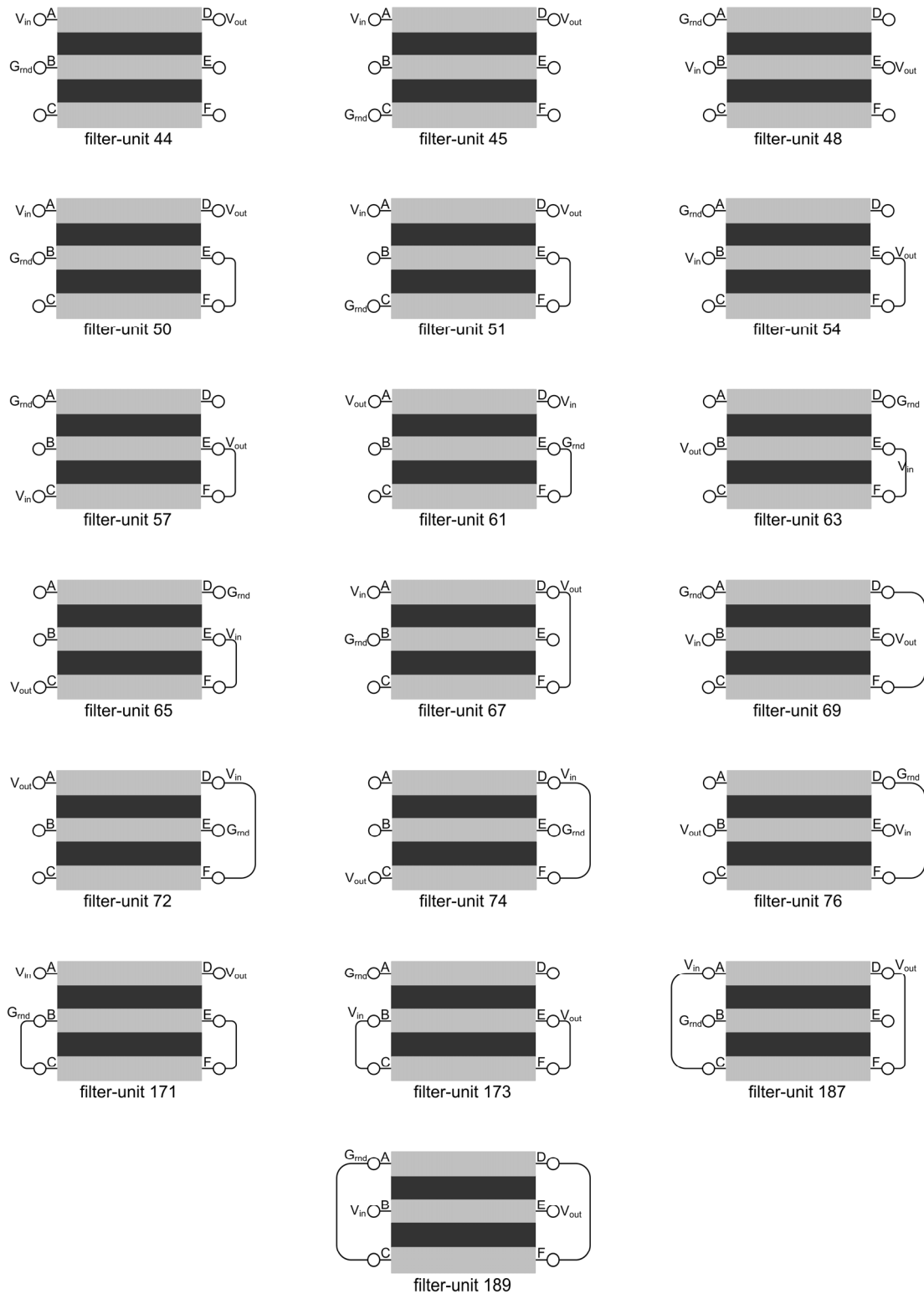
Fig. C.1: Schematic representation of the filter-units found in group 2, subgroup 1
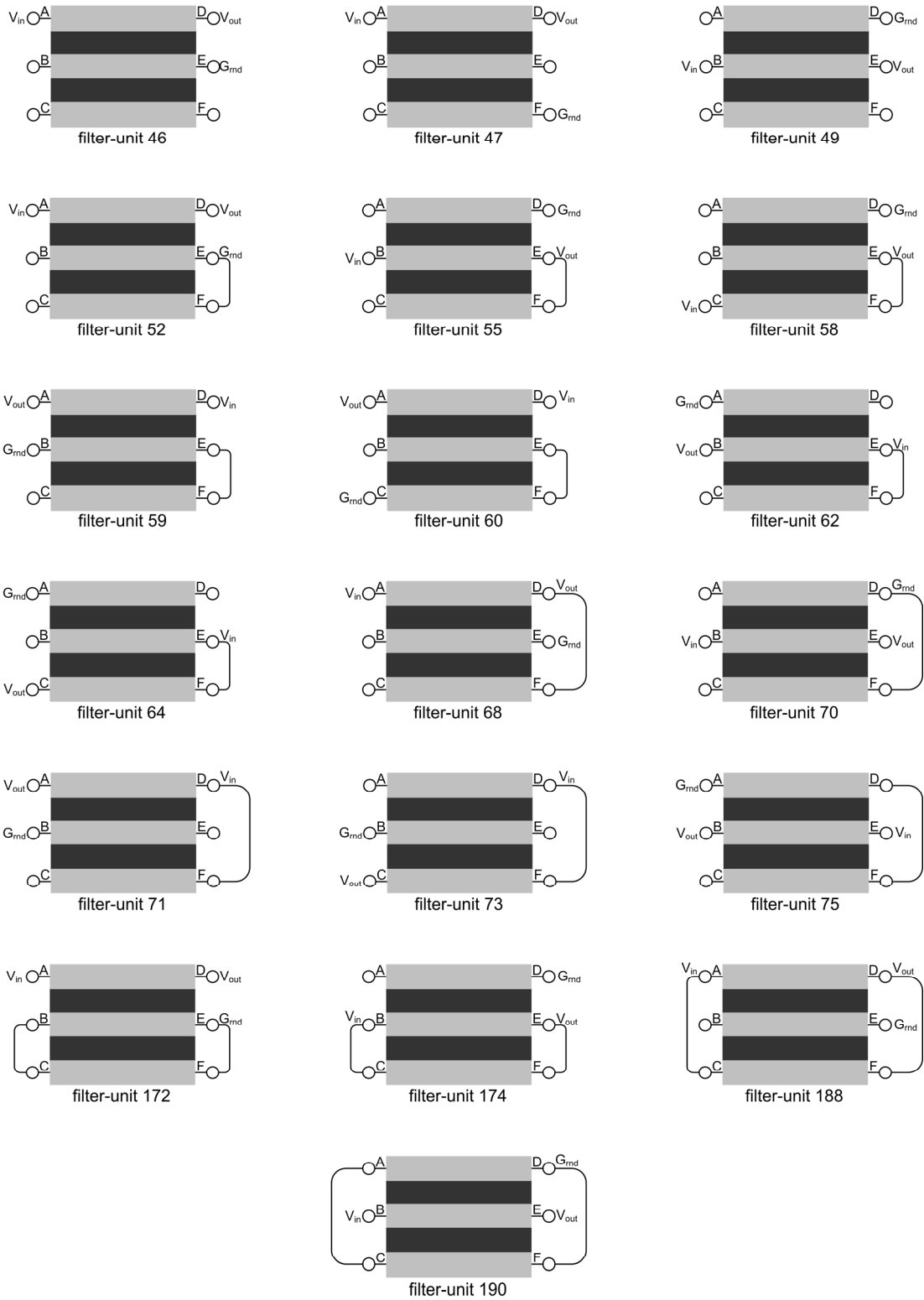
Fig. C.2: Schematic representation of the filter-units found in group 2, subgroup 2

APPENDIX D

C-Ply material investigation, test bench design and construction

D.1 Additional results from the investigation into physical and electrical properties of C-Ply

D.1.1 Physical properties
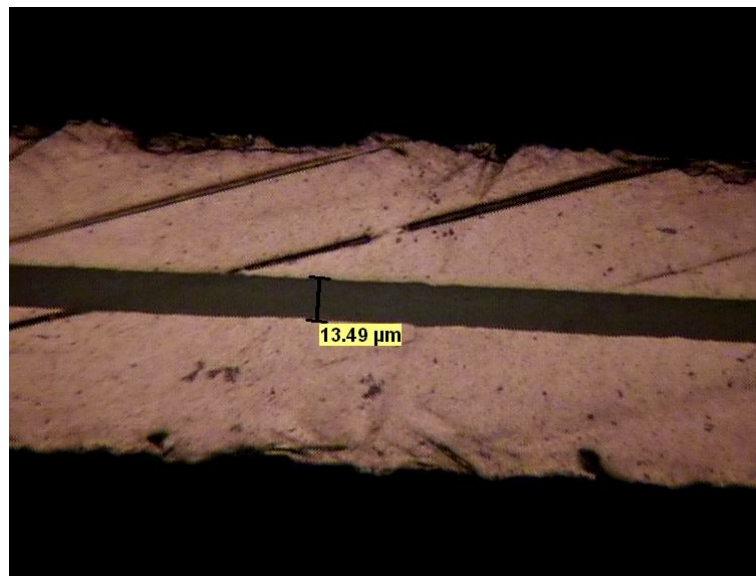
(a)
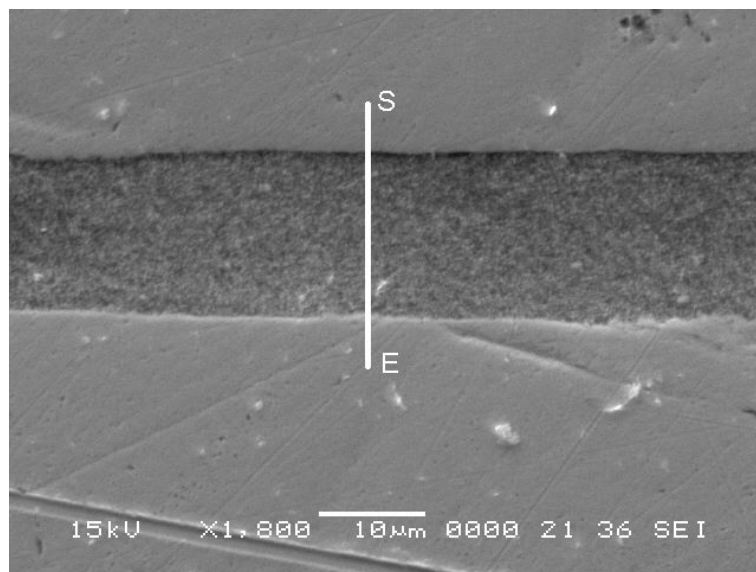
(b)

Fig. D.1: A side-on view of a C-ply sample as seen under (a) an optical microscope at 400× magnification and (b) an electron microscope at 1800× magnification

Table D-I: Measurements of the dielectric thickness

Interval	Dielectric Thickness (μm)
1	13.78
2	14.52
3	13.49
4	13.52
5	14.17
6	14.11
Average	13.93

(a)

(b)

(c)
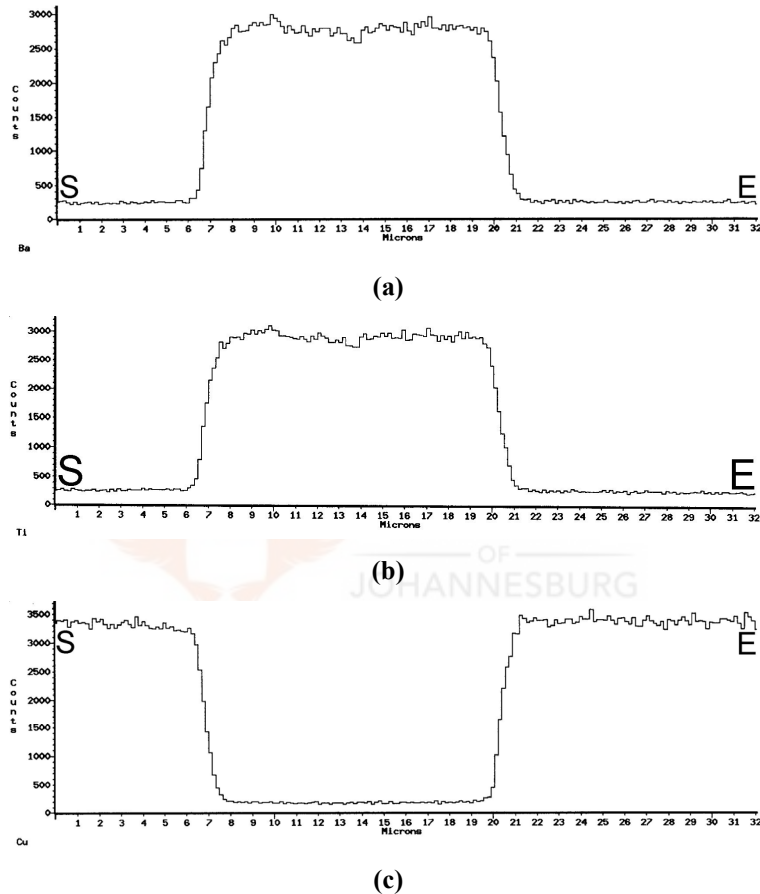
Fig. D.2: The concentration of (a) Barium, (b) Titanium and (c) Copper, found along the length of line SE

A side-on view of the C-Ply sample as seen under the optical microscope at 400× magnification is shown in Fig. D.1(a). Fig. D.1(b) shows a Back Scattered Electron Image (BSEI) of the same sample as seen at 1800× magnification with the aid of the electron microscope.

In Fig. D.1(a) the two copper layers are clearly seen to be separated by a dielectric layer. It was seen that the thickness of the dielectric did not deviate significantly over the entire length of the sample. The image capturing software of the optical microscope was used to measure the dielectric thickness at arbitrarily selected intervals along the sample. The results are shown in Table D-I.

Clearly the measured thickness of the dielectric was found to be less than the specified thickness of 16μm in the datasheet of Chapter 5. This could be attributed to a folding over of the copper onto the dielectric, as appears to be the case in Fig.

D.1(b). This phenomenon was most likely due to mechanical deformation of the copper during the polishing process of the sample preparation.

The composition of the material was investigated, with the electron microscope, along line SE as shown in Fig. D.1(b). A high concentration of barium and titanium was seen along the section of line SE that passed through the dielectric, while the copper concentration was found to be high on either side of the dielectric. Fig. D.2 shows plots of the Ba, Ti and Cu concentrations found along line SE.

D.1.2 Electrical properties

Four capacitors were constructed with the C-Ply material as discussed in Chapter 5. The dimensions of the capacitors' plates were measured and recorded in Table D-II.

Table D-II: Dimensions of the parallel plate capacitors made from C-Ply

Capacitor	Plate dimensions					
	Small plate			Large plate		
	Length (mm)	Width (mm)	Area (m^2)	Length (mm)	Width (mm)	Area (m^2)
1	33	14	0.000462	38	19	0.000722
2	25	17	0.000425	28	19	0.000532
3	28	16	0.000448	30	19	0.000570
4	28	16	0.000448	31	19	0.000589

$$C = \frac{1}{Z\omega\sin\theta} \qquad (D.1)$$

$$ESR = Z\cos\theta \qquad (D.2)$$

Table D-III: Impedance measurements of the capacitors

Capacitor	1				2			
Frequency(kHz)	Z (Ω)	θ ($°$)	C (nF)	ESR	Z (Ω)	θ ($°$)	C (nF)	ESR
2	15663	-89.66	5.08	92.95	17697	-89.64	4.50	111.19
10	3153	-89.52	5.05	26.41	3563	-89.51	4.47	30.47
20	1582	-89.42	5.03	16.01	1788	-89.41	4.45	18.41
100	320.49	-89.12	4.97	4.92	362.21	-89.11	4.39	5.63
200	161.4	-88.96	4.93	2.93	182.39	-88.96	4.36	3.31
1000	32.98	-88.59	4.83	0.81	37.25	-88.58	4.27	0.92
Capacitor	3				4			
2	17839	-89.67	4.46	102.74	17513	-89.64	4.54	110.04
10	3590	-89.53	4.43	29.45	3526	-89.51	4.51	30.15
20	1802	-89.43	4.42	17.93	1770	-89.42	4.50	17.92
100	364.87	-89.13	4.36	5.54	358.4	-89.12	4.44	5.50
200	183.75	-88.97	4.33	3.30	180.55	-88.96	4.41	3.28
1000	37.54	-88.59	4.24	0.92	36.88	-88.58	4.32	0.91

The impedance magnitude, Z, and impedance angle, θ, of each of the capacitors, over a range of frequencies, was measured using an HP 4284A Precision LCR me-

ter, the results of which are given in Table D-III. These measurements were used to calculate the capacitance, *C*, and the equivalent series resistance (*ESR*) of the capacitors as shown in equations (D.1) and (D.2). The impedance angle recorded in Table D-III was negative, indicating that the impedance was capacitive. The absolute value of the measured impedance angle was used in the calculation of *C* and *ESR*.

The capacitance of the test capacitors was seen to decrease with frequency. However, this was seen to be comparable with dielectric technologies found in power electronic applications [23].

These measurements were used to calculate the relative permittivity, ε_r, of the dielectric using the standard equation for a parallel plate capacitor, with plates of area *A* and a distance *d* between the plates, as given in equation (D.3).

$$C = \frac{\varepsilon_0 \varepsilon_r A}{d} \tag{D.3}$$

The area of the small plate of each of the capacitors was used to find ε_r as the fringing effects were assumed to be negligible. The thickness of the dielectric as given in the C-Ply datasheet was used in the calculations. The results can be found in Table D-IV.

Table D-IV: Relative permittivity of the capacitors as found using equation (D.3)

Frequency(kHz)	Capacitor				
	1	2	3	4	Average
2	15.1	14.5	13.7	13.9	14.3
10	15.0	14.4	13.6	13.8	14.2
20	14.9	14.4	13.5	13.8	14.1
100	14.7	14.2	13.4	13.6	14.0
200	14.6	14.1	13.3	13.5	13.9
1000	14.3	13.8	13.0	13.2	13.6

The average relative permittivity is seen to be close to 14 for a given value of frequency. The expected value was 16. The difference between the two values can be attributed to a deviation in the dielectric thickness from the nominal value of 16μm. However, a better approximation of the dielectric thickness could not be obtained due to the folding over of the copper onto the dielectric, as discussed in section D.1.1.

The value of ε_r was also seen to show a frequency dependence, as expected from the presence of a frequency dependence already seen in the value of *C*.

Table D-V: Average capacitance per unit area

Capacitor	Average Capacitance (nF)	Average Area (m²)	Capacitance per unit area (pF/mm²)
1	4.98	0.000592	8.41
2	4.41	0.000479	9.21
3	4.37	0.000509	8.59
4	4.45	0.000519	8.59
		Average:	8.70

The measured capacitor values were then used to find the average capacitance per unit area. As the two parallel plate capacitors were not of equal size, for any given capacitor, the average plate size was used as an approximate value of area. The results are shown in Table D-V.

The robustness of the dielectric was investigated by compressing one of the capacitors for a few hours. The impedance measurements were then performed again and compared to the previously measured values. As the values were comparable (refer to Table D-VI) with one another it was apparent that the dielectric was quite robust and the dielectric thickness would not be significantly altered if the material was compressed.

Table D-VI: Impedance measurements of capacitor 2 before and after compression

	Before compression	After Compression			
Frequency(kHz)	C (nF)	Z (Ω)	θ (°)	C (nF)	ESR
2	4.50	17705	-89.64	4.49	111.24
10	4.47	3566	-89.49	4.46	31.74
20	4.45	1791	-89.40	4.44	18.75
100	4.39	362.82	-89.10	4.39	5.70
200	4.36	182.74	-89.94	4.35	0.19
1000	4.27	37.33	-88.58	4.26	0.93

A number of arbitrarily constructed test samples were used to investigate the breakdown voltage of the material, as discussed in Chapter 5. Fig. D.3 shows a graph of the voltage at which these test samples experienced breakdown. The setup used to determine these values was limited to 600V. Consequently, the test samples under the 600V column had not yet experienced breakdown [23].
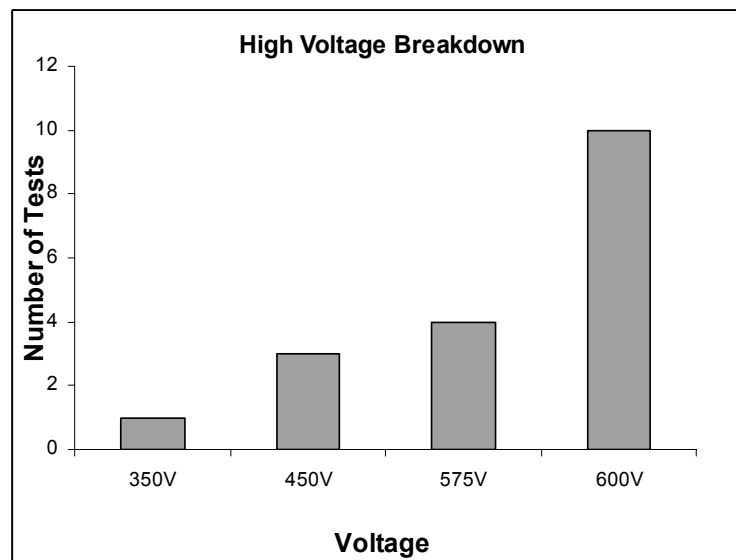
Fig. D.3: Occurrence of dielectric breakdown [23]

D.2 PWM switching scheme

The PWM switching scheme used in the three-phase inverter made use of commonly implemented carrier-based PWM [6]. The required bus voltage for such an inverter can be determined through use of the amplitude modulation ratio, m_a, as defined in equation (D.4), where $\hat{V}_{control}$ is the peak value of the control signal, $v_{control}$, and $\hat{V}_{saw}$ is the peak value of the switching frequency saw tooth waveform, v_{saw} [5].

$$m_a = \frac{\hat{V}_{control}}{\hat{V}_{saw}}$$
(D.4)

The amplitude modulation and the bus voltage can then be used to determine the amplitude of the line-to-line rms output voltage of the inverter as shown in equation (D.5) [5].

$$V_{LL_{rms}} = 0.5\sqrt{\frac{3}{2}}m_a V_{bus}$$
(D.5)

The line-to-line voltage rating of the induction motors, given in Chapter 5, and an amplitude modulation ratio of 0.667, as found in section D.3.2, was used in equation (D.5). In so doing the required bus voltage was found to be 37V.

D.3 Design and construction of a three-phase induction motor drive

A standard three-phase inverter topology was used to realise the inverter, along with the carrier-based PWM switching scheme discussed in section D.2. Other topologies and switching schemes could also have been used but a more complicated system was not deemed necessary. The objective of the test bench was not to build a highly efficient inverter but to rather create a source of EMI for the induction motor, which the IPPMs would have to eliminate through filtering.

The inverter could in turn be broken up into three main parts:

- The power section of the inverter, consisting of the DC bus and the three phase arms.

- The MOSFET driver circuitry.

- The three-phase sine wave generator used to generate the control signals for the PWM.
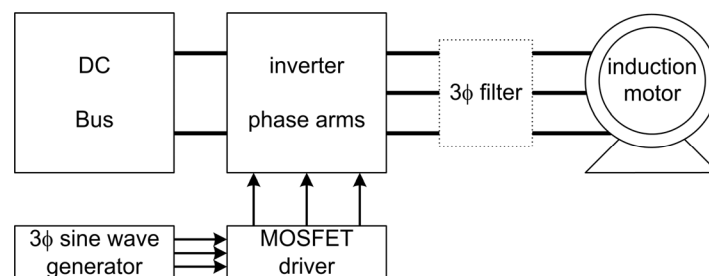

Fig. D.4: Basic layout of the test bench showing the placement of the three constituent parts of the PWM inverter

Fig. D.4 shows a block diagram representation of the placement of these three parts relative to one another in the overall test bench setup.

D.3.1 Power section

The power section of the inverter consisted of the three phase arms. Each phase arm in turn consisted of two switches, as shown in Fig. D.5 by the demarcated area. The switches were used to switch a DC bus voltage, V_{bus}, so as to obtain an AC voltage output. The lower switches, Q_2, Q_4 and Q_6, are referred to as the low side MOSFETs while the upper switches, Q_1, Q_3 and Q_5, are called the high side MOSFETs.
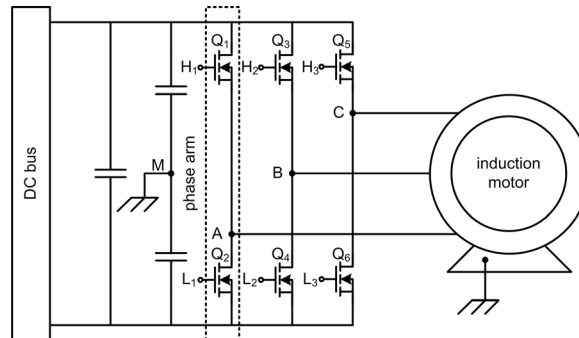
Fig. D.5: Schematic diagram of the three phase arms of the inverter relative to the DC bus and the induction motor

The complete circuit diagram of the three phase arms can be found in Fig. D.6. The midpoints, A, B and C, of the phase arms, as well as the midpoint of the DC bus, M, are labelled in both figures to facilitate comparison between the two figures. The midpoint of the DC bus and the casing of the motor were connected to earth to create a path for the flow of CM current in the setup, as discussed in Chapter 6.
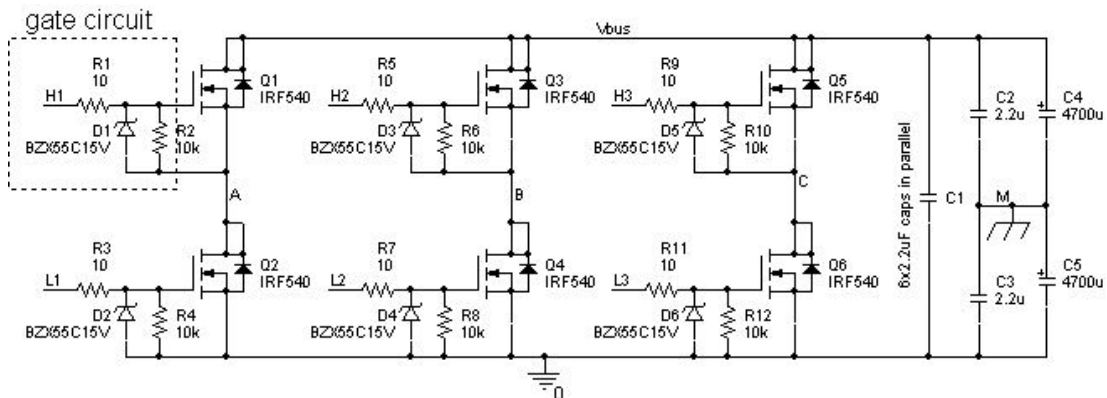
Fig. D.6: Circuit diagram of the three phase arms

The three inputs, H_1, H_2 and H_3, represented the high side MOSFET gate signals as obtained from the MOSFET driver circuitry discussed in a later section. Similarly the inputs L_1, L_2 and L_3 represented the low side MOSFET gate signals.

Gate circuit

Each of the MOSFET gates had a "gate circuit" preceding it that consisted of two resistors and a zener diode that were used to perform specific functions. Consider the gate circuit of switch Q_1, as seen in Fig. D.6.

- By keeping the gate resistor, R_1, as large as possible the HF noise of the switching signal could be limited. However, a smaller gate resistor would allow the gate capacitance to discharge quickly. The resistor value was chosen so as to try and satisfy both of these conditions.

- Zener diodes were used to clamp the gate voltage to a maximum value of 15V.

- The resistor, R_2, ensured that the gate voltage remained low, thereby keeping the switch in its off state, when the drive circuit was inactive.

Inverter layout

A number of layout issues were also considered when building the inverter so as to minimise the inductance of the setup and hence reduce HF noise in the inverter itself. This was necessary for the inverter to operate satisfactorily. Fig. D.7 shows a photograph of the layout used.

- The connections between the source of the high side MOSFETs and the drain of the low side MOSFETs were kept as short as possible in order to minimise inductance. This can be seen from Fig. D.7 through the close placement of switches Q_1 through Q_6 in each of the phase arms.

- The capacitors, represented by C_1 in figures D.5 and D.6, were placed as close to the MOSFETs as possible to limit the inductance introduced by long connecting leads.

- The gate driver circuitry was connected to the phase arms by means of twisted pairs. This reduced the DM inductance of the connections through loop minimisation. As a result the magnitude of any induced voltages was also limited.

- The twisted pairs were in turn wrapped around E-cores so as to increase the CM inductance, thereby limiting HF interference common to both lines.
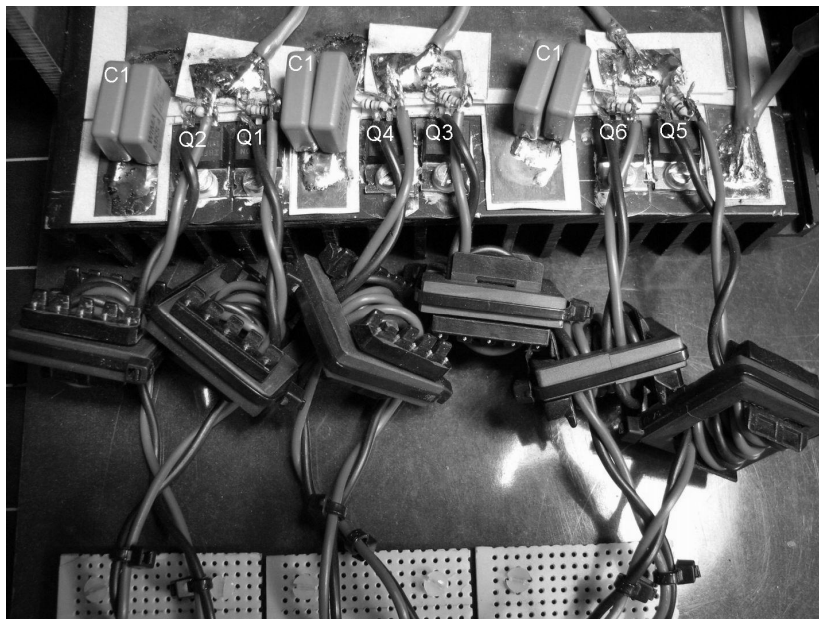
Fig. D.7: The inverter phase arms showing the physical construction used in order to minimise inductance

Measured waveforms of the operational phase arms

In order to show the basic functionality of the inverter a number of waveforms were captured using a digital oscilloscope. During all the measurements taken the bus voltage was kept at 15V and the frequency of the three-phase control signals was held at 50Hz unless otherwise specified. A bus voltage of 15V was selected as it was found that the speed of the motor was not influenced by an increase in the bus voltage above 15V.
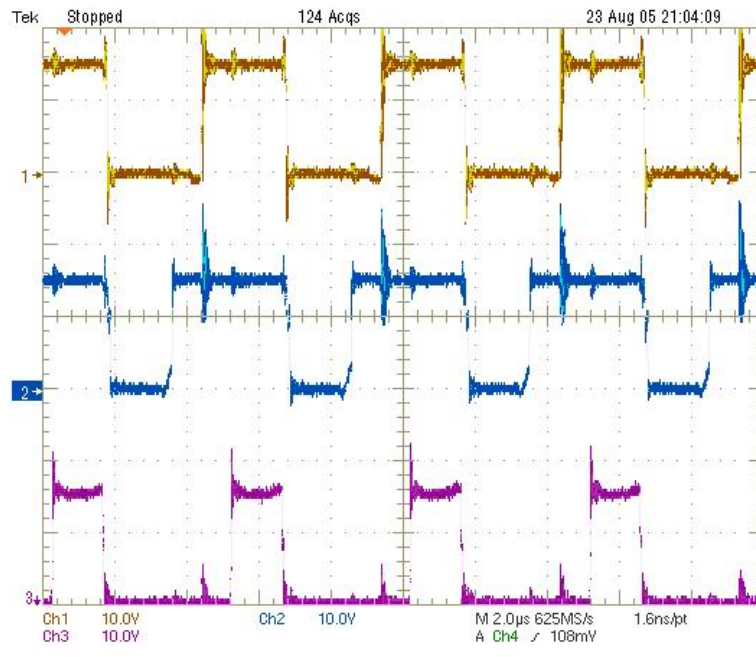
Fig. D.8: V_{ds} **waveforms measured across the low side MOSFETs for all three phase arms**

Fig. D.9: The motor phase current

Fig. D.8 shows the voltage measured across the low side MOSFETs between the drain and the source for all three phase arms. It can clearly be seen that the switching frequency is at 200kHz. The difference in duty cycle between the three waveforms can be explained due to the fact that these waveforms were captured at a sin-

gle point in time. The duty cycles of the three phase arms are expected to be different, at any given instant in time. This is due to the nature of PWM switching schemes and the fact that the switches of the three phase arms were switching in such a manner as to realise three-phase AC waveforms.

As the motor forms an inductive load it acts as a LPF for the current waveform. This can be seen by the fact that the measured current waveform is sinusoidal in nature as shown in Fig. D.9. The current was measured on a scale of 2A/div when the induction motor was typically loaded.

D.3.2 MOSFET driver circuitry

As there was three phase arms there had to be three driver circuits. However, as these circuits were identical only one circuit will be considered here. The purpose of the circuit was to generate a PWM signal that was to be used to control the switching of both the low and high side gates.
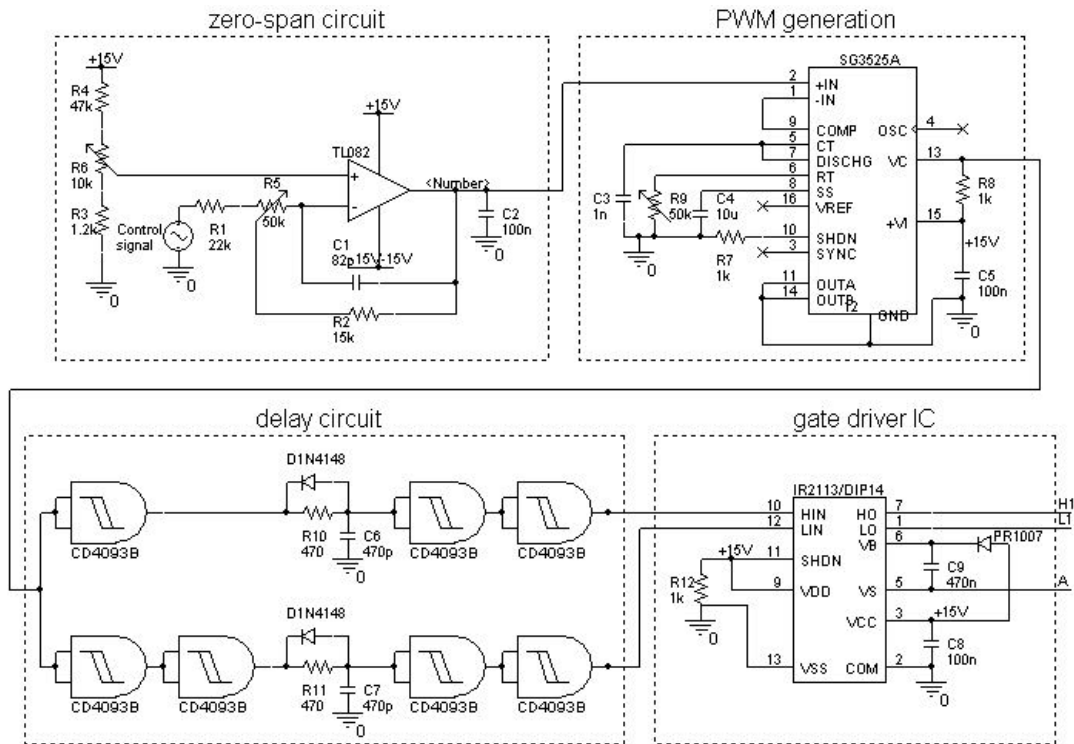

Fig. D.10: Circuit diagram of a single MOSFET driver circuit

The complete circuit diagram of the driver circuit used for the first phase arm consisting of switches Q_1 and Q_2 is shown in Fig. D.10. The circuit can be subdivided into a four different parts, namely:

- A zero-span circuit.

- A circuit responsible for PWM generation.

- A delay circuit.

- The gate driver IC.

Zero-span circuit

Two waveforms form the backbone of the PWM process, namely the control signal, $v_{control}$, and a sawtooth waveform, v_{saw}. The fundamental frequency, f_1, that is required at the output of the inverter corresponds with the frequency of $v_{control}$, while the frequency of v_{saw} is equivalent to that of the required switching frequency, f_s. These two waveforms are compared with one another in order to determine the width of the pulses in the PWM waveform at any given instant. Measurements of these two signals can be seen in Fig. D.11. The horizontal cursor lines were kept in the same place for both measurements for purposes of comparison. The two waveforms could not be measured simultaneously due to the large difference in their respective frequencies, namely 200kHz for v_{saw} and 50Hz for $v_{control}$. From these waveforms it was possible to estimate the value of m_a as 0.667 though using equation (D.4) and the peak voltage values of the two waveforms as measured above the placement of the lower cursor line.
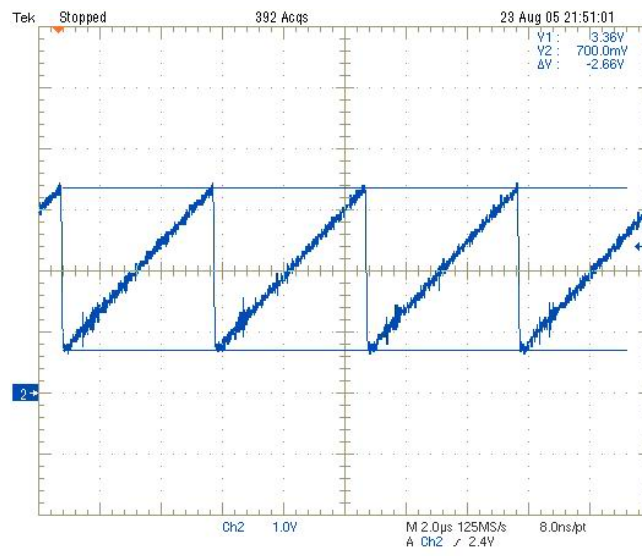
(a)
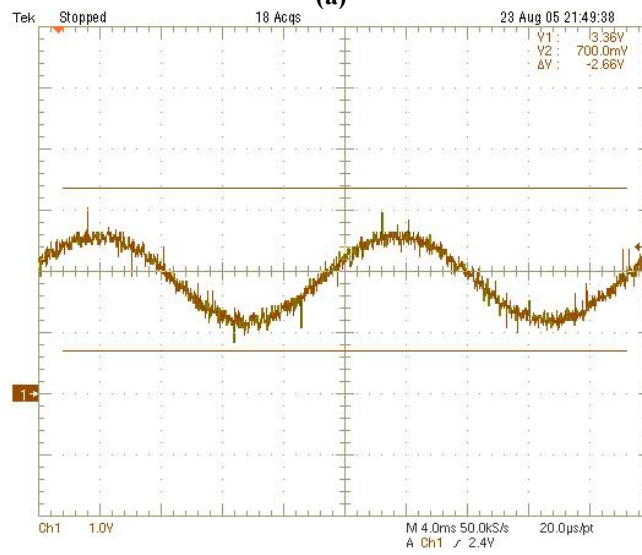
(b)

Fig. D.11: (a) Sawtooth waveform, v_{saw}, with cursors indicating its minimum and maximum values (b) Control waveform, $v_{control}$, seen to be positioned between the minimum and maximum cursor values of v_{saw}, note that the time scale for the two measured waveforms above is different

The zero-span circuit was realised with an op-amp. It was used to adjust the amplitude and the DC offset of $v_{control}$, thereby controlling the PWM waveform. This was necessary as adjusting the amplitude and offset of $v_{control}$ enabled the PWM signals to be balanced. In so doing it was ensured that the high side and low side MOSFETs of any one phase arm were on for an equal duration of time during one time period of the control signal.

Two additional aspects of the zero-span circuit were encountered when building and testing the circuit. It was found that the zero-span circuit went into resonance due to inherent parasitics present in the circuit layout. This was overcome through the introduction of capacitor C_1 (of Fig. D.10) into the circuit. In so doing a HF path was created thereby decreasing the amplification of any HF signals. Capacitor C_2 was also introduced so as to eliminate noise that was found to be present on the output of the zero-span circuit.

PWM generation

The actual comparison of $v_{control}$ and v_{saw} with one another in order to produce the PWM signal was achieved through the use of a PWM IC in the form of a SG3525A. It was opted to use this IC instead of the PWM available on the PIC, used later to realise the sine wave generator, due to the high switching frequency of the MOSFETs. At such a high frequency a PIC would generally be too slow too yield sufficient resolution of the PWM, hence the need for a PWM IC.

The value of the switching frequency, f_s, was determined by the values of R_9 and C_3 as given in equation (D.6) [30].

$$f_s = \frac{1}{C_3\left(0.7R_9\right)} \tag{D.6}$$

R_9 was realised with a variable resistor so that the switching frequency could be adjusted accordingly.

The three SG3525A ICs of the three separate MOSFET driver circuits also had to be synchronised so as to minimise HF interference caused by the switching of the MOSFETs. The circuits were synchronised by connecting the oscillator output (pin 4) of one of the circuits to the synchronisation pin (pin 3) of the remaining two circuits.

Fig. D.12 (a) shows the gate signal of one of the low side MOSFETs when the three SG3525A ICs were not synchronised while Fig. D.12 (b) shows the same waveform after synchronisation. In the former waveform noise can be seen to be present at various intervals on the waveform. However, in the latter this noise is reduced and concentrated at the gate turn on instant only.

Delay circuit

The PWM signal obtained from the SG3525A and its inverse were then obtained with the aid of Schmitt triggered NAND gates. The original signal was used as the gate signal for the high side MOSFET in the phase arm while its inverse was used to drive the gate of the low side MOSFET. This would ensure that only one of the switches in a phase arm would be on during a switching cycle. However, at the switching instant it was possible for both switches to be on simultaneously. This

would be problematic as it would result in the DC bus being short-circuited. In order to avoid this occurrence a small amount of dead time was introduced during which both switches in a phase arm would be off, before either one was subsequently switched on.

The two gate signals were applied to identical delay circuits, thereby introducing an equal amount of dead time into both signals.

The purpose of the RC circuit found in the delay circuit, refer to Fig. D.10, was to increase the time taken for the rising edge of the gate signal to reach its maximum value. The time by which this was increased was related to the RC time constant of the circuit. On the falling edge of the gate signal the diode would become forward biased causing the capacitor to discharge quickly. Consequently any delay introduced on the falling edge would be negligible. The influence of the delay circuit can be seen by comparing Fig. D.13(a) with Fig. D.13(b); the high and low side gate signals before and after the delay circuit respectively.
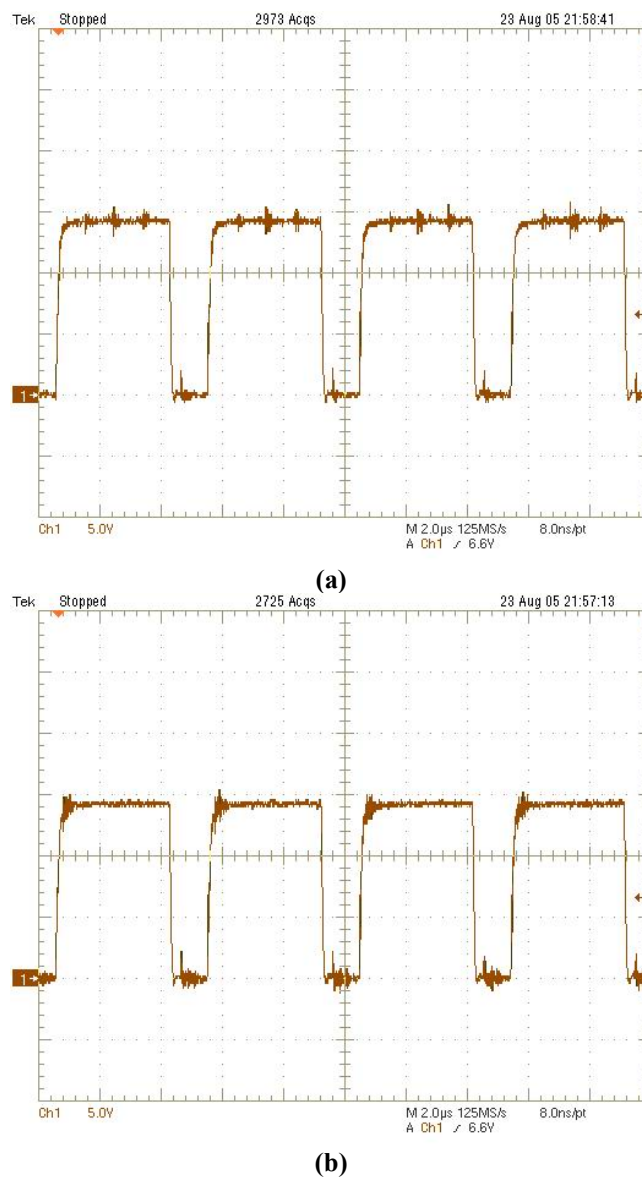

(a)

(b)

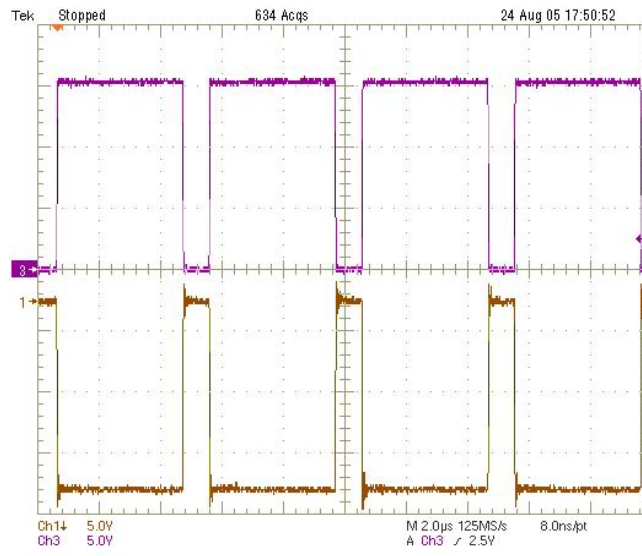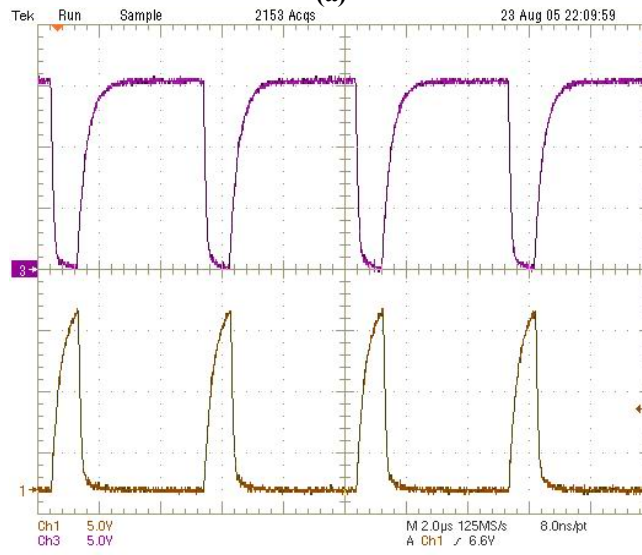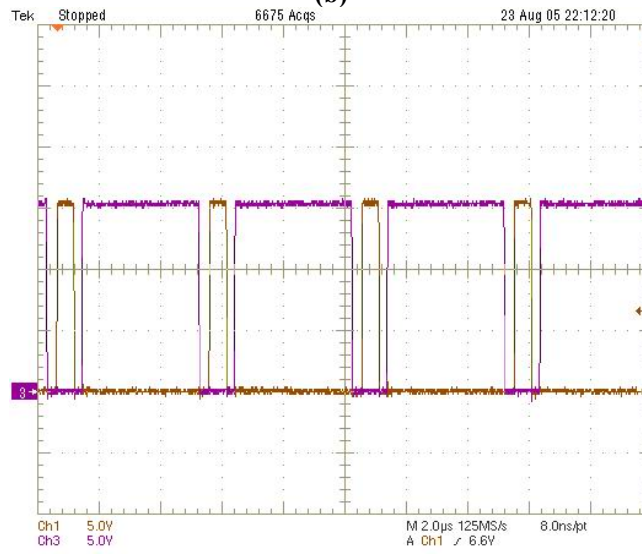**Fig. D.12: V_{gs} of the MOSFETs (a) without and (b) with synchronisation**

(a)

(b)

(c)

Fig. D.13: (a) Output obtained from the SG3525A and its inverse (b) The same signals as in (a) after the delay circuit showing the increased rise time (c) The two waveforms used as the high side and low side gate signals, clearly indicating the delay time introduced

The Schmitt triggered NAND gates found after the RC circuit were used to obtain a proper square wave from the delay circuit. Due to the fact that the NAND gates also inverted the signals it was necessary to use two NAND gates connected in cascade for each gate signal. The final output from these NAND gates can be seen in Fig. D.13 (c), where the dead time between turn on and turn off of the two gate signals can clearly be seen.

Gate driver IC

The IR2113 IC provides both a low and a high side MOSFET driver. The high side MOSFET driver makes use of a bootstrap configuration, consisting of the PR1007 diode and capacitor C_9 shown in Fig. D.10.

The principal behind the operation of the bootstrap is that when the high side MOS-FET is off, the diode turns on and charges C_9 to a value equal to that of the bus voltage. As soon as the high side MOSFET is turned on, the voltage of the charged capacitor is used to increase the gate signal to a voltage value above that of the bus voltage. This can be seen to be the case for the measured low and high side gate drive signals, with a 15V DC bus, as shown in Fig. D.14.
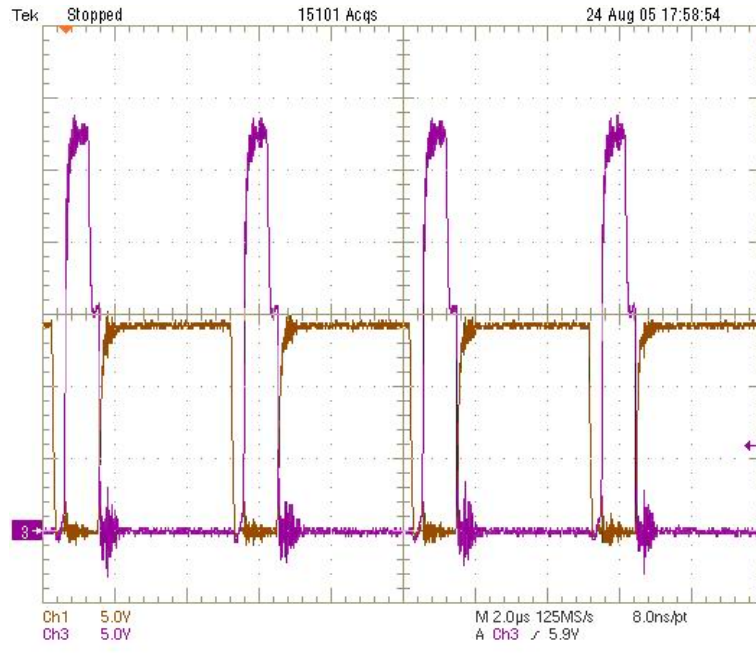
Fig. D.14: The high side and low side gate signals for a phase arm. The high side signal is clearly seen to be greater in amplitude than the low side signal due to the bootstrap configuration

The value of the capacitor used in the bootstrap configuration was found using equations (D.7) and (D.8), as given in [31]. A description of each of the variables as well as the values, found from various datasheets, that were used in the equations are listed in Table D-VII.

$$Q_{bs} = 2Q_g + \frac{I_{qbs(max)}}{f} + Q_{ls} + \frac{I_{Cbs(leak)}}{f} \qquad (D.7)$$

$$C_{bootstrap} \geq \frac{2Q_{bs}}{V_{cc} - V_f - V_{LS} - V_{min}} \qquad (D.8)$$

Table D-VII: Bootstrap component selection variables [31]

Variable	Description	Value
Q_g	Gate charge of high side MOSFET	59nC
$I_{qbs(max)}$	Quiescent current for high side driver circuitry	230µA
f	Frequency of operation	200kHz
Q_{ls}	Level shift charge required per cycle	5nC
$I_{Cbs(leak)}$	Bootstrap capacitor leakage current	Omitted as a non-electrolytic capacitor was used
Q_{bs}	Minimum charge to be supplied by bootstrap capacitor	124.15nC
V_{cc}	Low side fixed supply voltage of IR2113	15V
V_f	Forward voltage drop across bootstrap diode	1.3V
V_{LS}	Voltage drop across the low side MOSFET	$r_{on} \times I_D \approx 0.077\Omega \times 2A = 0.154V$
V_{min}	Minimum voltage across bootstrap capacitor	V_{bsuv}
V_{bsuv}	Undervoltage lockout	7.5V
$C_{bootstrap}$	Bootstrap capacitance	41nF

The value of the actual capacitor used in the bootstrap configuration should be 15 times larger than the value of $C_{bootstrap}$. This rule of thumb is followed to minimise the risk of overcharging and as a means of reducing ripple across the bootstrap capacitor [31]. A fast 470nF Wima capacitor was used for this purpose. The value of the capacitor was only about 11.5 times larger than the required value; however, the performance was seen to be satisfactory.

The diode used in the bootstrap configuration had to have the characteristics listed in Table D-VIII. The PR1007 diode selected for this purpose met most of the requirements. The reverse recovery time of the diode was greater than the required time, however, as already mentioned the bootstrap operation was found to be satisfactory.

Table D-VIII: Required characteristics of bootstrap diode

Variable	Description	Value
V_{RRM}	Peak repetitive reverse voltage	V_{bus}
t_{rr}	Reverse recovery time	100ns
I_F	Forward current	$Q_{bs} \times f$

The outputs of the IR2113 were connected to the gates and the midpoint of a phase arm. The labels shown for the outputs of Fig. D.10 correspond with the input labels of the phase arm realised with switches Q_1 and Q_2 in figures D.5 and D.6.
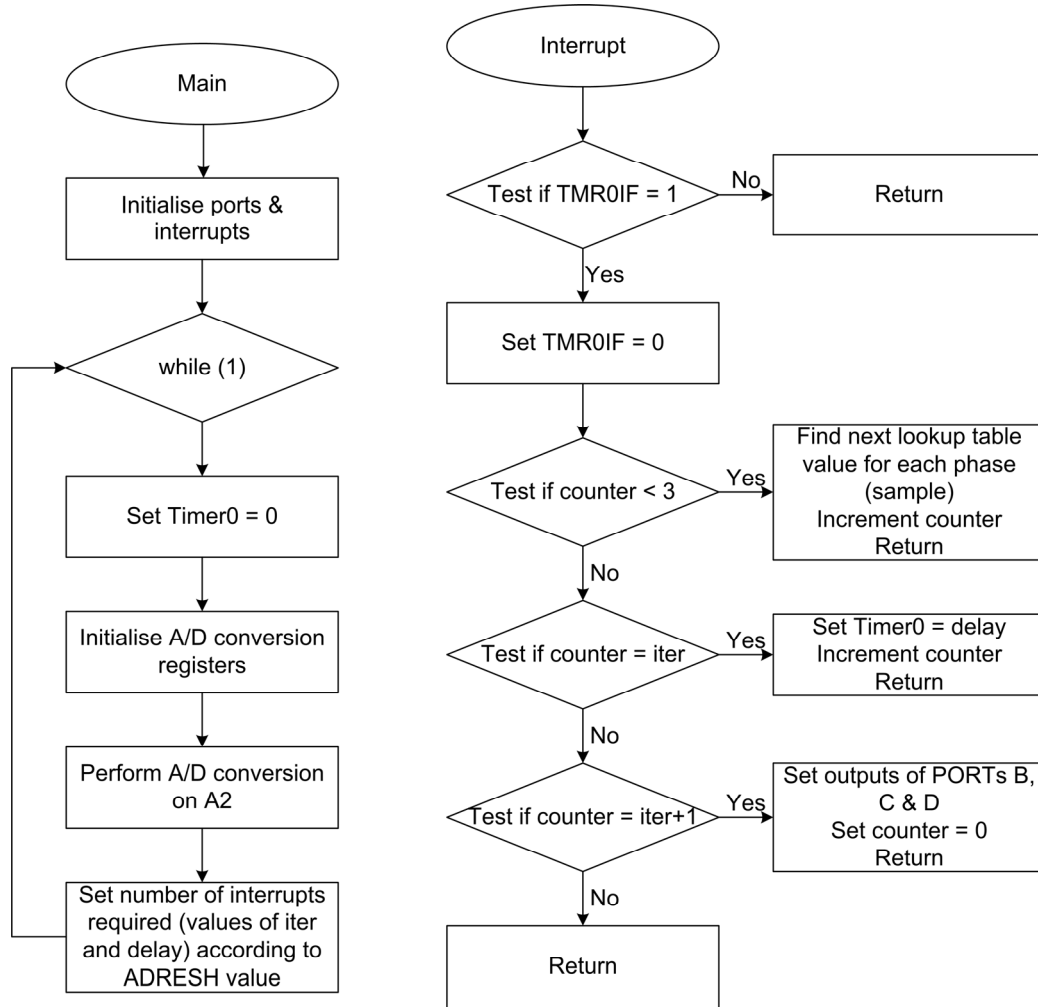
D.3.3 Three-phase sine wave generator

The control signals used in the PWM were required to be three-phase, sinusoidal and have variable amplitude and frequency. A variable frequency three-phase sine wave generator was consequently developed for this purpose. The sine wave generator did not allow for the adjustment of the amplitude of the sine waves, but only

their frequency. This was due to the fact that the zero-span circuit of the MOSFET driver already catered for amplitude adjustment.

The sine wave generator was realised with the aid of a PIC16F877 and three DAC0800s. The complete circuit diagram is given in Fig. D.15.

Fig. D.15: Circuit diagram of the three-phase sine wave generator

The PIC performed two main functions. It supplied the DACs with data, in order to generate the sine waves, by means of a lookup table and it allowed the frequency of these sine waves to be adjustable. A flow chart outlining the PIC code used to realise these two functions can be found in Fig. D.16.

The values in the lookup table corresponded with 8 bit binary values to be applied to the input ports of the DACs. As the DACs would then convert the digital signal to an analogue value the lookup table entries represented samples of the required sine wave. According to the Nyquist theorem [32] a sine wave can be reconstructed from sample values if the sampling rate is greater than twice the frequency of the sine wave. This implies that there needs to be more than two samples values in order to generate a sine wave for any frequency.

The lookup table contained samples for one half of a sine wave. The complete sine wave was obtained by reading values from the lookup table first in ascending order and then in descending order. The 120° phase shift between the three-phases was realised by setting the starting point in the lookup table, for each phase, to be at a sample value that was equivalent to sinusoids that were 120° out of phase with one another.

The lookup table used in the sine wave generator had thirty entries, corresponding to sixty samples of a sine wave. This value was chosen to be substantially higher than the number of samples required by the Nyquist theorem to ensure that the generated sine wave closely approximated a true sinusoid.

Fig. D.16: Flow chart of the PIC code showing the two procedures (a) main and (b) interrupt

The frequency of the sine waves was adjusted by controlling the delay time between successive values of the lookup table being placed on the output ports of the PIC. The value of this delay was determined with the aid of an A/D conversion on one of the PIC's pins that was connected to a variable resistor.

The DACs used were current output DACs. In order to convert this output into a voltage output an op-amp circuit was implemented. This circuit is labelled as the conversion circuit in Fig. D.15. The voltage output, which was still a quantised form of a sine wave, was then filtered using a low pass RC filter.

The frequency of the sine waves was chosen to be within a typical range: 30Hz – 70Hz. Consequently it was found that the sampling frequency for a 30 entry lookup table ranged from 1.8kHz – 4.2kHz. The cut-off frequency of the RC filter was chosen to be 100Hz to ensure that all the high frequency noise was eliminated while not influencing the desired signals.

$$\omega = \frac{1}{RC} \tag{D.9}$$

Taking the above into consideration the values of R and C were chosen to be 1MΩ and 1.5nF respectively. The filtered sine waveforms, sig_1, sig_2 and sig_3, as shown in Fig. D.15, were connected to the driver circuit through a buffer in the form of an op-amp voltage follower. These waveforms served as the control signals of the three driver circuits.
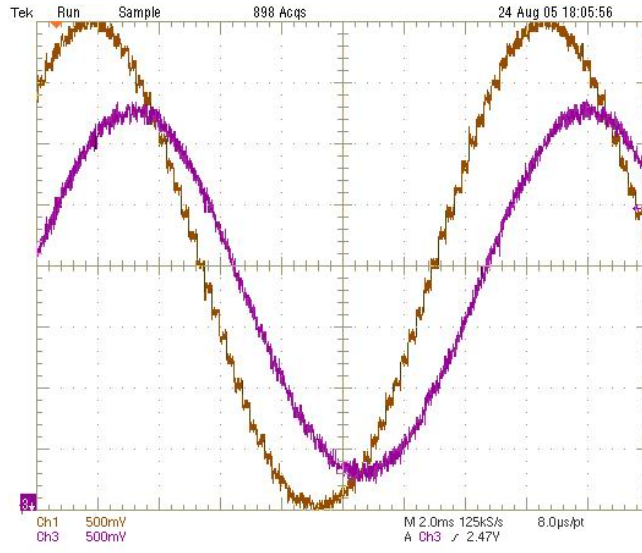
Fig. D.17: The quantised waveform generated and the same waveform after being passed through the RC filter
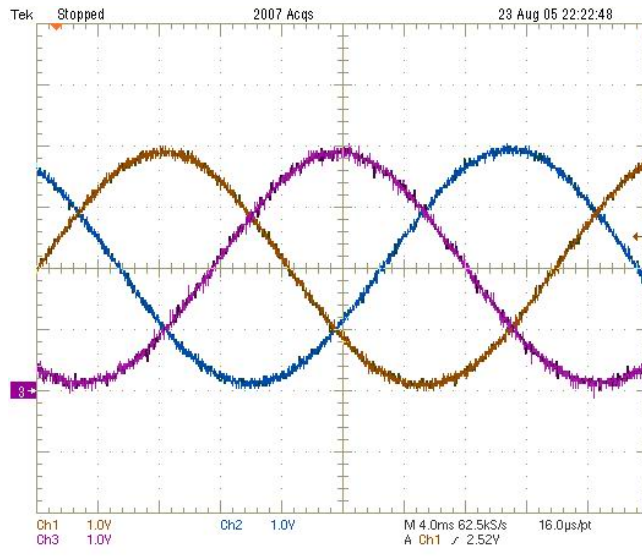
(a)
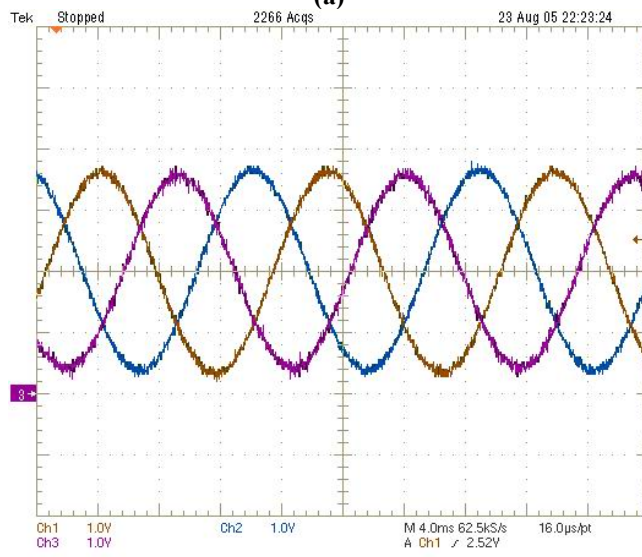
(b)

Fig. D.18: The three control signals produced with the aid of the PIC at (a) 30Hz and (b) 67Hz

Fig. D.17 shows the quantised sine wave before being passed through the RC filter as well as the filtered waveform obtained after the RC filter. The attenuation and phase shift experienced by the filtered waveforms can be explained by considering the transfer function of the RC filter, H_{RC}. Equations (D.10) and (D.11) give the magnitude and phase shift of H_{RC}.

$$\left|H_{RC}\right| = \frac{1}{\sqrt{1 + \omega^2 R^2 C^2}} \qquad (D.10)$$

$$\angle H_{RC} = \arctan \omega RC \qquad (D.11)$$

From these equations and through using the component values of the filter, an attenuation of 0.9 and a phase shift of -25° were found at 50Hz. These values indicate a difference in non-filtered and filtered waveforms that corresponds with the measured result.

Fig. D.18 shows the three control signals at the lowest and highest possible frequencies obtained from the three-phase sine wave generator. The phase shift between the three waveforms is clearly seen to be 120°.

D.4 E64 Core Dimensions

The dimensions of the E64 core and its accompanying I core, as found in [27], is shown in Fig. D.19.
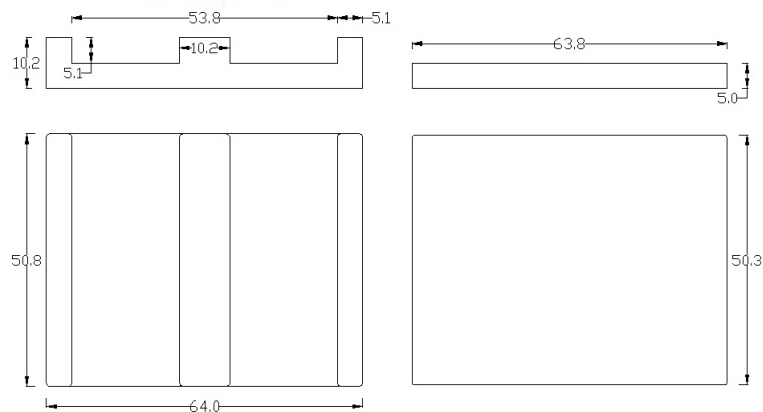

Fig. D.19: Dimensions of (a) the E64 core and (b) its accompanying I core [27]

APPENDIX E
CM and DM current measurements

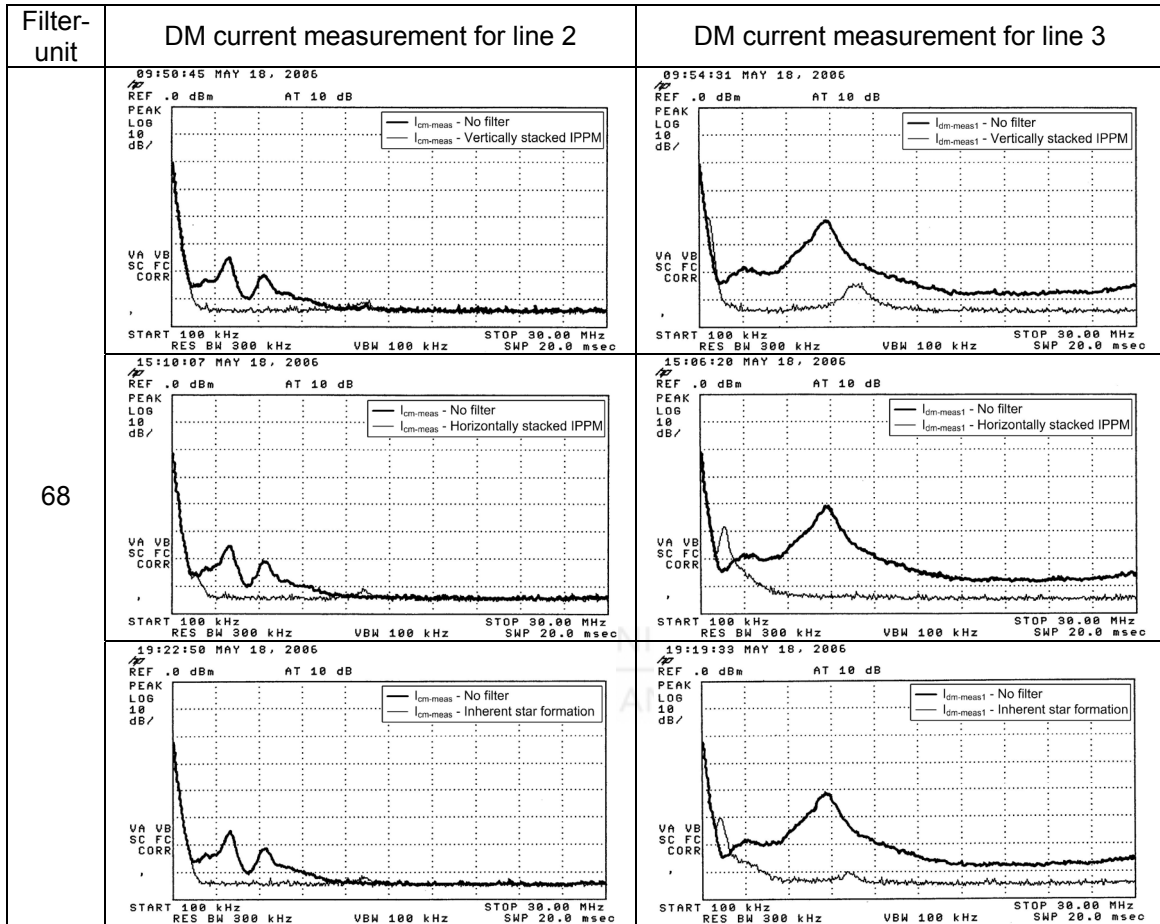**Table E-I: Measured results obtained for the physical realisation of topology 1**

Filter-unit	DM current measurement for line 2	DM current measurement for line 3
68		
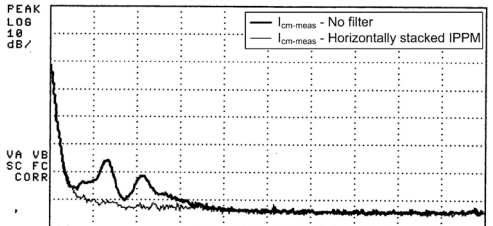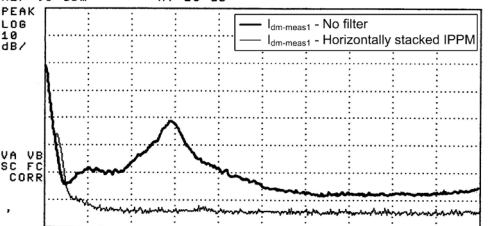
Table E-II: Measured results obtained for the physical realisation of topology 2

Filter-unit	DM current measurement for line 2	DM current measurement for line 3
68		
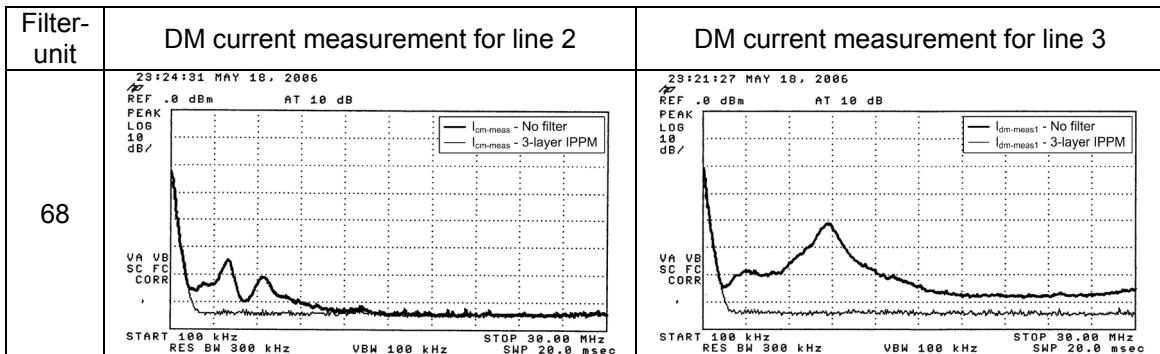
Table E-III: Measured results obtained for the physical realisation of topology 3
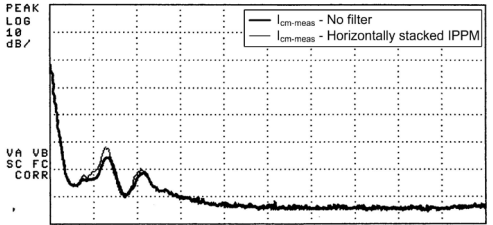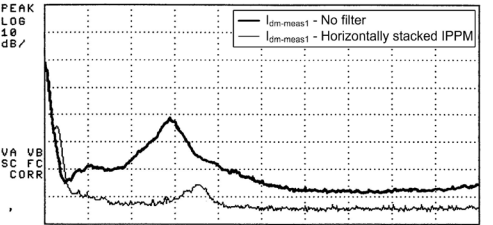
Filter-unit	DM current measurement for line 2	DM current measurement for line 3
67	16:30:53 MAY 18, 2006 REF .0 dBm AT 10 dB PEAK LOG 10 dB/ Icm-meas - No filter Icm-meas - Horizontally stacked IPPM VA VB SC FC CORR START 100 kHz STOP 30.00 MHz RES BW 300 kHz VBW 100 kHz SWP 20.0 msec	16:33:44 MAY 18, 2006 REF .0 dBm AT 10 dB PEAK LOG 10 dB/ Idm-meas1 - No filter Idm-meas1 - Horizontally stacked IPPM VA VB SC FC CORR START 100 kHz STOP 30.00 MHz RES BW 300 kHz VBW 100 kHz SWP 20.0 msec
68	16:13:26 MAY 18, 2006 REF .0 dBm AT 10 dB PEAK LOG 10 dB/ Icm-meas - No filter Icm-meas - Horizontally stacked IPPM VA VB SC FC CORR START 100 kHz STOP 30.00 MHz RES BW 300 kHz VBW 100 kHz SWP 20.0 msec	16:10:18 MAY 18, 2006 REF .0 dBm AT 10 dB PEAK LOG 10 dB/ Idm-meas1 - No filter Idm-meas1 - Horizontally stacked IPPM VA VB SC FC CORR START 100 kHz STOP 30.00 MHz RES BW 300 kHz VBW 100 kHz SWP 20.0 msec

References

[1]   F.C. Lee, J.D. van Wyk, D. Boroyevich, G.Q. Lu, Z. Liang, P. Barbosa, "Technology Trends toward a System-in-a-Module in Power Electronics", *IEEE Circuits and Systems Magazine*, Vol. 2, No. 4, Fourth quarter, 2002, pp. 4-23.

[2]   J.T. Strydom, J.D. van Wyk and M. A. de Rooij, "Integration of a 1-MHz Converter with Active and Passive Stages", *Applied Power Electronics Conference and Exposition* (APEC), Vol. 2, 2001, pp. 1045-1050.

[3]   Johan Tjeerd Strydom and Jacobus Daniel van Wyk, "Volumetric Limits of Planar Integrated Resonant Transformers: A 1 MHz Case Study", *IEEE Transactions on Power Electronics*, Vol. 18, No. 1, 2003, pp. 236-247.

[4]   Rengang Chen, J.D. van Wyk and W.G. Odendaal, "Planar Electromagnetic Integration Technologies for Integrated EMI Filters", *Industry Applications Conference*, Vol. 3, 2003, pp. 1582-1588.

[5]   Ned Mohan, Tore M. Undeland, William P. Robbins, *Power Electronics - Converters, Application and Design*, Third Edition, John Wiley and Sons Inc., 2003.

[6]   Edited by Bimal K. Bose, *Power Electronics and Variable Frequency Drives – Technology and Applications*, J. Holtz, *Chapter 4 - Pulse Width Modulation for Electronic Power Conversion*, IEEE Press, 1996.

[7]   Gary L. Skibinski, Russel J. Kerkman, Dave Schlegel, "EMI Emissions of Modern PWM AC Drives", *IEEE Industry Applications Magazine*, Vol. 5, No. 6, November/December 1999, pp. 47-81.

[8]   Clayton R. Paul, *Introduction to Electromagnetic Compatibility*, John Wiley and Sons Inc., 1992.

[9]   Li Ran, Sunil Gokani, Jon Clare, Keith John Bradley, Christos Christopoulos, "Conducted Electromagnetic Emissions in Induction Motor Drive Systems Part II: Frequency Domain Models", *IEEE Transactions on Power Electronics*, Vol. 13, No. 4, July 1998, pp. 768-776.

[10]   Jay M. Erdman, Russel J. Kerkman, David W. Schlegel, Gary L. Skibinski, *Effect of PWM Inverters on AC Motor Bearing Currents and Shaft Voltages*, IEEE Transactions on Industry Applications, Vol. 32, No. 2, March/April 1996, pp.250-259.

[11]   Hirofumi Akagi, Hiroshi Hasegawa, Takafumi Doumoto, "Design and Performance of a Passive EMI Filter for use with a Voltage-Source PWM Inverter having Sinusoidal Output Voltage and Zero Common-Mode Voltage", IEEE Transactions on Power Electronics, Vol. 19, No. 4, July 2004, pp. 1069 – 1076.

[12]   Richard Lee Ozenbaugh, "EMI Filter Deisgn", Marcel Dekker Inc., 1996.

[13]   W. Shen, F. Wang, D. Boroyevich, Y. Liu, "*Definition and Acquisition of CM and DM EMI Noise for General-Purpose Adjustable Speed Motor Drives*",

Power Electronics Specialist Conference (PESC), Vol. 2, 2004, pp. 1028-1033.

[14] P.H. Swart, C.G. Steyn, *Inleiding tot Stelsels*, Third Edition, AGS Drukkers, 1991.

[15] Roland E. Thomas, Albert J. Rosa, *The Analysis and Design of Linear Circuits*, Third Edition, John Wiley and Sons, Inc., 2001.

[16] Ralph, J. Smith, Richard C. Dorf, *Circuits, Devices and Systems*, Fifth Edition, John Wiley and Sons, Inc., 1992.

[17] Elliott R. Brown, "RF-MEMS Switches for Reconfigurable Integrated Circuits", *IEEE Transactions on Microwave Theory and Techniques*, Vol. 46, No. 11, November 1998, pp. 1868-1880.

[18] Lingyin Zhao, *Generalised Frequency Plane Model of Integrated Electromagnetic Power Passives*, Ph.D. thesis, Virginia Polytechnic Institute and State University, 2004, pp. 9-16, 23-60.

[19] G.S. McMullin, I.W. Hofsajer, "Frequency domain Modelling of Multi-conductor Planar Integrated Passive Structures", *Applied Power Electronics Conference and Exposition* (APEC), 2006, pp. 1611-1616.

[20] Richard C. Dorf, James A. Svoboda, *Introduction to Electric Circuits*, Fourth Edition, John Wiley and Sons, Inc., 1999, pp. 623.

[21] Allan H. Robbins, Wilhelm C. Miller, *Circuit Analysis Theory and Practice*, Second Edition, Delmar Thomson Learning, 2000, pp. 893.

[22] 3M^{TM} Flexible Circuits, Flex circuits and IC packaging at 3M.com, http://www.3m.com/us/electronics_mfg/microelectronic_packaging/contact/index.html, 2005.

[23] M.F. Ramabulana, K. de Jager, J. Claassens, G.S. McMullin, J.J. Wolmarans, E.C.W. de Jong, I.W. Hofsajer, "*Applications of Low Power Embedded Capacitor PCB Technology to High Power Integrated Passives*", South African Universities Power Electronics Conference (SAUPEC), January 2006, pp. 114-120.

[24] http://www.pwbrc.org/faq10.cfm, Accessed 24 may 2005, Printed Wiring Board Resource Center.

[25] Joel S. Peiffer, "Embedded Capacitor Material Evaluation", IPC SMEMA Council Apex, 2001.

[26] Jacobus Marthinus Barnard, *'n Nuwe Tipe Aandryfstelsel met Mikrorekenaarbeheer, Elektroniese Wiselrigters en Induksiemasjiene vir Elektriese Rolstoele met Batterye*, M.Ing dissertation, Rand Afrikaans University, January 1992, pp. 31.

[27] Ferroxcube, E64 datasheet, February 2002.

[28] Mario Olicar Crosato, *An Investigation of Charge Balancing in Planar Inductors from an Electro-Magnetic-Compatibility Perspective*, M.Ing dissertation, Rand Afrikaans University, February 2004, pp. 32-34.

[29] M.L. Heldwein, T. Nussbaumer, F. Beck, J.W. Kolar, "*Novel Three-Phase CM/DM Conducted Emissions Separator*", *Applied Power Electronics Conference and Exposition* (APEC), Vol. 2, 2005, pp. 797-802.

[30] STMicroelectronics, SG3525A datasheet, June 2000.

[31] International Rectifiers, Jonathon Adams, *Design Tip – Bootstrap Component Selection for Control ICs*, 4 September 2001.

[32] Lonnie C. Ludeman, *Fundamentals of Digital Signal Processing*, John Wiley and Sons Inc., New York, 1986, pp 59.